From Crystal to Adsorption: New Insights into Layered Double Hydroxides derived Sorbent Materials for Carbon Capture

Li Anne Cheah

Submitted for the degree of Doctor of Philosophy

Heriot-Watt University

School of Engineering and Physical Sciences

Institute of Mechanical Process and Energy Engineering

March 2023

Abstract

With the goal of designing mixed metal oxides (MMOs) that have better CO_2 sorption performance, such as sorption capacities greater than 1.35 mmol/g at the intermediate temperature range (200 – 400 ˚C), detailed investigation was performance on the MMOs and their precursor, layered double hydroxides (LDHs). The novelty of work lies in the crystal chemistry approach, which uses the crystal lattice parameter "*a*" of precursors LDHs to obtain the "true" chemical composition of sorbent material. Two systematic studies based on this approach were conducted to study the effects of different variables on the CO_2 adsorption performance of resultant MMOs, e.g., $x_{crystal}$ of LDH phase, synthesis methods and choice of precursors. Synthesis methods was found to be the most important variable affecting the properties of LDHs and MMOs phase; and co-precipitation method produces LDH-derived MMOs sorbent with the more desirable CO_2 capture performance, compared to the urea hydrolysis method. The results obtained from these systematic studies allow the establishment of a new crystal-chemical model for Mg-Al based LDHs that is fundamentally sound and more accurate when obtaining *x* from *a*. Finally, unambiguous characterization of the equilibrium isotherms and diffusion coefficient of pristine Mg-Al MMOs was conducted for the intermediate temperature range, using gravimetric and zero length column method. In the low-pressure region (< 8 bar) and 200 ˚C, the equilibrium capacities and diffusional coefficient values of pristine MMOs are found comparable to those promoted with alkali metal salts (AMS). However, in the high-pressure region (8 - 30 bar) and temperature range between 300 – 400 ˚C, the AMS-promoted MMOs shows almost a two-fold increase in the equilibrium capacities. Overall, the present work set a reference case for the CO_2 adsorption performance of LDH-derived MMOs.

Dedication

I dedicated this achievement to my home country, Malaysia and second country, Scotland,

My grandparents, father and mother, sister and brother, and friends that, with love and joy, supported and enlightened me in the journey.

And all the scientists and teachers I have encountered and learned from,

I appreciate this predestination with all of you.

Lots of Love.

Acknowledgement

Firstly, my heartfelt thanks to my primary supervisor, Prof. Susana Garcia Lopez. Thank you for your continuous support and guidance throughout the PhD journey, being a supervisor with wisdom and care for your students and team. I appreciate the time, inspiration, patience, freedom and encouragement you have given for the completion of this thesis.

Secondly, my sincere thanks to my second supervisor, Prof. M. Mercedes Maroto-Valer, who has given me this chance to join your group as a PhD student. I could not have undertaken this journey without you.

I am also thankful to my research group, the Research Centre for Carbon Solutions (RCCS) and especially my team, the RCCS Capture team, for bringing their brilliant mind into view, for exciting discussions and for teamworks.

A warm thank to Emeritus Professor, Alirio E. Rodrigues and his research group - Laboratory of Separation and Reaction Engineering (LSRE) from University of Porto. It has been a great pleasure working with the group and, with the brilliant and kind-hearted researchers who I still miss them very much. I especially thank Alexandre F.P. Ferreira and Ana M. Ribeiro, who have guided me throughout the three-month internship period and the online meetings we had after returned to Edinburgh.

I must also thank a number of individuals

Dr. Amir Jahanbakhsh, Dr. Manohara Gudiyor Veerabhadrappa, Dr. Sean Higgins, Prof. Raffaella Ocone, Dr. Giuseppe Bagnato, Dr. Rute Seabra, Dr. Paulo Carmo, Dr. Caroline Maria, the EPS PGR office team, IT help team

And those I have not named, who have supported, guided, and hearten me in this journey.

ACADEMIC REGISTRY

Research Thesis Submission

Name*:*	Li Anne Cheah		
School:	EPS		
Version: *(i.e. First, Resubmission , Final)*	Final	Degree Sought:	PhD chemical engineering

Declaration

In accordance with the appropriate regulations, I hereby submit my thesis and I declare that:

1. The thesis embodies the results of my own work and has been composed by myself
2. Where appropriate, I have made acknowledgement of the work of others
3. The thesis is the correct version for submission and is the same version as any electronic versions submitted*.
4. My thesis for the award referred to, deposited in the Heriot-Watt University Library, should be made available for loan or photocopying and be available via the Institutional Repository, subject to such conditions as the Librarian may require
5. I understand that as a student of the University I am required to abide by the Regulations of the University and to conform to its discipline.
6. I confirm that the thesis has been verified against plagiarism via an approved plagiarism detection application e.g. Turnitin.

ONLY for submissions including published works

7. Where the thesis contains published outputs under Regulation 6 (9.1.2) or Regulation 43 (9) these are accompanied by a critical review which accurately describes my contribution to the research and, for multi-author outputs, a signed declaration indicating the contribution of each author (complete)

8. Inclusion of published outputs under Regulation 6 (9.1.2) or Regulation 43 (9) shall not constitute plagiarism.

Signature of Candidate :		Date:	01/03/2023

Submission

Submitted By *(name in capitals):*	LI ANNE CHEAH
Signature of Individual Submitting:	
Date Submitted:	01/03/2023

For Completion in the Student Service Centre (SSC)

Limited Access	Requested	Yes		No		Approved	Yes		No	
E-thesis Submitted (mandatory for final theses)										
Received in the SSC by *(name in capitals):*						Date:				

Inclusion of Published Works

This thesis contains one or more multi-author published works. In accordance with Regulation 6 (9.1.2) I hereby declare that the contributions of each author to these publications is as follows:

Citation details	Cheah, L.A., Manohara, G.V., Maroto-Valer, M.M. and Garcia, S., 2020. Layered Double Hydroxide (LDH)-Derived Mixed Metal Oxides (MMOs): A Systematic Crystal-Chemical Approach to Investigating the Chemical Composition and its Effect on High Temperature CO2 capture. *ChemistrySelect*, 5(19), pp.5587-5594
Author 1 (Cheah L. A.)	conceptualization and design of the study, experiments, acquisition and interpretation of data, visualization, and writing of the first draft of the manuscript and revision
Author 2 (Manohara G.V.)	conceptualization and design of the study, writing—review and editing for important intellectual content.
Author 2 (Maroto-Valer, M.M.)	supervision, project administration, and funding acquisition.
Author 2 (Garcia S.,)	conceptualization and design of the study, writing—review and editing for important intellectual content, supervision, project administration, and funding acquisition.

Signature:	
Date:	01/03/2023

Citation details	Cheah, L.A., Manohara, G.V., Maroto-Valer, M.M. and Garcia, S., 2022. Impact of Synthesis Method and Metal Salt Precursors on the CO_2 Adsorption Performance of Layered Double Hydroxides Derived Mixed Metal Oxides. *Front. Energy Res.* 10:882182. doi: 10.3389/fenrg.2022.882182
Author 1 (Cheah L. A.)	conceptualization and design of the study, experiments, acquisition and interpretation of data, visualization, and writing of the first draft of the manuscript and revision
Author 2 (Manohara G.V.)	conceptualization and design of the study, writing— review and editing for important intellectual content.
Author 2 (Maroto-Valer, M.M.)	supervision, project administration, and funding acquisition.
Author 2 (Garcia S.,)	conceptualization and design of the study, writing— review and editing for important intellectual content, supervision, project administration, and funding acquisition.
Signature:	
Date:	01/03/2023

TABLE OF CONTENTS

Contents

LIST OF FIGURES

LIST OF TABLES

LIST OF ABBREVATIONS

AMS	Alkaline Metal Salt
BECCS	Bioenergy with CCS
BEIS	Department for Business, Energy & Industry Strategy
BET	Branauer-Emmett-Teller
CaO	Calcium Oxides
CCS	Carbon Capture and Storage
CCUS	Carbon Capture, Utilisation and Storage
CH_4	Methane
CO_2	Carbon Dioxide
CP	Co-precipitation Method
DAC	Direct Air Capture
DFT	Density Functional Theory
DRI	Direct Reduced Iron
DSL	Dual-Site Langmuir Equation
EAF	Electrification
EOR	Enhanced Oil Recovery
ET-PSA	Elevated Temperature Pressure Swing Adsorption
FTIR	Fourier Transform Infrared Ray
GHGs	Greenhouse Gases
HTPSA	High temperature PSA cycles
IDS	Industrial Decarbonisation Strategy
IEA	International Energy Agency
IGCC	Integrated Coal Gasification Combined Cycle
IPCC	The Intergovernmental Panel on Climate Change
LCA	Life Cycle Assessment
LDHs	Layered Double Hydroxides
LTR	Long time analysis
MgO	Magnesium Oxides
MMOs	Mixed Metal Oxides
MOFs	Metal-Organic Frameworks
MR	Membrane Reactor
MSB	Magnetic Suspension Balance
NDCs	National Determined Contributions
NETs	Negative Emission Technologies
NMR	Nuclear Magnetic Resonance
NO_x	Nitrous oxide
PSA	Pressure Swing Adsorption
PXRD	Powder X-Ray Diffractogram
SEM	Scanning Electron Microscopy
SERPs	Sorption Enhanced Reaction Processes
SEWGS	Sorption Enhanced Water Gas Shift
SMR	Steam Methane Reforming
TGA	Thermogravimetric Analyser

TSA	Temperature Swing Adsorption
UH	Urea Hydrolysis Method
UK	United Kingdom
US	United States
VSA	Vacuum Swing Adsorption
ZLC	Zero Length Column

LIST OF PUBLICATIONS

Journal Publications

Cheah, L.A., Manohara, G.V., Maroto-Valer, M.M. and Garcia, S., 2020. Layered Double Hydroxide (LDH)-Derived Mixed Metal Oxides (MMOs): A Systematic Crystal-Chemical Approach to Investigating the Chemical Composition and its Effect on High Temperature CO_2 capture. *ChemistrySelect*, *5*(19), pp.5587-5594.

Cheah, L.A., Manohara, G.V., Maroto-Valer, M.M. and Garcia, S., 2022. Impact of Synthesis Method and Metal Salt Precursors on the CO2 Adsorption Performance of Layered Double Hydroxides Derived Mixed Metal Oxides. *Frontiers in Energy Research*, *10*.

Lund, A., Manohara, G.V., Song, A.Y., Jablonka, K.M., Ireland, C.P., Cheah, L.A., Smit, B., Garcia, S. and Reimer, J.A., 2022. Characterization of Chemisorbed Species and Active Adsorption Sites in Mg–Al Mixed Metal Oxides for High-Temperature CO2 Capture. *Chemistry of Materials*, *34*(9), pp.3893-3901.

Journal Publications in Preparation

Cheah, L.A., Manohara, G.V., Maroto-Valer, M.M. and Garcia, S., 2022. A new Crystal-Chemical Model to Determine the True Chemical Composition of Layered Double Hydroxides (LDHs). *Inorganic Chemistry Frontiers*, **[Under Reviewed]**.

Conference Paper

Cheah, L.A., Manohara, G.V., Maroto-Valer, M.M. and Garcia, S., 2018, October. Layered Double Hydroxides: A Systematic Approach to Investigate the Effect of Mg: Al Ratio on CO2 Capture. In *14th Greenhouse Gas Control Technologies Conference Melbourne* (pp. 21-26).

Conference Presentations

Cheah, L.A., Manohara, G.V., Maroto-Valer, M.M. and Garcia, S., Layered Double Hydroxides for CO_2 Capture: A systematic approach to investigate the effect of Mg: Al Ratio. **Poster Presentation**. UKCCSRC Spring Conference 2018, Cambridge, United Kingdom.

Cheah, L.A., Manohara, G.V., Maroto-Valer, M.M. and Garcia, S., Layered Double Hydroxides for CO_2 Capture: A systematic approach to investigate the effect of Mg: Al Ratio. **Poster Presentation**. GHGT-14, Melbourne, Australia.

Cheah, L.A., Manohara, G.V., Maroto-Valer, M.M. and Garcia, S., Layered Double Hydroxides for CO_2 Capture: A systematic approach to investigate the effect of Mg: Al Ratio. **Poster Presentation**. UKCCSRC ECR Meeting, Edinburgh, United Kingdom.

Cheah, L.A., Manohara, G.V., Maroto-Valer, M.M. and Garcia, S., Development of energy-efficient novel hydrotalcite-based adsorbent system for Industrial CO_2 capture. **Poster Presentation**. EPS Poster Event, Heriot-Watt University, Edinburgh, United Kingdom.

Cheah, L.A., Manohara, G.V., Maroto-Valer, M.M. and Garcia, S., Layered Double Hydroxides for CO_2 Capture: A systematic approach to investigate the effect of Mg: Al Ratio. **Poster Presentation**. UKCCSRC 2019 Winter School, Sheffield, United Kingdom.

Cheah, L.A., Manohara, G.V., Maroto-Valer, M.M. and Garcia, S., Development of energy efficient novel mixed metal oxides-based sorbent system for Industrial CO_2 capture. **Oral Presentation**. Chem Eng Day 2019, Heriot-Watt University, Edinburgh, United Kingdom.

Cheah, L.A., Manohara, G.V., Maroto-Valer, M.M. and Garcia, S., Development layered double hydroxides derived sorbent for Industrial CO_2 capture at high temperature. **Poster Presentation**. Gordon Research Conference 2019, Les Diablerets, Switzerland.

Cheah, L.A., Manohara, G.V., Maroto-Valer, M.M. and Garcia, S., Development layered double hydroxides derived sorbent for Industrial CO_2 capture at high temperature. **Poster Presentation**. Trondheim CCS Conference 2019, Trondheim, Norway.

Cheah, L.A., Manohara, G.V., Ana M. Ribeiro, Aleandre F.P. Ferreira, Alirio E. Rodrigues, Maroto-Valer, M.M. and Garcia, S., High Temperature CO_2 capture using Hydrotalcite-based sorbents. **Poster Presentation**. Chem Eng Day UK 2020, University of Bradford, Bradford, UK [Online].

<center>**Chapter 1: Introduction**</center>

1.1 Relevance and Motivation

1.1.1 Global warming and CO_2 capture

Global warming is now widely recognized as one of the greatest global issues facing mankind. The rise in atmospheric concentration of greenhouse gases (GHGs), such as carbon dioxide (CO_2), methane (CH_4), nitrous oxide (NO_x), fluorinated gases, etc., is part of the cause of the warming. Among them, CO_2 is widely believed to be the major cause, as data shows it accounts for the majority of the emitted GHGs (72 %) [1]. However, CO_2 is inevitably produced from the burning of fuels for daily activities. Today the atmospheric CO_2 concentration has reached an alarming new high level of 420 ppm (Figure 1.1A) [2]. The forecast predicts that this concentration will exceed 600 ppm in 2050 if anthropogenic CO_2 emissions are not controlled. This likely cause an increase in global surface temperature of between 1.5 - 2 °C relative to the pre-industrial level by the end of the 21st century (Figure 1.1B) [3]. The world must reduce emissions to as close to zero as possible by middle of the 21st century to prevent further catastrophic events from happening. At the United Nations Climate Change Conference (COP21) in December 2015, 195 countries signed the Paris agreement to set a global action plan to keep the increase in global average temperature well below 2 °C and achieve zero net anthropogenic GHGs emission during the second half of the 21st century [4].
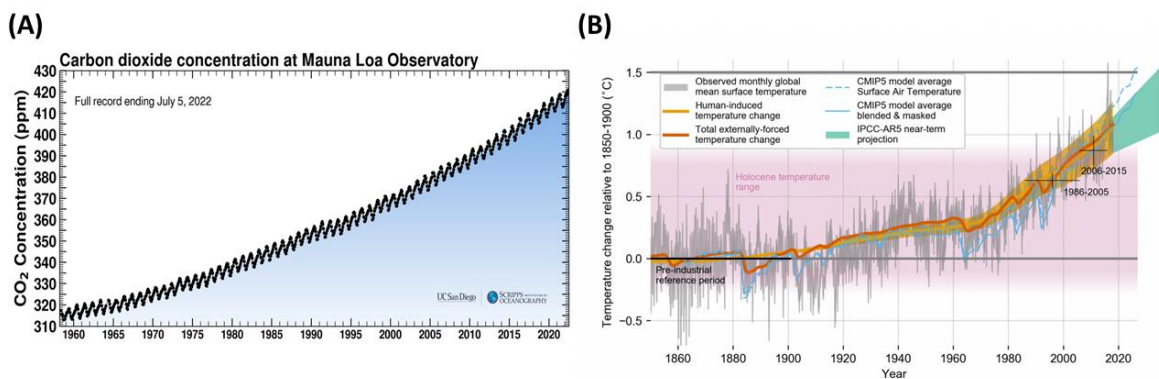
Figure 1.1 – (A) Keeling curve, graph of change in atmospheric CO_2 concentration from 1958 to the present [2] and (B) evolution of global mean surface temperature (GMST) over the period of instrumental observations [3]

Currently, global net anthropogenic GHG emissions are estimated to be 59 ± 6.6 gigatonnes CO_2 equivalent emission (Gt CO_2e) in 2019 (Figure 1.2) [5]. To achieve the Paris climate targets with a higher percentage probability (> 66%), The Intergovernmental Panel on Climate Change (IPCC) predicted that global GHGs emissions in 2030 must be maintained at approximately 42 Gt CO_2e per year for a 2 °C scenario, or 36 Gt CO_2e per year for a 1.5 °C scenario [3]. However, based on the IPCC sixth assessment report, the national determined contributions (NDCs) announced so far would likely result in warming exceeding 1.5 ℃ and make it harder after 2030 to limit warming to below 2 ℃ [5]. This clearly shows an emissions gap and the immediate need for decarbonization efforts.
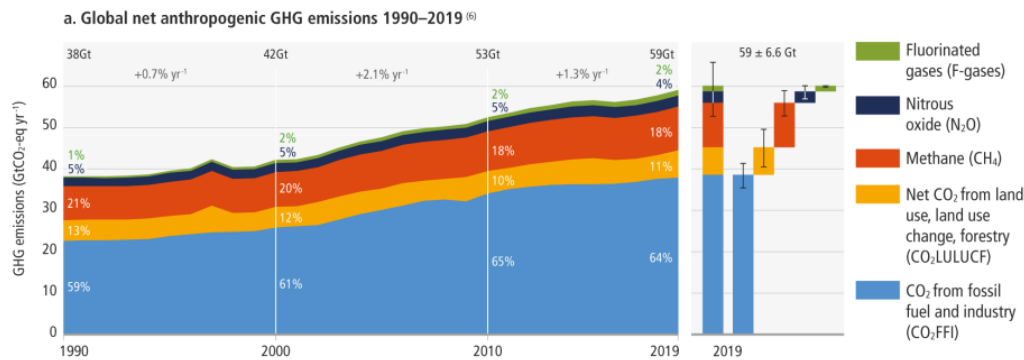
Figure 1.2 - Global net anthropogenic GHG emissions 1990 – 2019 [5]

In June 2019, the United Kingdom (UK) became the first major economy that passed laws to achieve net zero emissions relative to 1990 levels by 2050 [6]. Currently, the UK accounts for less than 1 % of the global GHGs emissions [7]. The territorial UK GHG emissions were estimated to be 454.8 Mt CO_2e in 2019, with CO_2 predominantly contributing 80 % of the emissions [8]. Figure 1.3 shows the UK GHGs emission by sector, with transportation being the highest contributing sector (27 %). While deep decarbonisation (i.e., gradual elimination of carbon-emitting fuels) can be achieved through electrification or fuel switching in most sectors, including transportation, some sectors require a combination of methods to achieve deep decarbonisation, such as the industry and aviation sectors. In total, the energy and industry sector accounts for approximately 40 % of the UK GHGs emission in 2019, with CO_2 being the most prominent gas.

Reaching net zero means tackling all sources of emissions, which means the need to transform every sector of the global economy. Efficiency improvements and a full switch to

a carbon-free energy source are deemed to be the ideal deep decarbonisation approaches, but realistically, present technological advances in those fields are still not capable of meeting both energy demand and zero emissions. It is predicted that fossil fuels are likely to continue being the primary energy source until 2050 [9]. Although renewables such as solar and wind energy are now widely available and sometimes can be cheaper than fossil fuel, their main pitfall is energy storage, which still requires major development. On a global scale, phasing out fossil-fuel-based energy will require time before our economies can rely on carbon-free systems. At the same time, new initiatives, such as nuclear energy, also involve the inevitable challenges from the public acceptance, implementation time and safety issues. Thus, the need for additional technologies capable of achieving deep emissions cuts to assist in this transition is unquestionable. For this reason, technologies such as carbon capture and storage (CCS) are necessary to meet the agreed net-zero GHGs emission targets.
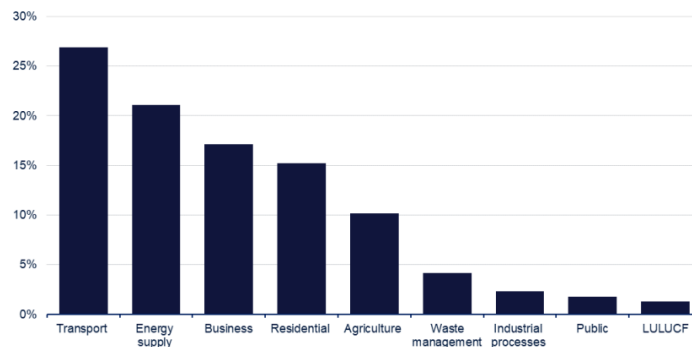
Figure 1.3 - Territorial UK GHGs by contributing sector, 2019 (%) [9]

1.1.2 Carbon Capture and Storage (CCS)

CCS is a proven technology used to prevent the release of CO_2 produced into the atmosphere permanently. The technology is mainly comprised of three components: 1) the capture of CO_2 from large point sources such as power plants and industrial plants; 2) its transport via, for instance, a network of pipelines or shipping, and 3) CO_2 storage in deep subsurface geological formation where CO_2 can be safely stored over a long geological period. Ideally, the capture site and the storage site would be in close proximity but this is rarely the case. If stored underground, close monitoring of the injected site is required by the relevant authority to ensure safe CO_2 storage and prevent abrupt leakages.

The term CCS is often interchangeable with CCUS, which stands for Carbon Capture, Utilisation and Storage. The only difference is the inclusion of utilisation, in which the purpose is to make use of the captured CO_2. One way of utilisation is using the captured CO_2 directly, without any conversion. For example, CO_2 injection for Enhanced Oil Recovery (CO_2-EOR), where the captured CO_2 is used as an injecting solvent to recover oil and gas from depleted reservoirs. CO_2-EOR operations are a mature technology since 1972 [10]. The other way of utilisation is the conversion of captured CO_2 into valuable products. Nevertheless, the IPCC report states that this type of CO_2 utilisation is likely not going to be a major source of CO_2 reduction due to the limited market capacity of the converted CO_2 products [11]. In a 2019 report, the International Energy Agency (IEA) also arrives at a similar conclusion that CO_2 utilisation cannot replace CO_2 storage in delivering the emissions reductions needed to meet the Paris Agreement ambitions [12]. Nevertheless, CCU still plays a critical role in the net zero landscape as it can target CO_2 sources that are too distributed for centralized capture or for locations without sufficient storage reservoirs.

In a net zero world, CCUS technologies play an important role in assisting the transformation to a decarbonised economy, as well as the creation of new energy economies. This is because CCUS has the capability of decarbonising large industries – power, steel, cement, petrochemical, and biofuels, with only modest modifications to the existing infrastructure. Gas-fired power stations equipped with CCS are one option to provide low-carbon electricity to complement renewables and ensure that the electricity grid remains resilient through the energy transition. CCUS is also the only option capable to decarbonizing "unavoidable" process emissions, such as those from cement and steel industries, which present a major challenge in the effort to reduce global CO_2 emissions. Achieving zero emissions in these sectors may be impossible without CCUS. Carbon capture processes that specifically target these industrial sources are now categorized as Industrial CO_2 capture.

CCUS also facilitates the production of low-carbon hydrogen – the so-called 'blue hydrogen' derived from non-renewable resources. At present, almost all the hydrogen in the UK is produced from steam methane reforming (SMR) without any of the CO_2 emissions captured [13]. With CCUS technology, a CO_2 capture rate of up to 80-90 % has been

demonstrated in commercial SMR projects, e.g., Shell Quest Project (Alberta, Canada) & Air Products' Port Arthur Project (Texas, USA) [14]–[16]. Although there is an added cost of 30 % due to CCUS, this percentage may be reduced with second-generation technologies, which are established based on insights from the first generations and may present interesting opportunities for process intensification [17]. One example is the Sorption Enhanced Reaction Processes (SERPs), which combines either the reforming or water gas shift reaction with the pre-combustion carbon capture process in a one-step reactor to produce high-purity hydrogen from syngas [18], [19]. Hydrogen has always been an important feedstock for many industrial processes, such as fertilisers, petrochemical products, semiconductors and more. Thus, the use of blue hydrogen as an alternative fuel/feedstock can greatly reduce the CO_2 footprint of industrial processes.

CCUS also helps in the delivery of negative emissions, which are required to achieve net carbon neutrality by compensating the residual emissions that cannot be avoided or offsetting excessive emissions in scenarios where there is an overshoot of climate targets. These types of technologies are called Negative Emission Technologies (NETs), which focus on extracting CO_2 from the atmosphere. Two main approaches for NETs include technology-based or nature-based solutions. Direct Air Capture (DAC) and Bioenergy with CCS (BECCS) are among the technological options that have received the most attention in recent years. BECCS makes use of crops grown to capture CO_2 from the atmosphere, which can be used as fuel for electricity and reduce emissions. DAC application utilise carbon capture systems to separate CO_2 from atmospheric air. As of November 2021, 19 DAC plants are operating worldwide, capturing more than 0.01 Mtonnes CO_2 per year [20]. Nature-based NETs utilize biological processes to remove CO_2 from the atmosphere, such as afforestation, reforestation, soil carbon management, enhanced weathering, and ocean fertilisation/alkalinisation.

For CO_2 transport, the most common approach is via pipelines. Other methods currently being investigated are shipping, truck, and rail. CO_2 transport via pipelines is a mature technology for large-scale transportation of CO_2, which has been widely used for more than 40 years, mostly for CO_2-EOR operations [21]. The most efficient way to transport CO_2 by pipeline is in its supercritical phase, which means at high pressures (~ 20 Mtpa) [22].

Realistically, pipeline-grade carbon steel is the only economical choice for long-distance and high-pressure CO_2 pipelines [23]. Similarly, transport of CO_2 via shipping and truck/rail is also common for food and beverage sector, but they mainly exist in small scale (< 2000 ktonnes CO_2). The business model of liquified natural gas (LNG) and liquified petroleum gas can be anticipated to be replicated for CO_2; but it is more challenging to transport CO_2 in these modes due to the more stringent phase properties of CO_2, i.e., it requires transportation in semi-pressurised vessels at pressures and temperatures near the triple point.

For CO_2 storage, saline aquifers present the largest storage capacity for CO_2 and are geographically abundant [24]. However, the saline formation has practically no or low economic value, thus there is very little investment for this type of CO_2 injection technology [25]. The injection of CO_2 into depleted oil fields, on the contrary, is much more well-developed and invested in as it is associated with CO_2-EOR operations. Although the main driver was to maximize oil production, the need for an inexpensive source of concentrated CO_2 may bridge CCUS technology and CO_2-EOR projects together. In the United States alone, 3 billion cubic feet of concentrated CO_2 are injected underground every day through CO_2-EOR operations [26]. However, the majority of CO_2 injected in these projects (70%) is produced from naturally occurring underground CO_2 deposits [27]. If industrially sourced CO_2 are used, then "carbon negative oil" may be produced. The IEA estimates that 34 % of future consumption of CO_2 will be driven by CO_2-EOR operations [12].

Nevertheless, considering the magnitude of the task at hand, the present global decarbonization efforts are still not satisfactory. IEA estimates that the global scale of CCUS in 2030 and 2050 has to be 10-15 times and 100 times greater than the current sequestration capacity, which is around 40 - 50 Mtonnes (Figure 1.4) [28]. However, high carbon mitigation costs and associated financial risks are the main challenges yet to be overcome. Power plants installed with CCUS usually suffer from high energy penalty, with a theoretical lower bound of 11 % to as much as 40 % [29]. The first generation CCUS projects have demonstrated that the cost of capture and compression of CO_2 from power stations are in the range of USD 70 – 105 per tonnes of CO_2 [30]. The capture of CO_2 is the

most expensive component of CCUS. The cost of capture can vary greatly by CO_2 source, from a range of USD15-25 per tonnes of CO_2 for industrial processes producing almost pure or highly concentrated CO_2 streams (such as ethanol production or natural gas processing) to USD 40-120 per tonnes CO_2 for processes with dilute gas streams, such as cement production and power generation [31]. The rest are then covered by transport and storage. Using an amine solvent-based system, the Shell's Quest CO_2 capture demonstration project shows that the capture cost accounts for 55 % of the capital expenditure investment for CCUS [32]. Thus, the reduction of the capture cost is a key aspect to overcome to make CCUS competitive and the widespread of technologies.
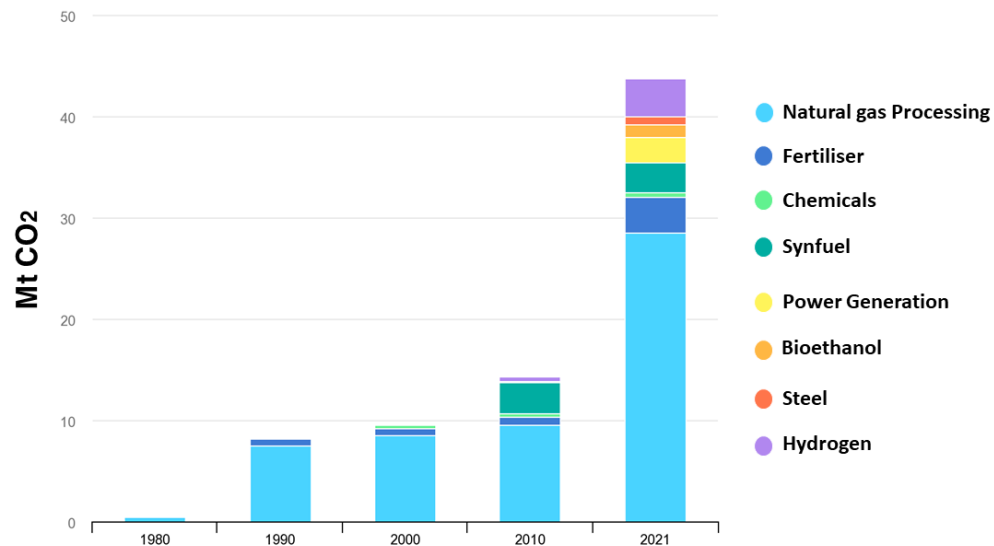
Figure 1.4 - CCUS facilities in operation by application, 1980 – 2021 [33]

Among the CO_2 capture technologies, liquid amine and solid sorbent systems are the closest to commercialisation. New processes such as membrane-based and cryogenic technologies still pose significant process challenges which require development until they are ready for large-scale projects. Despite all these facts, the selection of a suitable CCUS technology will depend on the type of emissions, the emitting sector/process, CO_2 destination and, the available resources in the specific local/regional setting; thereby it can vary significantly from country to country, industry to industry and even, process to process. Hence, it is important to consider all aforementioned factors when proposing a CCUS

strategy. All the decarbonisation pathways described here are crucial to meet the Paris Agreement and carbon neutrality in the UK by 2050.

1.1.3 The role of CCUS technologies in achieving the UK's 2050 net zero target.

In its effort to shift to a fully decarbonised economy by 2050, the UK government has published the Ten Point action plan, detailing pathways to decarbonise all the GHG-emitting sectors [33], [34]. The Ten Point Action Plan makes it clear that CCUS will play a central role in addressing the UK's ambitious climate targets, particularly in the production of low-carbon hydrogen and in decarbonising industrial sources. The report identifies that investing in CCUS technologies can save around 40 Mt CO_2e between 2023 and 2032, or 9 % of 2018 UK emissions. When it was first announced in November 2020, the UK government promised to establish CCUS in two industrial clusters by the mid 2020s [33]. By 2030, there should be four of these sites, capturing up to 10 Mt CO_2 per year across the economy. In October 2021, this figure was increased to 20 - 30 Mt CO_2e per year, including 6 Mt CO_2e per year of industrial emissions by early 2030 and at least ~50 Mt CO_2e per year by the mid-2030s [34].

More specifically, in the UK, emissions from industrial clusters (i.e., areas populated with several industrial sites) account for approximately half of the industrial emissions (37.6 Mt CO_2e; around 8 % of territorial UK GHGs emission). The Industrial Decarbonisation Strategy (IDS) published in March 2021 states that CCUS will be the predominant technology solution to abate process emissions in those clusters (~ 6 Mt CO_2e per year; including BECCS by 2050). Figure 1.5 shows the UK's strategy to reduce GHG emissions from each sector of the economy by 2037 while using NETs to eliminate any remaining emissions [34].
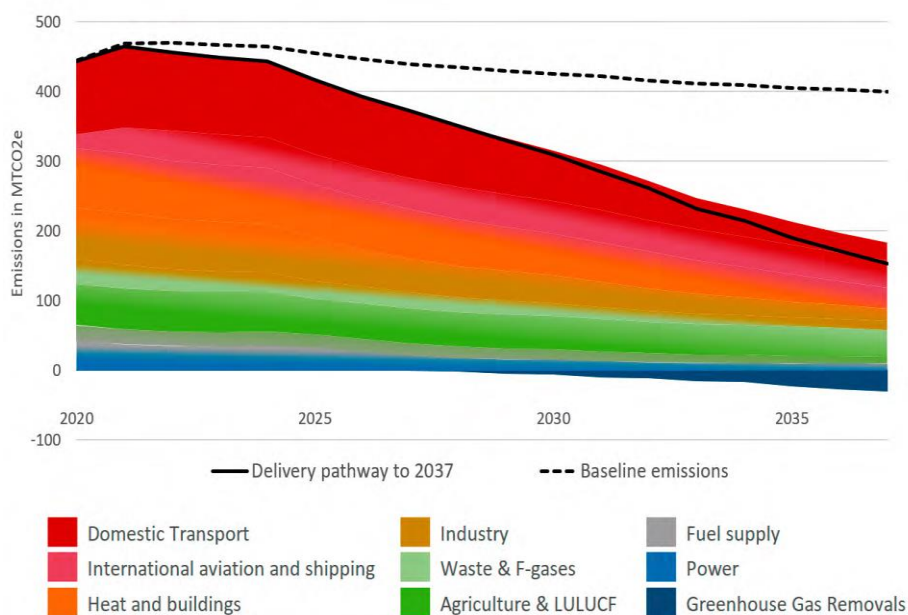
Figure 1.5 - Indicative delivery pathways to 2037 by sector in UK, 2019 [33]

Additionally, the Energy White paper released by the UK government in November 2021 proposes that at least one CCUS-enabled hydrogen project will be supported and operational in one of the four industrial clusters by 2030 [35]. This project will aid in the establishment of the commercial framework required to help stimulate the market required to deliver a future pipeline of power CCUS projects. Through the newly released British Energy Security Strategy in April 2022, the UK government has announced further investment in CCS technology to deliver a fully decarbonized electricity system by 2030, including 10 GW of low-carbon hydrogen, with 5 GW being CCUS-enabled hydrogen [36].

NETs, including natural ones such as trees or technological ones, such as carbon capture, are considered in these pathways. The deployment of BECCS and DACCS will depend on the UK's infrastructure and the availability of suitable, sustainable, and low-cost biomass feedstocks [33]. Nevertheless, the UK government has committed to a target for the deployment of engineered greenhouse removals of 5 $MtCO_2$ per year by 2030, as set out in the Net Zero Strategy [34].

The UK has identified several suitable offshore CO_2 sinks in the North and Irish Seas. Thus, it is usually assumed that the transport of CO_2 using pipelines is rather straightforward in the UK, as CO_2 is mainly captured from densely populated industrial

clusters, as outlined in the IDS. However, interestingly, a cost estimation report published by the UK Department of Business, Energy & Industry Strategy (BEIS) concludes that the CO_2 shipping costs may be lower than the equivalent CO_2 pipeline costs in the UK [37]. Nevertheless, the costs of shipment are rather unstable as they are affected by several variables, such as international regulations, fuel costs and more. Thus is harder to generalise.

1.2 Thesis aim, objectives, and structure

Due to the significance of CCUS technology for industrial CO_2 capture and hydrogen production, this thesis will mainly discuss carbon capture systems suitable for these processes. This focus is on the solid sorbent system, particularly at intermediate temperatures (200 – 400 ˚C), where it presents interesting opportunities for both industrial CO_2 capture and CCUS-enabled hydrogen production. The Mg-Al Mixed Metal Oxides (MMOs) derived from Layered Double Hydroxides (LDHs) were chosen as the solid sorbent for investigation. To gain a better understanding of the LDH-derived MMOs sorbent and aid in the design of new-generation sorbents with better CO_2 adsorption performance, the work in the thesis is structured as follow:

Chapter 2 is a literature review that gives an overview of the CCS technology and details the selection process of a suitable solid sorbent studied in the present work, i.e., LDH-derived MMOs. The gaps in knowledge that are covered in this thesis and addressed by the aim and objectives are presented at the end of the chapter.

In Chapter 3 a systematic study was conducted to investigate the effects of chemical composition (i.e., Mg/Al ratios) on the high-temperature CO_2 adsorption capacities of LDH-derived MMOs. A novel crystal-chemistry approach based on Vegard's law was used to investigate the "true" chemical composition of these LDHs, using the lattice parameter "*a*" to find the true composition, *x*.

Chapter 4 studied the impacts of synthesis method and metal salt precursors on the intermediate temperature CO_2 adsorption of LDH-derived MMOs. The present study investigated how two common synthesis methods (i.e., co-precipitation and urea hydrolysis) and two different salt precursors (i.e., metal chlorides and metal nitrates) affected the physical properties of LDHs and CO_2 capture performance of derived MMOs at 200 ˚C.

Chapter 5 is a crystal chemistry study for LDH phase. A new crystal-chemical model is established for Mg-Al-based Layered Double Hydroxides (LDHs) to determine their true chemical composition x (i.e., Mg/Al ratio) in the crystalline phase by using the unit cell parameter "a". The model was developed using the famous Vegard's law as the starting point and relates the geometrical relationships in the crystal structure of LDH.

Chapter 6 deals with the adsorption aspects of intermediate temperature CO_2 capture, using LDH-derived MMOs. This work aims to re-investigate the CO_2 adsorption behaviour of Mg-Al LDH-derived MMOs at the intermediate temperature ranges (200, 300 & 400 ˚C). First, a full characterization of precursor LDH is carried out and then the adsorption characteristics of resultant MMOs sorbent, i.e., adsorption equilibrium isotherms and intraparticle diffusion parameters, are measured.

Chapter 7 is the final chapter of this thesis, which presents the conclusions and suggestions for future work.

Chapter 2 Literature Review

2.1 Overview

This chapter first outlines an overview of CCUS technology and the current state-of-the-art. Then, a short review of CO_2 sorption is presented, along with the types of CO_2 sorbents typically proposed for the intermediate temperature range (200 – 400 ˚C). Finally, the aim and research objectives of the thesis are outlined at the end of this chapter.

2.2 Current technology for carbon capture

Before describing each of the CO_2 capture technologies and separation mechanism, it is first important to distinguish between the purification and separation processes. Purification is a process that removes undesirable components from a feed stream without recovering them, whereas separation aims to divide a feed into two or more fractions of different compositions, both of which contain valuable products that are recovered. In CCS operations, captured CO_2 is destined to be stored or converted into products. Thus, CO_2 capture is a separation process, where the recovery of CO_2 is a crucial element of the system.

There is a specific requirement for the CO_2 product stream that could be transported or stored somewhere. In most cases, pipeline specifications require the purity of the CO_2 stream to be at least above 95 % [22]. To prevent condensation and corrosion in the CO_2 pipelines, removal of water vapour and impurities (e.g., H_2S, O_2, N_2, NO_x, etc) to a very low concentration is essential. Table 2.1 presents a universal pipeline specification recommendation for CO_2 storage and CO_2-EOR operations.

For carbon capture technology, it is widely recognized that an amine-based chemical solvent system is the most established and economical technology optimized for CO_2 capture (i.e., Technology Readiness Level of 9). Amines are organic compounds that are basic in nature, so they can react with "acidic" gases (e.g., CO_2 and H_2S) to capture them. In natural gas processing industries, removing H_2S and CO_2 together is called the "Acid Gas Treatment". However, in the CO_2 capture field, only the removal of CO_2 is of concern.

Table 2. 1 Recommended CO₂ pipeline specifications and maximum allowable impurities for CO₂ storage and CO₂-EOR operation [23].

Gas components	CO₂ Storage	CO₂-EOR Operations
CO_2	> 95 %	> 95 %
H_2O	< 500 ppm	< 500 ppm
SO_x	< 100 ppm	< 100 ppm
NO_x	< 100 ppm	< 100 ppm
H_2S	< 200 ppm	< 200 ppm
CO	< 2000 ppm	< 2000 ppm
H_2	Total non-condensable	Total non-condensable
Ar	gases	gases
N_2	< 4 vol%	< 4 vol%
O_2		< 100 ppm
CH_4		< 100 ppm

Figure 2.1 shows a typical amine-based solvent absorption system. In the amine scrubbing unit, the reaction between amines and acidic gases is reversible by changing the system temperature, e.g., heating of spent solvent to recover CO_2. This type of regeneration method is called the Temperature or Thermal Swing. Since 1930, hundreds of amine-scrubbing plants with this configuration have been employed to separate CO_2 from process gases and demonstrated their capability to achieve capture rates up to 95 % (CO_2 purity up to > 99.9 %). Currently, the industry benchmark amine system is based on Monoethanolamine (MEA) with 30 % loading, which has a capture capacity of 0.66 $mol_{co2}/kg_{sorbent}$ [38]. The other popular amines being investigated for liquid systems are diglycolamine (DGA), methyl diethanolamine (MDEA), triethanolamine (TEA), etc.

The primary challenge of the amine system is that it still suffers from high capture costs. For instance, to achieve a 90 % CO_2 capture rate in a 550 MW supercritical pulverized coal-fired power station with 427 tonnes of CO_2 per hour emissions, the levelized cost of electricity (LCOE) of the power plant can increase by 58 % from those without CO_2 capture (USD 74.4 to USD 117.7 per MWh) and a CO_2 avoided cost of USD 64.4 per

tonnes CO_2 [39]. If a higher capture rate were to be achieved (e.g., > 99.7 %), this LCOE and CO_2 avoided cost would increase to USD 131 and USD 72 per tonnes CO_2 respectively. Although recent demonstration projects (e.g., Quest CCS) have shown that the CO_2 avoided cost is lower than predicted (USD 42.79 per tonnes CO_2); further reduction in capture costs is still desirable for wide deployment of the technology. Since the majority of the energy parasitic load is due to sorbent regeneration, the current research priority for amine-based system is the reduction in reboiler duty. Besides process economics, there are also two critical issues with the amine-based system: 1) it is very corrosive to steels, including stainless steel [40], particularly if the amine concentration exceeds 20 % and it is highly loaded with acid gas, 2) it has a high degradation rate in the presence of contaminants (e.g., O_2, SO_2, COS and CS_2), which may form heat-stable salts that cannot be regenerated at normal stripping column temperatures [41]. Due to these reasons, the amine system is preferably used in gas treatment that has low concentrations of CO_2 (3 – 25 %) and consists of essentially no contaminants, such as those in natural gas operations.
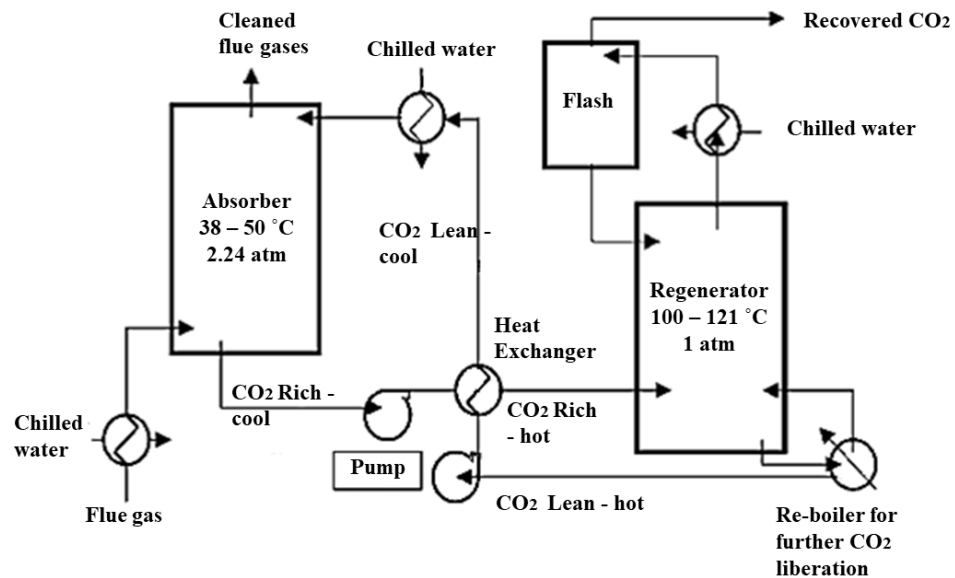
Figure 2.1 - A typical amine-based solvent absorption system

The physical solvent system is another type of absorption-based system. The distinction between the two absorption systems is that the physical solvent is based on the solubility of acidic gas within the solvent and is chemically inert in the separation, thus is more resistant

to degradation issues. Physical solvents are advantageous for gas streams consisting of high partial pressures of acidic gas, typically greater than 50 psi (~3.4 bar) [42], [43]. The system absorbs acidic gases by elevating the pressure (up to 100 bar) and releases CO_2 by simply lowing the system pressure in the stripping column. This type of regeneration is called Pressure Swing. The physical solvent system usually operates in the low temperate range, typically around 5 – 40 ℃ [11].

Technically, physical solvents should be more economical than chemical-based solvents because pressure swing regeneration requires significant less energy than the temperature swing method. However, physical solvent is not as effective as the chemical solvent in deep acid gas removal, so it is quite rare that a single-stage physical absorber can achieve CO_2 purity up to 95%. CO_2 product purity can be improved with additional flash stages, but this also means additional capture costs. Sometimes physical solvent and chemical solvent absorption are used in series to form a hybrid separation process to achieve deep acid gas removal. In commercial practices, Selexol® and The Fluor Solvent are physical solvent processes popularly used for CO_2 removal in gas processing.

Another popular CO_2 separation technology is the solid sorbent system, which makes use of materials that has features like high specific surface area and porosity to capture CO_2. The solid sorbents system has several advantages over the solvent system, such as it consumes lesser amount of energy due to lower heat capacities [44], has better mechanical and cyclic stability, can operate in a broad range of system conditions (e.g., gas compositions, temperature, and pressures) and solid sorbents has lower environmental concerns compared to the liquid waste. As the solid sorbent can be used for a wide range of adsorption temperatures (up to 1000 ℃), the need to cool down flue gases is eliminated, and a further reduction in overall energy penalty savings is expected.

Thermal swing (TSA) and pressure swing (PSA) are also used for the regeneration of adsorbents in solid sorbent systems. For CO_2 capture applications, only the PSA process has reached a technology readiness level of 9 (commercialized). The most successful PSA application in large-scale CO_2 capture projects is the Air Product's Port Arthur Steam Methane Reforming (SMR) CCS project, which is used to remove CO_2 from syngas for hydrogen production. The Port Arthur CCS project delivers a capture rate of 1 Mt CO_2 per

year and CO_2 purity of 97 %. On the contrary, the conventional TSA system (batch mode) is less developed compared to the PSA system (Current TRL is 6), due to the large amount of time needed to heat or cool down the bed. This is perhaps the reason its industrial applications are mainly related to front-end purification applications, such as elimination of trace elements, where the recovery of captured product is not important. Nevertheless, these drawbacks can be addressed by using a continuous temperature swing adsorption system. There are two solid sorbent systems currently being developed, e.g., Shell's the Solid Sorbent Technology (SST) and Svante's VeloxoTherm™, which utilises a rapid cycle continuous TSA for sorbent regeneration.

Finally, the membrane-based system is a popular choice for gas separation since the 1970s. Currently, state-of-the-art membrane technology has reached a demonstration stage (TRL 9), such as the Petrobras Santos Basin Pre-Salt Oil Field CCS, which has chosen a membrane system to remove CO_2 in natural gas processing [45]. The membrane-based technology separates molecules or atoms by selectively permeating them through membrane contractors. The separation process is performed under elevated pressure conditions (up to 200 bar) to aid in the diffusion process. However, creating a pressure difference through the membrane also means the large energy requirement for vacuum and compressors work, especially those flue gas streams that consist of low partial pressure of CO_2 and high volumetric flowrates (e.g., power plant stack). Thus, the membrane system is more advantageously applied to process streams with smaller flow rates and has high CO_2 concentration (> 20 vol%), such as those from the natural gas and process gas industries.

Nevertheless, the combined benefits of a membrane-based system might offer a possibility to offset the cost associated with compression work, such as a smaller volume of separation agent, the elimination of the expensive processing cost due to regeneration, compactness and lightweight design, These characteristics make it especially suitable for retrofitting purposes, and a modular design that allow for easy scale up and flexible operation. Modular plants are standardized capture units manufactured by mass production techniques, which are usually produced offsite, e.g., purposely-built facilities/factories, so they are ready to install when delivered to the site. Modular plants can reduce costs by minimizing lengthy design, engineering processes, and disruption caused to the site [25].

Another gas separation available in the market is cryogenic CO_2 capture, which relies on the phase change that occurs at very low temperatures, typically above -193 K and at elevated pressures. Due to the expected high cooling costs and compression work, cryogenic CO_2 capture has always been considered an unrealistic option for CO_2 capture. Nevertheless, cryogenic separation is becoming attractive as it offers high CO_2 recovery rates and purity levels (~ 99.9 %). It is proposed that the expensive refrigeration could be avoided when exploiting the cold duty available at liquefied natural gas regasification sites (LNG). However, this process is still in the early stages of development and requires further research. A good summary of cryogenic CO_2 capture can be found elsewhere [46].

Table 2.2 summarizes the characteristics of the CO_2 capture mechanism discussed in this section. The table also includes some of the engineering considerations when deciding on a CO_2 capture system [47]. For example, one of the parameters is operating flexibility, which refers to the ability to operate under variable feed quality conditions, either on a short- or long-term basis. Response to system variation refers to the response time of the capture system when there is a change in system conditions (e.g., feed compositions). The control requirement is also an important aspect to consider since a system that is too complicated is undesirable. Ease of expansion refers to the possibility of modularization, an emerging new trend in the CO_2 capture field.

This section provides a summary of the current carbon capture system and the state-of-the-art technologies. To select a suitable carbon capture system, the key factors are the properties of source gas and downstream operations, such as low/high pressure, temperatures, concentration of flue gas, presence of contaminants and purity of the product gas. These factors can affect the selection of these CO_2 capture mechanism, and additional treatments (e.g., heating or cooling, compression, or vacuum, etc) or processing units (e.g., removal of certain substance) may be required, which can be expensive. Thus, the following section will discuss the processes by which CO_2 capture can take place.

Table 2. 2 - Summary of the CO₂ capture mechanism discussed in this section (only the highest TRL).

System	Absorption		Adsorption		Membrane	Cryogenic
	Chemical	Physical	PSA (Zeolite)	TSA		
Preferred Feed composition	5 – 25 %	>20 %	>20 %	< 20 %	> 15 %	> 5%
Pressure Range	Atmospheric – intermediate pressures	Up to 100 bar	Up to 30 bar	Atmospheric	Up to 200 bar	Vacuum to Atmospheric
Temperature Range	< 120 ˚C	< 40 ˚C	< 40˚C	30 – 900 ˚C	30 – 100 ˚C	-393 to – 80 ˚C
CO_2 recovery (%)	80 - 95	60 – 75	80 – 95	90	60 - 90	99.99
CO_2 purity	>99%	>95%	>90 %	99.99	>95 %	99.99
Performance under Moisture	Good	Poor	Poor	Good	Poor	N/A
Chemical Stability	Poor	Good	Depending on the sorbent used	Depending on the sorbent used	Poor	N/A
Capture Cost / t_{CO2}	USD 50 - 150	USD 33 – 57	USD 40 - 100	USD 100	USD 15 – 55	USD 55 - 130
TRL level	9	9	9	6	9	6
Operating flexibility	High ($\%CO_2 < 10$) Low ($\%CO_2 > 25$)	Low	Low	High	High ($\%CO_2 > 25$) Low ($\%CO_2 > 25$)	Low
Response to system variations	Moderate	Moderate	Moderate	Moderate	Instantaneous	Slow
Control Requirement	High	High	High	Low	Low	High
Ease of expansion (modularization)	No	No	Yes	Yes	Yes	No

2.3 CO_2 capture processes

In most industrial processes, the largest point source of CO_2 emissions is usually from the combustion of fossil fuel for power or heat supply. Therefore, carbon capture technology is mainly categorized based on its relationship towards the combustion process, i.e., 1) pre-combustion capture, 2) oxyfuel-combustion capture and 3) post-combustion capture (Figure 2.1). Industrial CO_2 capture is an emerging class of carbon capture technology that mainly targets process-related (i.e., non-combustion) CO_2 emissions from industry sources, when fuel switching, and electrification is not possible to reduce the emissions. A short description of each carbon capture technology is provided as follow:
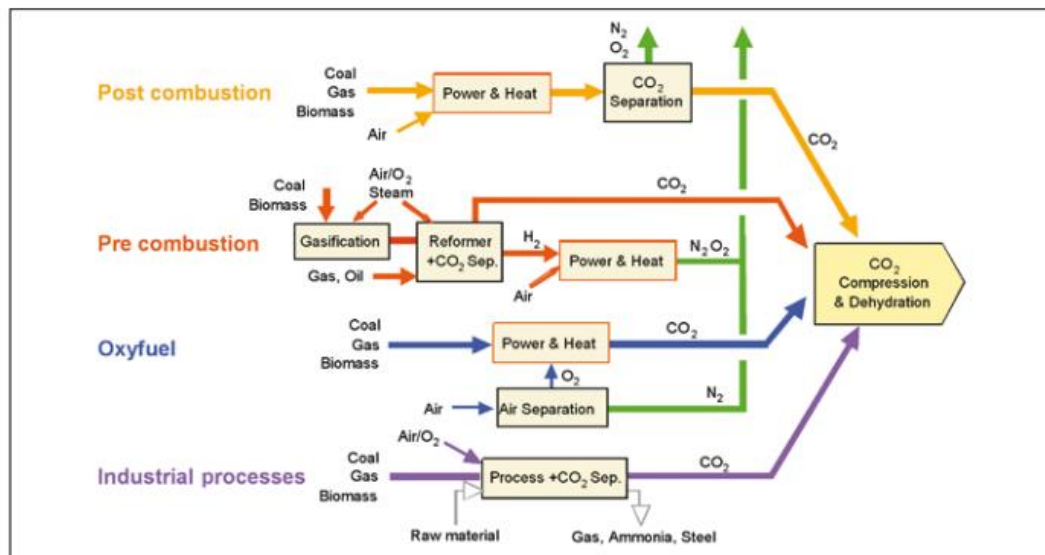
Figure 2.2 - Carbon Capture Pathways [11]

- Post-combustion capture is the capture of CO_2 after combustion is completed. Post-combustion CO_2 capture is widely regarded as the most straightforward method, as the tail-end processes have the benefit of not requiring any modification to the existing facilities. However, due to the low CO_2 partial pressure and large volumetric flow rate of exhausts resulting from the air-fueled combustion reaction, post-combustion capture usually suffers from low efficiency and requires larger equipment size to achieve good CO_2 recovery rate. Pre-treatment of flue gas may be required if the capture agent is sensitive to the impurities found in the flue gas.

- Pre-combustion capture is the capture of CO_2 before combustion is completed. In brief, the process first converts hydrocarbon-based fuels into synthesis gas (syngas), a mixture of hydrogen and carbon oxides (e.g., carbon monoxide and carbon dioxide) via gasification or reforming reaction. Then, the syngas undergoes water gas shift reactions (WGS) which an H_2-CO_2 rich gas is produced. CO_2 can be captured from this rich gas for sequestration, and the remaining H_2 can be used for fuel or feedstock for industrial applications. Production of low-carbon hydrogen with CCUS is categorized under this route.

Reforming reaction: $CH_4 + H_2O \leftrightarrow CO + 3H_2$ $(\Delta H_{298}^0 = +206.4 \text{ kJ/mol})$

WGS reaction: $CO + H_2O \leftrightarrow CO_2 + H_2$ $(\Delta H_{298}^0 = -41.1 \text{ kJ/mol})$
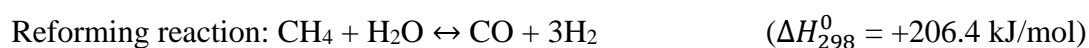
- Oxyfuel-combustion capture is an interesting CO_2 mitigation technology. Rather than capturing CO_2, the technique captures oxygen instead to create an enriched or pure oxygen stream for the combustion reaction. Fossil fuel combusted under this oxygen-rich environment produces flue gas consisting of zero or very low nitrogen content, thus significantly reducing the flue gas volume (about 75 % lesser than air-fueled combustion). The exhaust consists primarily of CO_2 and H_2O, which can be easily separated by condensation. The ease of downstream gas processing in oxy-combustion makes it potentially cost-competitive compared to other capture technologies, even though the oxygen production is energy intensive and expensive. However, the high flame temperature (~1000 °C) generated by oxyfuel combustion is a barrier to retrofitting the technology on some existing furnace/boilers, as most of them were set up to operate for 30 years or more and may not be able to withstand the temperature.

- Industrial CO_2 capture is the capture of CO_2 in carbon-intensive industrial processes, such as cement production, iron and steel, oil refining, etc. Industrial capture is applied when there is no obvious alternative other than the CCUS technology. The main challenge is that there is no single solution for industrial capture; carbon

capture solutions need to be tailored to the specific process or even equipment to achieve deep decarbonization.

As the thesis mainly focuses on the CO_2 separation process in industrial CO_2 capture and CCUS-enabled hydrogen production, which are the UK's current innovation priorities to achieve net zero emissions, the following section will only discuss carbon capture technologies related to these processes.

2.3.1 Hydrogen Production with CCUS

For hydrogen production in the UK, steam methane reforming (SMR) with CCS remains the most economical option to produce low carbon hydrogen in large quantities (£59/MWh), compared to other routes, such as autothermal reformation ATR (£62/MWh), coal gasification (£125/MWh), renewables electrolysis (£112/MWh), and grid electricity (192/MWh)[48]. The Hydrogen Strategy published by the UK government states that both SMR and ATR equipped with CCS will play a significant role in their ambitious goal to produce 5 GW of low-carbon hydrogen by 2030[13]. Figure 2.3 shows simplified SMR and ATR processes with a hydrogen purification unit (Pressure Swing Adsorption system). Sometimes the desulfurization unit is placed after the ATR unit.
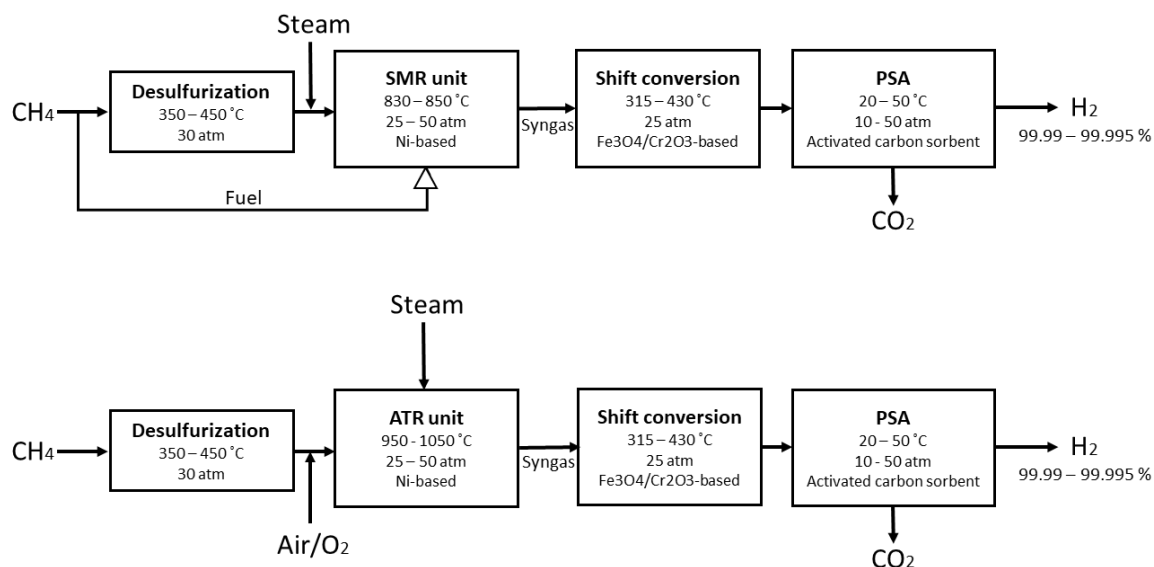
Figure 2.3 - Simplified SMR and ATR processes with a hydrogen purification unit (PSA system)

Hydrogen production via the SMR route is attractive for small to medium scale installations because the reaction condition are relatively mild (500 – 900 ˚C) and do not require enriched or pure oxygen produced from expensive cryogenic units. However, for large installations, H_2 production from ATR becomes more cost-effective than the SMR processes due to the economics of scale for oxygen production [49], [50]. Depending on the application, a water gas shift (WGS) may be needed downstream of the reformer to improve H_2 conversion and decrease the CO concentration. Since the WGS reaction is an exothermic reaction ($\Delta H = -41.2$ kJ/mol), this means that the equilibrium conversion tends to be higher at lower temperatures (around 200 – 400 ˚C), according to Le Chatelier's principle. Further temperature increases can shift the equilibrium back to the reactant side and reduce the conversion rate. However, the reaction usually suffers from slow kinetics in the low-temperature range. At higher temperatures (> 400 ˚C), the reaction kinetics are much improved, but the equilibrium conversion is low. Therefore, to overcome this thermodynamic limitation, in older hydrogen plants with amine scrubber as CO_2 removal unit, the WGS reaction usually occurs in two steps, high temperature (HT WGS) (350 – 450 ˚C) and a low temperature (LT WGS) (200 – 400 ˚C). The HT WGS step mainly increases the H_2 conversion and the LT WGS reduces the CO content (< 0.1 wt%) in the product gas stream. After the remaining CO content is then converted into CH_4 via the methanation reaction.

Table 2.3 shows the gas stream composition in SMR and ATR processes on dry basis. The concentration of steam in these gas streams is dependent on the stream-to-carbon ratio (S/C) of the WGS reaction, which usually leads to a steam concentration between 10 – 40 %.

In SMR equipped with PSA process (activated carbon as the adsorbent), only the HT WGS step is required. Albeit the fact that around 10 - 20 % of the H_2 is lost under the PSA operation, the elimination of the LT WGS reaction, the wet scrubber unit and the methanation unit and the production of high purity H_2 (99 – 99.995 vol%) makes the PSA hydrogen purification production attractive as it aligns with the concept of process intensification [51], [52]. In general, the amine scrubbing route is used to produce H_2 with lower purity (95 - 97 vol%), which is suitable for ammonia synthesis plants, whereas PSA

is used to produce ultra-pure H_2 (99 – 99.995 vol%). In some hydrogen production plants, these two systems are used in series, i.e., first treated with an amine scrubber unit to obtain a more concentrated H_2 stream then purified with an H_2-PSA unit to obtain ultra-pure purity [53].

Table 2. 3 Flue gas composition in SMR and ATR process

Sector	CO$_2$ source	Pressure (bar)	Temperature (°C)	Composition								Ref.
				H$_2$ (mol %)	CO$_2$ (mol %)	N$_2$ + Air (mol %)	O$_2$ (mol %)	CO (mol %)	CH$_4$ (mol %)	SO$_x$ (ppm)	NO$_x$ (ppm)	
SMR	HT WGS	20-30	315 - 430	74	16	0	0	3	7	0	0	[49]
	LT WGS	20-30	205 – 230	75	18.5	Trace	0	0.005 – 5	3 – 6	0	0	
O2 - ATR	HT WGS	10 – 30	315 - 430	69.8	23.8	0	0	6.4	0	0	0	[54]
	LT WGS	20-30	205 – 250	44 - 49	17	44 – 49	0	0.52 – 0.58	0.07 - 0.09	0	0	

Further process intensification can be achieved with emerging second-generation CCUS-enabled hydrogen production technology, such as Membrane Reactors (MRs) and Sorption Enhanced Reaction Processes (SERPs). As both SMR and WGS reactions are equilibrium limited, this means that the removal of reaction products (either H_2 or CO_2) can shift the reactions in favour of increased conversion and can be achieved by combining the conversion and separation steps, offering a promising route to decrease the cost of hydrogen production from SMR. These reactions are commonly known as reactive separation processes. There are four ways where the reaction and separation steps can be integrated:

- Water-gas shift membrane reactors (WGS-MR)
- Steam-methane reforming membrane reactors (SMR-MR)
- Sorption enhanced water-gas shift (SE-WGS)
- Sorption-enhanced steam-methane reforming (SE-SMR)

Technically speaking, the WGS reaction can be eliminated if the SMR reaction can produce sufficient H_2 yield. However, this is often difficult to achieve due to the thermodynamic properties of the SMR process. First, in a conventional SMR reaction, the amount of H_2 that can be produced is limited by its thermodynamic equilibrium conversion [53]. Then, the SMR reaction is a strongly endothermic reaction (ΔH_{298}^0 = +206 kJ/mol), which means it naturally favours high-temperature conditions (> 850 ˚C). However, at the same time, because the reforming reaction is accompanied by volume expansion, therefore it favours low-pressure conditions. These extreme conditions favoured by the SMR reaction (i.e., high temperature and low pressure) somehow contradict the conditions that are desirable for the current state-of-art adsorption and membrane processes explained in Section 2.2, e.g., lower temperature and high pressure. From a process perspective, milder SMR reaction conditions are advantageous because it allows the shift to a cheaper steel alloy for reforming and a smaller volume of treating gas. It also should be noted that the feedstock of the SMR reaction is CH_4 and the reaction produces CO. This means that a large portion of the SMR feedstock will be converted into CO and thus, reducing the H2 selectivity of the overall process. The presence of high CO content in process streams also poses several risks, such as 1) poisoning the catalyst or damaging downstream operations, 2) reducing the cyclic adsorption performance due to the possible irreversible interaction between CO and sorbent material, 3) possible safety hazards due to leakage of CO. A safe way to avoid this while maintaining high H_2 selectivity is to carry out the WGS reaction as much as possible, to reduce the CO concentration and obtain further H_2 conversion from shifting the CO. The exothermic nature of WGS reaction also allows it to favour low reaction temperature (200 – 400 ˚C) and high pressure (20 – 40 bar).

This paragraph gives a brief review of the membrane reactor (MR) technology. Both SMR-MR and WGS-MR technology has reached a TRL of 5 (i.e., lab scale plant) [55]–[57]. However, there seems to be considerably more attention given to SMR-MR technology, compared to the WGS-MR. Few studies have demonstrated that the combination of reforming reaction with the H_2-selective membrane in a single reactor can improve the methane conversion rate (79.5 - 99 %), at a milder operating condition, i.e., lower temperature (550 – 730 ˚C) and pressure (3 – 6 bar) [58]. Although CO_2 selective reactors have been studied, but the H_2 selective reactors offer greater efficiency, purity (99.99 –

99.995 %) and higher conversion rate, compared to CO_2 removal [59]. It has been demonstrated that CO_2 selective membrane (CO_2/H_2 selectivity of 6 - 10, CO_2/N_2 selectivity of 20 - 50 and CO_2/CO of 10 – 20) requires at least three steps to achieve more than 70 % capture rate from shifted syngas feed conditions [60], [61]. In comparison, only two steps are needed with the H_2 selective reactors to achieve the same capture rate [62].

The biggest challenge faced by MR technologies is the development of membrane materials with good thermal and chemical stability. The membrane must be able to operate under conditions where the reaction takes place and not be poisoned by the components present in the reformed syngas. Inorganic membranes, such as palladium membranes, are typically used for these types of applications as they can withstand high temperatures (up to 700 ˚C) and elevated operating pressure conditions (up to 30 bar) [63]–[65]. However, currently, the material is still vulnerable to impurities present in the feedstock, e.g., H_2S, HCl, CO_2 and CO [66]. In particular, H_2S can cause significant loss of hydrogen flux in the membrane system, but this issue has been found to improve when alloying the Pd membrane with noble metals such as Au, Ag, Cu, Ru, Ni, etc [67].

On the other hand, as the SMR-MR reaction operates at a much lower temperature (500 – 600 ˚C) than the conventional reforming reaction (800 – 1000 ˚C), the additional challenge is to search for a low-cost SMR catalyst that is highly active at lower temperatures. From a process perspective, the hydrogen flux of the membrane system (i.e., the ratio of hydrogen production rate to hydrogen permeation rate) is important. If the hydrogen production rate is significantly higher than the hydrogen permeation rate, it can result in a gas composition that favours carbon formation and the establishment of chemical equilibrium that can damage the membrane and stop the reaction from proceeding. It is also noteworthy to mention that the operating pressure has a negative effect on the H_2 equilibrium conversion of SMR reaction but at the same time, has a positive effect on the permeation driving force of the membrane. Thus, a compromise between the operating pressure and permeability of the membrane is required to minimize the overall energy efficiency of the SMR-MR process [68].

Following that, both SE-SMR and SEWGS are adsorption-based technology that are classified within Sorption Enhanced Reaction Processes (SERPs). The concept of SERPs

was originally developed for hydrogen production in the SMR reaction in the 1990s by Air Products & Chemical Inc. [19], [69]. Currently, the SERPs concept has been expanded to the production of H_2 with other hydrocarbons, such as ethanol (SE-ESR), glycerol (SE-GSR), etc., or utilises the captured CO_2 and H_2 into valuable products such as dimethyl ether (SEDMES), methanol, etc. [70], [71]. Among the SERPs, the SEWGS process has reached the highest TRL level of 6 (demonstration-scale), represented by the STEPWISE demonstration project led by TNO, whereas the SE-SMR process is currently at TRL level 4 (lab scale test) [38], [45], [72], [73].

The STEPWISE project demonstrates a SEWGS process that is capable to produce 2 from blast furnace gas while capturing CO_2, using potassium-promoted hydrotalcite as a bifunctional catalytic solid sorbent [19], [74]. Blast furnace gas was chosen due to its high CO content, which is beneficial for the process economy as CO is the feedstock for the SEWGS reaction. A previous techno-economics study has shown that the CO_2 avoided cost of the SEWGS process in the steel plant (58.4 €/t_{co2} and 61.1 €/t_{co2}) is comparable to that of amine scrubbing technology (50 – 70 €/t_{co2}) and pre-combustion capture in integrated gasifier combined cycle (IGCC) scenario (86.9 €/t_{co2} and 96.6 €/tco2) [75], [76]. In the STEPWISE's SEWGS process, a WGS is placed before the SEWGS unit to enhance the conversion rate of CO into H_2, i.e., CO content from 20 % to 2 – 6 %. Then, in the SEWGS unit, the conversion of CO is completed with the catalytic hydrotalcite-based sorbent and the sorbent, at the same time, separates CO_2 from H_2 (Figure 2.4). This gives a hot, high-pressure, H_2-rich product stream from the SEWGS outlet (e.g., 400 °C and up to 30 bar), which can be fed directly to the gas turbine or other applications in the steel mills, minimizing the cooling and heating step required for the process [76]. Pilot plant tests have proven that this type of reaction can produce high purity of CO_2 (> 95 %) and high purity of H_2 (> 99.9 %) [72], [77], [78]. The cyclic CO_2 performance of potassium-promoted hydrotalcite was also found satisfactory, e.g., stable over 2000 adsorption and desorption cycles can withstand H_2S conditions and the CO_2 slip through the sorbent bed is very low. Despite this fact, further improvement of the sorbent is still desirable to achieve further cost reduction, such as reducing the number of trains for the SEWGS process.
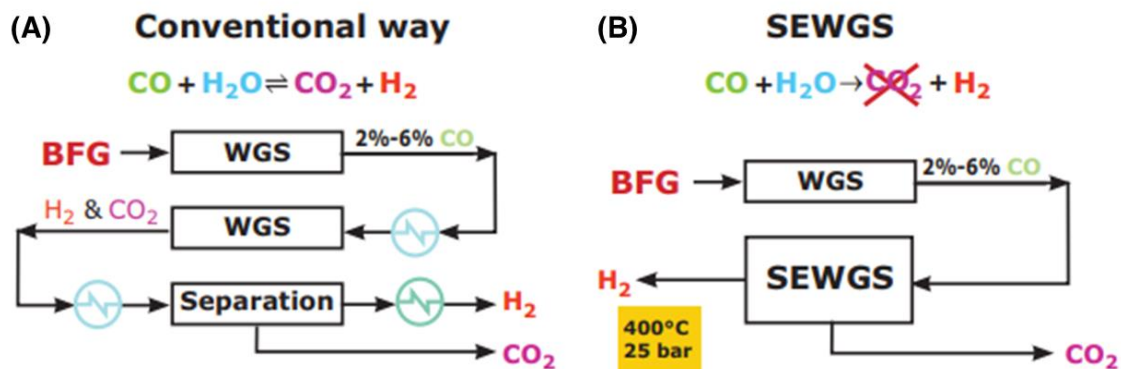
Figure 2.4 - (A) Conventional CO₂ capture unit and (B) SEWGS technology applied to hydrogen production from BFG in iron and steel plant [72]

The SE-SMR process has very similar issues like the SMR-MR process, such as requires a SMR catalyst that can operate at a lower reforming temperature (500 – 700 ˚C), while ensuring the carbon capture rate is quick enough so the chemical equilibrium does not arrive. At present, Ni-based catalyst is the preferred choice in industries as it is comparatively cheaper and has catalytic performance that is close to those exhibited by the noble metal catalysts, e.g., Ir and Pt. Currently, the adsorbents employed for SE-SMR are mainly based on calcium oxides (CaO) as they are cheap and have adequate CO_2 sorption performance at reaction temperature close to SE-SMR reaction (i.e., high sorption capacities (5-11 mmol/g) at 600 - 700 ˚C). However, the main disadvantage of CaO-based sorbent is their poor cyclic stability, which decays rapidly over multiple cycles due to sintering effects, and their high decarbonisation temperature (> 800 ˚C), which likely increases the energy consumption of the process. The lithium-based oxides (e.g., Li_2ZrO_3 and Li_4SiO_4) are another popular adsorbent class for SE-SMR reaction. They usually react with CO_2 at around 500 - 650 ˚C and have high adsorption capacities (5 - 6 mmol/g). However, the Li-based oxides are very expensive and have very slow sorption kinetics [79].

In summary, the common goals for new generation CCUS-enabled hydrogen technologies are to lower the operating temperature (200 – 500 ˚C) and development of new adsorbent/membrane/catalyst. The reactor and process configuration have been investigated as well and the reviews are available elsewhere. These review articles were recommended for the state-of-the-art of technologies, such as Habib *et al.* (2021) for a comprehensive

review of membrane reactor technology for hydrogen production [64], Masoudi Soltani *et al.* (2021) for a state-of-art review of SE-SMR and SE-WGS processes [73], Wang *et al.* (2021) for review of adsorbent and bifunctional adsorbent for SE-SMR process [80] and Wu *et al.* (2015) for a comprehensive review of SERPs technologies [73].

2.3.2 Industrial CO$_2$ capture

For industrial processes in the UK, BEIS identifies key CO$_2$ emissions abatement opportunities from iron and steel, oil refineries, chemicals, cement, glass, and lime production. For cement production, Bioenergy with Carbon Capture & Storage (BECCS) is attractive because the combination of fuel switching to biomass with CCUS technology can generate negative carbon emissions, which is more attractive than CCUS alone. For the iron and steel industry, there are two decarbonisation pathways available to decarbonise process emissions: (1) Electrification (EAF) and Direct Reduced Iron (DRI) and (2) CCUS option (post-combustion). If the EAF and DRI options are chosen, electricity and hydrogen source need to be of low carbon content, which means they are likely produced from SMR with CCS route in the near or medium term. If the CCUS option is chosen (most likely the post-combustion capture), it is estimated that CCUS will be capable of sequestering more CO$_2$ emission than the EAF and DRI route by 2040, i.e., 15 Mt CO$_2$e vs 8.8 Mt CO$_2$e[81]. However, one concern is that current sites in the UK (both Scunthorpe and Port Talbot) have difficulty retrofitting carbon capture units to existing infrastructure, and they may not be able to fully decarbonise all emissions by 2050. For the rest of high energy-intensive industries, such as chemicals, refinery, glass, lime, metal and paper, hydrogen is substituted for fuel or for electrification to generate industrial heat, whereas for the sectors where process emissions are available, CCUS is chosen to abate emissions. Table 2.4 presents the typical flue gas quality associated with industrial CO$_2$ capture.

Table 2.4 - Primary CO₂ sources in the industries sectors

Sector	CO₂ source	Pressure (bar)	Temperature (°C)	Composition H₂ (mol %)	CO₂ (mol %)	N₂ + Air (mol %)	O₂ (mol %)	H₂O (mol %)	CO (mol %)	CH₄ (mol %)	SOx (ppm)	NOx (ppm)	Ref.
Cement	Stack Gas	1	80-180oC	0	19 – 22	67 - 68	2 - 4	7-11	0	0	60	200 - 3000	[82]–[84]
Iron & Steel	Power plant stack	1	300	0	23-28	68	1	8	0	0	> 200	> 200	[85], [86]
	Blast Furnace gas	1	100 – 300	< 5	22 – 28	45 - 68	< 1	4 – 10	23	0	< 100	150	
	EAF off gas	1	300	0	40	56	3	0	0	0	<20	<20	
Chemical (Refineries)	Boilers (natural gas feed)	1	100-180	0	9	73	3	15	0	0	200	<20	[87], [88]
Paper and Pulp	Lime Kiln	1	250	0	16-21	47	1.2	30.9	0	0	50	175	[89]

2.3.3 Flue gas Composition associated with Hydrogen Production and Industrial Processes

Table 2.5 shows a summary of the properties of CO₂ source that exists in industries sectors and CCUS-enabled hydrogen production and the calculated partial pressures of carbon oxides.

Table 2. 5 - Partial pressures of CO₂ source in the industries sectors and low carbon hydrogen production

Source of gas	Temperature (ºC)	Pressure (bar)	Carbon oxides (CO_2 + CO) concentration (mol %)	Partial Pressure of carbon oxides (bar)
SMR (WGS outlet)	215 – 230	30	10.5	3.2
ATR (WGS outlet)	215 – 230	30	17.1	5.1
Cement	80 – 180	1	22.0	0.2
Iron & Steel Power Plant Stack gas	300	1	28.0	0.3
BFG gas	100 – 300	1	63.0	0.6
EAF off gas	300	1	9.0	0.1
chemical (refineries)	100 – 180	1	21.0	0.2
Paper & Pulp	250	24	14.4	3.5

The data in Table 2.5 show that some similarities exist between the CO_2 sources listed, summarized as follows:

- CO_2 source is mainly at moderate temperature (i.e., between 100 – 300 ˚C).
- CO_2 source for hydrogen production exists at high pressure (20 - 30 bar) whereas CO_2 source in industrial processes mainly exists at ambient pressure (1 bar).
- Wide range of CO_2 partial pressure, starting from as low as 0.1 bar to 5.1 bar.
- Each CO_2 source contains a significant number of impurities, *e.g.*, CO, H_2S, SO_x and NO_x.
- Most CO_2 source contains significant humidity (8 – 40 %), except the EAF off gas.

A CO_2 capture system capable of capturing CO_2 under conditions without the need for pre-treatment is generally preferred to avoid costly long train of treatment units. To achieve this, the CO_2 capture unit should have the following properties such as (1) the ability to capture at a moderate temperature window (100 – 300 ˚C), (2) the ability operate either at ambient pressure or high pressure, (3) the ability withstand moisture and 4) resistance to impurities and particulates, such as CO, H_2S, SO_x and NO_x. Based on current technology maturity levels and prospects of second-generation CCUS technology, the technology that fulfils these criteria here is the solid sorbent system, which is also more flexible in terms of the

pressure range and impurity resistance. Therefore, the solid sorbent system appears to have the greatest technical and economic potential within this category and is chosen as the focus os this thesis. Since the flue gas of industrial CO_2 capture and CCUS-enabled hydrogen is in the intermediate temperature range, so the sorption of CO_2 at intermediate temperature is the focus of this thesis. The sorbent with the following properties is desired: 1) good mechanical strength to withstand high pressure (20 – 30 bar), 2) tolerance to impurities (H_2S, SO_x, NO_x, etc), 3) adsorbs very little moisture, 4) good cyclic stability, and 5) low production cost. The following section will discuss the solid sorbent system in further detail.

2.4 Sorption of CO_2 at intermediate temperature

2.4.1 Overview

With the invention of synthetic zeolites in the 1930s and the recent emergence of various microporous adsorbents, sorption technology has now become a key gas separation method in the industry [90], [91]. Sorption is a general term referring to the processes involved between a sorbate (i.e., the adsorbing molecule) and a sorbent (i.e., the solid that adsorbs molecules). There are two types of sorption processes: absorption and adsorption. While the absorption that occurs in solid sorbent is very similar to liquid absorption - a bulk phenomenon where atoms penetrate through surface of sorbent and enter the bulk phase to form a solution; Adsorption is a surface-based phenomenon where atom forms a permanent/temporarily bond on the surface of sorbent material. Figure 2.5 illustrates the differences between adsorption and absorption in a solid sorbent. Depending on the type of sorbent material, sometimes both mechanisms can occur simultaneously in a single sorbent. For instance, the amine-based sorbents. However, it is often difficult or even impossible to distinguish between adsorption and absorption, so the wider term "sorption" is preferred which embraces both phenomena.
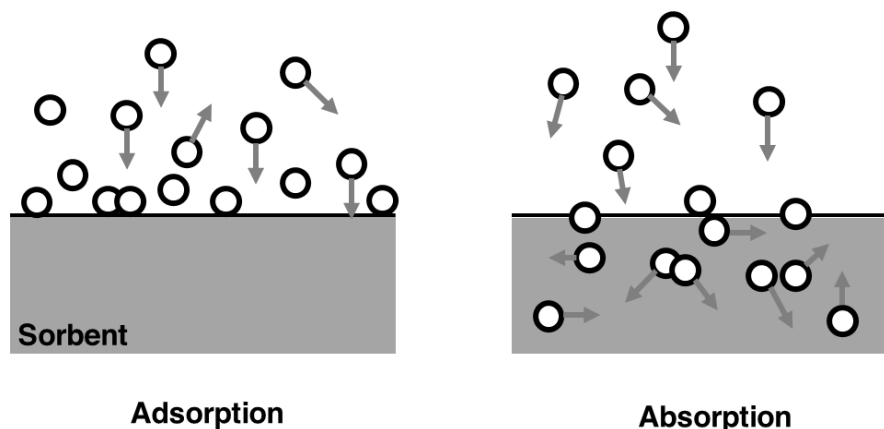
Figure 2.5 - Illustrative diagrams of adsorption and absorption

It is also useful to distinguish the type of interaction forces involved between the adsorbate and adsorbent, i.e., physical adsorption and chemisorption. Physisorption refers to reactions where only weak interaction forces (van der Waals forces) are formed, supplemented by

57

various electrostatic contributions, such as polarization, field-dipole, and field gradient-quadrupole interactions. As the van der Waals forces are non-specific interactions that can form between any kinds of molecules, thus adsorption relies on this force are poor in selectivity; unless the electrostatic contributions became dominant which allows the stronger selectivity for polar molecules. These types of interactions are normally reversible and have low adsorption energy (i.e., heat of adsorption in the region 25-50 kJ/mol), thus can be conveniently regenerated by pressure swing [92].

Chemisorption refers to the stronger interactions where chemical bonds are formed between the sorbate and active sites (i.e., functional group) of the sorbent. This means the chemisorption is a non-reversible reaction and is highly specific, thus having good selectivity towards sorbate of interest. The formation of chemical bonds in chemisorption also results in a significant larger heat of adsorption (usually in the region of 200 kJ/mol) than physisorption, which means it is more conveniently regenerated by temperature swing. However, as chemisorption by its nature is restricted by monolayer coverage of the surface, thus the adsorption capacities are usually much lower than the physical adsorption, where multilayer adsorption is common.

The primary requirement for an economic separation process is a sorbent with sufficiently high selectivity, followed by capacity, stability and life. The selectivity of a sorbent may depend on the difference in either sorption equilibrium or sorption kinetics. Before going into the details of the separation, it is important the define what is equilibrium and kinetic in the context of sorption.

Equilibrium is the state when there is no longer any net uptake of sorbate on the sorbent. For example, when there is a net flux of molecules flowing to or from the surface, there is either an sorption or a desorption process. When there is no longer any net flux of molecule flow, it is said that the sorption equilibrium has arrived. At this state, the rate of sorption of sorbate on the surface of the sorbent is equal to the rate of desorption from the surface.

Kinetics arises when porous solid sorbents are used. As adsorption is a surface-based process and the surface reaction is assumed to be very quick (especially for physisorption), therefore, the adsorption kinetics is considered mainly attributed from the process by which the sorbate finds its way towards the internal pores. Nonetheless, this does not hold true to

all adsorption processes, such as those involves with slow surface reaction or absorption. Therefore, the more precise term for this process is the diffusional resistance in the sorbent. Porous solid sorbents are desirable as the internal porosity can increase the amount of surface available for adsorption, contributing to extra uptake capacities. However, these internal pores need to be accessible and large enough to allow sorbate molecules to pass through. The molecule will flow continuously until the concentration of sorbate in the internal pores are same as the concentration at the surface of the sorbent particle, and finally, the point where adsorption equilibrium is achieved throughout the entire sorbent particle. The adsorption capacities obtained at this point are the maximum uptake capacities that can obtain from a solid sorbent at a given partial pressure. If the rate of adsorption at the surface is much quicker than the rate of diffusion, the adsorption is called diffusion/kinetically limited. If the rate of diffusion is quick but a low surface uptake rate is observed, the adsorption is known as equilibrium limited. Figure 2.6 illustrates the difference between equilibrium and kinetics in a solid sorbent.

The pore sizes in solid sorbent can be classified into 3 ranges: micropore, mesopore and macropore. One way to classify these pores is by the pore diameter, *e.g.*, micropores refer to the pores with diameter less than 2 nm, mesopores are pores between 2 to 50 nm and macropores are pores with diameter greater than 50 nm. This method is recommended by the International Union of Pure and Applied Chemistry (IUPAC) and is perhaps the most widely used classification method for pore sizes in porous solids. However, this classification is arbitrary to some extent and was developed based on the analysis of nitrogen adsorption-desorption isotherms at their normal boiling point (77 K).
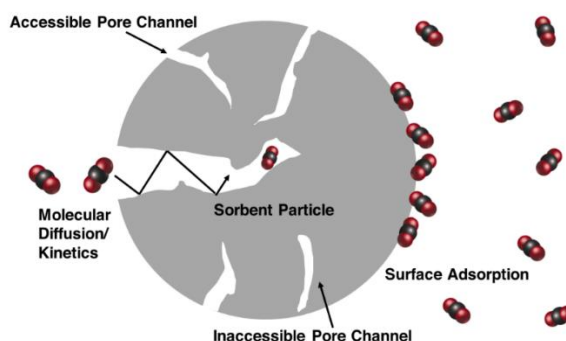
Figure 2.6 - Illustrative diagram of equilibrium and kinetics on a solid sorbent particle

Another method of classification, which is mainly used among the adsorption community, is based on the pore size relative to the diameters of the diffusing molecules. In this classification, only two types of diffusion were distinguished: micropore and macropore diffusion (Figure 2.7). Micropore diffusion refers to the diffusion in pores of dimensions comparable with the diameters of the diffusing molecule. In this situation, the diffusing molecule never escapes from the force field of the pore wall and thus the process resembles surface diffusion which is an activated process and shows dependency on temperature. However, as the size of the diffusing molecule is close to the pore sizes, the steric hindrance is also strong. Therefore, micropore diffusion is characterized by the well-defined correlation between temperature dependence and molecule diameter. Taking composite adsorbent as an example, the particles are formed by microporous particles and sometimes with the aid of a binder. As a result, the pore size distribution has a well-defined bimodal character with micropores inside microporous particles, connected by the large macropores networks within the pellet. Micropore diffusion is associated with the diffusion of molecules inside the micropores of crystals in the solid sorbent. On the other hand, macropore diffusion refers to the diffusion in the pores of dimensions much larger than the diameters of the diffusing molecule, i.e., the large macropores networks within a composite pellet.
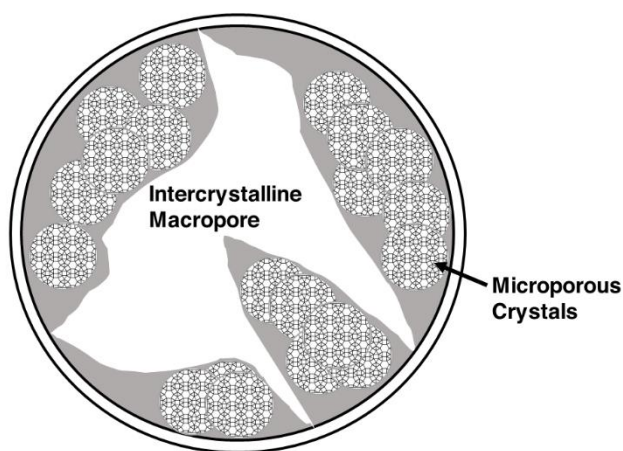
Figure 2.7 - Illustrative diagram of pores in a composite adsorbent particle

Nonetheless, the actual working capacities of an adsorbent are dependent on a combination of both equilibrium and kinetic properties. It should also be pointed out that the most

important scientific basis for adsorbent selection is the equilibrium isotherm, followed by diffusivity. Once obtained these parameters, further investigation of the sorbent performance can be carried out in more realistic settings, such as simulations studies and/or pilot plant testing, mimicking the sorption process in an adsorption column. Finally, a techno-economic analysis will be carried out to evaluate the economic performance of the adsorption process with the new sorbent material. Figure 2.8 shows the usual path taken to select a sorbent material for an adsorption application.
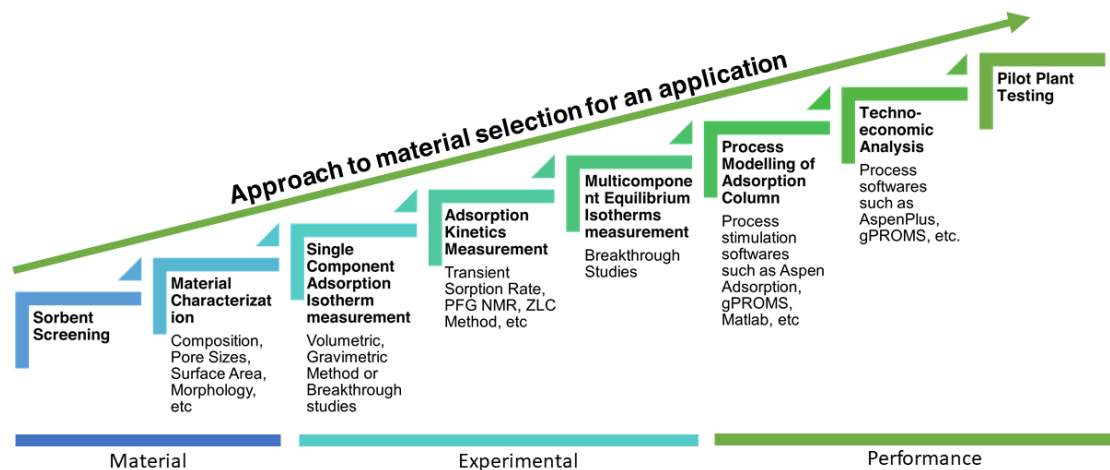
Figure 2.8 - The usual path taken to select a sorbent material for an adsorption application

2.4.2 Equilibrium vs Kinetic Separation

As mentioned before, the primary requirement for an economic separation process is an adsorbent with sufficiently high selectivity, followed by capacity, stability, and life [93]. Without selectivity, the adsorbent would not be able to separate a particular gas from a mixed gas phase. The selectivity of a sorbent may depend on the difference in either adsorption equilibrium or adsorption kinetics.

The kinetic selectivity is derived from the difference in diffusion rates between molecules, which is mainly determined by the kinetic diameter of a particular molecule. Generally, the pore size of adsorbents needs to be precisely tailored to lie between the kinetic diameters, σ of the two molecules that are to be separated. Molecular sieves, such as zeolites and carbon sieves are useful for this type of separation as the micropores are comparable with the dimensions of the diffusion molecules but the same time, small enough to exclude larger

61

molecules. This is of course not easy to achieve and in addition, the pore size needs to be thoroughly uniform for best performance. Nevertheless, it is foreseeable that kinetic separation might holds great potential in future, when tuneable pore size adsorbent is available, e.g., in Metal-organic frameworks (MOFs) where the pore size and architecture of crystalline can be designed to address specific requests for a selected application.

Equilibrium separation is based on the inherent properties of molecules which contribute to the adsorbate-adsorbent interactions, including but not limited to polarizability, magnetic susceptibility, permanent dipole moment and quadrupole moment. For physical adsorption, the polarizabilities of both sorbate and atom on the sorbent surface are both important. If the targeted molecule has high polarizability and magnetic susceptibility, but no polarity, high surface area non-polar sorbent such as carbon would be a good candidate. Sorbents with highly polar surfaces would be desirable for a target molecule that has a high dipole moment and polarizability. If the targeted molecule has a high quadruple moment, sorbents with surfaces that have high electric field gradients are suitable. Material with properties like this typically has cations dispersed above the negatively charged oxides on their surfaces. Cations with high valences (charges) and small ionic radii would result in strong interactions with the targeted molecule.

Generally, most separation operates through the equilibrium effect, with the kinetic separation being less common due to the challenge to matching the gas molecule with a suitable sorbent. Table 2.6 presents a summary of the adsorption-related physical parameters of gas adsorbates that are commonly found in flue gas conditions.

For carbon capture applications, CO_2 is highly polarized and has large quadrupole moment than the other gases commonly found in flue gas, such as O_2, N_2 and H_2. Thus, the separation of CO_2 from other gases is usually done through equilibrium selectivity. For these types of separation, the equilibrium isotherm presents the most important scientific basis for sorbent selection, followed by the adsorption kinetics/diffusion rate. The adsorption processes discussed in this thesis, such as PSA, TSA and PTSA, belong to this equilibrium group of separation.

Table 2. 6 - Summary of the adsorption-related physical parameters of gas adsorbates that are commonly found in flue gas conditions [94]

Species	σ (Å)	Polarizability $\times 10^{25}$/cm3	Dipole moment $\times 10^{18}$/esu cm	Quadruple Moment $\times 10^{26}$/esu cm
CO_2	3.300	29.11	0	4.30
CO	3.690	19.5	0	-
H_2O	2.640	14.5	1.8546	-
N_2	3.640	17.403	0	1.52
O_2	3.467	15.812	0	0.39
CH_4	3.760	25.93	0	0
H_2	2.827 – 2.890	8.042	0	0.662
He	2.551	2.04956	0	0
Ar	3.540	16.411	0	0
H_2S	3.623	37.8 – 39.5	0.97833	-
SO_2	4.112	37.2 – 42.8	1.63305	-
NO_2	-	30.2	0.316	-

2.4.3 PSA/TSA Regeneration Method and Cycle configurations

Similar to the absorption system, adsorption has adsorber and stripper units too, but they are performed in columns packed with sorbent particles. The process configurations are dependent on either in cycle batch (e.g., fixed bed) or a continuous manner (e.g., fluidising bed) (Figure 2.9) [95]. The term "raffinate" refers to the product stream that mostly contains the weak adsorptive or the "loosely light product". In the batch adsorption mode, both adsorption and desorption of solid sorbent occur within the fixed bed adsorber, by changing system conditions and/or flow of gas. In the continuous adsorption mode, a steady state is achieved by transporting solid sorbents between the adsorption and regeneration column, while maintaining system conditions and flow of gas. Both systems are widely researched for CO_2 capture applications [96]–[100].
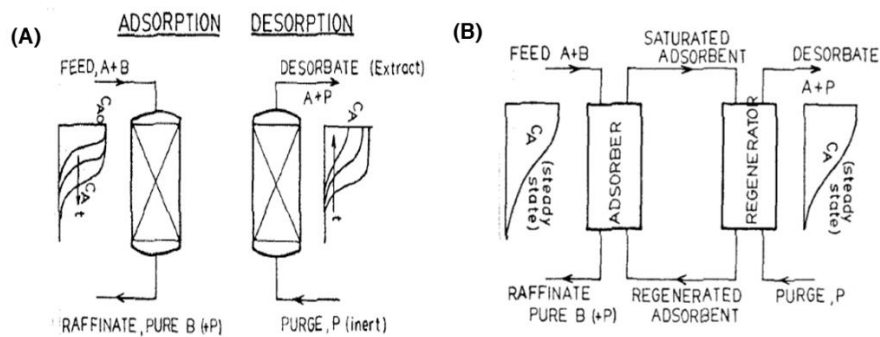
Figure 2.9 - Solid adsorption system operating in cyclic (A) batch and (B) continuous mode [101]

Since changing the system conditions and flow rates of gas are much easier than transporting the sorbent particle between two columns, more adsorption systems are operating in the batch mode. To achieve continuous feed processing in these batch systems, the Skarstrom cycle was introduced. The Skarstrom cycle was a basic stripping PSA cycle described by C.W. Skardstrom in 1960, for oxygen enrichment from air [102]. A scheme of the two-column PSA presented by the author is shown in Figure 2.10A. The Skardstrom cycle is important in the context of adsorption history because it is the first patent that describes a continuous feed process in a discontinuous (batch) process, like adsorption processes. To operate such unit cyclically, the column experiences a series of "steps", i.e., events like changing flow rate direction and valve arrangement for sequential opening. The sum of all the steps is termed as "cycle". With these cyclic configurations, a cyclic steady state can be achieved after some cycles even in batch mode. The invention of Skarstrom allowed a tremendous improvement in separation science and adsorbent development, which saw a huge interest in solid sorbent utilisation throughout the 1970s. For CO_2 capture, the rectifying cycle is normally used[103]–[105].

As mentioned earlier, the regeneration of solid sorbent through the desorption of sorbate can be realised by applying a temperature or pressure difference to the adsorption bed. These methods are known as the Pressure Swing Adsorption (PSA) and Temperature Swing Adsorption (TSA). Since the recovery of CO_2 is important in the context of CO_2 capture (required purity > 95 %), the regeneration method of choice became the key to achieving an efficient separation process. Figure 2.10B shows the difference between PSA

and TSA processes, illustrated using equilibrium adsorption isotherms. As a rule of thumb, estimation of the working capacity of the sorbent material can be derived from the difference in the equilibrium amount adsorbed between two isotherms. If the desorption of a PSA system operates in a vacuum condition (< 1 bar), then it is called a Vacuum Swing Adsorption (VSA) process. The creation of vacuum and consequent compressing of the column adds extra energy cost to the PSA/VSA system, thus the work of vacuum pumps and compressors is a key ingredient in the assessment of the economic viability of the processes.
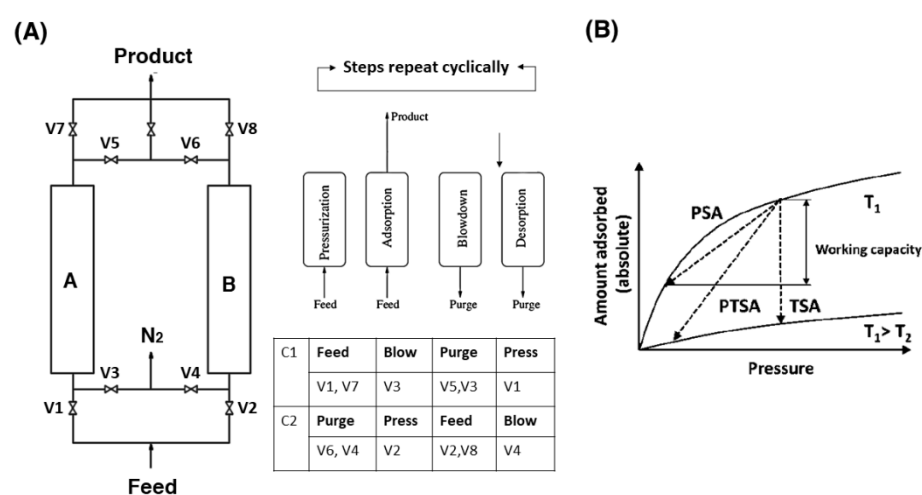
Figure 2.10 - (A) A scheme of the two-column Skardstrom Cycle and the 4-step cycle (B) Difference in adsorbed amount between two adsorption isotherms

TSA is normally not suitable for bulk separation processes because the change of temperature in bed (i.e., heat transfer) is a slow and often a rate-limiting step, resulting the length of each cycle usually ranges from several hours to over a day[106]. To make the time length of the adsorption step comparable with that of regeneration, the TSA cycle is used mainly for purification purposes. For bulk separation, PSA is more suitable as the pressure can be changed much more rapidly than the temperature, thereby making it possible to operate on a much shorter cycle (typically less than 10 minutes) and increasing the throughput per unit of adsorbent bed volume.

PSA is indeed a very versatile technology for bulk separation. Since 1960, several hundred thousand PSA units are operating around the world [102]. Nevertheless, there are several

limitations to PSA processes. First, PSA relies on weak interaction force which means it requires to operate at low-temperature range (< 40 ˚C). Second, rather than by the actual rate of equilibrium at surface, the rate of adsorption in PSA processes is usually controlled by diffusional limitations. Normally, the arrival of equilibrium is very rapid for physical adsorption. The surface diffusion of gas molecules is an activated process, which means it is influenced by temperature. Finally, PSA processes are restricted to components that are not too strongly adsorbed. For the adsorbed species that are strongly adsorbed, an uneconomically high vacuum is required to effect desorption during the regeneration step. Thus, for very strongly adsorbed components, TSA is generally preferred. If the heat transfer limitations can be overcome, the hybrid PTSA process may achieve higher working capacities.

To overcome the limitations of both PSA and TSA, the Elevated Temperature Pressure Swing Adsorption (ET-PSA) concept has emerged, which has the combined benefits of fast adsorption cycles, adsorption of strongly adsorbed species and better sorption kinetics at elevated temperature [107], [108]. [109]. ET-PSA has been applied in applications such as Sorption-Enhanced Reaction Processes (SERPs) and High-Temperature PSA cycles (HTPSA). The distinction between a SERP and an HTPSA system is that SERPs is a hybrid concept that combines sorption and catalytic reaction in a single column; the PSA column does not only adsorb but also acts as a reactor to shift the thermodynamic equilibrium of the reaction to increasing the yields. Another key advantage of SERPs is the possibility to reducing the number of PSA columns. In an early breakthrough study, Allam *et al.* (2005) demonstrates that the SERP reaction can achieve lower average carbon oxide concentration levels in the H_2 product gas, resulting in a product stream consisting of primarily bulk H_2 (> 90 %) and CH_4, which can be easily separated by using a simple 3-4 column PSA column, compared to a conventional SMR-PSA system which requires 8-12 adsorption columns[110], [111]. The HTPSA process, on the other hand, was based on the separation of gas at high temperatures (> 100 ˚C) [112].

There are also several other emerging PSA/TSA concepts. For example, novel PSA processes focusing on reducing the cycle time, such as rapid PSA, radial bed PSA, etc. There are also emerging TSA concepts which focus on overcoming the heat transfer

limitations, by using structured adsorbent [113], [114], microwave/sound assisted regenerated step [115], Moving Bed TSA [116], [117], thermal management towards internal heat exchanger [118], reactor configuration [119], etc. However, discussion of these advanced processes is beyond the scope of the present thesis and thus the following review articles were recommended to obtain further understanding of these processes [90], [93], [95], [101], [107], [120], [121].

2.5 Selection of sorbent material

2.5.1 Overview
Since the 2010s, huge interest in developing CO_2-capturing solid sorbent was observed in the scientific community [122]. Solid sorbents are divided into three main groups based on their sorption temperature: low temperature (< 200 ˚C), intermediate temperature (200 - 400˚C) and high temperature (> 400 ˚C).

The low-temperature range is primarily made up of physisorbents, such as carbon-based, zeolites, alumina, silica-based, etc, which have a long commercial history in the petrochemical industry and wide applications in CO_2 capture, olefin separation, biofuel production and water purification sectors. However, due to the weak physical adsorption force, these physisorbents are usually sensitive to temperature and have low selectivity towards CO_2, especially in the presence of moisture.

For the capture of CO_2 at higher temperatures (> 200 ℃), a chemisorbent must be used. Chemisorbents are usually made up of alkaline earth metal-based solid oxides, such as magnesium oxides (MgO), lithium oxides (Li_2ZrO_3 or Li_4SiO_4) and calcium oxides (CaO). The MgO-based oxides are popular for the capture of CO_2 at intermediate temperature range (200 – 500 ℃), such as those relevant to pre-combustion capture, to produce low-carbon electricity or hydrogen and post-combustion capture from hot flue gas, using TSA/PTSA processes. The Li-based oxides and calcium oxides are famous for CO_2 capture at higher temperatures (> 500 ℃), particularly in the SE-SMR and calcium looping applications. Due to the explosive amount of research conducted for these sorbents in recent years, it is impossible to summarize them within the scope of present work and therefore, the following articles are recommended for summaries of the works and timely review of the material advances [123]–[128]. For example, Dunstan *et al.* (2021) presented

a comprehensive review on the solid oxide-based sorbents (mainly MgO and CaO) for CO_2 capture at medium to high temperature, covering the fundamental aspects, thermodynamic properties, CO_2 carbonation mechanism, mechanistic insights, and recent advances in material optimization [129].

At the intermediate temperature range (200 – 400 ºC) – the condition of interest in the present thesis, there is technically only two main class of sorbent being investigated, which are the MgO-based sorbent and Mixed Metal Oxides (MMOs) derived from Layered Double Hydroxides (LDHs). As a matter of fact, the CO_2-capturing species in the LDH-derived MMOs sorbent is also the Mg-O species. This is because LDHs, more commonly known as Hydrotalcite (HTcs) in the adsorption community, are a derivation of Brucite, $Mg(OH)_2$ but have part of the Mg^{2+} ions substituted by the Al^{3+} ions. The general formula of LDHs is $[M_{1-x}^{2+}M_x^{3+}(OH)_2]^{x+}[A_{x/m}^{m-}]^{x-} \cdot nH_2O$, where M^{2+} and M^{3+} are di- and trivalent cations and A^{m-} is the balancing anion at the interlayers. The x is the molar ratio of the trivalent cation. Upon calcination at 400 ºC, the layer structure of LDHs/HTcs will collapse and forms MMOs, so it exists as a well-dispersed binary metal oxides phase (MgO and Al_2O_3). Figure 2.11 shows a representation of Brucite, Mg-Al LDHs and MMOs.
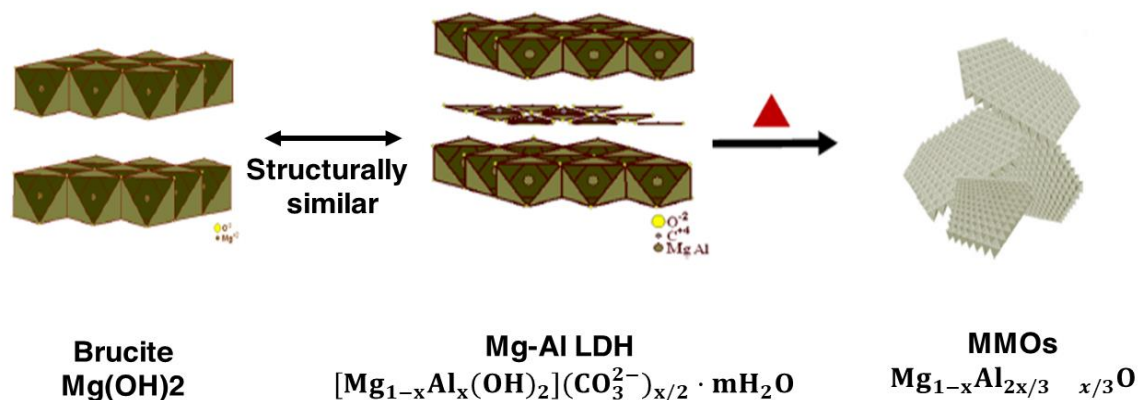
Figure 2.11 - Crystal structure of Brucite, Mg-Al LDH and MMOs

Hydrotalcite is the mineral name for the Mg-Al-CO_3 LDH phase, specifically for those having an Mg/Al ratio of 3. There is a difference mineral names for the LDHs phase with other Mg/Al ratios, e.g., Quintinite (Mg/Al ratio of 2) and different compositions, e.g.,

Pyroaurite (Mg/Fe ratio of 3). Therefore, to accommodate the different varieties of LDH phases and avoid confusion, this thesis will use the term LDH rather than HTcs to refer to this class of sorbent material. Besides the MgO-based sorbent, the other types of CO_2 sorbents being investigated for this temperature range are such as sodium-oxides based (e.g., $NaZr_2O_3$, Na_2O, Na_3SbO_4), graphene-oxides based, but the research of these sorbents only exists in limited quantities.

Considering the fact that the LDHs-derived MMOs sorbent has already been widely studied for the SEWGS process and has reached a high TRL level (6), it seems to be the best match for the scope of the project.

- Adequate sorption working capacity (~ 0.5 mol/kg)
- Can withstand impurities present in the flue gas of interest, i.e., moisture, CO and H_2S
- Can be mass manufactured (commercialized product)
- Proven to have stable mechanical stability up to 2000 adsorption-desorption cycles, under elevated pressure (20 bar)
- Has bifunctional properties, such as can act as a SEWGS catalyst to complete the conversion of CO in SEWGS reaction (100 %)

Several hypotheses make MMOs considered a better alternative to MgO. First, the addition of Al^{3+} into the MgO lattice may increase the basicity of MgO and improve the CO_2 adsorption capacity and sorption kinetics in the sorbent. Second, the secondary Al_2O_3 phase may act as support that can improve the mechanical stability of MgO species. Finally, the replacement of Mg by Al might reduce the cost of sorbent as MgO is relatively more expensive than Al_2O_3. These aspects will be discussed in further detail in the following section.

Nonetheless, there is a noticeable increase in interest towards pristine MgO-based sorbents for pre-combustion capture since 2015. Previously, the pure MgO-based sorbent was considered unfit for SEWGS reaction, because the $MgCO_3$ phase starts to decompose at 400 ºC but the usual operating temperature of SEWGS is between 400 – 550 ºC. Hence, a solid sorbent with better thermal stability was preferred. This situation has changed after

the discovery of the promotional effects of alkali metal salts (AMS) on the MgO species. It was found that the AMS (such as alkaline metal nitrates and alkaline metal carbonates) can alter the thermodynamic equilibrium of the MgO-$MgCO_3$ system, causing the optimal adsorption-desorption temperature window to shift above the conventional system[130]. Further to that, the molten state of AMS also improves the sorption kinetics of MgO sorbents by allowing the MgO to partially dissolves in the molten nitrates, and forms $MgCO_3$ nuclei/clusters with the dissolved CO_2 [131], [132]. This discovery has solved many of the limitations of the MgO system and has led to rapid growth in the fabrication of AMS-promoted MgO sorbent for pre-combustion capture [133], [134].

2.5.2 LDH-derived MMOs

A description of LDH and MMOs phase are discussed in depth in the following thesis chapters; therefore, this section will aim to give a summary of CO_2 capture work for LDH-derived MMOs sorbent.

Layered double hydroxides (LDHs) are a group of natural and synthetic layered materials with a chemical formula of $[M_{1-x}^{2+}M_x^{3+}(OH)_2]^{x+}$, alternating with interlayers containing anion groups and water molecules. Because of the positively charged layers, LDHs are also known as anionic clays. Mineral Hydrotalcite, $Mg_6Al_2(OH)_{16}[CO_3] \cdot 4H_2O$, was among the first and most thoroughly studied LDH phase. Hence, the group also famously known as hydrotalcite-like compounds (HTlcs). LDHs are well known to be compositionally and structurally diverse. So far there are 44 LDH minerals have been recognized and together with their synthetic analogues, a large varieties of M^{2+}/M^{3+} cations (*e.g.*, M^{2+} = Mg, Ni, Mn, Fe, Zn, Cu and Ca; M^{3+} = Al, Fe, Cr, Mn and Co), as well as anion species (*e.g.*, CO_3^{2-}, Cl^-, OH^-, SO_4^{2-}, NO_3^-, $Fe(CN)_6^{2-}$, VO_4^{3-}, $[Sb(OH)_6]^-$, etc) were reported [135]. In rare cases, cationic $[Ca(H_2O)_6]^{2+}$, $[Na(H_2O)_6]^+$ or neutral complexes $[Mg(SO_4)]^0$ are also found as the interlayer species[136]–[138]. Thus, LDHs have the characteristics of adjustable composition and adjustable anion between layers.

Structurally, the hydroxide layers of LDH are two-dimensional (2D) like nanosheets, which means different layer sequences can arise (Figure 2.12). This unique characteristic of 2D material is known as Polytypism, where the polytypes are differentiated by stacking sequences of hydroxide layers [139], [140]. Upon calcination/decomposition under an

inert/oxidizing environment, the 2D structure of LDHs collapses which leads to the formation of 3D mixed metal oxides (MMOs) with homogeneously dispersed metal cations, which is highly desirable for many industrial applications [141]. Through controlled decomposition, it is possible to tune the porosity, surface area or even catalysed the polymerization reaction of anion species to form heat-stable support for improved thermal and mechanical stability[142].
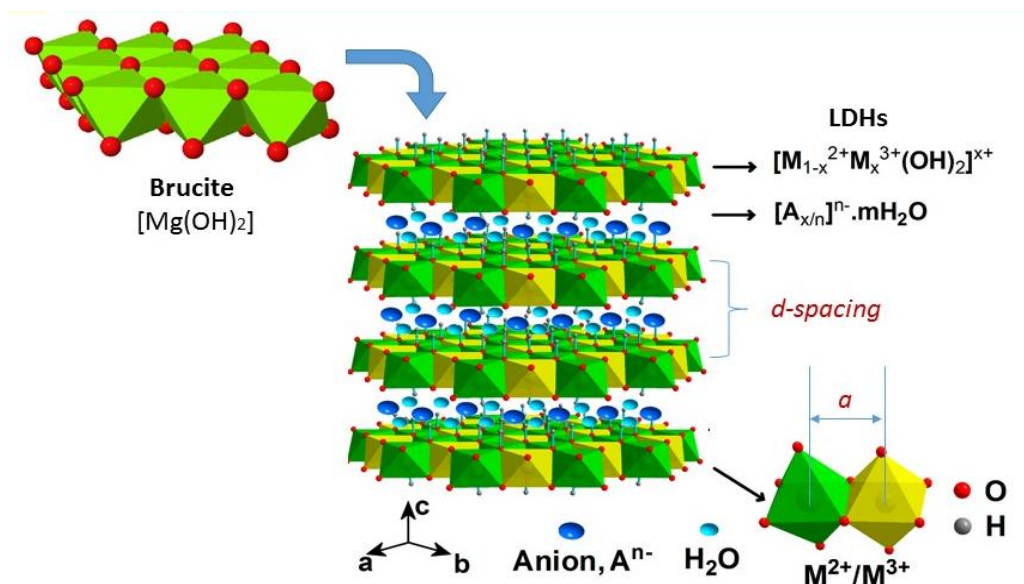
Figure 2.12 - Layered structure of Mg-Al Layered Double Hydroxides (LDHs)

The first patent of LDH appeared in 1973, which specifically referred to LDH as the optimal precursors for hydrogenation catalysts[143]. Since then, LDHs and derived MMOs have received great attention in many fields, including wastewater treatment, pharmaceutical, catalysis, adsorption and built environment[144]–[147]. Depending on the cation species used, the operating temperature of LDH-derived MMOs sorbent can vary between 25 – 700 °C, making them suitable for many flue gas conditions. For example, the Mg-based MMOs sorbent can capture CO_2 up to 400 ºC, whereas the Ca-based MMOs sorbent can capture CO_2 starting from 500 ºC, up to 700 ºC. Recently, Arstad *et al.* (2020) explored the use of Co-Mg-based LDH-derived MMOs for the capture of CO_2 at 400 ºC [148]. Nevertheless, the focus of the thesis is the Mg-Al LDH system, which is the most widely studied phase for CO_2 capture.

The first documented use of Mg-Al LDH-derived MMOs as cyclic CO_2 sorbent can be dated back to 1992, reported by Tagaya and co-workers [149]. During the time of investigation, it has already been known that the calcined products of the LDH phase can reconstruct back to their original layered structure under ambient conditions, by adsorbing atmospheric CO_2. This natural phenomenon of the LDH phase is termed the "memory effect". Through observation of the repeated formation of MgO and $MgCO_3$ peaks on XRD analysis, Tagaya and co-workers proves that the adsorption and desorption of CO_2 on LDH-derived MMOs are reversible and can be considered for industrial CO_2 separation application.

LDH-derived MMOs sorbent gained further popularity in 1996 when Air Products and Chemicals, Inc. reported its use in SE-SMR reaction for low-carbon hydrogen production[110]. Hydrotalcite promoted with 20 wt % K_2CO_3 was found satisfied all the preliminary performance targets set for a CO_2 sorbent suitable for the SE-SMR reaction, such as 1) having CO_2 working capacity more than 0.30 mol/kg at 300 – 500 ºC, in the pressure of steam, 2) adequate adsorption kinetics for CO_2, 3) stable CO_2 cyclic stability up to 20 cycles and 4) adequate mechanical strength after cyclic exposure to high-pressure steam. Actual breakthrough results show that the working capacity of K_2CO_3 promoted HTC is 0.45 mol/kg, under wet conditions (P_{H2O} =10 atm). However, Air Products Chemical and Inc. eventually concludes that the hydrotalcite-based high-temperature adsorption process would be more suitable for the SEWGS process, compared to the SE-SMR[111].

After that, research in the hydrotalcite-based SERPs processes began across the globe in 2000. Ding and Alpay, a research group from the United Kingdom investigated the CO_2 equilibrium and kinetics of potassium-promoted hydrotalcite pellets at 208, 302 and 480 ºC, under dry and wet feed conditions using a semi-technical breakthrough study apparatus [150], [151]. The authors found that both dry and wet adsorption isotherms of K-promoted hydrotalcite can be described by the Langmuir models. The presence of steam was also found to have a positive effect on the CO_2 adsorption capacities of K-promoted hydrotalcite sorbent (~ 10 % higher than dry feed condition). However, there is an order of magnitude difference between the adsorption (0.0058 s^{-1}) and desorption kinetics of CO_2 (0.0006 s^{-1})

in the K-promoted sorbent at 302 ℃, which can be an issue due to the need for longer desorption step.

Rodrigues and co-workers from the University of Porto, Portugal have investigated several aspects of K_2CO_3 impregnated commercial hydrotalcite sorbents (mainly from Sasol, Germany) on their adsorption performance at high temperatures (i.e., 29 – 400 ℃), such as the effect of aluminium content[152], the effect of alkali (K and Cs) and alkaline-earth metals (Sr) [153], [154], adsorption capacities [155], [156], adsorption kinetic [157], etc. Using these commercial K_2CO_3-promoted sorbents, they have conducted several process stimulations studies of SE-SMR to produce hydrogen [158]–[162].

Ritter and co-workers from the University of South Carolina, United States have conducted several process performance studies for K-promoted hydrotalcite-based high-temperature PSA applications [163]–[167]. Using the kinetics parameters reported earlier by Ding and Alpay (2001), Ritter demonstrates that the hydrotalcite-based PSA process might be limited by its desorption rate [165]. To improve the purity and CO_2 recovery of the process without increasing the number of beds in the PSA process, the adsorption and desorption kinetics parameter of hydrotalcite sorbent needs to be at least equal to each other. Through a series of investigations work, Ritter and co-workers demonstrate that the adsorption of CO_2 in the K-promoted hydrotalcite sorbent at 450 ℃ is a complex system with at least three different processes occurring at different kinetics, i.e., very fast, intermediate, and slow [166]–[168]. A reversible nonequilibrium kinetic model (RNEK), based in part on Langmuir-Hinshelwood type kinetics was proposed to describe the adsorption and desorption behaviour in the K-promoted HTcs sorbent [164].

A research group from the Energy Research Centre (ECN), Netherlands published their first work on K-promoted hydrotalcite sorbents in 2006 [169]. The research group eventually took part in both the CAESAR project and the STEPWISE project. In 2013, after the pilot test of the SEWGS process, it was found that the PURAL K-MG70 sorbent originally used in the CAESAR project showed poor mechanical stability and CO_2 slip during long-term testing under realistic conditions [74]. After more than 1200 cycles, the sorbent eventually fractured into powders due to the formation of $MgCO_3$, which has the slow kinetics demonstrated by Ritter and co-workers. To overcome this, the ECN group

developed a new HTcs sorbent with a lower Mg content (ALKASORB and ALKASORB+), which showed good mechanical stability over more than 2000 cycles and requires lesser steam for the regeneration (34 % lesser) [170]. Due to the large amount of research work published by the same group, the following review papers for the summaries of work on SEWGS processes are recommended [72], [171], [172] and also the mechanistic studies of hydrotalcite-based sorbent, e.g., in situ studies of phase formation at 400 ºC [173]–[175], impacts of sour gases (H$_2$S) [176], [177], CO$_2$ and H$_2$O chemisorption mechanism [178]–[185], and synthesis of novel/structured hydrotalcite-based adsorbent[148]. Walspurger *et al.* (2008) demonstrate that it was the dawsonite phase, $KAlCO_3(OH)_2$, a product formed after the reaction between the K$^+$ ions from K$_2$CO$_3$, aluminium oxides and the water in the feed stream that was dominating the adsorption of CO$_2$ in the K-promoted MMOs sorbents[173]–[175]. Finally, Cai and a co-worker, a research team from Tsinghua University, Beijing have published several articles on K-promoted hydrotalcite sorbents since 2013[109], [186]–[189]. Table 2.7 gives a summary of the selected work on hydrotalcite-based sorbents since 1996.

Thus far, it seems almost all the CO$_2$ capture studies on the LDH-based MMOs sorbent were primarily done on those promoted by AMS (K$_2$CO$_3$ in particular) and many of them were obtained from the same vendor (Sasol). Currently, the highest working capacity that was measured for these LDH-derived MMOs is 1.1 mol/kg [159]. Even though it is already a significant improvement of the material since 1996 (almost two-fold increase in working capacity), but several studies have indicated that the working capacity of MMOs sorbent needs to reach above 1.35 mol/kg to make the SEWGS substantially cheaper than the more conventional carbon capture technology [69], [74], [190], [191]. On the other hand, MMOs with an Mg/Al ratio of 3: 1 should have a maximum CO$_2$ uptake capacity of 16.27 mmol/g, assuming each Mg^{2+} is a basic site for CO$_2$ adsorption. However, even after being promoted with potassium, the highest working capacity obtained from MMOs sorbent is merely 7% of this theoretical capacity. To unveil this maximum capacity, there seems to be a need to investigate into this subject.

Table 2. 7 - Summary of CO₂ adsorption work using LDH-based MMOs sorbent

Author	Sorbent material	Condition	Fitted Model	LDF parameter at 400 ˚C	References
Hufton *et al.* (1996)	K-promoted hydrotalcite (commercial)	400 – 500 ˚C	Langmuir	N/A	[69]
Ding & Alpay (2000)	K-promoted hydrotalcite (commercial)	208 - 480 ˚C (dry and wet)	Langmuir	7.5×10^{-3} (dry); 1×10^{-2} (wet)	[150], [151]
Moreira *et al.* (2006)	PURAL MG50 (Sasol)	150 - 350 ˚C (dry)	Langmuir	10.4×10^{-3} (dry)	[155]
Lee *et al.* (2007)	K_2CO_3-promoted hydrotalcite (Air Products Ltd.)	400 - 520 ˚C (dry)	Langmuir + complexion	N/A	[192]
Oliveira *et al.* (2008)	20 wt% K_2CO_3-promoted PURAL MG30 (Sasol)	306 - 510 ˚C (wet)	Bi-Langmuir	2.9×10^{-3} (dry)	[154]
Ebner & Ritter (2007)	K-promoted LDH (co-precipitation	400 ˚C (dry)	RNEK	2.03×10^{-2}	[167]
Halabi *et al.* (2012)	22 wt% K_2CO_3-promoted PURAL MG61 (Sasol)	400 ˚C (dry and wet)	Freundlich	N/A	[193]
Chanburanasiri *et al.* (2013)	K_2CO_3 – promoted PURAL MG31w (Sasol)	360 – 467 ˚C (wet)	Bi-Langmuir	1.66×10^{-2} (wet)	[158]
Miguel *et al.* (2014)	K-, Sr-, Cs-, Mg-Al, Ga-CO_3 (co-precipitation)	300 - 400 ˚C (dry)	Freundlich	(fast)7.57×10^{-4}; (slow) 12.26×10^{-4}	[153]
Boon *et al.* (2014)	20 wt% K_2CO_3 – promoted Hydrotalcite (Sasol)	400 ˚C (dry and wet)	Langmuir + Freundlich	N/A	[185]

Zhu *et al.* (2019)	20 wt% K_2CO_3 – promoted MG30, MG63 & MG70 (Sasol)	300 – 450 ˚C (dry)	N/A	N/A	[188]

The main reason is likely due to the lack of in-depth understanding of the material. As demonstrated earlier, almost all the sorbents studied relied on the impregnation of K_2CO_3 to achieve higher sorption capacities, which resulted in a very limited material breakthroughs in this class of sorbent group. Although the promotional effect of K_2CO_3 has been thoroughly studied by several authors, but the exact role of K^+ ions on the CO_2 capture mechanism of MMOs sorbent are still unclear [152], [194], [195]. Nonetheless, a wide consensus is that the optimal loading rate of K_2CO_3 in the sorbent is 20 wt%. Further increase in the loading rate will negatively affect the high-temperature CO_2 adsorption performance of MMOs sorbent, likely caused by the blockage of accessible pores by alkaline promoters.

An alternative route to improve the CO_2 capture capacity of MMOs sorbent is through the precursor engineering of the LDH phase. One example is from Wang et. al (2012), who have attempted utilising the interlayer anions as a template to improve the CO_2 capture performance[196]. The author demonstrated that the morphology, surface area and thermal stability of derived MMOs can be altered by changing the anions into the LDHs, i.e., intercalating long-chain carbon-chain organic anions (such as stearate and carboxylate). The derived MMOs showed a remarkable increase in CO_2 uptake capacity from 0.5mmol/g to 1.25mmol/g. The improved CO_2 uptake capacity was believed a result of the decomposition of larger organic anions, which cracks up the LDHs crystal planes and created more surface basic sites for adsorption. This finding confirms the tuneable potential of LDH-derived MMOs for CO_2 capture. However, until this date, very limited attempts with this approach are seen. To design MMOs with better sorption capacities, perhaps a further understanding of the material is required, such as basic site formation mechanism, CO_2 adsorption mechanism, and adsorption performance.

Nevertheless, there still lies significant ambiguity about the adsorption performance of this class of material. There is a dispersed trend in the adsorption equilibrium isotherms of K-promoted hydrotalcite sorbent. Previously, Allam (2005) and Ding & Alpay (2000) reported a clear temperature dependence trend in the K-promoted hydrotalcite sorbents. The sorption capacities of K-promoted hydrotalcite sorbents decreases as temperature increase. However, in 2008, Oliveira et $al.$ measured the sorption equilibrium isotherms of CO_2 (in the presence of steam) in the MG30-K hydrotalcite sorbent and found that a maximum is seen at 403 ℃, indicating the sorption capacity at 403 ℃ is higher than at 306 ℃ and 510 ℃. The authors explain that the existence of a maximum in the CO_2 equilibrium capacity suggests that there are two types of sorption interactions in the hydrotalcite sorbent, which might arise from the specific interactions between the CO_2 molecules and the alkali metals promoter in the hydrotalcite sorbent. The equilibrium isotherms reported by Lee et $al.$ (2007) measured at 400 and 520 ℃ seem to echo with this finding [192]. However, they recorded a new isotherm shape that is different from those recorded by Allam, Ding & Alpay and Oliveira, i.e., a step increase was seen in the low-pressure range (~ P_{co2} = 0.5 bar). Coincidentally, Boon et $al.$ (2014) also recorded a similar adsorption isotherm shape with the ones of Lee et $al.$ (2007), under the presence of steam[185]. In a more recent study, the adsorption isotherms measured by Ramirez-Moreno et $al.$ (2014) showed a, where a remarkable increase in the sorption capacities was seen above 20 bar [196], which seems to suggest that the CO_2 adsorption capacities of MMOs sorbent amplifies at high pressure range [197].

As the equilibrium sorption capacity represents the maximum CO_2 molecule that can adsorb by the sorbent material at a given partial pressure and is directly proportional to the number of basic site available for adsorption, therefore, it is of utmost importance to understand the equilibrium isotherms behaviour to design better MMOs. However, noted that the pressure range of these equilibrium isotherms measured has been extremely varied, i.e., P_{co2} = 0.05 – 43.5 bar, making it almost impossible to compare them and obtain better insights into the adsorption equilibrium behaviour of this class of sorbent. To design better MMOs sorbent, the unambiguous measurement of adsorption equilibrium isotherms, covering the full range of temperature and pressure range of interest for the flue gas conditions of present work is required.

However, the next question is which LDH-derived MMOs sorbent to measure for the adsorption equilibrium isotherms. Since there already exists very thorough investigations on the adsorption performance of K-promoted hydrotalcite sorbents, it is perhaps not of significant important to carry out similar research on the same type of sorbent. Interestingly, there is no sorption equilibrium data measured for pristine/unpromoted LDH-derived MMOs sorbent yet, which is crucial to understand the nature of basic sites of the pristine MMOs sorbent. As mentioned before, the Mg^{2+} species is responsible for CO_2 adsorption in the MMOs and thus the chemical composition of LDH-derived MMOs should show a direct proportional relation to its CO_2 adsorption capacities. Nevertheless, based on a large amount of data analysis, we found that the effect of chemical composition on the CO_2 adsorption properties of unpromoted LDH-derived MMOs still remains unclear (Figure 2.13). On a very basic level, it is still uncertain why the MMOs sorbent derived by the same synthesis method and compositions shows large variation in their CO_2 adsorption capacities. For example, LDH-derived MMOs derived from co-precipitation method and Mg/Al ratio of 3 shows significant differences in their adsorption capacities at the same reaction temperature (200 ˚C). The difference in sorption capacities varies by almost 0.7 mmol/g, which is likely not due to measurement errors. Considering the largest sorption capacity measured for this material is 0.83 mmol/g, this variation of 0.7 mmol/g in the sorption capacity is significant.
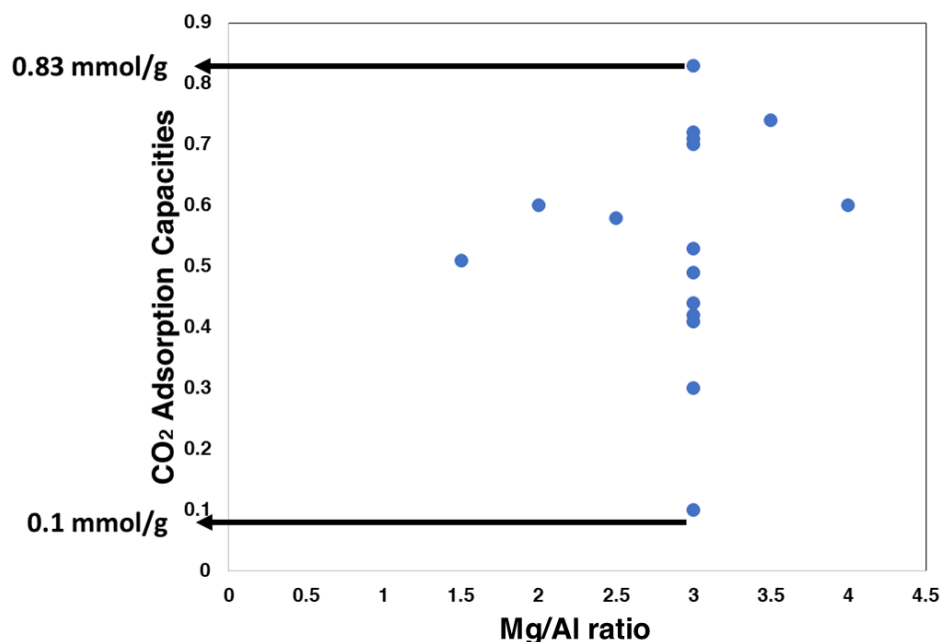
Figure 2.13 - Comparison of CO$_2$ adsorption capacities of unpromoted MMOs sorbent derived from co-precipitation method and various Mg/Al ratios

After careful inspection of the LDH chemistry, we found that there is in fact no reliable method to determine the true chemical composition of the LDH phase. This is perhaps why very little effort has been made to improve the sorbent from the precursor engineering route, despite the material have been extensively studied for many applications since 1970. There seems a need to revisit the chemical composition aspects to obtain better insights for LDH-derived MMOs sorbents. A chemically meaningful relationship between the composition of LDH precursors and the CO$_2$ adsorption performance of MMOs must first associated.

To derive the true chemical composition of LDHs, it is necessary to study the crystal structure. In this work, an innovative crystal chemical approach was proposed to identify the true chemical composition of LDHs in the crystal phase. A novel crystal chemical equation was eventually developed to give a better estimation of chemical composition for the LDH phases. To achieve this, any variables that may affect the chemical composition of the LDHs phase must first be identified (Table 2.8). Once the chemical composition is established, the true adsorption performance of the LDH-derived MMOs phase can be measured. Table 2.8 also presents some of the composition variables that can be observed

from LDH with varied chemical compositions. These aspects of LDH phases will be discussed in the following thesis chapters.

Table 2. 8 - Composition and preparation variables in the synthesis of LDH phase [198]

Composition variables	Preparation variables
Cation size	pH values
Value of x	Precipitation method
Cation nature and ratio	Precipitation temperature
Cation stereochemistry	Reagent concentration
Nature of balancing anions	Ageing
Amount of interlayer water	Washing and drying
Crystal morphology and size	Presence of impurities

2.6 Aim and Research Objectives

Based on the urgent need to achieve the UK's 2050 net zero targets while securing the country's energy demand at the same time, the widespread deployment of intermittent clean technologies such as CCUS, are desired. In the present work, the solid adsorption system was identified to present the largest technological and economical potential to sequestrate CO_2 emissions from hydrogen production plants and industrial sources in the UK. LDH-derived MMOs sorbent has been chosen to study for the flue gas conditions.

Nevertheless, the major barrier to the system is the low working capacity of adsorbents. For the system to be comparable to conventional capture technologies, the working capacity of the LDH-derived MMOs sorbent needs to be increased to a minimum of 1.35 mmol/g. Currently, their working capacity is in the range of 0.3 – 1.1 mmol/g.

To design MMOs sorbent with better CO_2 capture performance, several aspects of the material, including both LDHs and MMOs, were investigated. Specifically, the following research objectives have been pursued to obtain a better understanding of their applications in this area:

- Establish a chemically meaningful relationship between the chemical composition of LDHs and the CO_2 adsorption capacities of MMOs derived. (Chapter 3)

- Investigate the impact of the synthesis method and metal salt precursors on the CO_2 adsorption performance of LDH-derived MMOs. (Chapter 4)

- Establish a reliable method to measure the true chemical composition of LDHs. (Chapter 5)

- Re-evaluation of CO_2 adsorption performance of LDH-derived MMOs after obtaining better insights into the material and chemical composition (Chapter 6)

Chapter 3: A Systematic Crystal Chemical Approach to Investigating the Chemical Composition of LDH-based MMOs and its Effect on High Temperature CO$_2$ Capture

Critical Review

This chapter has been published as Cheah, L.A., Manohara, G.V., Maroto – Valer, M.M. and Garcia, S., 2020. Layered Double Hydroxide (LDH) – Derived Mixed Metal Oxides (MMOs): A Systematic Crystal-Chemical Approach to Investigating the Chemical Composition and its Effect on High Temperature CO$_2$ capture. ChemistrySelect, 5(19), pp.5587-5594 and in part, is published as Cheah, L.A., Manohara, G.V., Maroto-Valer, M.M. and Garcia, S., 2018, October. Layered Double Hydroxides: A Systematic Approach to Investigate the Effect of Mg/Al Ratio on CO$_2$ Capture. In 14th Greenhouse Gas Control Technologies Conference Melbourne (pp. 21-26). Author Contributions statement: LC, GM, and SG: conceptualization and design of the study. LC: experiments, acquisition and interpretation of data, visualization, and writing of the first draft of the manuscript. GM and SG: writing—review and editing for important intellectual content. SG and MM-V: supervision, project administration, and funding acquisition.

The primary aim of the study is to investigate the true effect of chemical composition on the CO$_2$ capacity of LDH-derived MMOs sorbents, which is one of the current knowledge gaps in the field (See Chapter 2 Section 2.7). As mentioned before, the relationship between the chemical composition (i.e., Mg/Al ratios) of precursor LDHs and the CO$_2$ capture performance of their derived MMO sorbents remains disputable. For instance, different optimal Al content has been proposed for the same LDH material, e.g., $x = 0.22$, 0.37 and 0.5, as optimal for carbon capture applications [152], [199], [200]. Even when prepared by the same synthesis method (e.g., co-precipitation method) and composition (nominal Mg/Al ratio of 3), very different reported values for the CO$_2$ capacity of the materials (0.3 – 0.71 mmol/g) have been reported [197], [199], [201]. Despite that, previous mechanistic studies suggest that the chemical composition (i.e., amount of Mg^{2+}) should have a proportional effect on the CO$_2$ capture capacity of MMOs, as MgO species is the active site for CO$_2$ adsorption [202]. Nevertheless, none of the LDH studies has demonstrated this relationship, revealing the lack of a chemically meaningful relationship between composition and CO$_2$ capture performance of LDHs derived MMOs sorbents.

The culprit for the lack of a clear relationship between the chemical composition of LDHs and the CO_2 capture performance of their derived MMO sorbents is likely the complex solution chemistry of LDHs, which ranges from their synthesis to application. To date, the formation mechanism of LDHs remains poorly understood. Typically, LDHs-based materials are synthesized by the co-precipitation method, using sodium hydroxide (NaOH) as a pH agent to precipitate LDHs from an aqueous solution of divalent (M^{2+}) and trivalent (M^{3+}) ions. It is generally agreed that LDHs form at a pH analogous to the precipitation of divalent hydroxide, and for the case of Mg-Al LDHs, the precipitating pH is above 7. However, in most cases, trivalent hydroxides will precipitate before LDHs form, due to their solubility product being significantly smaller than divalent hydroxides (Al hydroxides, $K_{sp} = 2$ x 10^{-31}, pH ~ 4 - 6; Mg hydroxides, $K_{sp} = 5.61$ x 10^{-12}, pH ~ 9) [203]. The matter is further complicated when the trivalent hydroxide is both amorphous and amphoteric in nature, such as $Al(OH)_3$. For example, in the titration process, $Al(OH)_3$ will precipitate first at low pH range and redissolve before the pH where LDH forms. However, this equilibrium between LDHs and $Al(OH)_3$ phase can take up to 100 days to stabilize [204]. The same goes for other commonly used trivalent hydroxides, such as $Fe(OH)_3$ and $Cr(OH)_3$. Therefore, the competitive precipitation of trivalent hydroxides as secondary phases makes it difficult to achieve the desired composition for this class of materials.

Furthermore, conventional characterization techniques for LDHs have limitations in detecting these amorphous impurities. For example, PXRD cannot detect amorphous phases, and chemical analysis cannot distinguish between crystalline and amorphous phases present in the sample. Relying on these techniques alone may result in misleading compositions, and is perhaps the main reasons behind the disputable relationship between the reported chemical composition and the CO_2 capture capacity of the resultant MMOs.

To address these gaps, this chapter presents a systematic study to investigate the effect of the chemical composition of LDHs on the CO_2 adsorption capacities of MMOs derived. Four samples of LDHs with varied Mg/Al ratios (2, 3, 4 and 5) were synthesized using the co-precipitated method. A novel crystal chemistry approach was used to arrive at the true chemical composition of precursors LDHs, using lattice parameter as an indicator, and coupled with various other techniques such as elemental analysis and solid-state ^{27}Al NMR

to identify any presence of impurities phase in the samples. To our best knowledge, this crystal chemistry approach has not been employed elsewhere. CO_2 adsorption capacity tests of LDHs were carried out in a TGA 5500 thermal gravimetric analyser (TA Instruments), at intermediate temperature (200 ºC) for 2 hours and under constant gas flow (90 vol % CO_2).

PXRD diffractograms and FTIR spectra confirm the successful synthesis of Mg-Al-CO_3 LDHs in all four samples synthesized using different nominal compositions and demonstrated that besides LDHs, no other obvious crystallized phase is seen from the patterns. The lattice parameter, a of synthesized LDHs ranging from 3.051 – 3.070 Å and resulted in values of x between 0.22 – 0.28, using the crystal-chemical model proposed by Richardson (2013). There seems to be a tendency for LDHs to crystallize in a composition that is close to that of the naturally available mineral Hydrotalcite ($x = 0.25$; $a = 3.054$ Å), irrespective of the nominal composition taken for the synthesis. Results from the elemental analysis show all four samples deviate from their desired composition and consist of a notable quantity of sodium content (9 - 14 wt %). Solid-state ^{27}Al NMR experiments reveal the presence of at least two different amorphous aluminium-based hydroxide/oxyhydroxide in all the resultant LDHs, which is in line with the discrepancies observed from the results of elemental analysis and lattice a-parameter. CO_2 capture capacities of LDH-derived MMOs at 200 ºC ranged between 0.69 – 0.82 mmol/g and are shown strongly correlated to the amount of sodium in the samples. Interestingly, there is no obvious correlation between Mg/Al ratios and the CO_2 capture capacity of LDHs.

Overall, this chapter establishes the relationship between the chemical composition of the LDH phase, the tendency to form various amorphous impurities, the presence of remnant sodium, and their role in the high-temperature CO_2 capture properties of derived MMOs. The observations of lattice parameters and impurities phase demonstrate the challenges of obtaining the desired compositions for the LDH phase. Interestingly, our findings reveal that the sodium content in the bulk phase has a stronger effect on the CO_2 adsorption properties of MMOs, than the chemical composition (Mg/Al ratios) of LDH crystals. This discovery highlights the importance of understanding the existence of impurities and the need to carefully handle the sorbent material, from synthesis to applications to maintain the desired properties of the bulk samples. This work also demonstrates the benefits of

combining crystal chemistry with systematic analytical approaches in establishing the true chemical compositions of LDHs.

3.1 Introduction

Like other solid sorbents, the chemical composition of the LDHs precursor plays a vital role in the CO_2 capture performance of the derived MMOs sorbent. This is because MMOs share the same chemical composition as their LDHs precursors. Taking Mg-Al based MMOs as an example, MgO is the active adsorbent species in the sorbent material; thus a direct correlation between the LDHs composition and the CO_2 capture capacity of the resultant MMOs should exist [202]. However, such a relationship is not yet observed in the literature, and the highest CO_2 adsorption capacities are not always measured from the MMOs having the highest Mg content. For instance, Yong et al. (2001) measured the highest adsorption capacities from MMOs having Mg content of 50 %, which contradicts the 63 % and 78 % observed by Sharma *et al.* (2008), and Gao *et al.* (2013), respectively [152], [199], [200]. In addition to this ambiguity, MMOs obtained from LDHs with the same synthesis method and composition also shows varied CO_2 capture capacities [151], [198], [199]. For example, for MMOs synthesized by the co-precipitation method and Mg/Al ratio of 3, the CO_2 capture capacities varied from 0.1 to 0.83 mmol/g [197], [199], [205]. Clearly, there is a disputable relationship between the reported chemical composition of the LDHs precursor and the CO_2 capture capacities of the resultant MMOs. Because of these discrepancies, it is important to establish a chemically meaningful relationship between precursor LDHs and derived MMOs to optimally develop high-temperature CO_2 capture sorbents based on LDHs.

Most LDH studies derived their measured chemical compositions from chemical/elemental analysis. Establishing the composition using chemical analysis is simple for most solid sorbents, but not so for LDHs due to their complex solution chemistry, from synthesis to application (e.g., anion exchange reaction). The physical properties of the unitary hydroxides, such as pH of formation, solubility product, thermodynamic stabilities and amphoteric nature of the metal cation, can have a significant influence on the final composition of the LDHs formed [205]–[208]. As a matter of fact, the formation mechanism of LDHs is still not clearly understood, with some reports proposing a topotactic mechanism, while others suggest a dissolution-reprecipitation (D-R) route [206], [207]. The nature of the reaction mechanism involved could impact the composition of the LDHs, and competing and parallel reactions such as formation of amorphous

hydroxides/oxy-hydroxides [209], [210] and leaching out of metal cations from the hydroxide lattice [146] are also commonly reported under the conditions employed for the LDH synthesis [208], [209]. Because of these complex factors, it is difficult to establish a meaningful LDH composition based on chemical analysis alone, as it does not distinguish between amorphous (as impurity) and crystalline phase; and tend to give misleading compositions of the resultant LDHs.

Given the significance that LDHs and related materials gained in recent years in catalysis in general, and high-temperature CO_2 capture in particular, it is crucial to establish a precise chemical composition. A chemically meaningful composition for LDHs can be established by using a combination of the crystal-chemical approach and analytical techniques. The lattice parameter a is directly proportional to the isomorphous substitution of M^{2+} ion in the hydroxide lattice with the M^{3+} ion in the solution. In this work, we report the results of the crystal-chemistry model to determine the true chemical composition of precursor LDHs, coupled with various other techniques such as elemental analysis and solid-state ^{27}Al NMR, and correlate the results with the CO_2 adsorption performance of resultant MMOs.

3.2 Experimental Details

3.2.1 Materials

The reagents used for the preparation of LDHs were $Mg(NO_3)_2 \cdot 6H_2O$ (ACROS Organics; MW = 256.4 g/mol, $\geq$ 98.0 %), $Al(NO_3)_3 \cdot 9H_2O$ (Fluka®; MW = 375.13 g/mol, $\geq$ 98.0 %), Na_2CO_3 (Fisher Chemical; SLR grade), NaOH (Fisher Chemical; SLR grade) and deionized water (Milli-Q® Reference ultrapure water, Type 1, resistivity = 18.2 MΩ cm at 25 °C). All reagents were used as purchased without further purification.

3.2.2 Preparations of LDHs and MMOs

The co-precipitation method used for the preparation of LDHs was based on Miyata's method [210]. First, a mixed metal solution containing Mg^{2+} and Al^{3+} ions in 2: 1 ratio was prepared using metal nitrates ($Mg(NO_3)_2 \cdot 6H_2O$ & $Al(NO_3)_3 \cdot 9H_2O$) and was added deionized water to arrive at a final concentration of 0.5 M. The mixed metal solution was then added dropwise into a base solution containing Na_2CO_3 (500 ml). The amount of Na_2CO_3 used was 3 times the stoichiometric amount of Al^{3+} ions. Throughout the titration, temperature was kept constant at 70 °C with continuous stirring at 400 rpm and pH was

maintained at 10 (± 0.02) with the addition of 1 M NaOH solution using an auto-titrator (Metrohm auto-titrator). The time of titration reaction was controlled within 3 hours and the solution containing the precipitates was left aged for another 18 hours, at 70 ˚C and with continuous stirring at 400 rpm. The solution was then filtered and washed 3 times with copious amount of deionized water by centrifugation before dried overnight in an oven. All the steps were repeated to prepare LDHs with different Mg/Al ratios (2, 3, 4 & 5). For MMOs characterization, the samples were prepared by calcining LDHs at 400 ˚C for 4 hours using a ramping rate of 10 ˚C/min and under a N_2 gas flow of 50 mL/min.

3.2.3 Characterization Techniques

Powder X-ray Diffraction (PXRD) patterns were recorded on a Bruker D8 Advance powder diffractometer, using Ge-monochromated Cu-Kα1 radiation (λ = 1.5406 Å) from a sealed tube, operating at 40 kV and 40 mA with a LynxEye linear detector in reflectance mode. All data were collected over angular range of 5 – 85 ˚ in 2θ values over one-hour span, with a step size of 0.009 ˚ 2θ per second. Fourier Transform Infrared (FT-IR) spectra were measured using Perkin Elmer Frontier IR Single-Range Spectrometer under ATR mode, recorded from wavenumber 4000 to 600 cm^{-1} with a 4 cm^{-1} resolution. Elemental analysis (ICP-OES) was carried out by atomic emission using Perkin Elmer Optima 5300 DV. Concentrated hydrochloric acid was used to dissolve the LDHs solid samples (50 mg) and diluted 20 times prior to analysis. Solid-state ^{27}Al NMR spectra were recorded on a Bruker Avance III spectrometer equipped with a wide-bore 9.4 T superconducting magnet (Larmor frequency of 104.3 MHz for ^{27}Al). Samples were packed into standard 4 mm rotors and rotated at the magic angle at a rate of 14 kHz. Magic angle spinning (MAS) spectra were recorded with a short pulse (0.25 μs, inherent flip angle of ~ 10 °) to ensure quantitative integrals for Al(IV) and Al(VI) signals. Signal averaging was carried out for between 1024 and 8192 transients with a recycle interval of 1 s. The multiple-quantum (MQ) MAS NMR spectra were recorded using an amplitude-modulated z-filtered experiment. Signal averaging was carried out for 96 or 144 transients for each of 36-72 t_1 increments of 71.43 μs with a recycle interval of 1 s. After acquisition the spectra were sheared and referenced in the indirect dimension according to Pike *et al.*[211]. Chemical shifts are reported in ppm relative to 1.1 M Al(NO$_3$)$_3$ solution using solid Al(acac)$_3$ as a secondary reference (δ_{iso} = 0.0 ppm, C$_Q$ = 3.08 MHz, η_Q = 0.15).

3.2.4 CO$_2$ Adsorption Tests

CO$_2$ adsorption tests were carried out in the thermal gravimetric analyser (TA Instruments; TGA Discovery 5500; Resolution: < 0.1 μg, weighing precision: ± 0.01 %). Fresh LDHs were used to prepare MMOs in each run to avoid CO$_2$ contamination. MMOs were first prepared by calcining LDHs at 400 °C for 4 hours, using a ramping rate of 5 °C/min and under a constant pure N$_2$ gas flow (purity 99.998 %, 50 mL/min, oxygen free) at ambient pressure (1 bar). Once the decomposition step was completed, MMOs were cooled down to the desired temperature (200 °C) and hold for 10 min before CO$_2$ gas flow (purity 99.98 %, 90 v/v % after diluted with N$_2$ gas purity 99.998 %) was introduced for the CO$_2$ adsorption test for 2 hours.

3.3 Results and Discussion

3.3.1 Characterization of LDHs and MMOs

The successful synthesis of Mg-Al-CO$_3$ LDHs using different nominal compositions is evidenced in the PXRD patterns (Figure 3.1A), and the samples are labelled with the molar Mg/Al ratios used at synthesis. The sharp and intense diffraction peak at low angle yielding a *d*-spacing value of 7.6 Å (2θ = 11.5 °) represents the average distance between hydroxide layers in the (*003*) plane of the LDH crystal system and is the characteristic value of carbonate anion intercalated LDHs [146]. The submultiple peak is seen at 3.8 Å (2θ = 23.5 °). The 'saw-tooth' shaped reflections at higher angles (2θ = 60 - 62 °) are assigned to (*110)* and (*113)* planes. Among them, the peak with a *d*-spacing value of 1.5 Å (2θ = 60.5 °) represents the average metal-oxygen (M-O) distance at the crystal lattice, and twice this value gives the unit cell parameter "*a*" of LDHs ($a = 2 \times d_{110}$). This is similar to the unit cell parameter "*a*" of Brucite, Mg(OH)$_2$ as LDH is essentially Brucite having some of the Mg^{2+} ions replaced by Al^{3+} ions at the octahedral sites in the hydroxide layers [212]. Besides LDHs, no other obvious crystallized phase is seen in the diffractograms.

Table 3.1 lists the *a*-parameter of all LDHs synthesized with different nominal compositions. All *a* values of the synthesized LDHs are lower than the *a* value of Brucite (3.142 Å), indicating the successful replacement of Mg^{2+} ions (0.72 Å) by smaller Al^{3+} ions (0.53 Å) at the octahedral sites [213]. The fact that the *a* values are decrease with smaller Mg/Al ratios suggests a progressive incorporation of Al^{3+} ions into the crystal lattice, which

is consistent with Vegard's law [214]. This is supported by the decreasing d_{003} values, which suggests increased interactions between hydroxide layers and anion interlayers due to higher Al content. Interestingly, the two samples synthesized with nominal Mg/Al ratios of 3 and 4, show almost have identical a and d_{003} values, suggesting a similar chemical composition. For the sake of convenience, the chemical composition of LDHs is represented by x, the amount of Al in the LDHs (x = Al/ Mg + Al) for the rest of the chapter.
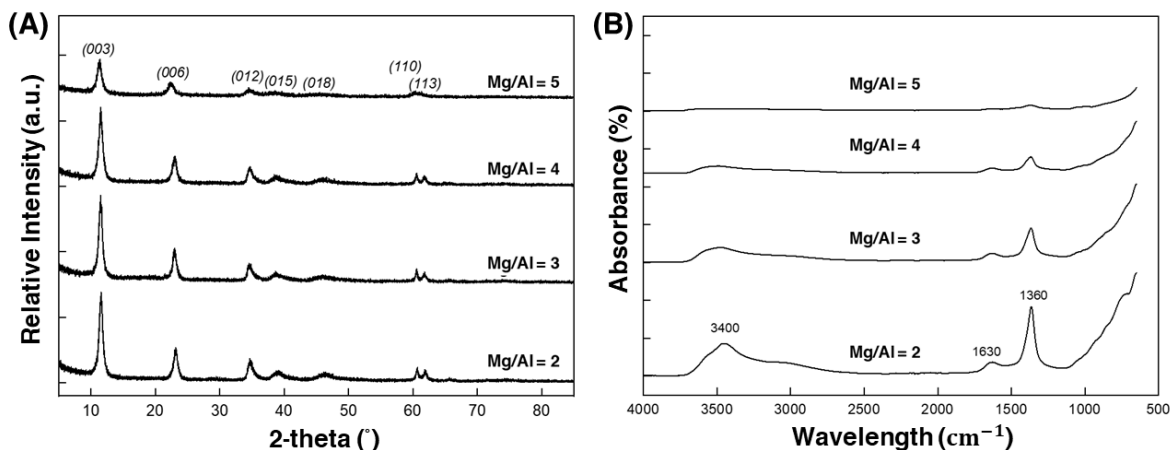
Figure 3.1 – (A) PXRD patterns and (B) FTIR spectra of LDHs synthesized with different Mg/Al ratios

Table 3.1 - Nominal composition and lattice parameters of LDHs with different Mg/Al ratios

Nominal Mg/Al Ratios	$x_{nominal}$	a (Å)	d_{003} (Å)	$x_{crystal}$
2	0.33	3.051	7.647	0.28
3	0.25	3.055	7.673	0.27
4	0.20	3.056	7.674	0.27
5	0.17	3.070	7.812	0.22

Further successful synthesis of carbonate-LDHs is confirmed by the FTIR spectra, as shown in Figure 3.1B. The characteristic vibrations due to intercalated carbonate ion (around 1360 cm^{-1}) and hydroxyl ions from layered hydroxides (around 3400 cm^{-1}) confirm the successful formation of LDHs [215], [216]. The weak vibration band at 1630 cm^{-1} is due to bending mode of the intercalated water molecules.

Upon calcination at 400 °C, the formation of poorly crystallized mixed metal oxides is revealed by the PXRD patterns (Figure 3.2A). The characteristic peaks due to LDHs are no longer observed, which indicates the collapse of layered structure. Three broad reflections with *d*-values of 3.03 Å ($2\theta = 36.9$ °), 2.09 Å ($2\theta = 43.2$ °) and 1.48 Å ($2\theta = 62.7$ °) are observed and assigned to the Periclase MgO phase [217]. It is noteworthy to mention that no trace of aluminium oxides or other phases was observed from the PXRD pattern of all samples. Figure 3.2B shows the FTIR spectra of MMOs, and the characteristic vibrations of LDHs were significantly reduced, suggesting the formation of MMOs [218]. The weak 1400 and 1630 cm^{-1} bands are due to the adsorption of atmospheric moisture and CO_2 species. The vibration band below 1000 cm^{-1} became more intense, indicating the formation of M-O bonding after calcination.
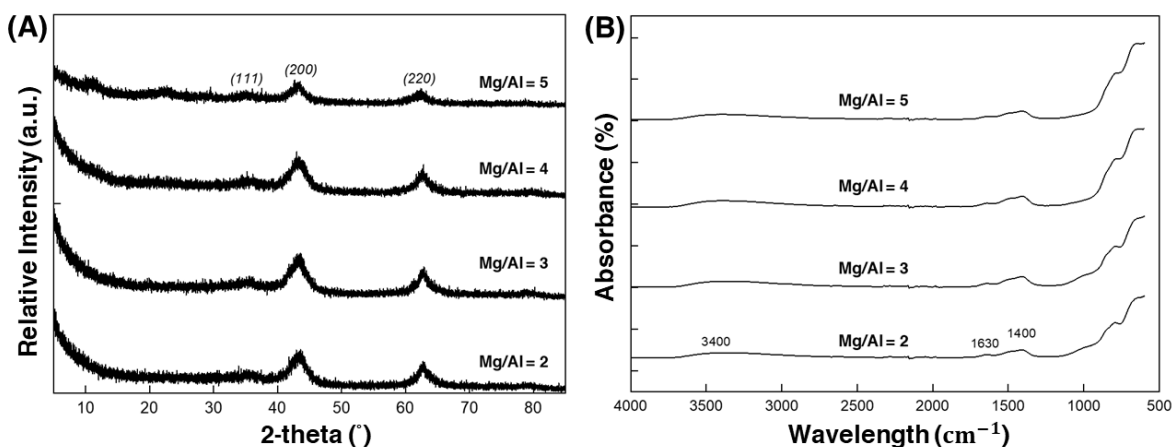
Figure 3.2 – (A) PXRD patterns and (B) FTIR spectra of MMOs synthesized with different Mg/Al ratios

3.3.2 Crystal-chemical model of LDHs

The structural-composition relations for brucite-like hydroxides were first investigated by Brindley *et al.* (1979) for divalent hydroxides and later extended to LDHs by Richardson (2013), using a combination of geometrical arguments and crystal-chemical aspects [219], [220]. The models derived by Richardson (2013) demonstrate the possibility to calculate *x* from *a* for Ni- and Mg-based LDHs and the crystal-chemical model for Mg-based LDHs was used to determine *x* for the LDHs synthesized in the study [Eq. 3.1]. The *r* stands for ionic radii and α is the angle between metal cation and two oxygen sites of the same basal

plane. We used the Shannon's effective ionic radii of Mg^{2+} (0.72 Å) and Al^{3+} (0.53 Å) having the octahedral coordination for $r(Mg^{2+})$ and $r(Al^{3+})$ values [213]. For α and $r(OH^-)$ values, we used 97.41 ° and 1.365 Å, respectively, which are the values recommended by Richardson (2013). It is important to point out that these values were obtained from a wide-ranging set of experimental a-parameters reported in the literature and their nominal x used at synthesis. Upon substitution of these values for the different parameters in Eq. 3.1 and further rearrangement, Eq. 3.2 was derived.

$$a = 2 \sin \frac{\alpha}{2} \ (r(Mg^{2+}) + r(OH^-)) - 2 \sin \frac{\alpha}{2} x(r(Mg^{2+}) - r(Al^{3+}))$$

[Eq. 3.1]

$$x = (3.133 - a)/0.2855 = 10.9737 - 3.5026a$$

[Eq. 3.2]

By employing this equation and substituting the "a" values, the "x" values for the synthesized LDHs, as shown in Table 3.1. For simplicity's sake, this "x" value derived from Richardson's crystal-chemical model is denoted as "$x_{crystal}$". It is important to note that "$x_{crystal}$" represents the actual Al content in the crystal lattice and should not be confused with the "$x_{nominal}$", which is directly derived from the nominal Mg/Al ratios used during synthesis.

As shown in Table 3.1, the "x" values derived from Richardson's model fall within the possible x range for the LDHs phase (0.17 - 0.33). A narrow range of "$x_{crystal}$" (0.22 - 0.29), which is close to the LDH composition found in nature ($x = 0.25$) in the mineral hydrotalcite ($Mg_6Al_2CO_3(OH)_{16}\cdot4H_2O$) [221]. This suggests that synthetic LDHs tend to have a chemical composition that is close to that of Hydrotalcite ($a = 3.054$ Å). For example, when attempting to synthesize LDHs with a higher nominal "x" value (0.33) than that of Hydrotalcite, the composition tends to move towards $x = 0.25$ by intercalating lesser amount of Al^{3+}, as evidenced by the obtained "$x_{crystal}$" (0.28). Similarly, when attempting to synthesize LDHs with a lower x value (0.17), the observed "$x_{crystal}$" moves towards $x = 0.25$ (i.e., "$x_{crystal}$" = 0.22).

3.3.3 Elemental Analysis of LDHs

To verify "$x_{crystal}$", the expected concentration of metal ions in LDHs calculated based on nominal Mg/Al ratios and compared with the observed concentration obtained from elemental analysis (Table 3.2). Elemental analysis also revealed a significant amount of residual sodium in all samples, ranging between 9 to 14 %. From Table 3.2, a clear discrepancy between the expected and observed metal ion concentrations is observed, notably the Mg^{2+} concentrations, proved the deviation from the expected (nominal) composition. The observed Mg^{2+} concentration detected in the samples is higher, suggesting that the synthesized LDHs have more Mg content than anticipated. This is consistent with the observation of crystal lattice parameters above, where the "$x_{crystal}$" of synthesized LDHs tends to be larger than their nominal ones ($x_{nominal}$). The only exception is the sample synthesized with a nominal Mg/Al ratio = 2, which shows a smaller "$x_{crystal}$" than the "$x_{nominal}$". No clear correlation is seen between "$x_{nominal}$" and the calculated "$x_{chemical}$". For example, the compositional deviation from the nominal value is relatively small in the case of LDHs with Mg/Al = 3 and 5 compared to the other two LDHs (Mg/Al = 2 and 4).

Table 3. 2 - Expected (nominal) and observed (measured) concentration of LDHs measured from elemental analysis (ICP-OES).

Nominal Mg/Al ratios	Expected Concentration (wt %)		Observed Concentration (wt %)			$x_{nominal}$	$x_{crystal}$	$x_{chemical}$
	Mg	*Al*	*Mg*	*Al*	*Na*			
2	20.5	8.7	20.8	11.4	9.0	0.33	0.28	0.28
3	21.6	8.3	23.5	8.7	9.5	0.25	0.27	0.26
4	21.4	7.3	25.1	7.0	13.8	0.20	0.27	0.23
5	22.9	5.7	26.1	5.9	13.5	0.17	0.22	0.18

The clear deviation between "$x_{crystal}$" and "$x_{chemical}$" indicates the presence of phases other than LDHs. LDHs are known to crystallize only within a specific range of x (0.17 - 0.33). It is commonly believed that using nominal concentration of this range yields pure LDHs. Whenever attempts were made to synthesize LDHs beyond this range, impurity phases were reported along LDHs [222], [223]. As described before, the "$x_{chemical}$" calculated from

chemical analysis does not distinguish between the metal cations in the LDHs crystal lattice and the ones in impurities. If any of these phases have form, elemental analysis tends to include them as part of the total metal concentration. In addition, some of the previously reported impurity phases, such as Al-based hydroxides/oxy-hydroxides, are amorphous in nature and therefore undetectable by PXRD measurements. To avoid this, in the present study, only x within this range (0.15 – 0.33) were used to synthesize LDHs, but still resulted in a clear deviation between "$x_{chemical}$" and "$x_{crystal}$". This suggests the presence of phases other than LDHs. To address this potential presence of impurity phases, it is necessary to discuss the formation mechanism of LDHs.

The formation mechanism of LDHs is not as clearly established compared to their counterparts, cationic clays. The ambiguity lies between topotactic and dissolution-reprecipitation (D-R) mechanisms, owning to the significant differences between solubility products (K_{sp}) of the unitary hydroxides present in LDHs. For instance, trivalent metal hydroxides ($K_{sp} = 10^{-31} - 10^{-38}$) precipitate at a much lower pH, between 4 – 6, than the divalent metal hydroxides ($K_{sp} = 10^{-10} - 10^{-16}$) that occurs above pH 8 [203]. In an earlier study. Boclair $et\ al.$ (1999) suggested LDHs are formed after the topotatic reaction between precipitated $Al(OH)_3$ and Mg^{2+} ions, whereas a later study from Radha $et\ al.$ (2003) proposed a D-R mechanism, where the precipitated amphoteric $Al(OH)_3$ first dissolves and reprecipitates at higher pH along with magnesium hydroxide that forms LDHs [206], [207]. In light of these discussions revolving around the formation mechanism of LDHs and the likely formation of Al^{3+} phases, solid-state ^{27}Al NMR experiments were carried out to identify the aluminium phases present in samples.

3.3.4. Solid State ^{27}Al NMR of LDHs

The solid state ^{27}Al NMR technique was employed to examine the local Al environment in the LDHs and MMOs phases. The ^{27}Al nuclide was chosen over the ^{25}Mg nuclide for NMR experiments due to several reasons. Firstly, Mg-based phases only exist in the crystalline phase, and no other crystalline phase besides LDHs was observed in the PXRD diffractogram, thus it is assumed that all the Mg^{2+} is crystallized within the LDHs lattice. Secondly, the chance of amorphous Al-based impurities being present in the LDH samples is high, as evidenced by the discrepancies between "$x_{crystal}$" and "$x_{nominal}$". Since all the

reagents were prepared according to the nominal (i.e., expected) compositions, the excess Mg content in the obtained LDHs crystal indicates that part of the Al^{3+} ions have not been incorporated into the LDH lattice and likely precipitated as a secondary impurities phase, as explained by the formation mechanism (Section 3.3). Additionally, the ^{25}Mg nuclide has relatively unfavourable characteristics for NMR experiments, such as low natural abundance (10.13 %), relatively large quadrupolar broadening, and low gyromagnetic ratio. Thus, examining the local environment of Mg is more challenging than that of Al. Nonetheless, studies of ^{25}Mg NMR spectroscopy for LDH phases are available in the literature [224], [225].

Figure 3.3A presents the solid-state ^{27}Al NMR two-dimensional (2D) MAS spectra for the LDHs synthesized in the present work. The sharp peak close to δ *ca.* 9.3 ppm found in all spectra is assigned to the six-coordinated Al species (AlO_6) located at the octahedral sites of LDHs [226]. The chemical shifts for other coordination states of Al^{3+} like AlO_5 (δ 30 - 35 ppm) and AlO_4 (δ 55 - 75 ppm), were not observed, indicating their absence in the synthesized LDHs. However, a closer look at the enlarged MAS spectra plots (Figure 3.3B) shows that the AlO_6 peak tails on both sides between 15 and –5 ppm, suggesting the potential presence of other AlO_6 species with chemical shifts that fall within the range, e.g. Gibbsite (6 & 8.3 ppm) [227], Bayerite (8.8 ppm) [228], Boehmite (9.0 ppm) [228] or Pseudoboehmite (11.2 ppm) [229]. It is also possible that the two other polymorphs of $Al(OH)_3$, Nordstrandite and Doyleite, also fall within this range, but their solid-state ^{27}Al NMR information is not found in any literature. Therefore, if any of the abovementioned phases have precipitated as amorphous ones together with the LDHs, especially in minor quantities, it is difficult to identify these from the 2D NMR spectra due to the close resonance of the peaks.
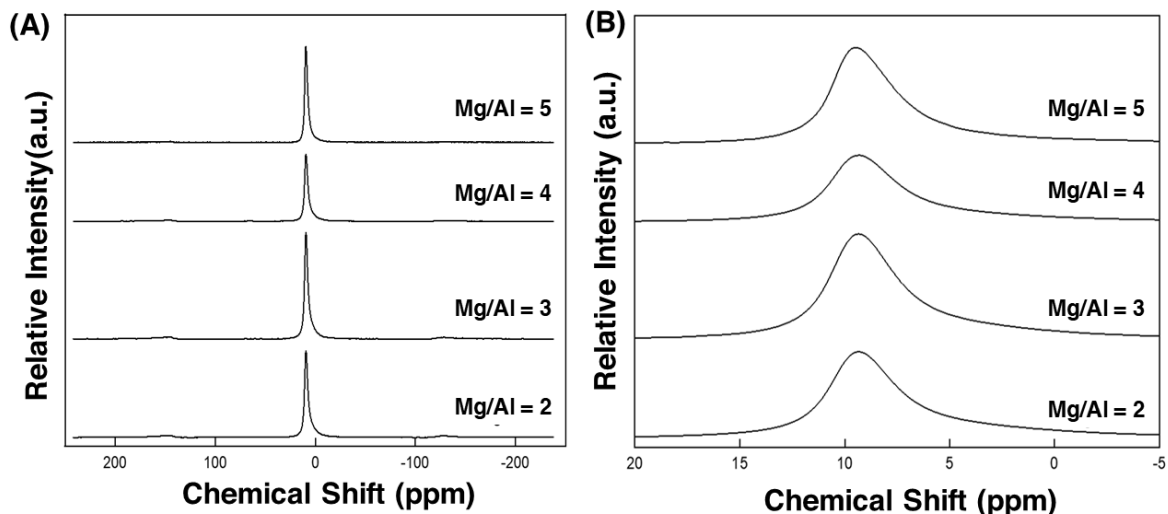
Figure 3.3 - (A) Full and (B) enlarged part (20 to -5 ppm) of solid-state ^{27}Al MAS NMR spectra of LDHs synthesized with different nominal Mg/Al ratios

To further interpret the NMR spectra, three-dimensional (3D) MQMAS spectra of LDHs were recorded (Figure 3.4). These shoulders extending from the centre at δ_2 *ca.* 10 ppm (δ_1 *ca.* 6 ppm), and reaching towards lower δ_1 values of LDHs (-5 ppm) observed from all samples are consistent with the 2D MAS spectra above and suggest the presence of Al^{3+} in a different octahedral environment in LDHs. Similar observation has been reported previously [230], [231]. This difference in Al environment was explained by Rocha *et al.* (1999) as a result of the "random insertion of Al^{3+} in the layers". However, based on the extensively studied ordering of Al^{3+} within the LDHs hydroxide lattice, which is widely understood to be based on mutually repulsing nature of Al^{3+}, which tends to locate as far as possible from each other with known ordering manner [220]. Therefore, random insertion of Al^{3+} into the crystal lattice is unlikely [231]. To get a better understanding of the AlO_6 species present in LDHs, the 2D NMR signals of all the LDHs were deconvoluted.
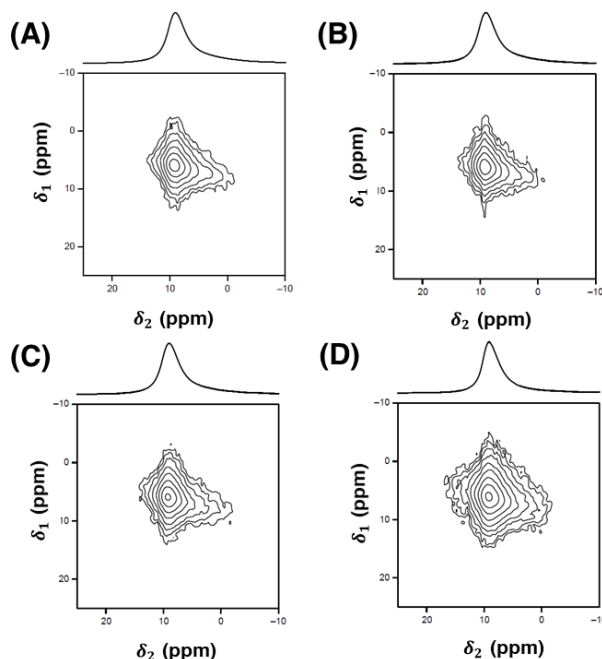
Figure 3.4 - Solid-State ^{27}Al MQMAS NMR spectra of LDHs with nominal Mg/Al ratios of (a) 2, (b) 3, (c) 4 and (d) 5

Figure 3.5 presents all the deconvoluted 2D NMR spectra of LDHs, and the deconvoluted signals are tabulated in Table 3.3 Surprisingly, deconvolution shows that at least two additional resonances besides the one for LDHs (δ 9.3 ppm) are present in all samples. The chemical shifts obtained from deconvolution (δ 5.6, 5.8, 6.2, 8.5 and 8.6 ppm) are a close match to those of Gibbsite, Bayerite and Boehmite. Given the complex solution chemistry during the formation of LDHs, precipitation of these phases as amorphous compounds is highly plausible. However, we are unable to assign these secondary phases to only one particular compound due to the overlapping chemical shifts of the abovementioned phases. Overall, ^{27}Al NMR data of LDHs shows the presence of secondary Al^{3+} phases as impurities, which is in line with the discrepancies observed in $x_{crystal}$ and $x_{chemical}$ values.

The 2D MAS spectra for all MMOs are included in Figure 3.6. A new broad asymmetric line shape resonance emerged near 70 ppm, suggesting the presence of four-coordinated Al species (AlO$_4$). This is consistent with the previously reported movement of Al^{3+} from octahedral to tetrahedral sites in the MMOs lattice [230]–[232]. Interestingly, the AlO$_6$ peak of calcined LDHs synthesized with nominal Mg/Al ratio of 2 and 3 is visibly narrower (Figure 3.6B) compared to the two other samples, suggesting a more ordered and

symmetric Al environment. This is in agreement with the result from elemental analysis as both samples showed the minimum deviation between $x_{chemical}$ and $x_{crystal}$.
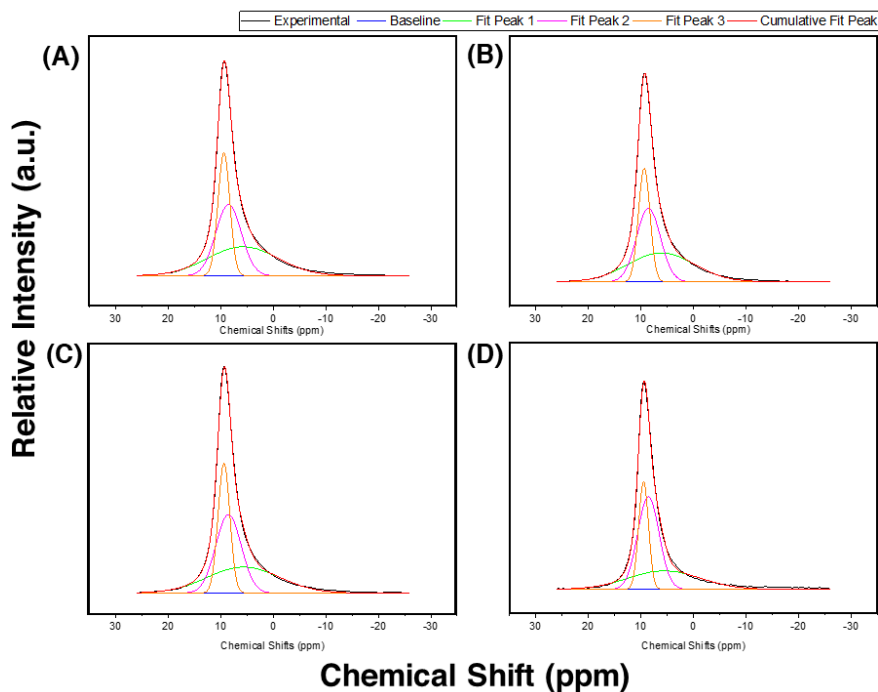
Figure 3.5 - Solid-State ^{27}Al MQMAS NMR experimental and fit spectra of LDHs with nominal Mg/Al ratios of (a) 2, (b) 3, (c) 4 and (d) 5

Table 3.3 - Solid-state ^{27}Al MAS NMR chemical shifts obtained from deconvolution and fitness test

Nominal Mg/Al ratios		2	3	4	5
Fitted Peak Signals (ppm)	**I**	5.8	6.2	5.6	5.6
	II	8.5	8.6	8.5	8.6
	III	9.4	9.4	9.4	9.5
Adj. R-Square		0.9995	0.9996	0.9995	0.9986
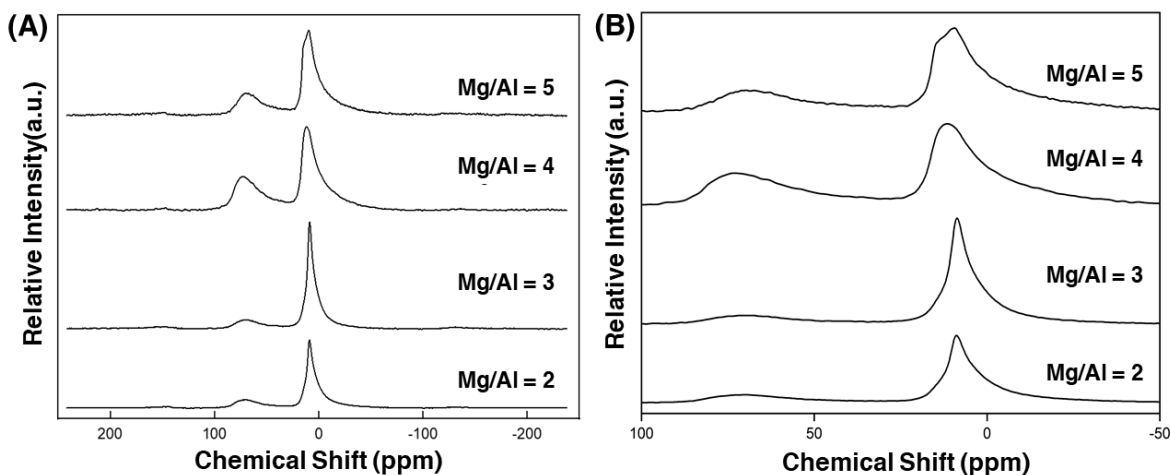
Figure 3.6 - (A) Full and (B) enlarged part (100 to -20 ppm) of solid-state ^{27}Al MAS NMR spectra of MMOs synthesized with different nominal Mg/Al ratios
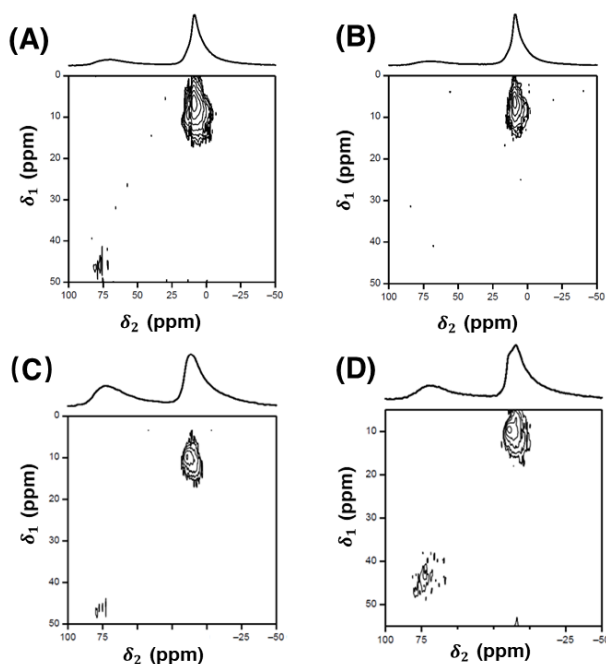
Figure 3.7 - Solid-state ^{27}Al MQMAS NMR spectra of MMOs synthesized with different nominal Mg/Al ratios

When translated into 3D MQMAS, significant differences in spectra are observed across the samples. The most remarkable observation is the disappearance of the AlO$_4$ resonance in the MQMAS spectra of MMOs samples with Mg/Al ratios of 3 (Figure 3.7). However,

this does not mean that four-coordinated Al species were not formed in the particular sample, as the AlO_4 peak was clearly seen in 2D MAS (Figure 3.6A) and 3D MQMAS spectra (Figure 3.7B). We speculate that this is due to the large AlO_6 to AlO_4 ratio of the sample, which caused the AlO_4 intensity to virtually "disappear" from the spectrum. The obvious dissimilarities at the AlO_4 site across the samples also proved the presence of different Al phases.

3.3.5 CO₂ Adsorption

Figure 3.8A shows the CO_2 adsorption capacities of LDH-derived MMOs at 200 °C versus $x_{nominal}$, $x_{chemical}$ and $x_{crystal}$. There seems to be no obvious linear correlation between the composition of LDHs and CO_2 adsorption capacities of MMOs. Interestingly, the highest capacity (0.82 mmol/g) is measured from the MMOs having $x_{crystal}$ value of 0.27, rather than the LDHs with higher Mg content (e.g., 0.22). In addition to that, the three samples having very close $x_{crystal}$ values (0.27 - 0.29) were shown to have slightly different CO_2 adsorption capacities (0.69 - 0.82 mmol/g), which suggests a disputable relationship between them. Logically, materials of the same chemical composition and prepared by the same synthesis method should exhibit similar properties. However, this is clearly not the case and is similar to the observations of the previously reported results in the literature[109], [199]. The impurities phase reported earlier may have played role in the CO_2 capture capacities of MMOs.

The concentration of different metal ions obtained from elemental analysis is plotted against the observed CO_2 capture capacities in Figure 3.8B. Again, there is no direct relationship between the Mg^{2+} content of the samples and CO_2 capture capacities. However, there seems to be a trend between the amount of sodium present in each sample and the CO_2 capture capacity. For instance, the highest amount of sodium is present in LDHs with a nominal Mg/Al ratio of 4, which the derived MMOs is also measured with the highest CO_2 capture capacity. Similarly, LDHs with a nominal Mg/Al ratio of 2 show the lowest amount of sodium and CO_2 capture capacity. This observation is consistent with the strong basic nature of sodium, which is commonly used as promoter to enhance CO_2 adsorption of MMOs.[41] However, the presence of sodium in all samples is somewhat intriguing. All the samples were synthesized according to the protocol reported in literature and washed with

copious amount of water to remove excess sodium and metal salts used in the preparation[197], [222], [233], [234]. The washing was stopped when the sample started to leach out or unsettle and this is widely regarded as an indication that all the excess chemicals used in the synthesis have been removed. In our washing, the water volume was constant for all samples, but the sodium content varied drastically (9 – 14 %) across the samples.
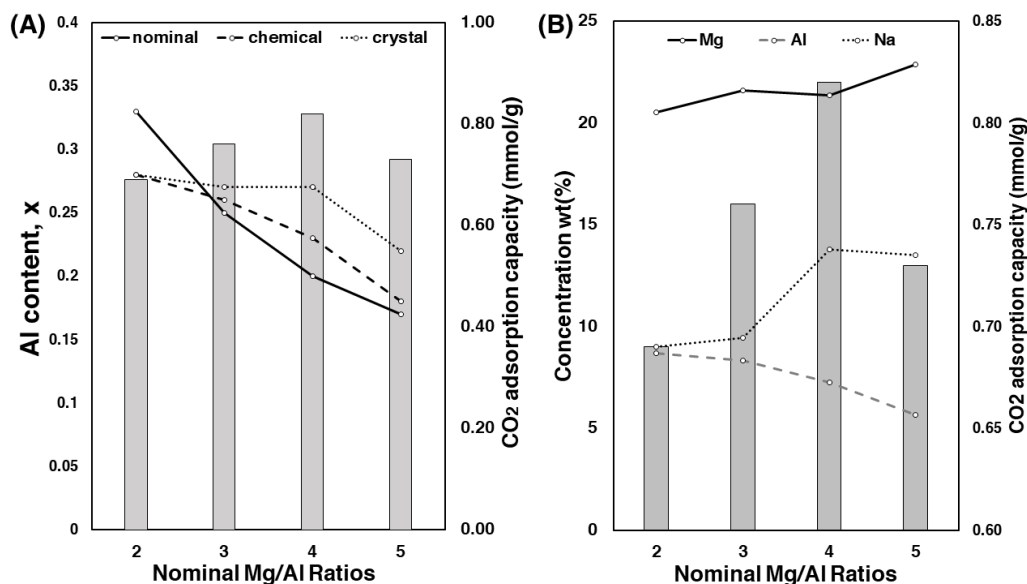
Figure 3.8 - CO₂ uptake capacities of MMOs plotted with (A) *x* of LDHs and (B) concentration of metal cations obtained from ICP-OES

Complete removal of sodium used in the synthesis of LDHs is challenging due to the nature of unitary hydroxides involved, namely $Mg(OH)_2$ and $Al(OH)_3$. Previous studies attempted to remove excessive nitrate ions and sodium by washing the LDHs until pH of filtrate close to neutral or reaching 7. However, at this pH, $Mg(OH)_2$ is thermodynamically unstable and becomes unsaturated. This means that leaching out of $Mg(OH)_2$ from the LDHs phase could happen and leads to the partial dissolution of the LDHs crystals. Hence, with the current washing technique, complete removal of sodium without affecting the composition of pristine LDHs seems difficult. Due to the sodium being the uncontrollable factor, this is perhaps why inconsistent CO_2 adsorption capacities of LDHs have been reported from different CO_2 capture studies (0.3 – 0.83 mmol/g), even though the materials were prepared by the same synthesis method and nominal compositions[197], [199], [205], [234].

101

Although we tried to establish a chemically meaningful relationship between the composition of LDHs and CO_2 adsorption of MMOs, it is however not as straightforward as it seems. There is no obvious direct relationship between the composition of LDHs and the CO_2 capture properties of their derived MMOs, due to the presence of impurities and uncontrolled formation mechanisms involved. This new finding urged us to face the existence of impurities more seriously and understand that the handling of the sorbent material, starting from the synthesis method to applications, can affect the properties of the bulk samples.

3.4 Conclusions

The present work proposes to establish a chemically meaningful relationship between the Mg/Al ratio of precursor LDHs and the CO_2 adsorption capacities of derived MMOs sorbents. LDHs with four different Mg/Al ratios (2, 3, 4, and 5) were synthesized *via* the co-precipitation method and calcined at 400 °C to form MMOs capable of capturing CO_2 at high temperature. Using a crystal-chemistry model and the lattice parameter "*a*", the true composition of LDHs was obtained, and a tendency to acquire the natural composition, close to the mineral Hydrotalcite ($x = 0.25$) was observed. Solid-state ^{27}Al NMR reveals the presence of aluminium-based hydroxide/oxyhydroxides as amorphous impurities in all the resultant LDHs. This study also demonstrates the necessity to combine crystal-chemistry with analytical approaches to establish the chemical compositions of LDHs. Elemental analysis shows a notable quantity of sodium content in all samples (9 - 14 wt %). The CO_2 capture capacity of MMOs derived from synthesized LDHs shows no direct correlation with established compositions of the LDHs. However, the CO_2 capture capacity seems to be more correlated with the amount of remnant sodium present in the samples. The sodium content in LDHs solution is highly inhomogeneous and uncontrollable, even with the same post-synthesis protocol. The presence of unavoidable impure phases in LDHs, especially ones synthesized from the co-precipitation method, prompts us to examine its effects on CO_2 uptake more seriously in future studies.

Chapter 4: Impact of synthesis method and metal salt precursors on the CO₂ adsorption performance of Layered Double Hydroxides derived Mixed Metal Oxides (MMOs)

Critical Review

This chapter has been published as Cheah, L.A., Manohara, G.V., Maroto-Valer, M.M. and Garcia, S., 2022. Impact of Synthesis Method and Metal Salt Precursors on the CO₂ Adsorption Performance of Layered Double Hydroxides Derived Mixed Metal Oxides. *Front. Energy Res.* 10:882182. doi: 10.3389/fenrg.2022.882182. Author Contributions statement: LC, GM, and SG: conceptualization and design of the study. LC: experiments, acquisition and interpretation of data, visualization, and writing of the first draft of the manuscript. GM and SG: writing—review and editing for important intellectual content. SG and MM-V: supervision, project administration, and funding acquisition.

This chapter is a follow up investigation of previous work presented in Chapter 3, which introduced a systematic crystal chemical approach to investigating the chemical composition of LDHs and its effect on high temperature CO₂ capture. The previous work found that the presence of impurities phase, particularly the residual sodium, had a direct impact on the CO₂ adsorption capacities of LDH-based MMOs synthesized by the co-precipitation method. This could explain the inconsistent CO₂ capture performance reported for this class of sorbent material. Interestingly, several studies have also reported a similar observation that sodium residues can affect the catalytic performance of co-precipitated LDH-derived materials[235], [236]. Although the catalytic and adsorption performance of the derived material is mostly boosted by the presence of sodium residues, the problem is that the performance may not be reproducible between two batches. Another major risk of using these types of materials is that the alkali metals promoter (including those intentionally added) may leach out and cause downstream problems, such as deactivation of other catalysts or cause massive corrosion issues. Thus, controlling the alkali metal content in the LDHs is important.

Nevertheless, it seems almost impossible to control or completely remove residual sodium from co-precipitated MMOs, as explained in Chapter 3. To avoid this, some studies have suggested alternative synthesis routes for LDHs, such as the urea hydrolysis method, which

does not involve any sodium precursors in the synthesis process [235], [237]. However, the detailed comparison between LDHs synthesized from urea hydrolysis method and co-precipitation method is still lacking, especially for CO_2 capture applications. It is generally agreed that for CO_2 capture applications, MMOs prepared by the co-precipitation method perform better than those prepared by urea hydrolysis method, due to their higher CO_2 adsorption capacities (almost two times in excess) [199]. However, the selection of a suitable CO_2 capture sorbent does not rely on a single metric (e.g., CO_2 adsorption capacity). Other synthetic factors are equally important, as they can cause sustainability and environmental concerns. For example, the nature of the reagents, conditions of the synthesis reaction, atom efficiency/ synthesis yield, reactant usage, toxicity, and the post-synthesis processes involved. These aspects will be discussed in detail in this chapter [223], [224], [240], [241], [242].

Hence, the main objective of this work is to study the impacts of synthesis method and metal salt precursors on the properties of LDHs and MMOs, and their effect on their high temperature CO_2 performance. Two common synthesis methods, the urea hydrolysis method and co-precipitation method, were employed to synthesize $Mg-Al-CO_3$ LDHs with different compositions (2, 3 & 4) and different metal salt precursors (metal nitrates and metal chlorides). These synthesized samples were comprehensively characterized by techniques such as PXRD, FTIR, Elemental Analysis (ICP-OES). The true chemical composition of the LDHs samples is again examined by the lattice parameter "*a*". As a novelty of this work, the synthesis efficiency of different synthesis methods and salts precursors is evaluated in terms of product yields, purity, and percentage of unreacted metal ions. This can be achieved by carefully analyzing the filtrates collected during the synthesis process. To the best of our knowledge, this has not been attempted for LDH for CO_2 capture studies yet. The textural properties of MMOs samples, e.g., surface area and pore structures, are then characterized by BET and SEM analysis. The CO_2 adsorption performance (e.g., adsorption capacity, kinetics, and cyclic stability of the synthesized LDHs) is evaluated by using a TGA 5500 thermal gravimetric analyser (TA Instruments) and correlated with the synthesis efficiency metrics.

The characterization of LDHs samples synthesized in this work shows that urea hydrolysis (UH) method tends to give LDH with lower product yields (54 – 81 %) and high Al content, due to the smaller a values obtained (3.033 – 3.038 Å). The chemical composition of urea hydrolysis LDHs seems to be fixed, as the variation of a-parameter is very small, irrespective of nominal compositions and salt precursors used. Chemical analysis reveals the presence of large amount of amorphous Al-based hydroxides in all the samples. On the contrary, the co-precipitation (CP) method produces high products yields (~ 100 %) and high purity LDHs, evidenced by the good agreement between a-parameter, nominal compositions, and bulk compositions. The a-parameters obtained from co-precipitated LDHs vary significantly (3.037 - 3.067 Å) and shows a dependence on the nominal compositions used, which means that the co-precipitation method can produce LDHs with wider chemical compositions.

Elemental analysis of the filtrates of urea hydrolysis LDHs shows the presence of large amount of unreacted Mg^{2+} ions (34 – 74 % of the concentration of Mg^{2+} ions used at synthesis), which is consistent with the observation of low product yield (54 – 81 %). On the other hand, the co-precipitation method shows close to zero content of unreacted cations in the filtrates. Surprisingly, elemental analysis of all LDHs samples shows traces amount of sodium content, including the urea hydrolysis samples. The only possible source of sodium in the urea hydrolysis samples is most likely from the metal salt precursors, although it exists in small concentrations in all reagents (less than 10 – 100 mg/kg) . On the other hand, due to the different centrifuge machine and resolution being used for washing step, the amount of sodium in the co-precipitated samples has been greatly reduced to less than 1 %, compared to close to 9 % in previous work. Nevertheless, despite employed a consistent protocol for all the samples, the sodium content still varied, between 0.3 to 0.9 %.

The CO_2 adsorption performance of MMOs derived from urea hydrolysis and co-precipitated method shows varied results. In essence, the presence of impure secondary phases and the sodium content were shown to have a significant effect on the CO_2 adsorption performance of LDH derived MMOs. For urea hydrolysis MMOs, the LDH yield and purity were shown to be the most important factors affecting its CO_2 performance, as the highest adsorption uptakes, kinetics and cyclic stability were all measured from the

MMOs exhibiting the highest LDH yield and lowest amounts of Al-based impurities. For co-precipitated MMOs, sodium content is still the primary parameter affecting their CO_2 adsorption performance. Both the highest CO_2 uptakes and best CO_2 kinetics were measured from the MMOs having the highest sodium content. However, MMOs having high sodium content were also found to exhibit poorer cyclic stability. It also be noted that despite the lower sodium content, the CO_2 adsorption capacities of MMOs still fall in the same range (< 1 mmol/g), as those previously synthesized with higher sodium content ($9 - 14$ wt %) in Chapter 3.

Compared to the synthesis method, the choice of metal salt precursors is relatively significant. Nevertheless, MMOs synthesized by metal chlorides generally shows a small improvement in LDH purity than the ones obtained by metal nitrates. Due to the higher sodium content in metal nitrates, MMOs that were synthesized shown to have better CO_2 adsorption performance than the ones synthesized by metal chlorides.

Overall, this work aims to establish the relationship between CO_2 adsorption performance of Mg-Al-LDH-based MMOs, and synthesis efficiency of synthesis methods used, e.g., purity, synthesis yields, and percentage of unreacted reactants. The result from this work confirms that the synthesis method has a large impact on the CO_2 capture performance of derived MMOs. This work is also an attempt to provide detailed information of the LDH synthesis process that is necessary for future life cycle assessment (LCA) of CO_2 capture process using LDH derived sorbents, which is currently lacking in the literature.

4.1 Introduction

LDH precursors have significant influence and often determine the CO_2 capture and reactivity of derived MMOs. Variables that affect the properties of LDHs, such as synthesis method, composition, structure, surface area, are important to understand in order to design better MMOs for different applications. Among these variables, the synthesis method arguably has one of the most significant impacts and should be carefully selected at the beginning of material development stage. For example, a number of LDHs were synthesized using reconstruction and anion exchange methods. However, both these methods are cumbersome and are not sustainable for producing LDHs at an industrial scale because they require multistep synthetic processes that are often not stoichiometric in nature and may produce large amounts of unwanted side products[238]. Additionally, the formation of LDHs is highly sensitive to synthesis conditions [147], and LDHs derived from different synthesis methods are likely to show wide differences in physical properties [239].

For CO_2 capture applications, LDHs were mainly synthesized by co-precipitation method because it is the simplest preparation method and is amenable to scaling up[240], [241]. However, some recent studies have suggested the hydrothermal urea hydrolysis method as a better route to synthesize LDH based sorbents to avoid the presence of impurities and their effect on the overall CO_2 capture properties[235], [242], [243]. Indeed, MMOs synthesized from co-precipitation and urea hydrolysis method have shown different CO_2 adsorption values (0.30 – 0.72 mmol/g) [199]. Nevertheless, the selection of a promising CO_2 capture sorbent does not depend entirely on a single metric, e.g., CO_2 sorption capacity [244]. Other synthetic factors are equally important as they can cause sustainability and environmental concerns, e.g., nature of the reagents, condition of the synthesis reaction, atom efficiency/synthesis yield, reactant usage, toxicity and the post synthesis processes involved[245]. Several studies have reported the non-stoichiometry nature of both co-precipitation and urea hydrolysis method in the synthesis of LDHs, but the exact implications are not widely understood [239], [246], [247]. Additionally, the role of salt precursors is not clear as well. Both, lab-scale and industrial scale synthesis of LDHs, employ soluble metal salts (i.e., nitrates and chlorides) as precursors to provide metal ions; but their impacts on the properties and performance of the resultant LDHs and MMOs are

seldom being discussed. Previous study has highlighted the different environmental impact of effluents derived from different metal salt precursors and the need to consider this aspect [248].

Given the importance that LDHs and related materials have gained in recent years as CO_2 capture sorbents, further insights on the effect of the synthesis method and role of the metal salt precursors on the properties of LDHs, as well as the impact on the CO_2 capture properties of the resultant MMOs, are required. In this work, these gaps are addressed by employing the two widely used synthesis methods, co-precipitation and urea hydrolysis, to prepare Mg-Al-CO_3 LDHs with varied Mg/Al compositions (Mg/Al = 2, 3 and 4) and different salts precursor, metal nitrates and metal chlorides. These synthesized LDHs are comprehensively characterized by techniques such as Powder X-ray Diffraction (PXRD), Fourier Transform Infrared Ray (FTIR), elemental analysis (ICP-OES). The true chemical composition of synthesized LDH phase is determined using the lattice parameter "a". The lattice parameter "a", which gives information about the metal-metal distance on the LDH crystal lattice and is directly proportional to the extent of isomorphic substitution. This parameter is not affected by the presence of impurities, making it ideal for determining the exact composition of the synthesized LDHs. We evaluate the synthesis efficiency of different methods and salts precursors by analyzing the the yields, purity, and percentage of unreacted metal ions. Finally, the CO_2 adsorption performance of the synthesized LDHs, including adsorption capacity, kinetics, and cyclic stability, is evaluated and correlated it with the synthesis method.

4.2 Experimental Details

4.2.1 Materials

All the reagents for LDH synthesis were used as received, for example: $Mg(NO_3)_2 \cdot 6H_2O$ (ACROS Organics; ≥ 98.0 %), $Al(NO_3)_3 \cdot 9H_2O$ (Fluka®; ≥ 98.0 %), Na_2CO_3(Fisher Chemical; SLR grade), $MgCl_2$ (Fluka®; ≥ 98.0 %), $AlCl_3$ (Fluka®; ≥ 99.0 %), Urea (Sigma Aldrich; ≥ 98.0 %) and NaOH (Fisher Chemical; SLR grade). Deionized water (Milli-Q® Reference ultrapure water, Type 1, resistivity = 18.2 MΩ cm at 25 ˚C) was used throughout the experiment.

4.2.2 Preparation of Mg-Al-CO₃ LDHs.

Co-precipitation. The employed co-precipitation method was based on Miyata's method and was targeted to synthesize 1 gram of Mg-Al-CO₃ LDHs[249]. A mixed metal solution containing Mg^{2+} and Al^{3+} ions in 2: 1 ratio was prepared using metal nitrates $(Mg(NO_3)_2 \cdot 6H_2O$ & $Al(NO_3)_3 \cdot 9H_2O)$ and was added deionized water to arrive at a final concentration of 0.5 M. Then, the mixed metal solution was added drop-wise into a base solution containing Na_2CO_3 (500 mL). The amount of carbonate ions in the Na_2CO_3 solution was 3 times excess than the moles of carbonate ions in 1g of LDH. Prior to the addition, the Na_2CO_3 solution was heated to 70 ˚C and pH were kept constant at 10 (± 0.02), with the addition of 1 N NaOH solution (4.5 g of sodium hydroxide per 100 mL distilled water) using an auto-titrator (Metrohm 907 Autotitrator) and continuous stirring (400 rpm). The same condition was maintained throughout the addition reaction (1 hour). After that, the resultant LDHs were aged in the mother liquor at 70 ˚C for 24 hours, without any stirring. Next, the LDHs were recovered by centrifugation, then followed by washing with 150 ml of water. The LDHs were dried overnight in an oven at 70 ˚C. All the steps were repeated to prepare LDHs with different Mg/Al ratios (2, 3 & 4). LDHs were also prepared by using metal chlorides ($MgCl_2$ and $AlCl_3$) instead of metal nitrates while keeping all other experimental conditions unchanged. The samples prepared by the co-precipitation method were labelled as CPXXY, where CP represents the co-precipitation method, XX stands for the metal salt used in the synthesis (Chloride, CL or Nitrate, NI) and Y is the molar Mg/Al ratios used (2, 3 & 4).

Urea Hydrolysis. The urea hydrolysis method used for the preparation of Mg-Al-CO$_3$ LDHs was based on a modified Costantino's method and targeted to synthesize 1 gram of LDHs[250]. Mixed metal solutions containing Mg(NO$_3$)$_2$·6H$_2$O and Al(NO$_3$)$_3$·9H$_2$O were prepared in different molar Mg/Al ratios (2, 3 & 4) and added deionized water to arrive at a final concentration of 0.25 M. Solid urea having 3.3 times more than the total moles of metal ions (Urea: Mg + Al = 3.3) were added into the same mixed metal solutions and then sealed in a hydrothermal autoclave reactors. All the resultant reaction mixtures were then hydrothermally treated in an oven at 90 ˚C for 48 hours. The pH of the supernatant solution/mother liquor for all the urea hydrolysis samples was measured after cooling down to room temperature.   After that, the hydrothermally treated solutions were then centrifuged and washed with 100 ml of water to recover the LDHs. The LDHs were dried overnight in an oven at 70 ˚C. The same protocol was followed to prepare LDHs from metal chlorides (MgCl$_2$ and AlCl$_3$) instead of metal nitrates. The samples prepared by urea hydrolysis method are labelled as UHXXY, where UH represents the urea hydrolysis method, XX is the metal salt used in the synthesis (CL or NI) and Y stands for the molar Mg/Al ratios used (2, 3 & 4).

4.2.3 Preparation of Mg-Al-CO$_3$ derived MMOs.

The MMOs samples were prepared by calcining as-prepared LDHs at 400 ˚C for 4 hours in a furnace, using a ramping rate of 5 ˚C/min under N$_2$ gas flow (purity 99.99%, 50 mL/min, oxygen free).

4.2.4 Characterization

Powder X-ray Diffraction patterns (PXRD) were recorded on a Bruker D8 Advance powder diffractometer, using Cu-K$_\alpha$ radiation (λ = 1.5406 Å) and data were collected over angular range of 5–85 °2θ (one-hour span; step size = 0.009 °2θ per second). Fourier Transform Infrared (FTIR) spectra were measured in the range of 4000 to 600 cm^{-1} with 4 cm^{-1} resolution, using Perkin Elmer frontier IR single-range spectrometer under ATR mode. Elemental analysis (ICP-OES) was carried out by atomic emission spectra using Perkin Elmer Optima 5300DV. The LDH solid samples for elemental analysis were prepared by dissolving 30 mg of LDHs in concentrated sulphuric acid and diluted with 25 ml deionized water prior to analysis. The elemental analysis (ICP-OES) of the filtrate collected during

the centrifugation of LDHs were analysed without further dilution to check the presence of unreacted/leached out metal ions. Morphology of the MMOs was characterized using scanning electron microscopy (SEM) technique (JEOL JSM IT800). The gas adsorption/desorption experiments were carried out at 77 K using N_2 (ASAP 2420 V2.09). Prior to the gas adsorption experiments, the samples were degassed at 150 °C for 2 hours.

4.2.5 CO₂ Capture studies

CO_2 adsorption tests were carried out in a thermal gravimetric analyser (TA Instruments; TGA Discovery 5500; Resolution: < 0.1 μg, weighing precision: ± 0.01 %) and pristine LDHs were used to prepare MMOs to avoid CO_2 contamination. Approximately 50 mg of LDH powder was loaded into a platinum pan and decomposed under a continuously flow of pure N_2 gas (purity 99.998 %, 50 mL/min, oxygen free) at 400 °C for 4 hours, under ambient pressure (1 bar). The ramping rate was set at 5 °C/min. Once the decomposition was complete, the temperature was brought down to the desired temperature (200 °C) and hold for 10 minutes. After that, CO_2 gas flow (purity 99.98 %, 80 % v/v, diluted with N_2 gas purity 99.998 %) was introduced for 2 hours and the CO_2 uptake capacity of MMOs was recorded.

For cyclic test, fresh MMOs were prepare using the same protocol above and brought down to the desire temperature for CO_2 adsorption. The adsorption cycles were performed at 200 ˚C for 30 minutes, under CO_2 gas flow (purity 99.98%, 80 % v/v, diluted with N_2 gas purity 99.998 %) while the regeneration/desorption cycles were carried out at 400 ˚C for 30 minutes, under pure N_2 gas flow (purity 99.998%, 100 % v/v). The same CO_2 adsorption and regeneration step are repeated until 10 cycles are completed.

4.3 Results and Discussion

4.3.1 Impact of synthesis method and precursor salts on Mg-Al-CO₃ LDHs

PXRD & FTIR characterization. Figures 4.1 & 4.2 show the PXRD patterns of the as-synthesized samples, revealing the successful synthesis of Mg-Al-CO₃ LDHs using both the co-precipitation and urea hydrolysis methods with different nominal Mg/Al ratios, as well as with different metal salt precursors. The characteristic peaks of LDHs are clearly seen in all the samples and are matching with the *d*-values of the carbonate intercalated LDH system, i.e., 7.60, 3.80, 1.53 and 1.50 Å [146], [221]. For example, the sharp intense peak at low 2θ value (~ 11.5 °2θ) that yields *d* values between 7.45 - 7.80 Å for different Mg/Al LDHs, representing the interlayer distance between two successive metal hydroxide layers (d_{003}) and is the characteristic value for carbonate intercalated LDHs. The two "sawtooth" shaped peaks at high 2θ value (60 - 62 °2θ) correspond to 2*d* reflections of the LDHs and gives the information across the *ab* plane.
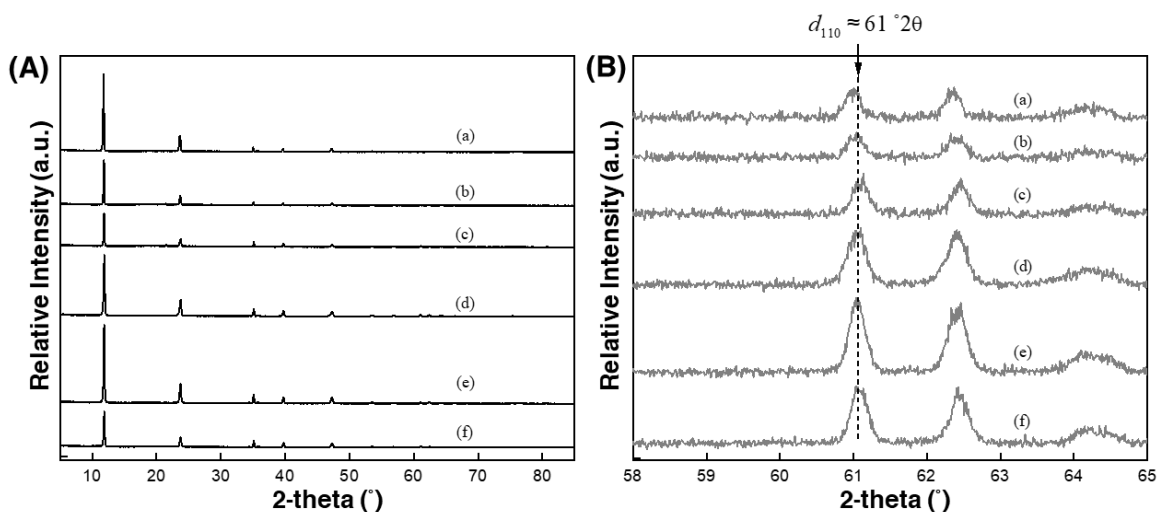
Figure 4.1 - PXRD patterns of LDHs synthesized using urea hydrolysis method in different nominal Mg/Al ratios and salt precursors between (A) 5-85 °2θ and (B) 58-65 °2θ; (a) UHNI2, (b) UHNI3, (c) UHNI4, (d) UHCL2, (e) UHCL3 & (f) UHCL4
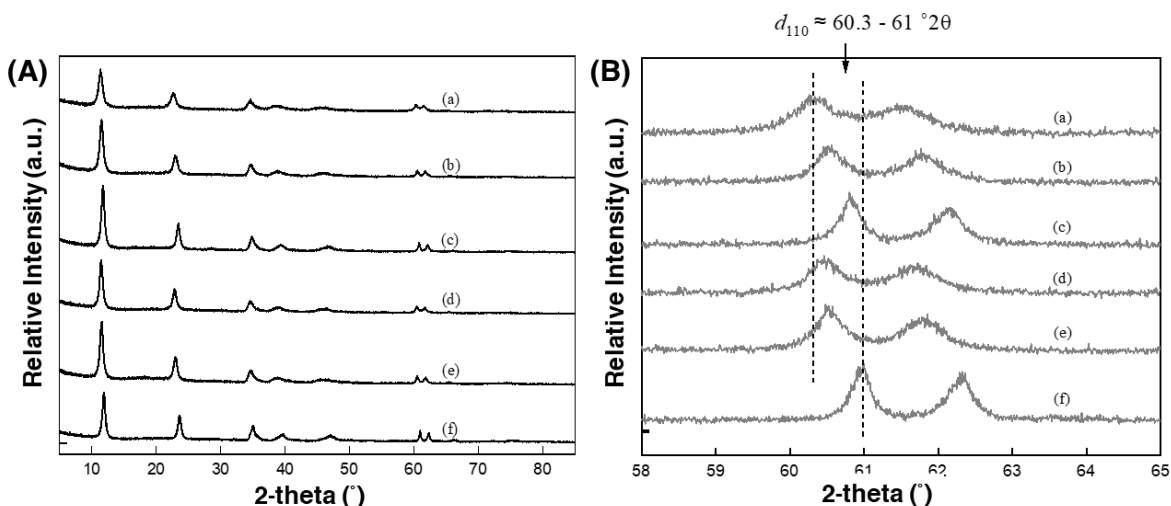
Figure 4.2 - PXRD patterns of LDHs synthesized using co-precipitation method in different nominal Mg/Al ratios and salt precursors between (A) 5-85 °2θ and (B) 58-65 °2θ; (a) CPNI2, (b) CPNI3, (c) CPNI4, (d) CPCL2, (e) CPCL3 & (f) CPCL4

The first peak of the "saw-tooth" in Figure 4.1 & 4.2 gives the average d value of 1.52 Å and that corresponds to the average metal-oxygen distance at the hydroxide layers in the *(110)* plane $(d_{110} = d(\text{M-O}))$, is related to the lattice parameter a of LDH $(a = 2 \times d_{110})$. PXRD patterns of the urea hydrolysis samples show peaks with higher intensities compared to the co-precipitated samples, indicating a better crystallinity and agrees well with literature reported data. However, the higher peak intensity of the basal reflections of urea hydrolysis LDHs caused the 2d reflections not to be clearly visible in the Figure 4.1A.

Figure 4.1B & 4.2B shows a close inspection into the *(110)* peak of LDHs synthesized by both co-precipitation and urea hydrolysis method, which have clearly indicated that the 2θ values have varied between 60.3 – 61.0 °2θ and resulted a wide different a value (3.032 – 3.067 Å). As described in the introduction, the lattice parameter a is a direct indicator of the true chemical composition of LDHs. This shows the clear impact of synthesis method on the chemical composition of LDHs. Further discussion on the relationship between synthesis method and lattice parameters (a & c) on the chemical composition of LDH is in the next section.

Further evidence of carbonate intercalation and successful synthesis of LDHs is observed from the FTIR spectra shown in Figure 4.3. All the vibrations observed in the samples is matching the characteristic for carbonate intercalated LDHs [251]. For example, all the samples show a broad peak centred around 3400 cm^{-1}, which corresponds to the hydrogen bonded hydroxyl ions due to layered hydroxyls and intercalated water molecules. The strong vibration around 1360 cm^{-1} represents the CO_3^{2-} ion at the interlayers, while the stretching vibration at 1630 cm^{-1} represents the bending mode of the water molecules present in the interlayer gallery. The vibrations below 1000 cm^{-1} represent the metal-oxygen (M-O) and metal-metal (M-M) bonds at the hydroxide layers.
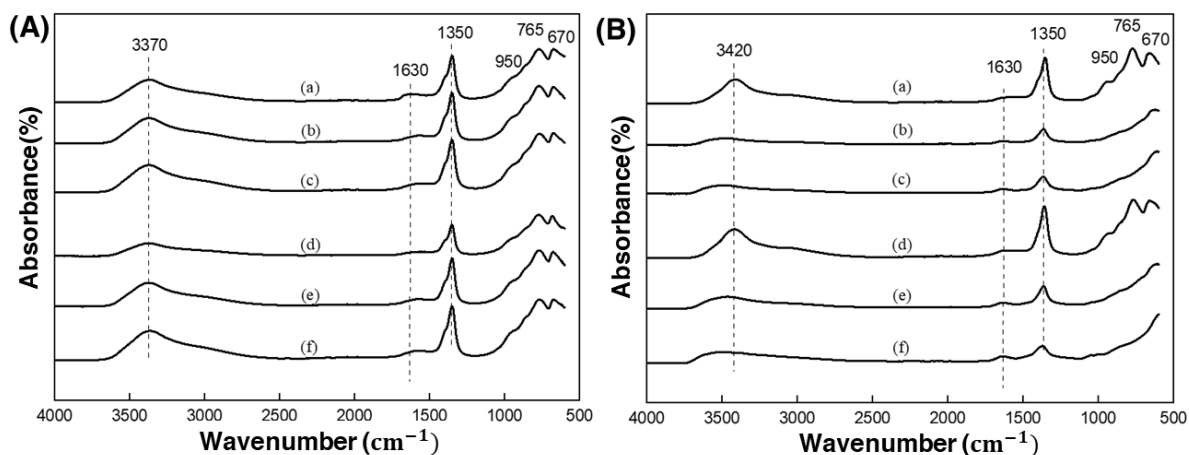
Figure 4.3 - FTIR patterns of LDHs synthesized using (A) urea hydrolysis method and (B) co-precipitation method in different nominal Mg/Al ratios and precursors; (a) UH/CPNI2, (b) UH/CPNI3, (c) UH/CPNI4, (d) UH/CPCL2, (e) UH/CPCL3 & (f) UH/CL4

Chemical Composition. LDHs are known to obey Vegard's law, which means the lattice parameters of LDH are very sensitive to its chemical composition, specifically the Mg/Al ratio at the double hydroxide layers (Brindley and Kikkawa, 1979; Ian G Richardson, 2013b) [219], [220]. The lattice parameter a of LDH corresponds to the average metal-metal distance, d(M-M) at the octahedral sites of hydroxide layers and therefore can be obtained from the value of d_{110} measured from PXRD ($a = 2 \times d_{110}$). Since Al^{3+} (0.53 Å) has a smaller octahedral ionic radius than Mg^{2+} (0.72 Å), the isomorphic substitution of Mg^{2+} by Al^{3+} directly affect the unit cell parameter a of LDHs and can provide an

114

indication of the Mg/Al ratio at the hydroxide layers. The effect of cation ionic radius is best elucidated using the single hydroxides as example. For instance, the average cation-cation distance, d(Mg-Mg) in Magnesium Hydroxide, $Mg(OH)_2$, is 3.142 Å, whereas the average cation-cation distance, d(Al-Al) in Aluminium Hydroxide, $Al(OH)_3$, is 2.763 Å. For Mg-Al LDHs, only part of the Mg^{2+} is substituted by Al^{3+} (x usually varies between 0.15 and 0.33), thus the lattice a values should lie within these two values (e.g., d(Al-Al) < d(Mg-Al) < d(Mg-Mg)). The same holds true for the lattice parameter c, which is the distance between three successive hydroxide layers, as the columbic attraction between successive metal hydroxide layers is affected by the amount of Al^{3+} ions at the octahedral layers. However, unlike the lattice parameter a, the lattice parameter c is not entirely affected by chemical composition but also number of other factors, e.g., extent of hydration, the number, size, orientation of anions, and the strength of pseudo-bonds between anions and edge of hydroxide sheets [146], [254]. Thus, it is harder to predict the lattice parameter c from chemical composition alone. From PXRD, the lattice parameter c of LDHs is obtained from three times the value of d_{003} measured ($c = 3 \times d_{003}$).

The lattice parameters a and c of LDHs are given in Table 4.1, and their variation with the nominal Mg/Al ratios is shown in Figure. 4.4A-B. The smaller a-values (3.033 - 3.038 Å) of LDHs synthesized by the urea hydrolysis method, compared to the co-precipitation method (3.037 - 3.067 Å), suggest a higher isomorphic substitution of Al^{3+} in the synthesized LDHs. Interestingly, the variation in the a-values is very small for the urea hydrolysis samples, irrespective of the nominal Mg/Al ratio and precursor metal salt employed. For example, a value (3.032 Å) of LDHs synthesized with a high nominal Mg/Al ratio (e.g., UHNI4) is very close to those synthesized using lower nominal Mg/Al ratio (3.033 - 3.034 Å for UHNI2 and UHNI3). This indicates the urea hydrolysis method generates LDHs with similar Mg/Al ratios, irrespective of their nominal ones.

Such findings are in good agreement with the literature, which reports a values of urea hydrolysis LDHs as typically Al-rich LDHs, with a values close to 3.04 Å[199], [237], [255], [256]. Nevertheless, it should be noted that most of these published urea hydrolysis LDHs follow the procedure reported by Constatino *et al.* (1995) and use a similar nominal composition (Mg/Al ratio = 2) [257]. Hence, it is not a surprising that these a values are

close to each other. The observation of fixed *a* values found in present work is interesting because these nominal compositions (Mg/Al ratio of 3 & 4) were not studied in detailed before, and they might provide a hint on the formation mechanism of LDH *via* urea hydrolysis method.
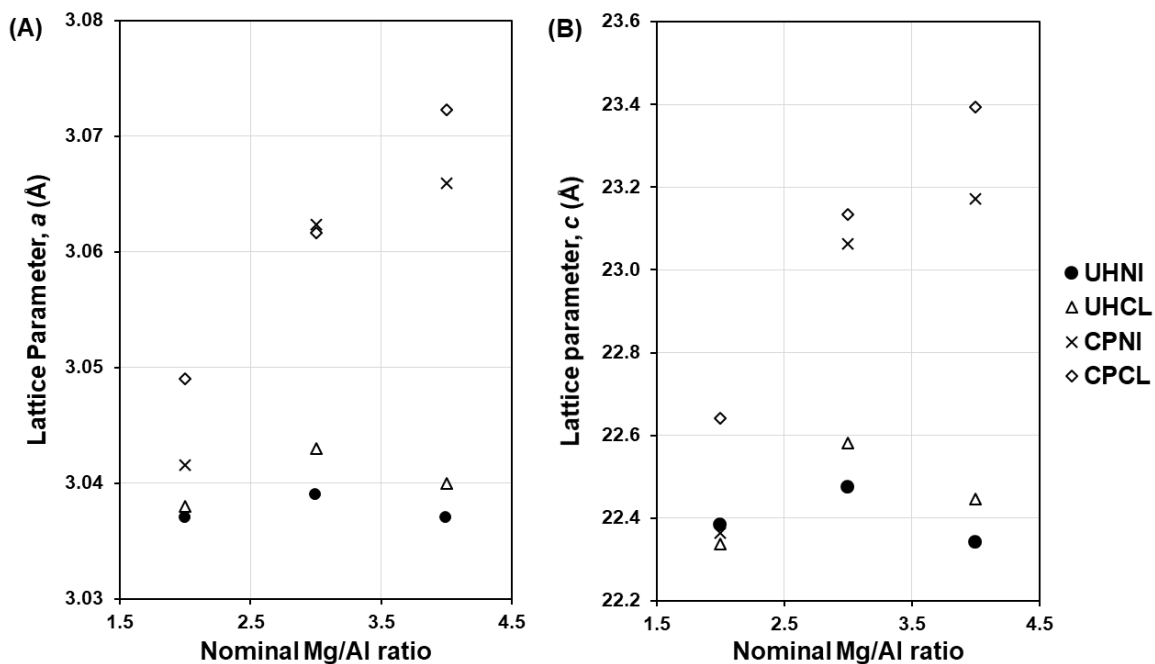
Figure 4.4 - (A) Lattice parameter, *a* and (B) *c* values of LDHs plotted against nominal Mg/Al ratios

Table 4.1 - Lattice parameters *a* and *c* of LDHs synthesized from urea hydrolysis and co-precipitation method

Urea Hydrolysis Method				Co-precipitation Method		
Sample ID	Lattice Parameter, $a \pm 0.001$ (Å)	Lattice Parameter, $c \pm 0.001$ (Å)		Sample ID	Lattice Parameter, $a \pm 0.001$ (Å)	Lattice Parameter, $c \pm 0.001$ (Å)
UHNI2	3.033	22.355		CPNI2	3.037	22.610
UHNI3	3.034	22.436		CPNI3	3.057	23.133
UHNI4	3.032	22.343		CPNI4	3.061	23.394
UHCL2	3.033	22.322		CPCL2	3.044	22.366
UHCL3	3.038	22.581		CPCL3	3.057	23.064
UHCL4	3.036	22.443		CPCL4	3.067	23.171

In contrast to the urea hydrolysis LDHs, the *a*-values of co-precipitated LDHs vary significantly (3.037 – 3.067 Å) and show a dependence on the nominal Mg/Al ratio used. This is more evident from the LDHs prepared by employing chloride salts (CPCL), which show a linear relationship between *a*-parameter and nominal Mg/Al ratio (Figure 4.4A). This confirms the progressive substitution of Al^{3+} ions into the crystal lattice of LDH and that co-precipitation method can generate LDHs with different Mg/Al ratios. This observation is supported by the variation in the *c* parameter (Figure 4.4B) which shows a direct correlation between the *c*-parameter and nominal Mg/Al ratios. These findings are consistent with the literature observation of co-precipitated LDHs, where a wide range of *a*-values is reported (3.02 – 3.11 Å) [223], [258], [259].

Synthesis yield. The formation mechanism of LDHs *via* co-precipitation and urea hydrolysis method has given below:

Co-precipitation method:

$$(1\text{-}x)Mg^{2+}{}_{(aq)} + xAl^{3+}{}_{(aq)} + \frac{x}{2}Na_2CO_{3(aq)} \xrightarrow{\text{NaOH, pH 10}} Mg_{1\text{-}x}Al_x(OH)_2(CO_3^{2-})_{x/2} \cdot (1\text{-}\frac{3x}{2})H_2O_{(s)} + Na^+{}_{(aq)}$$

[Eq. 4.1]

Urea Hydrolysis method:

$$(1\text{-}x)Mg^{2+}{}_{(aq)} + xAl^{3+}{}_{(aq)} \xrightarrow{\text{Urea, 3.3 times the total moles of metal ions}} Mg_{1\text{-}x}Al_x(OH)_2(CO_3^{2-})_{x/2} \cdot 1\text{-}\frac{3x}{2}$$
$$H_2O_{(s)}$$

[Eq. 4.2]
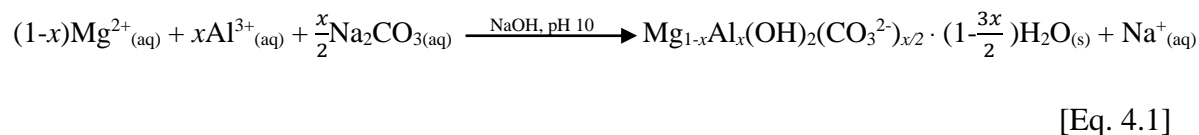
The synthesis reaction yield is obtained by dividing the measured weight (i.e., actual yield) of the synthesized products over the expected weight (i.e., theoretical yield) of LDHs, calculated based on the stoichiometry reactions above and *x* derived from nominal Mg/Al ratios used at synthesis. The formula is presented below as Eq. 4.3, and the results are tabulated in Table 4.2.

$$\text{Synthesis Yield } (\%) = \frac{\text{Actual Yield (g)}}{\text{Theoretical Yield (g)}} \times 100\%$$

<div align="right">[Eq. 4.3]</div>

Table 4. 2 - Synthesis yields for co-precipitation and urea hydrolysis methods.

Urea Hydrolysis Method		Co-precipitation Method	
Sample ID	Synthesis yield (%)	Sample ID	Synthesis yield (%)
UHNI2	81.2	CPNI2	96.0
UHNI3	66.7	CPNI3	100.9
UHNI4	57.0	CPNI4	100.9
UHCL2	77.0	CPCL2	94.9
UHCL3	67.1	CPCL3	99.6
UHCL4	54.3	CPCL4	100.7

As shown in Table 4.2, not all the samples achieved a 100 % synthesis yield, and both synthesis methods show quite different results. For example, samples synthesized by the urea hydrolysis method show low yields, between 54 - 81 %, whereas samples synthesized by the co-precipitation method show better yields, and some even reach a 100 % yield. Interestingly, varying the nominal Mg/Al ratios seems to have a different effect on the resultant synthesis yield from both synthesis methods. For instance, when a larger nominal Mg/Al ratio (3 & 4) is employed to synthesize LDHs, the synthesis yield decreases for the urea hydrolysis method but increases for co-precipitation method. On the contrary, employing different salt precursors does not show a large effect on the synthesis yields for both synthesis methods.

To understand this phenomenon, further insights into the formation mechanisms of LDHs by the employed synthesis methods are required. Broadly speaking, the formation/precipitation of LDHs from a solution of metal ions depends on the pH and solubility products of unitary hydroxides. For Mg-based LDHs, the precipitating pH can start from approximately 7.5 and remain stable up to pH 13 [206], [207], [258], [260]. Table 4.3 shows that the final pH of most LDHs prepared is within this range (7 – 10). Therefore, if the reaction is quantitative and follows the path described in Eq. 4.1 and Eq. 4.2, then the synthesis yield obtained should be equal to the theoretical yield (100 %). However, this is clearly not the case, particularly with the urea hydrolysis samples.

Interestingly, among them, the LDHs synthesized with the lowest pH (UHNI2 & UHCL2) show higher yields than the rest with higher pH. This suggests that other factors are affecting the yields of LDHs, besides the pH condition.

Generally, formation of LDHs competes with a series of side reactions. These reactions often produce secondary phases, which are usually metal hydroxides/oxy-hydroxides and carbonate species [223], [261]–[263]. For urea hydrolysis method and at elevated temperatures (> 80 °C), urea hydrolyses in a two-step reaction which caused pH of the reaction medium to gradually increases with time and produces ammonium (NH_4^+) and carbonate (CO_3^{2-}) as final products. During the process, Al-based hydroxides precipitate before Mg hydroxides because they have much lower solubility products and pH of formation, e.g., Al hydroxides, $K_{sp} = 2$ x 10^{-31}, pH ~ 4 - 6; Mg hydroxides, $K_{sp} = 5.61$ x 10^{-12}, pH ~ 9. However, due to the amphoteric nature of Al hydroxide, it redissolves before the pH where LDHs precipitates (i.e., dissolving at pH 6). It has been reported that the equilibrium between the dissolution of $Al(OH)_3$ and Mg-Al-LDHs can take up to 100 days to achieve [204]. This means that it is possible these precipitated Al hydroxide phases have not been completely dissolved or reprecipitated. This might explain the low synthesis yields of urea hydrolysis method.

Further to that, the type of impurity phase formed will have a different effect on the resultant yield. For instance, the molecular weight of aluminium hydroxides, $Al(OH)_3$ is 78 g/mol, which is very close to the molecular weights of LDHs having different compositions ($x = 0.25$, 77.73 g/mol; $x = 0.33$, 78.18 g/mol). Therefore, when $Al(OH)_3$ is formed as impurity phase along with the LDH, they are likely to compensate for the loss in percentage yield. The distinction between product weight and impurity weight becomes even more complicated when the formed impurity is in amorphous state since it is not easy to detect. On the other hand, the aluminium oxy-hydroxide, AlOOH, has a lower molecular weight (59.99 g/mol) that those for LDHs. If part of Al^{3+} is converted as AlOOH, then the resultant yield could reduce even if all Al^{3+} ions in the solutions are precipitated.

Although the co-precipitation method also follows a similar reaction, but pH is pre-calibrated to the condition where LDHs precipitates (i.e., pH = 10) and is well-controlled with the aid of auto-titrator. This should technically minimize the chance of Al-based

hydroxides being precipitated and is probably why close to theoretical yields (~100 %) were obtained in all co-precipitation methods. Despite this, several studies reported that further characterization of co-precipitated samples with advanced techniques (e.g., solid state ^{27}Al NMR) still found small amounts of Al-based impurities [224], [231], [243]. Moreover, handling of LDHs in the post-synthesis step may also cause variation in yield due to events such as leaching of metal cations from the crystal lattice, dissolution of LDHs during aging, or incomplete removal of precipitation agents, e.g., sodium hydroxide/potassium hydroxide [208], [235], [264]. This might explain why some of co-precipitated samples have resultant yields less than or exceeding the theoretical 100 %. All of this demonstrates the challenges in obtaining the information on the purity and the composition of LDHs based on observed yield alone. Hence, we demonstrate here the necessity of the supplementary characterization techniques in arriving at the actual yield, purity, and the composition of the LDHs.

Table 4. 3 - Synthesis conditions of LDHs prepared from urea hydrolysis and co-precipitation methods.

Sample ID	Mg/Al Ratio	Metal Salt Precursor	Temperature (°C)	Precursor concentration (mol/dm³)	Washing Water Volume (ml)	Aging Time (hours)	Final pH
UHNI2	2	Metal nitrates	90	0.25	100	48	7-8
UHNI3	3	Metal nitrates	90	0.25	100	48	8
UHNI4	4	Metal nitrates	90	0.25	100	48	8
UHCL2	2	Metal chlorides	90	0.25	100	48	7-8
UHCL3	3	Metal chlorides	90	0.25	100	48	8
UHCL4	4	Metal chlorides	90	0.25	100	48	8
CPNI2	2	Metal nitrates	70	0.25	150	24	10
CPNI3	3	Metal nitrates	70	0.25	150	24	10
CPNI4	4	Metal nitrates	70	0.25	150	24	10
CPCL2	2	Metal chlorides	70	0.25	150	24	10
CPCL3	3	Metal chlorides	70	0.25	150	24	10
CPCL4	4	Metal chlorides	70	0.25	150	24	10

Since the obtained synthesis yields do not distinguish between LDHs and impurities, elemental analysis of LDH samples and filtrate solutions was carried out to gain further insight into the composition.

4.3.2 Elemental Analysis (ICP-OES) of LDH samples and filtrates

Elemental analyses of Mg^{2+} and Al^{3+} ions precipitated in the samples (Table 4.4) and filtrate solution (Table 4.5) were carried out to have a comprehensive understanding of the LDH composition and synthesis yield.

Table 4. 4 - The expected (nominal), observed (bulk) Mg/Al ratios and sodium content of LDHs synthesized from urea hydrolysis and co-precipitation methods.

Urea Hydrolysis Method				Co-precipitation Method			
	Mg/Al ratios		Sodium content (wt %)		Mg/Al ratios		Sodium content (wt %)
Sample ID	Expected	Observed		Sample ID	Expected	Observed	
UHNI2	2.0	0.9	0.16	CPNI2	2.0	2.7	0.91
UHNI3	3.0	0.8	0.22	CPNI3	3.0	3.0	0.65
UHNI4	4.0	1.7	0.19	CPNI4	4.0	4.0	0.53
UHCL2	2.0	1.3	0.13	CPCL2	2.0	2.2	0.34
UHCL3	3.0	1.6	0.19	CPCL3	3.0	3.0	0.48
UHCL4	4.0	1.8	0.04	CPCL4	4.0	4.0	0.40

Table 4. 5 - Percentage of unreacted metal ions in the filtrates collected during the synthesis of LDHs using urea hydrolysis and co-precipitation methods.

Urea Hydrolysis Method				Co-precipitation Method		
Sample ID	Percentage Unreacted (%)			Sample ID	Percentage Unreacted (%)	
	Mg	Al			Mg	Al
UHNI2	57.5	0.0		CPNI2	0.1	8.6
UHNI3	73.9	0.0		CPNI3	0.0	0.2
UHNI4	56.8	0.0		CPNI4	0.1	0.3
UHCL2	33.6	0.1		CPCL2	0.0	2.3
UHCL3	45.6	0.4		CPCL3	0.1	0.2
UHCL4	55.3	0.1		CPCL4	0.1	0.2

Urea Hydrolysis method. Table 4.4 reveals the observed Mg/Al ratios in the solid samples obtained from elemental analysis (ICP-OES) and compared with their expected Mg/Al ratios at synthesis. All the urea hydrolysis samples show lower observed Mg/Al ratios (0.8 – 1.8) than their expected ones, suggesting a higher Al content in these samples. As described above, the minimum possible Mg/Al ratio in crystalline LDH is 2 ($x = 0.33$). Thus, the observation of these low observed Mg/Al ratios (0.8 – 1.8) indicates the presence of Al-based impurities in all urea hydrolysis samples. This result is matching with the hypothesis proposed earlier based on the LDH formation mechanism *via* the urea hydrolysis method and incomplete dissolution of Al-based hydroxides. Another strong evidence supporting this is the huge differences in observed Mg/Al ratios obtained from samples having similar *a* values, e.g., UHNI4 (0.9) and UHNI2 (1.7). Similar *a*-values (3.032 Å) indicate those two samples have the same amount of Al^{3+} substitution in the LDH phase, but their observed Mg/Al ratio are not the same, which means they have a different Al content in bulk phase. This clearly evidences the presence of impure Al phases in these samples. Their PXRD patterns (Figure 4.1 & 4.2) do not show any crystalline impurity phases, which corroborates the amorphous nature of the Al-based impurities.

The amount of impure phase seems affected by the metal salt precursors employed, based on the different observed Mg/Al ratios obtained from the two methods (UHCL and UHNI). Those samples employing metal chlorides (UHCL) show larger observed Mg/Al ratios (1.3 – 1.8) than those measured for the UHNI samples, suggesting a higher Mg content. Considering that Figure 4.1 and 4.2 show no other crystalline phases apart from the LDH were detected in the PXRD patterns and that amorphous Mg-based impure phases are not yet known, hence, the Mg-content should be measured directly from the LDH phase and could be used as an indication of LDH purity. Based on the close agreement between the expected and observed Mg/Al ratio of UHCL samples, metal chlorides seem to be a more effective precursors to produce high purity LDHs.

Table 4.5 shows the percentage of unreacted metal ions measured in the filtrates of all samples collected from the washing step, with respect to the nominal Mg/Al ratios at synthesis. It is observed that the amount of Al^{3+} ions in all filtrates from urea hydrolysis method is negligible, indicating that most Al^{3+} ions were precipitated. However, a large

content of Mg^{2+} ions (34 – 74 % of the concentration of Mg^{2+} ions used at synthesis) is found in these filtrates, indicating the incomplete precipitation of these ions into LDHs. This aligns with the earlier hypothesis that part of the precursors (Al^{3+}) precipitates as impurity phases, rather than LDHs, which caused the low synthesis yields (54 - 81 %) obtained from the urea hydrolysis method. Nevertheless, it is also possible that part of these Mg^{2+} ions is a result of leaching out from the LDH crystal lattice during the aging and/or washing stage of urea hydrolysis method.

Again, the percentages of unreacted Mg^{2+} ions are lower in the filtrates of metal chlorides (UHCL), compared to the metal nitrates (UHNI). This agrees well with the earlier analysis of observed Mg/Al ratios and confirms that metal chlorides are a more effective precursor to precipitate metal ions into LDHs. However, although more metal ions (i.e., Mg^{2+}) have precipitated, the final product yield of UHCL samples is still lower than that for UHNI samples, e.g., UHCL2 (77.0 %) and UHNI2 (81.2 %). This proves the non-quantitative nature of the urea hydrolysis method and confirms the presence of a large amount of amorphous Al-based impurities phase in the UHNI samples. So far, all evidence present in this section is matching with the previous solid state ^{27}Al NMR studies of urea hydrolysis LDHs; the author found two different AlO_6 octahedral aluminium sites and implies that the amount of impurities phase can be significant, as the signal intensity due to impurities phase is as high as 37 % in relative to the intensity of pure LDHs (67 %) [230].

It is apparent now that the formation mechanism proposed for urea hydrolysis method is mostly valid. However, it still needs an explanation for the fixed *a* value observed in all urea hydrolysis samples. One explanation for this is that there exists a thermodynamic preference to synthesize LDHs of this composition (*a* ~ 3.04 Å), as the hydrothermal conditions is very close to the formation condition of naturally occurring LDHs.

Surprisingly, elemental analysis revealed small amounts of sodium (0.04 – 0.22 wt %) in all urea hydrolysis samples. This is rather unanticipated because unlike the co-precipitation method, the urea hydrolysis method does not involve any sodium precursors in the synthesis steps, e.g., NaOH and Na_2CO_3. All the samples were carefully handled, and containers were acid-washed prior to usage. Hence, the only possible source of this sodium

content is from the metal salt precursors, where the sodium content was expected to be negligible due to the low concentration (10 - 100 mg/kg) in all reagents.

Co-precipitation method. Table 4.4 shows that the observed Mg/Al ratios of co-precipitated samples agree well with their expected values, which means the co-precipitation method can produce LDHs close to the desired compositions. The only two exceptions are the samples CPNI2 and CPCL2, which were targeted to synthesize LDHs close to the upper limit of x (0.33). For the other compositions (Mg/Al ratios of 3 & 4), the good agreement between a-parameters, synthesis yields and observed Mg/Al ratios proves the higher LDH purity of the co-precipitated samples versus the urea hydrolysis ones.

A small amount of sodium content (0.34 – 0.91 %) was observed in all the co-precipitated LDHs, which may have originated from the sodium precursors used during synthesis, e.g., NaOH and Na_2CO_3. The employed washing protocol reduced the sodium content to a very small percentage (< 1 %) and explains why some of the synthesis yields of LDHs are slightly in excess of 100 % (100.6 – 100. 9 %). Further washing may cause the leaching out of metal ions from LDH lattice, which can affect the final chemical composition of LDHs and risk sacrificing the synthesis yields. Therefore, we did not attempted to completely remove the sodium content but rather kept a consistent washing protocol for all samples.

Elemental analysis of the filtrates (Table 4.5) revealed the full conversion of reactants in the co-precipitation reaction as the amount of metal ions (both Mg^{2+} and Al^{3+}) in the filtrates is almost zero in most of the samples. Only a small percentage of unreacted Al^{3+} ions was measured in the two samples CPNI2 and CPCL2, which is consistent with their observed Mg/Al ratios (Table 4.4) and synthesis yields (Table 4.2).

When a Mg/Al ratio of 3 was used in the synthesis *via* co-precipitation method, LDHs with a composition close to that of the mineral Hydrotalcite ($Mg_6Al_2CO_3(OH)_{16}\cdot4H_2O$) were obtained. Both CPNI3 and CPCL3 showed the lowest content of unreacted Mg^{2+} and Al^{3+} ions in the filtrates, and their synthesis yields were closest to the ideal 100 %. Additionally, both samples showed an a-parameter value (3.057 Å) that matches with that of the mineral Hydrotalcite (3.054 Å). The good agreement between yields, a-parameter and observed Mg/Al ratio indicates that the reaction is quantitative. In contrast, syntheses targeting LDHs with other compositions show discrepancies in their a-parameters and yields.

4.3.3 Impact of synthesis method and precursor salts on MMOs

MMOs sorbent yields. All of the LDHs synthesized were subjected to thermal decomposition as described in the experimental section to obtain MMOs. PXRD patterns of the MMOs are shown in Figure 4.5. The LDH characteristic peaks previously seen in PXRD patterns (Figure 4.1 & 4.2) have now disappeared and are replaced by three broad reflections that are corresponding to MgO having *d*-values of 2.43, 2.11 and 1.49 Å[217]. The formation of MMOs was further characterized by FTIR spectra, as shown in the Figure 4.6. All the characteristic vibrations due to LDHs (e.g., 3400, 1630 and 1360 cm^{-1}) were significantly reduced on the FTIR spectra of MMOs, showing different signals at 1400 cm^{-1} and 1540 cm^{-1}. In literature, these two peaks are commonly seen in decomposed MMOs and are attributed to the adsorption of atmospheric water and CO_2 species. Table 4.6 shows the percentage weight loss of MMOs during the thermal decomposition step. The heterogeneity of the sample bulk resulted in an experimental inconsistency of less than $\pm$ 1 % for percentage weight loss.
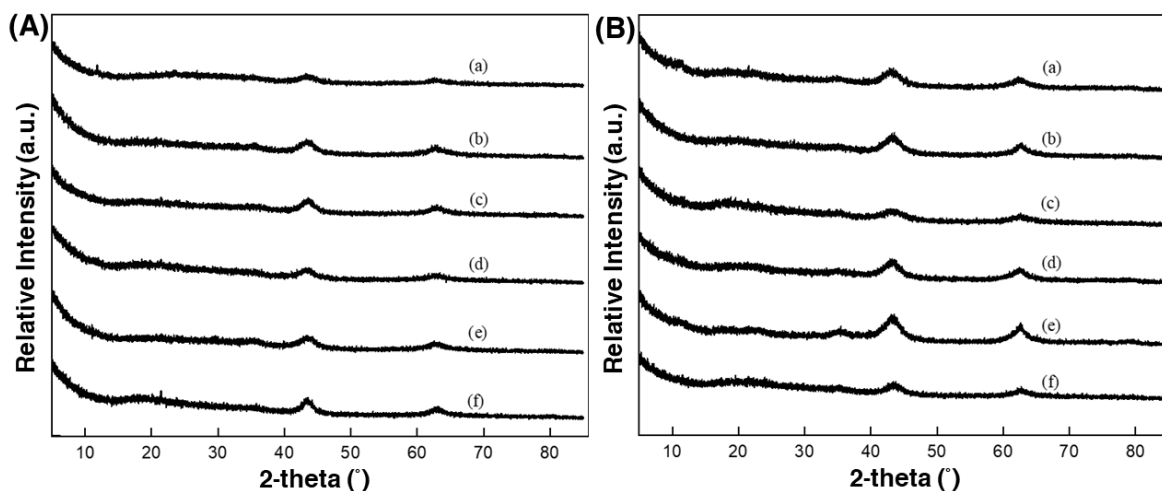
Figure 4.5 **PXRD diffractograms of MMOs synthesized using (A) urea hydrolysis method and (B) co-precipitation method in different nominal Mg/Al ratios and precursors; (a) UH/CPNI2, (b) UH/CPNI3, (c) UH/CPNI4, (d) UH/CPCL2, (e) UH/CPCL3 & (f) UH/CL4**
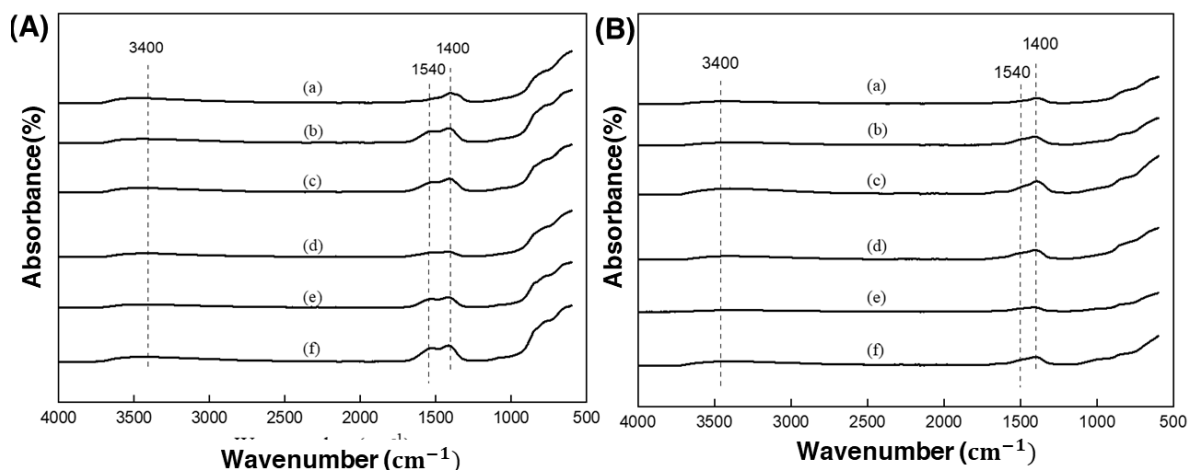
Figure 4.6 FTIR patterns of MMOs synthesized using (A) urea hydrolysis method and (B) co-precipitation method in different nominal Mg/Al ratios and precursors; (a) UH/CPNI2, (b) UH/CPNI3, (c) UH/CPNI4, (d) UH/CPCL2, (e) UH/CPCL3 & (f) UH/CL4

Table 4.6 - Percentage loss of LDHs in the thermal decomposition step

Sample ID	Percentage weight loss (%)	Sample ID	Percentage weight loss (%)
UHNI2	41.7	CPNI2	41.9
UHNI3	37.8	CPNI3	41.5
UHNI4	38.6	CPNI4	41.8
UHCL2	40.6	CPCL2	39.2
UHCL3	37.0	CPCL3	40.9
UHCL4	37.3	CPCL4	41.1

The theoretical weight loss for complete dehydroxylation, dehydration and deanation (i.e., removal of CO_3^{2-} anion at interlayer) of LDH having x between 0.15 – 0.33 is in the range of 43.9 – 45.2 %. As seen in Table 4.6, none of the MMOs sample have achieved the theoretical weight loss values although their FTIR spectra confirms the complete decomposition of LDHs precursors. Among the two synthesis methods, the percentage weight loss in the case of urea hydrolysis LDHs is lower (37 - 41.7 %) compared the co-precipitated LDHs (39 – 42 %). It is likely that the presence of impurities phase contributed to the discrepancies in weight loss.

BET and SEM analysis. Figures 4.7 & 4.8 show the nitrogen adsorption isotherms at 77 K of MMO samples prepared by urea hydrolysis and co-precipitation method. Interestingly, MMOs synthesized by different methods show different types of isotherms profile. For example, all urea hydrolysis MMOs shows Type II Isotherms, suggesting that they are non-porous or macroporous materials, whereas co-precipitated MMOs shows Type IV isotherms, suggesting that they are microporous or mesoporous materials. Hysteresis loops provide more information about the textural properties of MMOs. For example, the narrow hysteresis loop of urea hydrolysis MMOs that ends in the middle of isotherm is documented usually caused by inter-particle capillary condensation and by material that is non-rigid plate-like particles. On the other hand, the co-precipitated MMOs exhibit a hysteresis loop only at the beginning of desorption branch, suggesting that they have a more complex pore structures that is made up of interconnected networks of pores of varying size and shapes. Figure 4.9 shows the calculated BET surface areas using information from nitrogen adsorption isotherms at 77 K. It seems that the BET areas of co-precipitated MMOs are at least two times larger than those of urea hydrolysis MMOs.
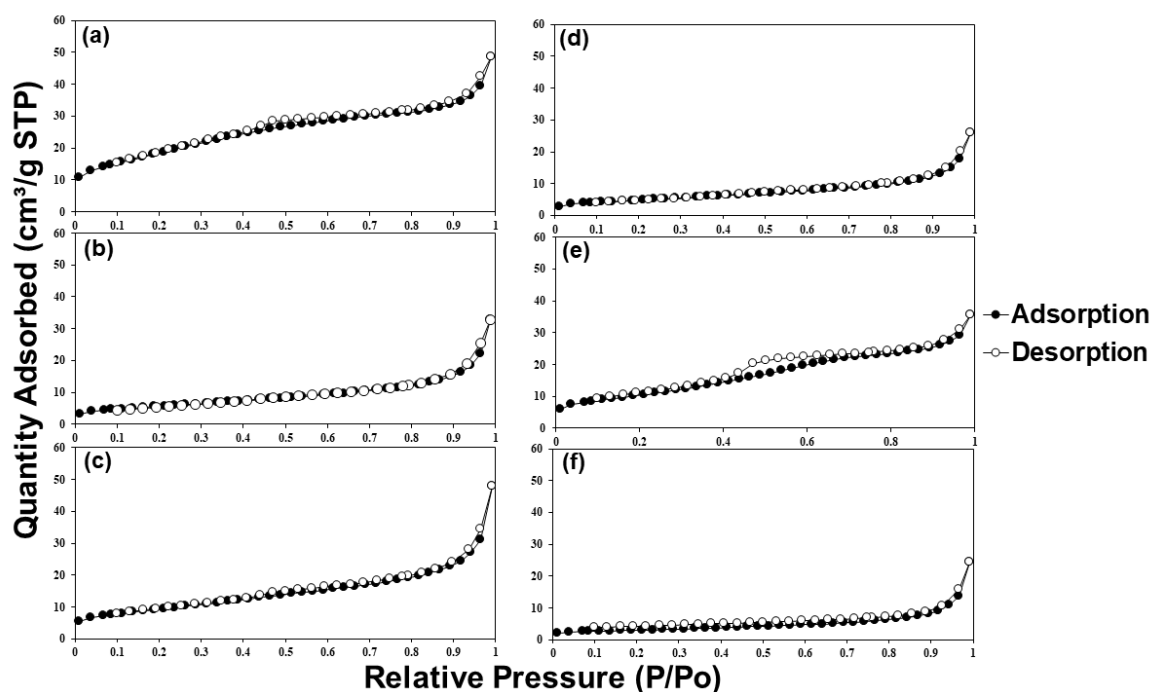
Figure 4.7 - Nitrogen adsorption isotherms (77 K) of MMOs synthesized by (a) UHNI2, (b) UHNI3, (c) UHNI4, (d) UHCL2, (e) UHCL3 & (f) UHCL4
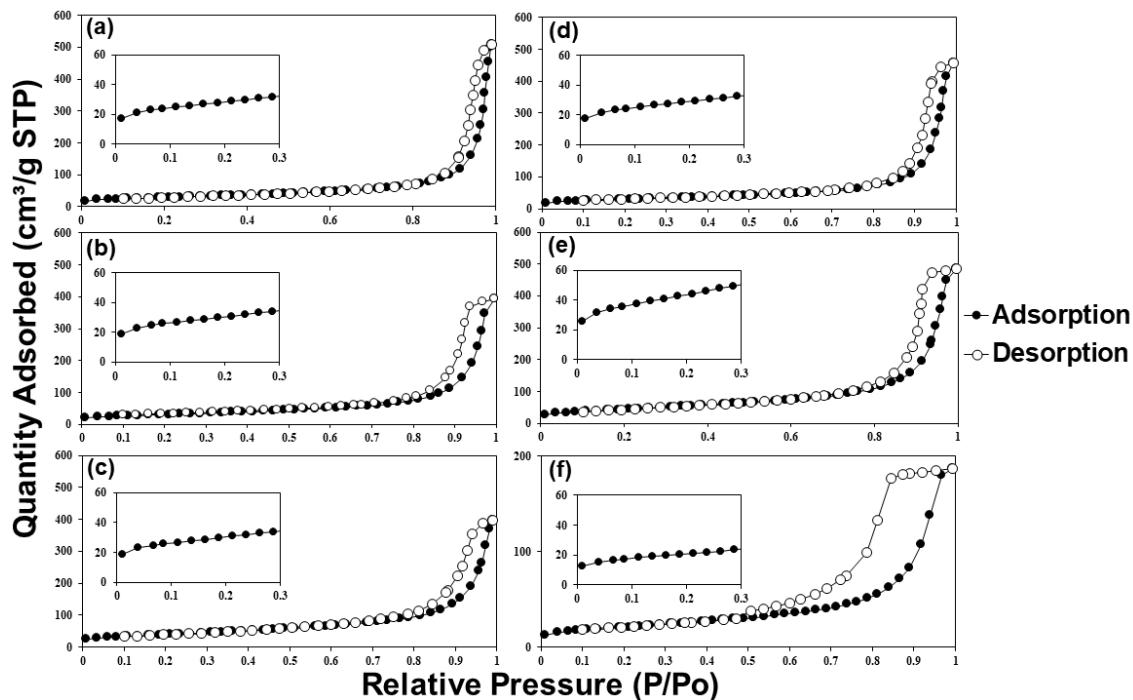
Figure 4.8 - Nitrogen adsorption isotherms (77 K) of MMOs synthesized by (a) CPNI2, (b) CPNI3, (c) CPNI4, (d) CPCL2, (e) CPCL3 & (f) CPCL4
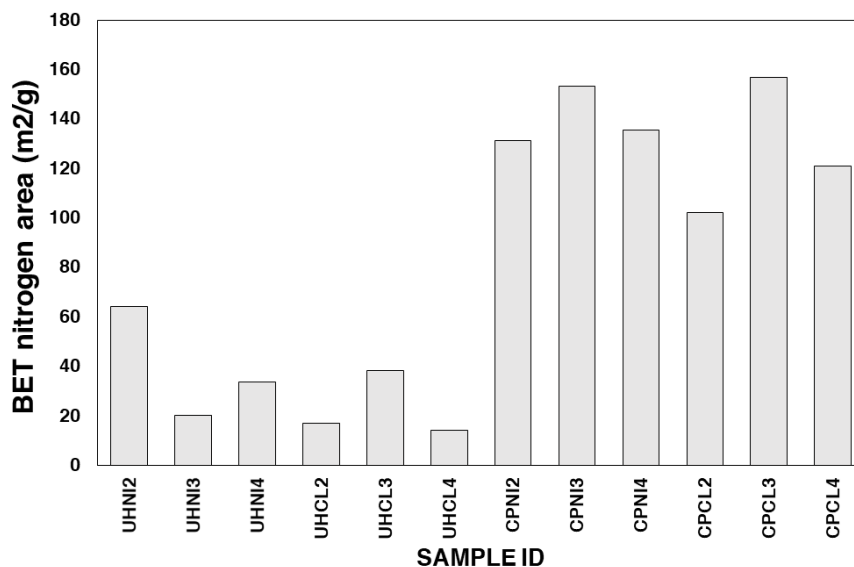
Figure 4.9 - BET surface areas of MMOs synthesized from urea hydrolysis method and co-precipitation method

Scanning Electron Microscopy (SEM) analysis was carried to study the morphology of MMOs synthesized from the two synthesis methods. SEM micrographs of all MMOs samples are available in the Figure 4.10 – 4.13. Overall, the SEM images obtained for urea hydrolysis MMOs (Figure 4.10 & 4.11) show large plate-like hexagonal crystallites that are several microns in size. In contrast, MMOs obtained from co-precipitated LDHs consist of large aggregates of smaller crystallites (Figure 4.12 & 4.13). A closer look at the surface of these coprecipitated MMOs reveals decomposed sand-rose like particles, while the surface of urea hydrolysis MMOs appears to be smooth under SEM examinations. This might explain why the BET areas of co-precipitated MMOs are larger than those of urea hydrolysis MMOs (Figure 4.9). Thus far, the observed morphologies for MMOs agree well with the nitrogen isotherms analyses above and literature reports.
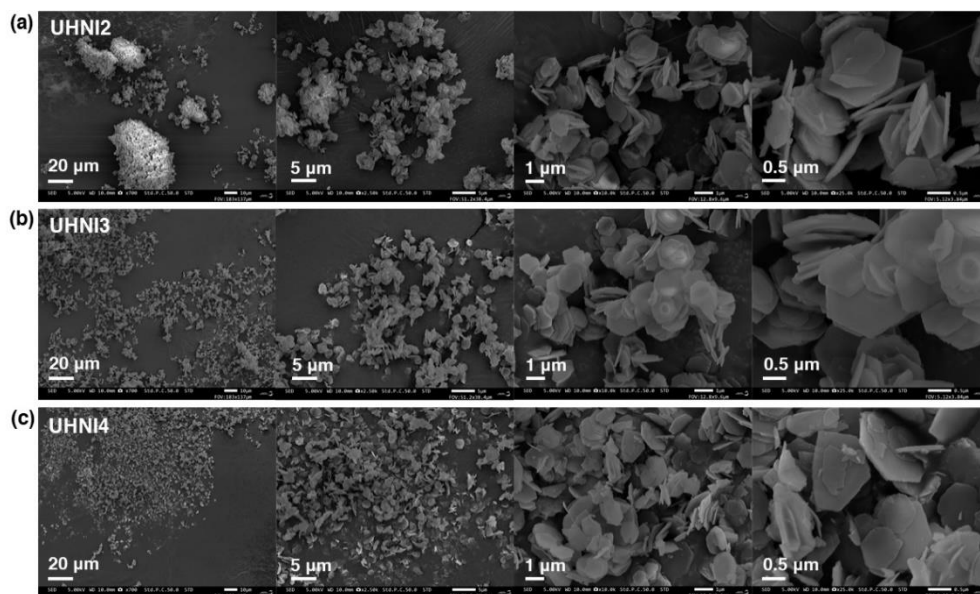
Figure 4.10 - SEM micrographs of MMOs derived from synthesized using urea hydrolysis method in different nominal Mg/Al ratios and in different resolution; (a) UHNI2, (b) UHNI3 & (c) UHNI4
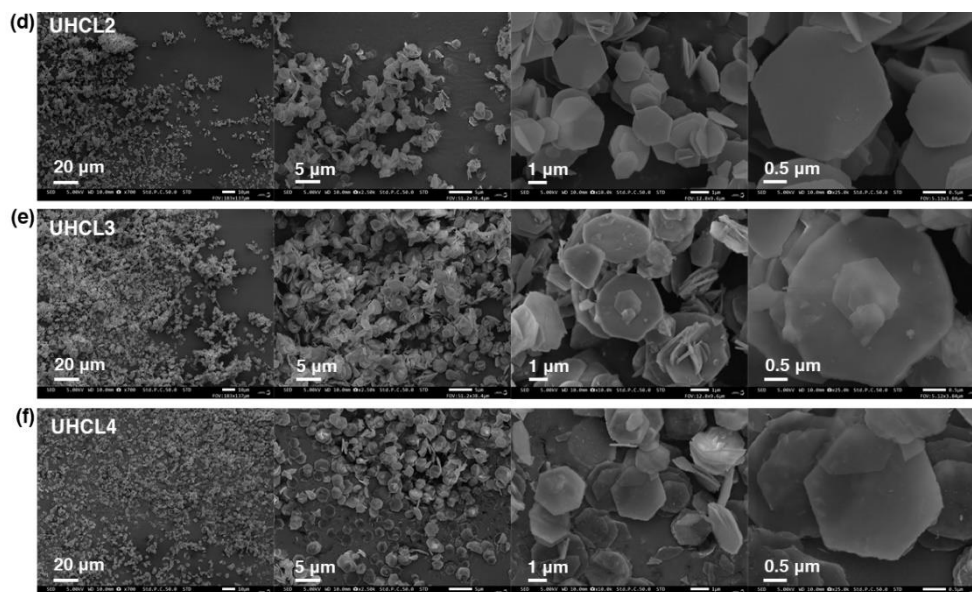
Figure 4.11 - SEM micrographs of MMOs derived from synthesized using urea hydrolysis method in different nominal Mg/Al ratios and in different resolution; (d) UHCL2, (e) UHCL3 & (f) UHCL4
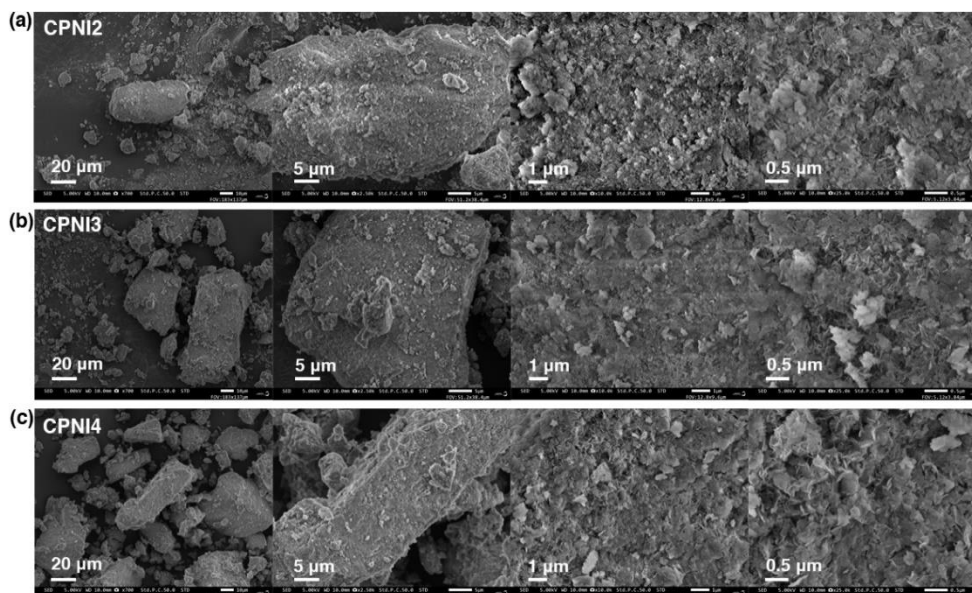
Figure 4.12 - SEM micrographs of MMOs derived from synthesized using co-precipitated method in different nominal Mg/Al ratios and in different resolution; (a) CPNI2, (b) CPNI3 & (c) CPNI4
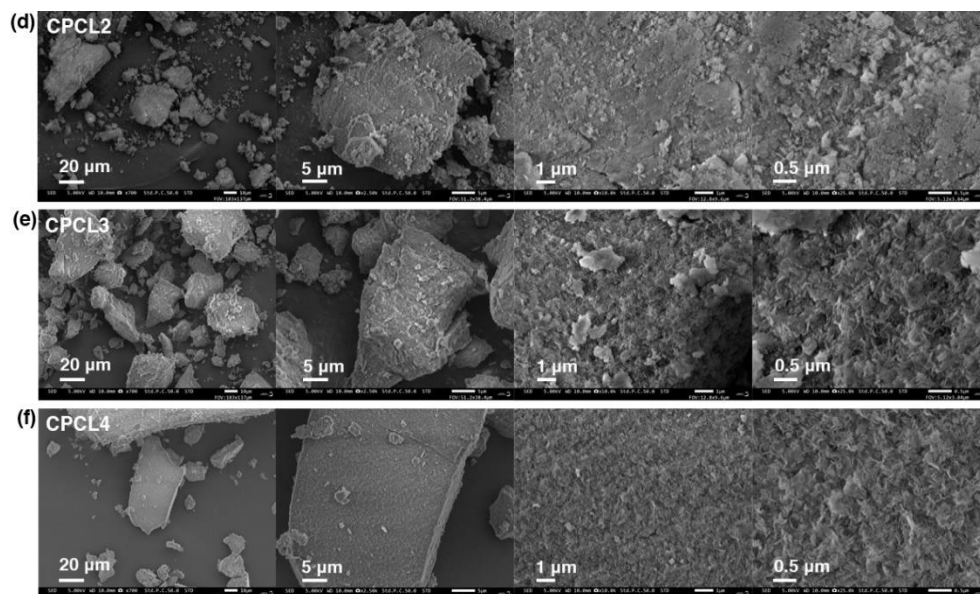
Figure 4.13 - SEM micrographs of MMOs derived from synthesized using co-precipitated method in different nominal Mg/Al ratios and in different resolution; (d) CPCL2, (e) CPCL3 & (f) CPCL4

4.3.4 CO_2 Adsorption Tests

CO_2 adsorption capacities. Figure 4.14 shows the CO_2 adsorption capacities measured for MMOs derived from LDHs synthesized in the present study, at 200 ˚C and CO_2 partial pressure of 0.8 bar (80 vol%). The observed Mg/Al ratios and sodium content of the LDHs are also plotted in Figure 4.14 to investigate their relationship with the CO_2 adsorption capacities of derived MMOs. The error bars on the histogram represent the range of uncertainty due to weighting precision of thermogravimetric analyzer.

Figure 4.14 shows that CO_2 adsorption capacities of MMOs obtained from the co-precipitation method (0.5 – 0.9 mmol/g) are generally higher than those obtained from the urea hydrolysis method (0.3 – 0.7 mmol/g). The higher observed Mg/Al ratios (i.e., Mg content), sodium content and surface area of co-precipitated MMOs are likely the factors causing their CO_2 adsorption values to be higher than the urea hydrolysis derived MMOs. Among these parameters, the CO_2 adsorption capacities of co-precipitated MMOs seem to be more strongly influenced by their sodium content. For example, the highest CO_2 adsorption capacities were recorded from samples CPNI2 and CPCL3, which also presented the highest sodium content. No clear correlation between BET surface area

131

(Figure 4.14B) and CO_2 amount adsorbed is seen. From Figure 4.14A, the Mg/Al ratio of the co-precipitated sorbents (both crystal and bulk Mg/Al ratios) does not seem to have an obvious impact on the CO_2 adsorption capacities, i.e., the samples having different *a* values and observed Mg/Al ratios (CPNI3, CPNI4, CPCL3 and CPCL4) showed close values of CO_2 adsorption capacities (0.75 – 0.81 mmol/g). Coincidentally, these samples also showed similar synthesis yield values (~100 %). In contrary to the synthesis method, different precursor salts do not play a major role on the CO_2 adsorption of MMOs. However, MMOs synthesized by metal nitrates do show a slightly higher CO_2 adsorption capacity than those synthesized with metal chlorides in both synthesis methods. This is likely due to the higher sodium content in the precursor metal nitrates used to synthesize LDH samples.
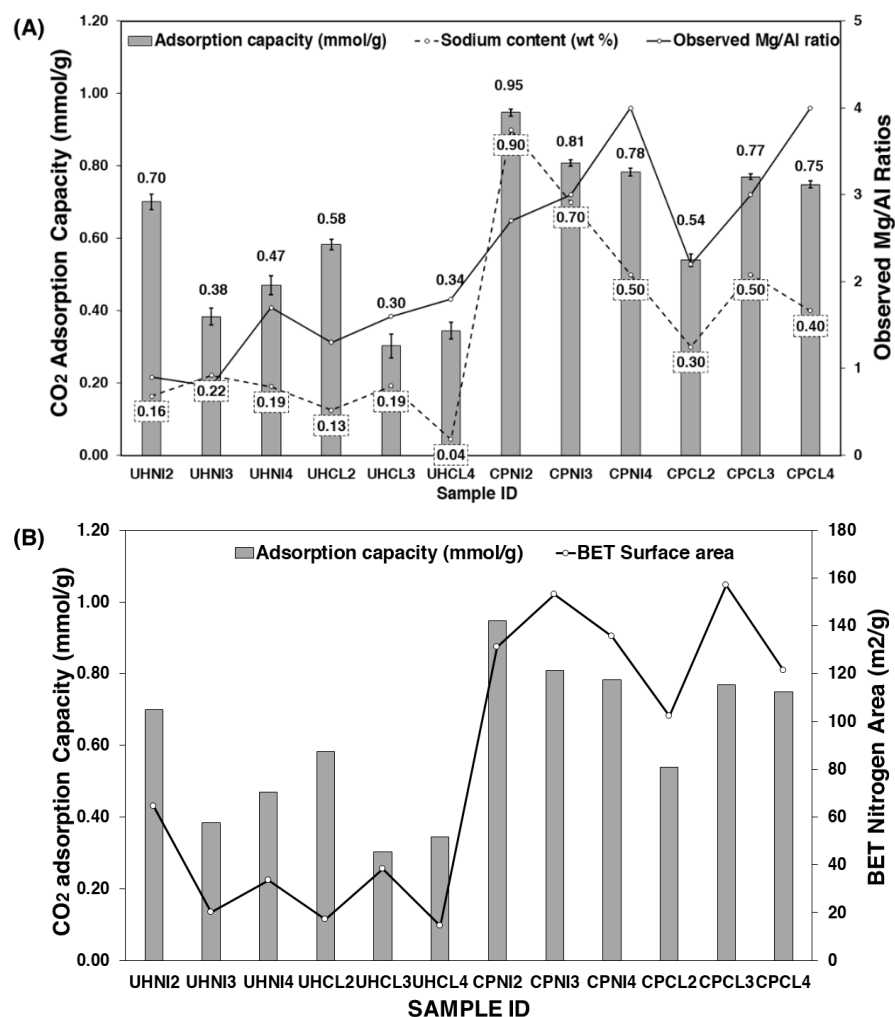
Figure 4.14 - CO₂ adsorption capacities of MMOs synthesized via urea hydrolysis and co-precipitation method at 200 ˚C, plotted against the (A) observed (measured) Mg/Al ratios and sodium content and (B) BET nitrogen area (m2/g)

In the case of urea hydrolysis derived MMOs, none of the metrics determined earlier (e.g., sodium content, observed Mg/Al ratios and BET surface area) shows obvious correlation with their CO_2 amount adsorbed. However, a further investigation shows that the two highest CO_2 adsorption capacities were in fact measured from the samples having the lowest observed Mg/Al ratios (e.g., UHNI2 and UHCL2). This means that the low LDH purity and presence of impurities in the urea hydrolysis samples may have played a role in this. For instance, despite having the lowest observed Mg/Al ratios, samples UHNI2 and UHCL2 showed the highest yields (81.2 and 77.0 %) and the smallest deviation from expected Mg/Al ratios, which suggests they have the lowest amount of impurities and high LDH purity. This is probably why they exhibit the highest CO_2 adsorption capacities among the urea hydrolysis derived MMOs. It is also possible that the impure phases have hindered the access of CO_2 to the active sites (i.e., Mg^{2+} species) of urea hydrolysis MMOs.

CO₂ adsorption kinetics. Figure 4.15 shows the profile of CO_2 adsorption capacity *vs* time (minutes) for MMOs derived by the LDHs synthesized by both urea hydrolysis and co-precipitation method. This is done to evaluate the effects of synthesis method and metal salts precursors on the CO_2 sorption kinetics of MMOs. The absence of a clear plateau in all sorption profiles after 120 minutes indicates the the nonequilibrium adsorption behavior of CO_2 in the LDH-derived MMOs sorbents. The vast difference in the uptake slopes of these profiles suggests two different kinetic regimes, i.e., a steep increase in the first few minutes of adsorption (fast reaction), followed by the small increase until the end of the adsorption step (slow reaction). In a cyclic adsorption operation, the fast reaction is often preferred as it mostly occurs on the sorbent surface and requires lower heat of adsorption [265]–[268]. The slow reaction, on the other hand, is generally not favored and forms bulk $MgCO_3$ species, which tend to be difficult to regenerate and cause process issues such as poor mechanical stability and CO_2 slip through the adsorption bed [269].
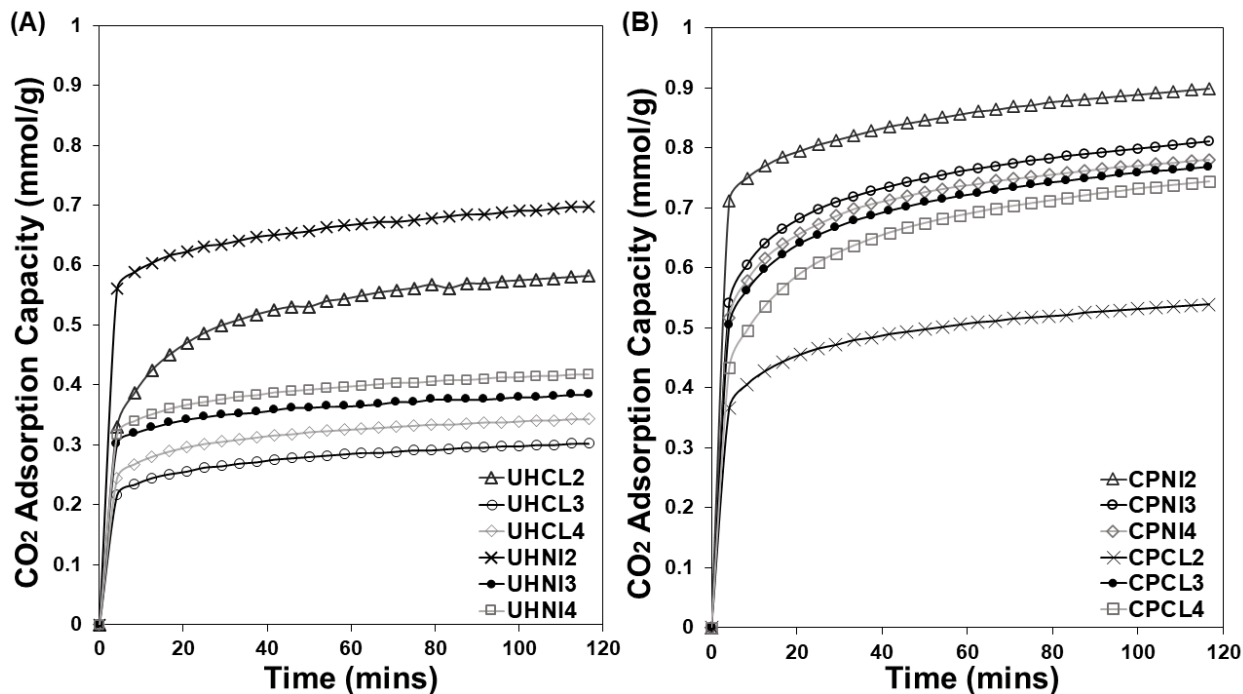
Figure 4.15 - CO₂ adsorption capacity vs time (minutes) profile of MMOs derived by the LDHs synthesized by (A) urea hydrolysis and (B) co-precipitation method

Overall, the co-precipitated MMOs clearly have better CO_2 adsorption kinetics than urea hydrolysis MMOs. The better kinetics of co-precipitated MMOs seems to be directly linked to the sodium content of samples, which gives higher CO_2 uptakes in the fast reaction step. For example, MMOs that achieved the highest CO_2 uptake in the fast reaction step are CPNI2, followed by CPNI3, CPNI4, CPCL3, CPCL4 and CPCL2; which follows the same order as the one with the highest concentration of sodium present in Table 4.4. For the urea hydrolysis MMOs, the UHNI2 sample shows remarkably higher CO_2 uptake than the rest of its kind during the fast reaction step. This is likely due to the combined effects of high LDH purity of the sample and additional sodium content from the precursor metal nitrates, which provided more active sites for CO_2 adsorption.

In the slow reaction step, all urea hydrolysis MMOs show similar kinetics, except the UHCL2 MMOs having an obviously steeper profile, which suggests a higher carbonation rate. Since the slow reaction corresponds to the formation of bulk $MgCO_3$ species, this higher uptake by the UHCL2 sample is likely to do with its higher Mg content, as a result of high LDH purity and a high observed Mg/Al ratio (Table 4.4), which provided more Mg-

134

O sites for the carbonation reaction. This is the same with co-precipitated MMOs, where the samples having higher Mg/Al ratios (i.e., 3 & 4) shows higher carbonation rate in the slow reaction step compared to the lower ones (i.e., CPCL2 & CPNI2).

For both co-precipitation and urea hydrolysis methods, MMOs synthesized from metal nitrates tend to show better CO_2 kinetics than the ones synthesized from metal chlorides, by having higher CO_2 uptakes in the fast reaction step. For the slow reaction step, no obvious effect due to the choice of metal salt precursors is seen. Overall, the sodium content of sample seems to have a direct positive impact on the CO_2 adsorption kinetics of LDH derived MMOs.

Cyclic Stability. Cyclic CO_2 adsorption tests were carried out to test the cyclic stability of selected LDH-derived MMOs sorbents and compared with pure magnesium oxide (MgO), obtained by calcining $Mg(OH)_2$ at 400 ˚C for 4 hours, which serves as the reference case. MgO is a suitable benchmark to assess the cyclic stability of LDH derived MMOs because the MMOs sorbents were originally proposed as an alternative option to MgO, which was found to have poor cyclic stability in general. Only four MMOs were selected to study for cyclic tests, based on three criteria: 1) highest LDH yields, 2) good agreement between expected and observed Mg/Al ratios and 3) adequate CO_2 adsorption capacities. Note that the adsorption and desorption were carried out for 30 minutes each. Figure 4.16 shows the CO_2 adsorption capacities of tested MMOs sorbents in each cycle and the percentage reduction in CO_2 sorption capacities calculated with respect to the amount adsorbed in the first cycle.

Figure 4.16A shows that all LDH-derived MMOs and MgO sorbents show a slow, gradual drop in CO_2 adsorption capacities over 10 adsorption cycles, and there is no obvious plateau, which means the capacities might reduce further. A similar trend is observed in Figure 4.16B, which shows the percentage drop of adsorption capacities calculated with respect to the first cycle. It seems that all the sorbents experience the largest drop in the adsorption capacities after the 1st cycle. No obvious correlation from either the synthesis method or metal salts precursors is found to be affecting this large initial drop in adsorption capacities. Among the MMO samples, Figure 4.16A shows that CPNI3 sample presents the highest CO_2 adsorption capacities in all 10 cycles. Interestingly, despite the promising

outlook of CPNI3, a close look in Fig. 4.16B reveals that in fact, the same sorbent shows the largest reduction in overall cyclic stability (31.2 %) and is the only MMOs sorbent performing worse than MgO sorbent (26.5 %). On the contrary, the urea hydrolysis samples show relatively good cyclic performance than their co-precipitated counterparts, as their CO_2 adsorption capacities after the first cycles are almost similar in Figure 4.16A. Overall, LDH-based MMOs appears to have better cyclic stability than pure MgO sorbent, i.e., lower percentage loss in CO_2 adsorption capacities after 1st cycle.
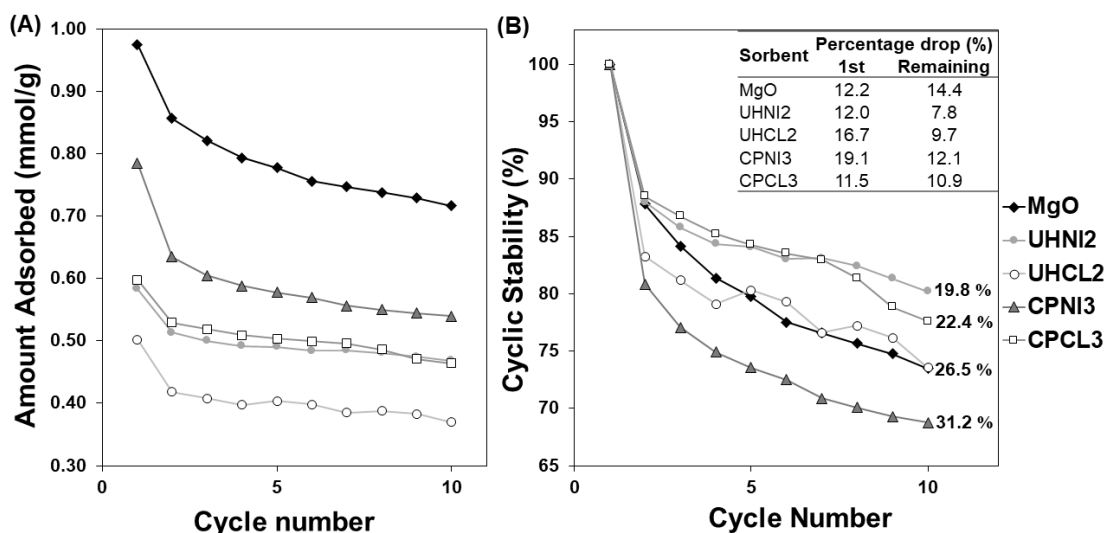
Figure 4.16 - (A) CO₂ adsorption capacity and (B) percentage reduction in adsorption capacity by cycles of selected MMOs synthesized with urea hydrolysis method and co-precipitation method

4.3.5 Comparison with literature LDH derived MMOs

A performance comparison of MMOs synthesized in this work with relevant analogues previously reported in literature is shown in Figure 4.17, at 200 ˚C [151], [152], [199], [270]–[276]. In this figure, MMOs refer to those derived from pristine Mg-Al-CO₃ LDHs, unless otherwise specified, e.g., Mg-Al-stearate and Mg-Al-SDS. MMOs investigated under different application (> 300 ˚C and elevated pressures) are excluded. Commercial LDH-based MMOs sorbents were also included as benchmark materials, even though some of them have been promoted with alkali metal carbonates and salts, such as K_2CO_3, KNO_3

& NaNO$_3$. Full details of these MMOs and the adsorption conditions, e.g., synthesis method employed, temperature, CO$_2$ partial pressure, are summarized in Appendix Table A4.1. As shown in Figure 4.17, CO$_2$ adsorption capacities of MMOs synthesized in this work is lower than those promoted with alkali metal salts and carbonates. However, the capture capacities are still better than most of the MMOs derived from unpromoted Mg-Al LDHs, except for MMOs derived from Mg-Al-stearate LDHs, which has been modified for larger surface area and smaller particle sizes.
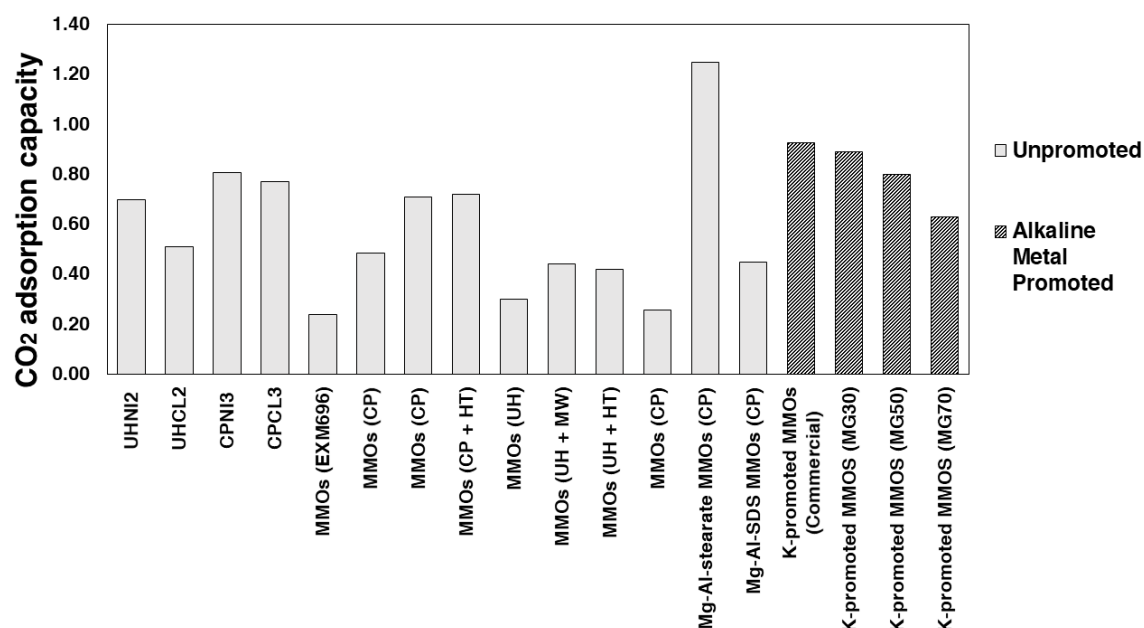
Figure 4.17 - CO$_2$ adsorption capacities of MMOs synthesized in the present work and those previously reported; The grey bars indicate MMOs derived from unpromoted Mg-Al-LDHs whereas dark bars represent MMOs derived from alkali-metal promoted Mg-Al-LDHs

Overall, this work highlights that the selecting a suitable CO$_2$ capture material does not just rely on its CO$_2$ adsorption performance. Other factors are equally important such as productivity, environmental sustainability, cyclic stability, and efficiency of the overall synthetic process including the generation of waste (i.e., effluents). For example, nitrate precursors tend to be more costly than the chloride ones, and they might also have disposal issues due to the ecologically unsafe nitrate ions generated in the effluents. However, from an environmental sustainability viewpoint, it is hard to conclude here which synthesis

137

method or which metal salt precursors are more superior, unless a completed life cycle assessment (LCA) is carried out.

4.4 Conclusions

The selection of the appropriate synthesis method and salt precursors is a crucial decision in the development of a CO_2 capture adsorbent. In the present study, the impact of the synthesis method and choice of salt precursors on the chemical composition of LDHs was investigated. Additionally, the CO_2 adsorption behaviour of Mg-Al-LDHs based MMOs was studied, and its relationship with synthesis efficiency metrics, e.g., purity, synthesis yields and percentage of unreacted reactants, was established.

LDHs synthesized by the urea hydrolysis method showed higher Al^{3+} substitution (a = 3.032 – 3.038 Å) and higher amorphous Al-phases as impurities, resulting in low purity LDHs. The synthesis yield was found to be relatively low (51 – 82 %), and a high percentage of unreacted Mg^{2+} ions was found in the reaction filtrates. In contrast, LDHs synthesized *via* co-precipitation showed more varied compositions (*a* = 3.037 – 3.069 Å), which were in close agreement with the targeted ones at synthesis. The synthesis yields were close to 100 % in all the samples, and negligible amounts of metal ions were found in the filtrates. All the samples showed trace amounts of sodium (0.04 – 0.9 wt %), which are likely to be originated from the precursor employed. Metal chlorides were found to be a better precursor for efficient precipitation of LDHs compared to metal nitrates for both co-precipitation and urea hydrolysis methods.

The resultant MMOs showed different textural properties. MMOs generated from urea hydrolysis method shows large hexagonal crystallites, whereas MMOs generated from co-precipitation show large aggregates of irregular shapes. The presence of impure phases and the sodium content were shown to have a significant effect on the CO_2 adsorption capacities of LDH derived MMOs. The highest CO_2 uptakes were measured for MMOs derived from urea hydrolysis samples (0.70 mmol/g), exhibiting the highest LDH yield and lowest amounts of Al-based impurities, and from co-precipitated LDH derived MMO samples (0.81 mmol/g) with the highest sodium content. The impact of synthesis method and metal salt precursors on the CO_2 adsorption kinetics of LDH derived MMOs was also

demonstrated. MMOs that were synthesized by co-precipitation method and metal nitrates were shown to have better CO_2 sorption kinetics than the ones synthesized by urea hydrolysis method and metal chlorides. Most MMOs sorbent was found to have better cyclic stability than pure MgO sorbent, although their sorption capacities are lower.

Appendix A4.1

Table A4.1 - CO₂ adsorption capacities and reactions conditions of MMOs presented in Figure 4.17

Sample ID	Synthesis/Preparation method	CO₂ adsorption capacity (mmol/g)	Adsorption Time (minutes)	Temperature (˚C)	CO₂ partial pressure (bar)	Ref.
UHNI2	Urea hydrolysis method	0.70	120	200	0.8	This work
UHCL2	Urea hydrolysis method	0.51	120	200	0.8	
CPNI3	Co-precipitation method	0.81	120	200	0.8	
CPCL3	Co-precipitation method	0.77	120	200	0.8	
EXM696	Commercial	0.24	Equilibrium	200	1	[1]
Mg-Al-CO₃ MMOs	Co-precipitation method	0.49	Equilibrium	200	1	[2]
Mg-Al-CO₃ MMOs	Co-precipitation method	0.26	60	200	1	[3]
Mg-Al-CO₃ MMOs	Co-precipitation method	0.71	120	200	1	[4]
Mg-Al-CO₃ MMOs	Co-precipitation + Hydrothermal method	0.72	120	200	1	
Mg-Al-CO₃ MMOs	Urea Hydrolysis method	0.3	120	200	1	
Mg-Al-CO₃ MMOs	Urea Hydrolysis + Microwave method	0.44	120	200	1	
Mg-Al-CO₃ MMOs	Urea Hydrolysis + Hydrothermal method	0.42	120	200	1	
Mg-Al-	Co-	1.25	120	200	1	[5]

140

stearate MMOs	precipitation method					
Mg-Al-SDS MMOs	Co-precipitation method	0.45	90	200	1	[6]
K-promoted MMOs	Commercial	0.93	Equilibrium	208	1 (humid)	[7]
K-promoted MMOs (MG30 - Sasol)	Commercial	0.89	Equilibrium	200	1.01	[8]
K-promoted MMOs (MG50-Sasol)	Commercial	0.8	Equilibrium	200	1.01	
K-promoted MMOs (MG70-Sasol)	Commercial	0.63	Equilibrium	200	1.01	
K-promoted LDHs based MMOs	Co-precipitation method	1.23	Equilibrium	240	1	[9]
NaNO$_3$ promoted Mg-Al-CO$_3$ MMOs	Modified Urea Hydrolysis Method	1.69	60	200	0.5	[10]

References

[1] Z. Yong, V. Mata, and A. E. Rodrigues, "Adsorption of carbon dioxide at high temperature—a review," *Sep. Purif.*, vol. 26, no. 2–3, pp. 195–205, Mar. 2002, doi: 10.1016/S1383-5866(01)00165-4.

[2] M. K. Ram Reddy, Z. P. Xu, G. Q. Lu, and J. C. D. Da Costa, "Layered double hydroxides for CO$_2$ capture: Structure evolution and regeneration," *Ind Eng Chem Res*, vol. 45, no. 22, pp. 7504–7509, 2006, doi: 10.1021/ie060757k.

[3] C. Megías-Sayago, R. Bingre, L. Huang, G. Lutzweiler, Q. Wang, and B. Louis, "CO$_2$ Adsorption Capacities in Zeolites and Layered Double Hydroxide Materials," *Front*, vol. 7, no. August, pp. 1–10, 2019, doi: 10.3389/fchem.2019.00551.

[4]   Y. Gao *et al.*, "Comprehensive investigation of CO_2 adsorption on Mg-Al-CO$_3$ LDH-derived mixed metal oxides," *J Mater Chem A*, vol. 1, no. 41, pp. 12782–12790, 2013, doi: 10.1039/c3ta13039h.

[5]   Q. Wang, H. H. Tay, Z. Zhong, J. Luo, and A. Borgna, "Synthesis of high-temperature CO_2 adsorbents from organo-layered double hydroxides with markedly improved CO_2 capture capacity," *Energy Environ. Sci*, vol. 5, no. 6, pp. 7526–7530, 2012, doi: 10.1039/c2ee21409a.

[6]   Q. Liu, Y. Zhao, Z. Jiang, Y. Cui, J. Wang, and N. Ai, "Computational and experimental studies on the CO_2 adsorption of layered double hydroxide intercalated by anionic surfactant," *Appl Clay Sci*, vol. 190, no. March, p. 105556, 2020, doi: 10.1016/j.clay.2020.105556.

[7]   Y. Ding and E. Alpay, "High temperature recovery of CO_2 from flue gases using hydrotalcite adsorbent," *Process Saf.*, vol. 79, no. 1, pp. 45–51, 2001, doi: 10.1205/095758201531130.

[8]   H. J. Jang, C. H. Lee, S. Kim, S. H. Kim, and K. B. Lee, "Hydrothermal synthesis of K_2CO_3-promoted hydrotalcite from hydroxide-form precursors for novel high-temperature CO_2 sorbent," *ACS Appl Mater*, vol. 6, no. 9, pp. 6914–6919, 2014, doi: 10.1021/am500720f.

[9]   J. M. Lee, Y. J. Min, K. B. Lee, S. G. Jeon, J. G. Na, and H. J. Ryu, "Enhancement of CO_2 sorption uptake on hydrotalcite by impregnation with K_2CO_3," *Langmuir*, vol. 26, no. 24, pp. 18788–18797, 2010, doi: 10.1021/la102974s.

[10]   X. Kou *et al.*, "Adsorption of CO_2 on MgAl-CO$_3$ LDHs-Derived Sorbents with 3D Nanoflower-like Structure," *Energy and Fuels*, vol. 32, no. 4, pp. 5313–5320, 2018, doi: 10.1021/acs.energyfuels.8b00024.

Chapter 5: A new Crystal-Chemical Model to Determine the True Chemical Composition of Layered Double Hydroxides (LDHs)

Critical Review

This chapter is currently reviewed for journal publication. Author Contributions statement: LC, GM, and SG: conceptualization and design of the study. LC: methodology, acquisition and interpretation of data, visualization, and writing of the first draft of the manuscript. GM and SG: writing—review and editing for important intellectual content. SG and MM-V: supervision, project administration, and funding acquisition.

This chapter presents a new crystal chemistry model to determine the true chemical composition of Mg-Al Layered Double Hydroxides (LDHs). As explained in Chapter 3, there is still no clear method to determine the true chemical composition of LDHs. The most accurate way is through the crystal chemistry method, which studies the relationship between unit cell lattice parameters and chemical composition x. Given a suitable crystal-chemical model, the chemical composition x of LDH phase can be calculated from the experimentally measured unit cell parameters, lattice parameter a and c. The major advantage of this method is that the lattice parameters can be easily measured by PXRD and are not affected by the presence of secondary phases, unlike results from direct chemical analyses, which can reliably reflect the chemical composition of crystalline LDH phase.

In Chapter 3, the model developed by Richardson (2013) was employed to calculate "x" from the lattice parameter "a" of the Mg-Al LDHs synthesized. However, the results show some deviation between the theoretical and calculated x obtained from Richardson's model. For example, Richardson's model predicts that any a value below 3.039 Å corresponds to an x exceeding 0.33, which is beyond the theoretical upper x limit for LDHs phase. As shown in Chapter 4, these "a" values are commonly associated with LDHs synthesized with the hydrothermal method (3.032 – 3.038 Å), such as urea hydrolysis method. The existence of these low a values obtained from the urea hydrolysis method has prompted the need to revisit the crystal chemistry method for LDHs.

In the quest to establish a reliable crystal chemistry model, knowledge gaps related to the chemical composition of this class of material were first identified. The chemical composition x of LDH phase is characterized by the M^{2+}/M^{3+} ratio ($x = M^{3+}/(M^{2+}+M^{3+})$), which represents the amount of trivalent cation (M^{3+}) substituted at the crystal lattice of LDHs. According to Pauling's cation-cation avoidance rule, there should be a limit for the amount of M^{3+} ions that can substitute into the LDH crystal lattice. Many studies have postulated that this range of x is between $0 - 0.33$; however, the precise boundaries of x are still not clear. Specifically, the value of the lowest possible x remains ambiguous, as this x varied significantly from experiment to experiment (e.g., $0.1 - 0.2$ [219], [222], [223], [259], [277], [278]). The understanding of this precise range of x is crucial for model validation.

Furthermore, almost all previous attempts to develop a crystal chemical model for LDH phases have mainly employed an empirical approach, i.e., regression analysis of experimental data. Regression analysis is generally a useful approach for modelling the relationship between two variables, but unfortunately not in this case for the determination of the chemical composition for LDHs phase. Accurate results from regression analysis require a reliable set of data. In this case for LDHs, the data set are the a-parameter of synthesized LDHs and the reported chemical composition, x. Most LDH studies report their chemical composition based on either the nominal composition or the one obtained from chemical analysis. However, the results from Chapter 3 and Chapter 4 have demonstrated the chemical composition of synthetic LDHs usually shows deviates from their nominal compositions and consists of impure phases. Thus, the x collected from those studies likely does not reflect the true chemical composition of the synthesized LDHs. In addition, most of those studies have not considered the impacts of the synthesis method on the a-parameters of LDHs, an important variable previously identified in our earlier studies. Hence, the regression analysis of these data sets might lead to a biased outcome.

To address these gaps, a *theoretical top-down* approach has been employed to develop a new crystal chemical model for the LDH system. This approach is a further improvement of previous crystal chemistry studies from Brindley & Kikkawa (1979) and Richardson (2013). The crystal chemistry investigation of LDHs phases conducted by these studies

form the basis of the current work, and this work demonstrates that the model can be further improved by accounting for the two different local environments within the LDH structure. The fundamental of this new approach builds on the famous Vegard's law, which states a linear relationship between lattice parameters and chemical composition should be observed in a substitutional solid solution. The only input required is the lattice information of the two end-point compounds, which are $M(OH)_2$, the phase that has zero Al^{3+} substitution ($x = 0$) and $M(OH)_3$, the phase that has full Al^{3+} substitution ($x = 1$). Using this approach, the need of experimental data as the input for the crystal chemical model is eliminated. In this work, the Mg-Al LDH system is the focus due to the large amount of data that is available for validating our crystal chemical model. These data also demonstrate the impact of empirical data on the accuracy of crystal chemistry models, due to the huge uncertainty in the experimentally determined chemical composition in literature. Finally, the new x range that is valid for LDHs was redefined, based on experimental evidence discovered from literature.

For Mg-Al-LDHs, a new crystal chemistry model was obtained by using the d(M-M) values derived for $Mg(OH)_2$ and $Al(OH)_3$. The crystal chemical model developed in the present work shows clear deviation from all the models previously developed. Our model predicts a larger range of a values (3.017 - 3.085 Å; $\Delta a = 0.068$ Å), compared to other models such as Brindley's (3.055 – 3.104 Å; $\Delta a = 0.048$ Å) and Richardson's (3.039 – 3.090 Å; $\Delta a = 0.051$ Å). Richardson's model was used as a reference case as it is the most recent and comprehensive one in the literature. When taking the a values of LDHs found in literature, a few x calculated from Richardson's model clearly exceeded the upper limits of x for LDH phase (i.e., 0.33), especially those data points having a value less than 3.04 Å. For example, the lowest value of a found in literature is 3.016 Å, the x calculated from the Richardson's model is 0.41. On the contrary, using our model, the same a value arrives at an x equal to 0.33. This shows all the x calculated using our model are well within the valid x range ($x < 0.33$). Consequently, the largest a value of Mg-Al-LDHs found in literature is 3.110 Å. Using this value, our model predicted an x value of 0.084 Å. The Richardson's model also predicted a very similar value, $x = 0.08$ Å. Coincidently, this is also the point where two crystal chemistry models overlapped in Figure 5.5. This result agrees well with previous theoretical and experimental studies on LDHs, which have suggested this x value

of 0.083 or Mg/Al ratio of 11 might be the chemical composition where lowest possible substitution of Al^{3+} can occur in LDH crystalline phase. Based on these observations, it was concluded that the lowest possible x for LDH phase is 0.083.

Up to this stage, a precise boundary of x is defined for Mg-Al-LDHs, i.e., 0.083 – 0.33. Then, with the a value of 3.04 Å, the present work model predicted an x value of 0.25. This observation is very interesting as this a value is commonly associated with the composition of maximum Al^{3+} substitution in the literature (0.33), but our model gives a totally different value of x. However, this actually aligns with our data analysis, which found a number of pure phases LDHs with a lower than this value ($\sim$ 3.024 Å). Considering that the 3.04 Å value is very close to the median value of a range revealed for Mg-Al-LDH phase (3.02 – 3.11 Å), the inference drawn from our model is highly plausible. As mentioned before, this x value is the same as the composition of mineral Hydrotalcite ($x = 0.25$), the LDH phase found in nature. This finding might explain why LDHs synthesized by the urea hydrolysis method tend to show close values of a (3.03 - 3.04 Å), given the fact that the synthetic condition in hydrothermal method are actually very similar to the conditions under which natural LDHs form, e.g., high temperature (100 ˚C - 1000 ˚C) and elevated pressure.

Based on our results, LDHs are thermodynamically favored at $x = 0.25$, likely due to the abundance of the specific compositions found in LDHs synthesis studies. In contrast, the composition $x = 0.33$ appears to be rarely formed under synthetic conditions.

In conclusion, this work demonstrates that the crystal chemical model developed here can serve as a tool for deriving the true chemical composition of LDHs, based on a simple parameter (a parameter) that can be easily obtained from PXRD analysis. This avoids the need for intensive characterization for LDHs phase. It is anticipated that the findings discovered in this study can lead to a new trend of LDH nature discussion and, furthermore, aid in the design of LDH and MMOs material for optimized performance.

5.1 Introduction

LDHs are a subject of massive interest from the material science perspectives. However, despite being studied for decades, determination of the chemical composition for LDH phases remains a huge challenge. The chemical composition of LDHs is characterized by the M^{2+}/M^{3+} ratio or x ($x = M^{3+}/(M^{2+}+M^{3+})$), which represents the amount of trivalent cation (M^{3+}) substituted at the crystal lattice of LDHs. To minimize the mutual electrostatic repulsion caused by two neighbouring M^{3+}-M^{3+} ions, the amount of incorporated M^{3+} is limited - probably in the range between 0.15 – 0.33. Albeit already being discussed quite rigorously in some highly cited previous studies, determination of the precise boundaries of x for which LDHs can form is still an ongoing topic as the lowest limit of x remains unclear [219], [279]. Nonetheless, the chemical composition of LDHs is a vital aspect to elucidate as it has direct influence on the cation ordering, charge distribution, structural stability, and interlayer anion composition which each of them can affect upon their physical properties. For example, the M^{2+}-M^{3+} ratio determines the number of active site available for adsorption and catalytic activity. The cation ordering is important with the position of adjacent M^{3+} sites and distribution of anions in the interlayer space, which is critically important for intercalation reactions and a possibility to engineer the physicochemical properties of LDHs and related material, e.g., delamination, particle size, surface area and pore structures[145], [280].

For synthetic LDHs, the determination of their chemical composition is challenging because the formation of LDHs is known to be highly sensitive to their synthesis conditions, namely relative cation activities, pH of solution, temperature, aging time, pressure, etc., which were all shown to have control over the final product composition [206], [281]. Such phenomenon is well-demonstrated by the co-precipitation reaction – the most widely used synthesis method for LDHs – where the chemical composition of final product is not always guaranteed and may vary due to a small change in reaction condition [241]. For other synthesis methods that have been adopted, the reaction is not necessarily stoichiometry and may form amorphous impure phases, which are difficult to detect and distinguish via chemical analyses [230], [243], [282]. As a result, deviation between nominal and final composition is commonly observed in synthetic LDHs and is an issue frequently reported in structural studies of these LDHs. This is the same for natural LDHs,

in which the specimens tend to contain impurities and have different parallel intergrowth LDH polytypes. Even an experienced mineralogist might confuse these LDH phases with one other. One good example is the characterization of Hydrotalcite (x = 0.25) and Quintinite (x = 0.33). Although being the most studied minerals within the LDH supergroup, it was only recently justified that the widely cited single crystal refinement of Hydrotalcite was in fact done on specimen of Quintinite [283], [284]. All these factors make the determination of the true composition for LDH phases a difficult task even to-date.

Therefore, there is an urgent need to develop a reliable method to determine the chemical composition for LDHs. The most accurate way is, arguably, through the crystal chemistry method, which studies the relationship between unit cell lattice parameters and chemical composition x. Given a suitable crystal-chemical model, the chemical composition x of LDH phase can be calculated from the experimentally measured unit cell parameters, i.e., lattice parameters. The major advantage of this method is that the lattice parameters can be easily measured by Powder X-Ray diffraction (PXRD) and – unlike results from direct chemical analyses - are not affected by the presence of secondary phases, thus can reliably reflect the chemical composition of crystalline LDH phase. Although there have been a few studies attempting to build a crystal-chemical model for LDHs, so far none of them can precisely describe the lattice parameters and x relation for LDHs. Amongst them, Brindley and Kikkawa (1979) firstly attempted to establish the a vs x relation by using crystal chemistry arguments, and considering an ideal octahedral layer for the LDH structure[219]. The next crystal chemistry attempt was from Richardson (2013), who conducted a detailed geometrical investigation onto the LDH structure and suggested that octahedral layers are not ideal within LDH structure [220]. These two studies form the basis for the current work, where we demonstrate that the model can be further improved by accounting the two different local environments within the LDH structure. The presence of these different local environments has been confirmed in several structural refinements and high resolution solid-state NMR studies [224], [225], [285], [286].

To address this, the present study proposes an alternative *theoretical top-down* approach to obtain a new crystal chemical model for the LDH system. The fundamental of this new approach builds on the famous Vegard's law, which states a linear relationship between

lattice parameters and chemical composition should be observed in a substitutional solid solution[287]. The only input required is the lattice information of the two end-point compounds, which are M(OH)$_2$, the phase that has zero Al^{3+} substitution (x = 0) and M(OH)$_3$, the phase that has full Al^{3+} substitution (x = 1). In this work, the Mg-Al LDH system was chosen as focus due to the large amount of data that is available for validating our crystal chemical model. Using these data, the impact of empirical data on the accuracy of crystal chemistry models, as a result of the huge uncertainty in the experimentally determined chemical composition in literature, was demonstrated. On the contrary, the crystal chemical model developed here is simple and unambiguous as it establishes reliable values of LDH lattice parameters as a function of composition, x. Finally, a new x range valid for LDH was redefined, based on experimental evidence discovered from literature. The ultimate aim of this work is to highlight the importance of combining crystal-chemistry and analytical chemistry in the development of LDH materials.

5.2 Methodology: Development of Crystal-chemical model

The crystal structures of Mg-Al-CO$_3$ LDH and the related single hydroxides (e.g., Brucite and Gibbsite) are shown in Figure 5.1. A detailed description of similarities and disparities between LDHs and single hydroxides crystal structure can be found in the crystal chemistry investigation conducted by Richardson (2013) [220]. In essence, the structure of LDHs is very similar to that of Brucite, except a portion of the divalent cations (Mg^{2+}) are substituted by trivalent cations (Al^{3+}) at the octahedral sites of hydroxide layer. This substitution causes a net positive charge on the LDH hydroxide layers and requires a negative charged anion to balance at the interlayers, along with water molecules. Since the substitution of Al^{3+} is an isomorphous one, thus the structure of the octahedral layers of LDH (i.e., a cadmium iodide (CdI$_2$) type structure) remain unchanged. Consequently, the hydroxide layers of LDH can be viewed as a solid mixture comprised of [Mg(OH)$_6$]$^{4-}$ and [Al(OH)$_6$]$^{3-}$-octahedra, whilst the nature of bonding in the octahedra should be similar to those in single hydroxide phases, e.g., Mg(OH)$_2$ and Al(OH)$_3$. This has been confirmed by the structural refinement of mineral Quintinite (x = 0.33) from the studies undertook by Krivovichev et $al.$ (2010) and Zhitova et $al.$ (2010), which reveal two distinct average M-O bond lengths and bond angles ($\alpha_{\angle O\text{-}M\text{-}O}$) distinguishing the two types of cation sites in the LDH [285], [286].
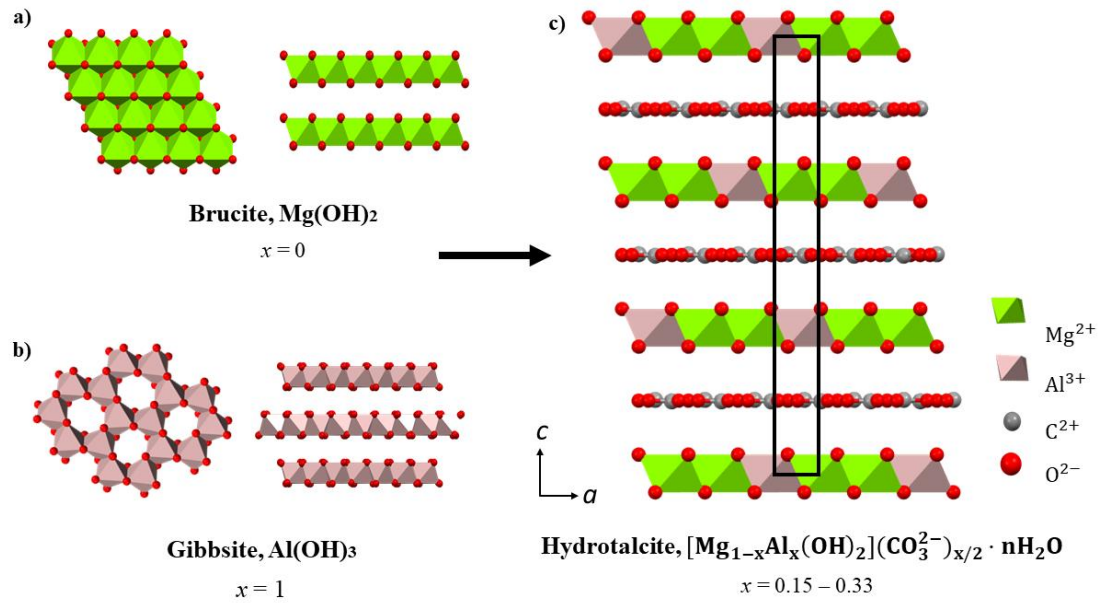
Figure 5.1 - Crystal structures of a) Brucite, Mg(OH)₂ ($x = 0$), b) Gibbsite, Al(OH)₃ ($x = 1$) and c) Hydrotalcite, [Mg$_{1-x}$Al$_x$(OH)₂](CO₃²⁻)$_{x/2}$·nH₂O having rhombohedral 3R stacking sequences, space group = R$\overline{3}$m; unit cell parameter $a \sim 3.054$ Å, $c \sim 24$ Å [29]

For a binary substitutional solid solution like this, Vegard's law should be valid. Vegard's law states that the lattice parameters of a mixed solid solution (AB) should vary linearly with composition, if derived from two components A and B having the same crystal structure in their pure form [214], [287]. The simplest mathematical expression for Vegard's law is therefore:

$$\text{Lattice parameter}, l_{LDH} = l_{M(OH)2}(1 - x) + l_{M(OH)3}x$$

[Eq. 5.1]

Where l represents a given lattice parameter of LDH, x is the mole fraction of trivalent cations at the octahedral layers ($x = M^{3+}/(M^{2+}+M^{3+})$), and M(OH)₂ and M(OH)₃ are the unitary hydroxides for the selected LDH system. Lattice parameters are physical vectors that are used to describe a unit cell in a three-dimensional crystal lattice, and they are referred to as a, b and c, depending on the plane direction. It is widely agreed that both lattice parameters a and c of the LDH system vary with chemical composition. As seen

150

from Figure 5.1c, similarly to the Brucite system, the lattice parameter a of Mg-Al-LDHs system is equivalent to the distance between two adjacent cations at the octahedral sites. Therefore, the isomorphic replacement of M^{2+} by M^{3+} ion at the octahedral sites of LDHs will affect the metal-metal cation distance, d(M-M), especially when these cations have different ionic radii, e.g., Al^{3+} has much smaller ionic radius (0.53 Å) than Mg^{2+} (0.72 Å). The experimental value of the a-parameter is determined from the position of *(110)* reflection in the XRD analyses ($a = 2 \times d_{110}$). On the other hand, the lattice parameter c corresponds to the distance between two cations of three successive hydroxide layers, along the stacking direction parallel to the c-axis. As the hydroxide layers are held by the columbic electrostatic attractions induced by the substitution of M^{3+} ion, thus the amount of M^{3+} will affect the thickness of basal spacing (determine from the position of *(003)* reflection in XRD analyses) and consequently the lattice parameter c ($c = 3 \times d_{003}$). However, it should be noted that both, the basal spacing and lattice parameter c, also respond to a number of variables such as the number, size and orientation of intercalated anions, extent of hydration and the strength of the pseudo-bonds between anions and the hydroxyl groups at the edge of hydroxide sheets [146], [288]. Therefore, it is harder to determine chemical composition of LDHs from lattice parameter c. Nevertheless, Zhitova *et al.* (2016) has established the correlation between d_{003} and the M^{2+}/M^{3+} ratio of the mineral form of Mg-Al-CO$_3$ LDHs and found it to be an effective way to distinguish Hydrotalcite from Quintinite [289]. As the present work proposes to use Vegard's law relation to establish the relationship between lattice parameter vs x, and single hydroxides usually do not have interlayer species, therefore the lattice parameter c will not be examined further in the following discussion. On the other hand, the lattice parameter a corresponds directly to the M^{2+}/M^{3+} ratio at the hydroxide layers and is widely applicable to characterize most LDHs, regardless of the interlayer species. Therefore, the lattice parameter a is as important as the lattice parameter c as a tool to determine the chemical composition of a LDH system. The rest of this work will then primarily focus on establishing the a vs x relations.

For the Mg-Al LDH system, Eq.1 cannot be directly applied due to the different crystal system of the single hydroxides. For example, Brucite, Mg(OH)$_2$ has a *hexagonal* crystal structure, which is different than all the polymorphs of Al(OH)$_3$, i.e., Gibbsite, Bayerite =

151

monoclinic and Doyleite, nordstrandite = *triclinic* [212], [290]–[293]. Moreover, one-third of the octahedral sites of aluminium hydroxides ($Al_{2/3}\square_{1/2}(OH)_2$, $\square$: cation vacancies) are unoccupied (See Gibbsite Unit in Figure 5.1b). As a result, the lattice parameter a of $Al(OH)_3$ polymorphs ($a = 5.01 – 8.64$ Å) varies significantly from Brucite ($a = 3.142$ Å). Hence, a further derivation for Eq. 5.1 is needed.

Geometrically speaking, each hydroxide layer in an LDH is made up by infinite edge-sharing octahedra which have a metal cation (M) occupying the center and oxygen atom (O) of the hydroxyl ion at the vertices. The schematic diagram of a single octahedron is shown in Figure 5.2a. As described before, the lattice parameter a of LDH is essentially the distance between two adjacent cations at the octahedral sites, d(M-M) and this equivalent to the distance between two oxygen atoms at the same plane (SP), d(O-O)^{SP} [220]. Figure 5.2b shows the geometrical relationship describing the lattice parameter a and the atoms in an octahedron; α is the angle between a metal cation and two oxygen atoms of the same plane (SP), α = O-M-O. Since Al^{3+} has smaller ionic radius (0.53 Å) than Mg^{2+} (0.72 Å) [294], the lattice parameter a of Mg-Al-LDH should be smaller than the one of Brucite (3.142 Å).
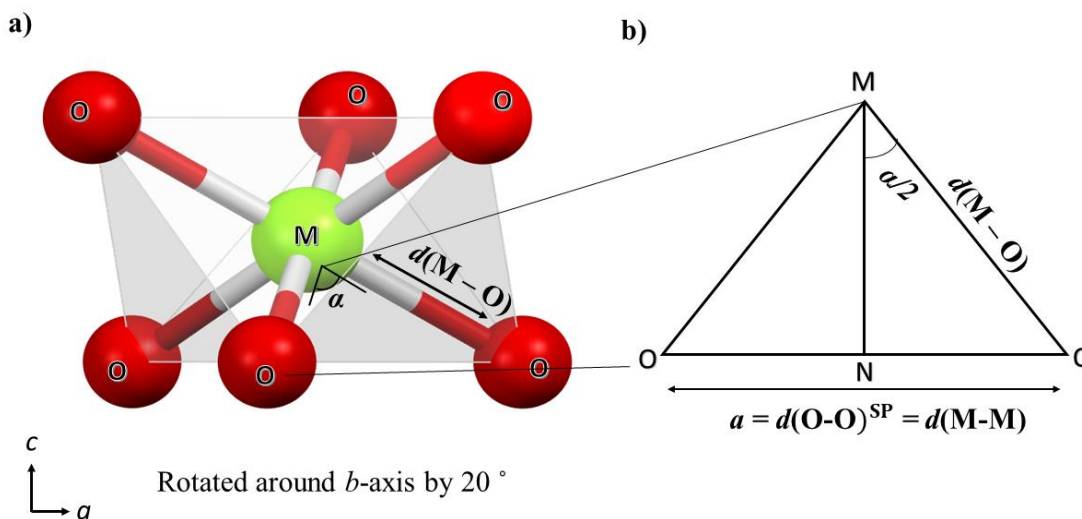
Figure 5.2 - Schematic diagram of a single octahedron that forms the hydroxide layer of LDH, and b) geometrical relationship describing the lattice parameter *a* and the atoms in an octahedron

Due to the inherent polarization nature of cation and anion, the local geometry of octahedra within single and double hydroxides is in fact strongly distorted away from a regular arrangement. This causes the octahedra to be compressed along the stacking axis c, thus flattening the octahedral layer structure ($\alpha > 90$ °) and increasing the atomic distance of the parallel planes, such as d(M-O), d(O-O)^{SP}, and d(M-M)[147]. For such relationship in octahedrally coordinated layers with a flattened angle, the a-parameter is given by Eq. 5. 2 [219]:

$$a = d_{(M-M)} = 2\sin\frac{\alpha}{2}d_{(M-O)}$$

[Eq. 5.2]

The extent of distortion is dependent entirely on the polarization power of cations occupying the center of the octahedron. Al^{3+} ions, owning to its smaller radius and higher charge, have more polarization power than Mg^{2+} ions. As a result, the $Al(OH)_6$-octahedra show a slight different local geometry environment than the $Mg(OH)_6$-octahedra. Table 5.1 shows all the α, d(M-O) and d(M-M) values of $Al(OH)_6$-octahedra obtained from $Al(OH)_3$ system (e.g. Gibbsite & Bayerite) and $Mg(OH)_6$-octahedra obtained from $Mg(OH)_2$ system (i.e. Brucite).

Table 5. 1 - Bond angles, d(M-O) and d(M-M) of Brucite, Gibbsite and Bayerite.

Brucite				Gibbsite					Bayerite		
Atom	α (°)	d(M-O), (Å)	d(M-M), (Å)	Atom	α (°)	d(M-O), (Å)	d(M-M), (Å)	Atom	α (°)	d(M-O), (Å)	d(M-M), (Å)
Mg-O	96.9	2.099	3.142	Al-O1	97.0	1.97	2.951	Al-O1	91.4	1.74	2.488
				Al-O2	90.3	1.95	2.765	Al-O2	96.4	1.90	2.831
				Al-O3	95.0	1.92	2.831	Al-O3	97.3	1.90	2.854
				Al-O4	85.7	1.89	2.571	Al-O4	88.5	1.92	2.682
				Al-O5	90.1	1.86	2.633	Al-O5	95.7	1.98	2.942
				Al-O6	91.1	1.98	2.827	Al-O6	88.1	2.06	2.869
					Average		2.763		Average		2.778

* d(M-M) = $2 \times \sin(\alpha/2) \times d$(M-O)

Gibbsite and Bayerite are selected as the Al-based reference hydroxides as they are the most common among the four polymorphs of $Al(OH)_3$. The main difference between these

two polymorphs is the stacking sequence of the hydroxide layers, i.e., if hydroxyl ion positions are represented by the upper-case symbols A and B, stacking sequence of Gibbsite is AB BA AB BA..., whereas in Bayerite is AB AB AB AB....[295] Nevertheless, the local octahedral geometry of the two polymorphs is still similar as evidenced by the close values of α and d(M-O) in Table 5.1. These values are very close to the M-O bond lengths in Quintinite that were revealed by Krivovichev *et al.* (2010) and Zhitova *et al.* (2010) in structural refinement studies and those postulated by Hofmeister and von Platen (1992) for ordered and disordered Mg-Al-LDHs[285], [286], [296]. By substituting Eq. 5.2 into Eq. 5.1 and assigning respective cations for the Mg-Al-LDH system Eq. 3 is obtained:

$$a_{LDH} = 2 \sin \frac{\alpha_{O-Mg-O}}{2} d_{(Mg-O)} (1 - x) + 2 \sin \frac{\alpha_{O-Al-O}}{2} d_{(Al-O)} x$$

[Eq. 5.3]

Expand and rearrange Eq. 5.3 will arrive to Eq. 5.4:

$$a_{LDH} = 2 \sin \frac{\alpha_{O-Mg-O}}{2} d_{(Mg-O)} - [2 \sin \frac{\alpha_{O-Mg-O}}{2} d_{(Mg-O)} - 2 \sin \frac{\alpha_{O-Al-O}}{2} d_{(Al-O)}] x$$

[Eq. 5.4]

The first term on the right-hand side of model (Eq. 4), which is also the intercept of vertical axis (y-intercept), is essentially a translation of the *a*-parameter of the Brucite, $Mg(OH)_2$. Such derivation agrees well with the widely accepted lattice parameter *a* vs *x* relation postulated by Taylor (1973), where the crystal chemical model of LDH should give *a* values of divalent cation phase, $M(OH)_2$ when extrapolated to *x* = 0[297]. A similar mathematical derivation is also seen from the crystal-chemical model derived by Richardson (2013). Conversely, when *x* = 1, the equation is reduced to the Al^{3+} form (e.g., d(Al-Al)), which calculates the distance between two adjacent Al^{3+} ions when all octahedral sites is occupied by Al^{3+}. This is, of course, just a hypothetical scenario since substitution of Al^{3+} in adjacent sites is energetically unfavorable unless accompanied by a vacant cation site (see Gibbsite Unit in Figure. 5.1b).

154

The slope of the crystal chemical model is given by the second term of model (Eq. 5.4) and has a negative value.

$$\frac{\Delta a}{\Delta x} = -[2 \sin \frac{\alpha_{O-Mg-O}}{2} d_{(Mg-O)} - 2 \sin \frac{\alpha_{O-Al-O}}{2} d_{(Al-O)}]$$

[Eq. 5.5]

Eq. 5.5 represents the deviation of the LDH crystal structure from the divalent hydroxide $M(OH)_2$, due to the substitution of trivalent cations (Al^{3+}). The importance of this term is obvious as it dictates the relationship between lattice parameter a and composition x of LDH phase in a crystal chemical model. Since x for LDHs is only valid for a short range ($0 < x < 0.33$), it is expected that a small change in the slope will have large effect on the a vs x relation. Eq. 5.5 shows that four input parameters are required to obtain the slope value, which are the bond lengths, $d(M-O)$ and bond angles, $(\alpha_{\angle O-M-O})$ from the two types of cations occupying octahedra (i.e. Mg^{2+} and Al^{3+}). To the best of our knowledge, this is the first crystal chemical model that accounts for the different local octahedra environments caused by the two cations with distinct polarization power. These input parameters can be easily obtained from the two end-member single hydroxide phases, i.e., $Mg(OH)_2$ and $Al(OH)_3$.

To obtain the final crystal chemical model, the $d(M-O)$ and α values of Brucite ($x = 0$) and Gibbsite ($x = 1$) from Table 5.1 are substituted into Eq. 5.4 and the model is expressed as Eq. 5.6:

$$a_{LDH} = 2 \sin \frac{96.9}{2}(2.099) - (2 \sin \frac{96.9}{2}(2.099) - (2.763)) = 3.142 - 0.378x$$

[Eq. 5.6]

Eq. 5.6 describes a linear relationship between the lattice parameter a and composition x for Mg-Al-LDHs, which agrees with the statement of Vegard's law. The y-intercept of equation matches well with the a-parameter of Brucite (3.142 Å) and the negative slope value is 0.378.

5.3 Results and Discussion

5.3.1 Comparison between Crystal Chemical models

Table 5.2 shows all the crystal chemistry models proposed in literature so far, and the method to obtain these models. There is clearly a variation in the slope values and y-intercept across the crystal chemical models proposed so far. Most notably, the negative slope of crystal chemical models, which dictates the *a* vs *x* relation, shows significant deviations from each other. Interestingly, the slope of the crystal chemistry model developed here shows the highest negative value (0.378) and clearly deviates from the rest of models (0.235 – 0.286). It is also worth noting that the three empirical models present a wide range in slope values, e.g., 0.252 0.306 and 0.235. This range confirms the large uncertainty in the experimentally observed composition *x* of synthesized LDHs and its effect on the lattice parameter.

Table 5. 2 - Crystal chemical equations for Mg-Al-LDHs in literature and the method to obtain these models.

Author	Model	Method	Ref
Brindley and Kikkawa (1979)	$a = -0.269x + 3.144$	Geometrical arguments based on ideal octahedron to obtain slope equation: $\Delta a/\Delta x = -\sqrt{2}\,[r(M^{2+}) - r(M^{3+})]$ and extrapolated to obtain y-intercept	[219]
Miyata, 1980	$a = -0.252x + 3.141$	Experimentally *a* value against *x* of synthesized LDHs	[261]
Kukkadapu et al., 1997	$a = -0.306x + 3.140$	Experimentally *a* value against *x* of synthesized LDHs	[298]
Kaneyoshi & Jones, 1999	$a = -0.235x + 3.120$	Experimental *a* value data and regression fits into literature data	[259]
Richardson, 2013	$a = -0.286x + 3.133$	Geometrical arguments based on squashed octahedron to obtain model: $a = 2\sin\frac{\alpha}{2}\,[r(M^{2+}) - r(OH^{-})] - 2\sin\frac{\alpha}{2}\,[r(M^{2+}) - r(M^{3+})]x$ and regression fits into literature data	[220]
This work	$a = -0.378x + 3.142$	Vegard's law relation and geometrical arguments based on squashed octahedron and two distinct cation sites in LDHs	

The lattice parameters obtained by the different crystal chemical models for the full range of concentration are plotted in Figure 5.3, and their range of values for a fixed range of composition x (i.e., 0.15 – 0.33) are presented in Table 5.3. Our model predicts a larger range of a values (3.017 - 3.085 Å; Δa = 0.068 Å), compared to other models such as Brindley's (3.055 – 3.104 Å; Δa = 0.048 Å) and Richardson's (3.039 – 3.090 Å; Δa = 0.051 Å). It is also noticeable that wide different a values are obtained for the same x (Table 5.3). On the other hand, the value of the y-intercept obtained from all the crystal chemical models is very close to the a-parameter of Brucite (3.142 Å), which agrees well with the Vegard's law. Except two models, Kaneyoshi *et al.* (1998) and Richardson (2013), which y-intercept deviates more from the a-parameter of Brucite. This larger deviation can be attributed to the fact that both studies employed the same strategy to obtain their model, i.e., linear regression analyses from literature LDH data.
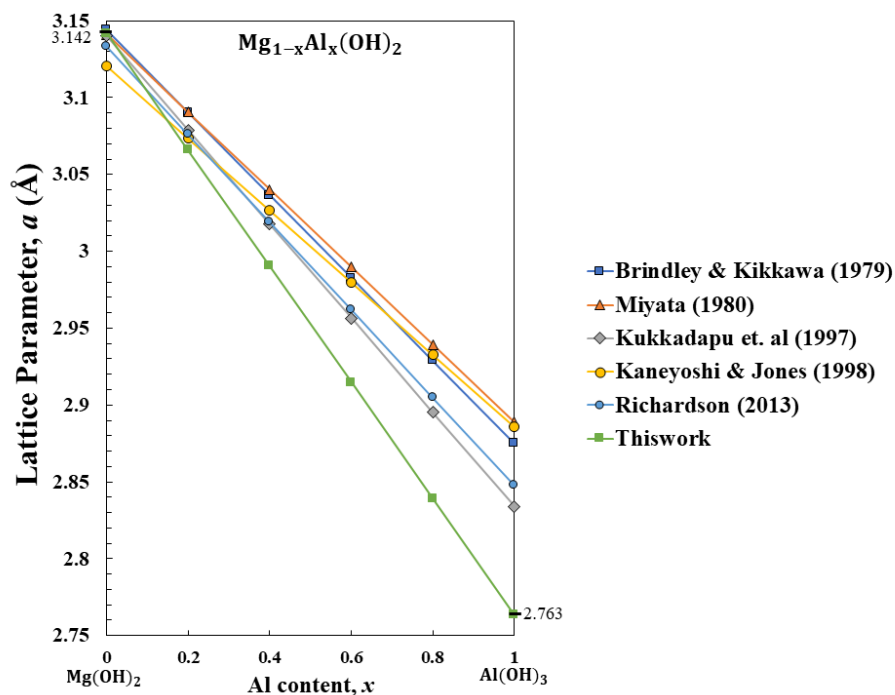
Figure 5.3 - Crystal Chemical models proposed so far in literature and in present work

Table 5.3 - Possible range of *a* for LDH predicted by crystal chemistry models

x	Brindley & Kikkawa (1979)	Miyata (1980)	Kukkadapu *et al.* (1997)	Kaneyoshi & Jones (1998)	Richardson (2013)	This Work
0	3.144	3.141	3.140	3.120	3.133	3.142
0.15	3.104	3.103	3.094	3.085	3.090	3.085
0.33	3.055	3.058	3.039	3.043	3.039	3.017

As seen in Table 5.2, most studies obtained the *a* vs *x* relation empirically, i.e., experimental observation of *a*-parameters against *x* derived nominal composition and/or direct chemical analyses. As mentioned before, Brindley & Kikkawa (1979) and Richardson (2013) were the only two studies that attempted a structural-geometrical approach to obtain a mathematical expression that would describe *a* vs *x* relation for LDHs. Brindley & Kikkawa (1979) obtained the slope equation: $\Delta a/\Delta x = -\sqrt{2}\,[r(M^{2+}) - r(M^{3+})]$ by assuming an ideal octahedral geometry ($\alpha = 90$ °) and Shannon-Prewitt ionic radii to represent metal-oxygen distance $r(M)$, e.g., Mg^{2+} (0.72 Å) and Al^{3+} (0.53 Å) [219]. By substituting these values into the slope equation, a slope value of 0.269 is obtained for Brindley's model. Such derivation was reasonable, considering the limited information available for LDHs at the time when that work was published. However, it is now widely understood that the octahedra in LDH phases are distorted (compressed along the *c*-axis), as in the single hydroxides. In addition to that, since the structure of LDH is eutactic (i.e., arrangement of ions is the same as in a closed packed array, but the ions are not necessarily touching), the ionic radii of cations cannot represent the distance between adjacent cations in the LDH.

Conversely, the Richardson model (2013) did consider that the octahedra is not ideal ($\alpha \neq 90$ °) and introduced the flattened angle, α, into the slope equation: $\Delta a/\Delta x = -2\sin\frac{\alpha}{2}\,[r(M^{2+}) - r(M^{3+})]$ [220]. However, this model again uses ionic radii to represent the d(M-O) distance and assumed that the LDH structure has only one α value – as in the single hydroxides – which itself is a conclusion obtained from the empirical validation of literature data. As described before, LDH has two cations, rather than one, so

there should be two different α values. These issues are addressed in our model (Eq. 5.5) by accounting for the different α values in LDH systems and replacing the ionic radii with the more precise d(M-O) values obtained directly from Mg- and Al- single hydroxides, as both structures have been thoroughly investigated. A larger slope (0.378) is then obtained using our model since the α and d(Al-O) values of Al(OH)$_3$ systems are much smaller than those ones in the Mg(OH)$_2$ system (Table 5.1). On the other hand, the slope values of Brindley & Kikkawa (1979) and Richardson (2013) are similar, e.g., 0.269 and 0.286, mainly due to similar mathematical models been employed and the small difference in the sine values, even though the α values are not the same (α = 90 ° and 97.41˚).

For the case of y-intercept, both Brindley and Richardson obtained their values by simply extrapolating their model to y-axis. The y-intercept obtained using Brindley's model is very close to the a value of Mg(OH)$_2$, e.g., 3.144. However, the Richardson's model obtained a low y-intercept value (3.133 Å) for Mg-based LDHs, in which the author attributed this to being the one corresponding to the α-form of the divalent hydroxide [M(OH)$_2$·mH$_2$O], rather than the naturally occurring $β$ polymorphs [M(OH)$_2$]. Indeed, for Ni- based LDHs which the author investigated along with Mg-Al LDHs, their single hydroxides Ni(OH)$_2$ do have two well-characterized polymorphs in α and $β$ form (occurs naturally as mineral Theophrastite) [299], [300]. However, thus far there is no clear evidence of Magnesium Hydroxide existing in the α form, i.e., Mg(OH)$_2$·mH$_2$O. Nevertheless, the crystal chemical model developed by Richardson (2013) is probably the closest to describing the true a vs x relation for LDH phase, since first attempted by Brindley & Kikkawa (1979) several decades ago. The model uniquely combines the efforts of structural-geometrical relationships and linear regression analysis based on a large collection of literature LDH data. However, perhaps the biggest drawback of these types of models is the reliance on regression analysis results for validation, so the quality of the obtained regression is subject to the quality of the data used for the fitting. As briefly described before, there is no clear guidance on how to determine chemical composition of LDHs, especially the synthetics one. Thus, any variables that can affect the data points (i.e., chemical composition x of LDHs) should be identified; otherwise, the model would lead to unreliable conclusions. Among all the variables, the synthesis method was found to have the largest effect on the observed lattice parameter a but none of the previous studies have considered this factor

into their analyses. For example, we previously found that despite different starting nominal compositions ($x = 0.2 – 0.33$), synthesis *via* the hydrothermal method tends to produce LDH with fixed composition, which was evidenced by the short range of obtained values for the lattice parameter *a* (3.03 - 3.04) [301]. Conversely, LDHs synthesized by the co-precipitation method did show a wider range of *a* values (3.03 – 3.07 Å) and a dependency on nominal composition. Unfortunately, none of the previous regression studies have highlighted this issue. Given now that we have a better understanding of variables that affect the chemical composition of LDH, there is a need to re-visit all these data points if used to fit models.

5.3.2 Variables affecting a vs x relation.

Figure 5.4 shows the lattice parameter *a vs* chemical composition *x* of LDHs for all data points that were used to derive Richardson's model (Figure 5.6a of Richardson, 2013) [223], [256], [259], [261], [298], [302]–[315]. Here, these data was categorized based on the synthesis method employed (i.e., co-precipitation and hydrothermal reaction). Since Richardson did not specify any selection criteria or data filtering, data points collected here are those corresponding to all samples where the Mg-Al-LDH phase was identified in their PXRD patterns. The fitting of the data to the crystal chemical model developed in the present work (dashed line) and the one developed by Richardson (solid line) are also presented in Figure 5.4. It is worth mentioning that Richardson's model is a result of linearly regressing all these data, thus it is not a surprise it seemingly a better fit to these data points than the present work model.
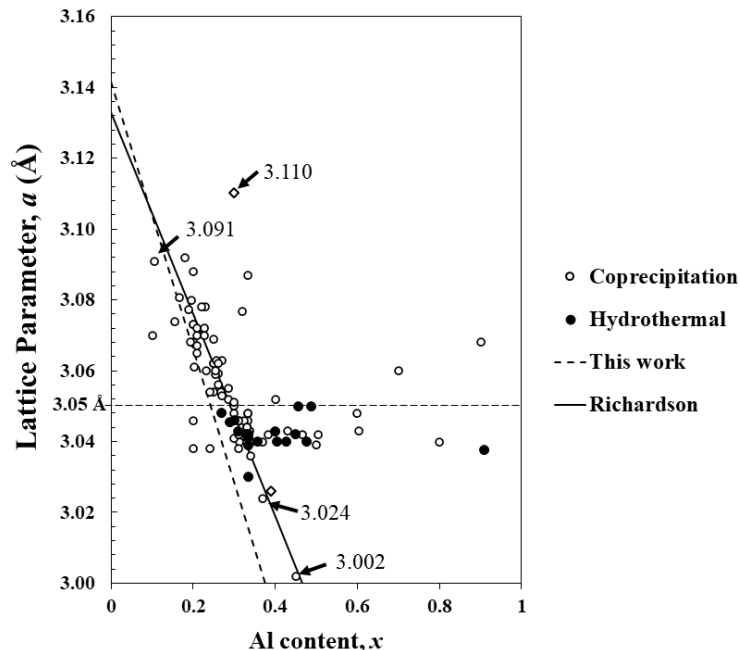
Figure 5.4 - Plot of lattice parameter *a* vs *x* of LDHs phases reported in the literature cited in Richardson's work; Open circles are the LDHs synthesized by co-precipitation method and the closed circles are the LDHs synthesized by hydrothermal method

Additionally, data points which have not been taken account in Richardson's model were restored, e.g., those high *a* values close to 3.110 Å, which were not considered previously due to its extreme deviation from the rest of data. PXRD analyses of these samples reported from the original studies did show the presence of LDH phase [259], [261], [316]. Hence, we believe these values are important and may provide insights into the largest *a* value possible for LDHs (i.e., minimum Al^{3+} substitution). On the other hand, the low *a*-parameter obtained at 3.002 Å included in Richardson's work is most likely an erroneous value [298]. The LDH sample (Sample D; Kukkadapu *et al.*, 1997) was synthesized at pH 6.5, which is below the precipitating pH (~7.5) of Mg-based LDHs [206], [281] and resulted in poorly crystallized LDH peaks as well as bayerite impurity phase observed in PXRD analysis. The author concludes this low value of *a* (3.002 Å) corresponds to an Al-rich LDH (*x* = 0.45), but we suspect it might be a result of wrong indexing of *d*(110) peak for LDH phase. Nevertheless, the other sample synthesized by the same author is still interesting. For example, the sample synthesized with pH 7.5 (Sample C; Kukudapu *et al.*,

1997) shows *a* value of 3.024 Å and the PXRD pattern did show the characteristics of a single phase LDH. We believe this data point is important and is likely one of the lowest *a* values reported for Mg-Al-LDHs. Another study which has reported a similar value for Al-rich LDH is Tsuji *et. al* (3.026 Å), said to have synthesized a highly substituted single phase LDH with *x* equals to 0.43 [317].

As seen in Figure 5.4, a huge range of values for the *a* parameter has been reported in literature, between 3.020 and 3.110 Å (3.002 Å was not considered). A linear trend between *a*-parameter vs *x* can be established between the *x* range 0.1 – 0.4, which agrees well with the Vegard's law. For *x* values higher than 0.4, the *a* parameter seems remains constant at approximately 3.04 Å. This suggests that no further substitution of Al^{3+} into the LDH structure has occurred, despite the larger Al content in the precursor mix or bulk phase of LDH synthesized. This confirms the existence of an upper limit for the Al^{3+} substitution in the LDH phase. There is also a clear trend in the *a* values based on the synthesis method employed. For example, *a* values of LDHs synthesized by the hydrothermal method are between 3.03 - 3.05 Å, compared to *a*-values of LDHs synthesized by the co-precipitation method which show a wider range (3.02 – 3.11 Å). This observation is in good agreements with our previous study which investigated the impact of synthesis method on the lattice parameter *a* of synthetic LDHs.

5.3.3 Re-defining the x limits for Mg-Al-LDHs
Figure 5.5 shows the *x* calculated from all the *a*-parameter data points presented in Figure 5.4, using the Richardson model and present work model. As described earlier, the *x* of LDH is only valid for a very limited range of concentrations. As discussed in many studies, *x* equals to 0.33 is widely acknowledged as the composition corresponds to the maximum substitution of Al^{3+} into the LDH structure - since each Al^{3+} is already surrounded by six $Mg(OH)_6$-octahedra [219], [279], [289]. Further substitution will caused $Al(OH)_6$-octahedra to be directly adjacent to each other and will start forming a secondary Al-hydroxide phase. Hence, *x* beyond 0.33 is not valid for pure LDH phases. From Figure 5.5, a few *x* calculated from Richardson's model clearly exceeded 0.33, especially those data points having *a* value less than 3.04 Å. Whereas all the *x* calculated using our model are well within the valid *x* range (*x* < 0.33). As an example, when taking the lowest value of *a*

(3.024 Å) previously reported in Figure 5.4, the x calculated from the Richardson's model is 0.38 whereas the x from present work model is 0.31.
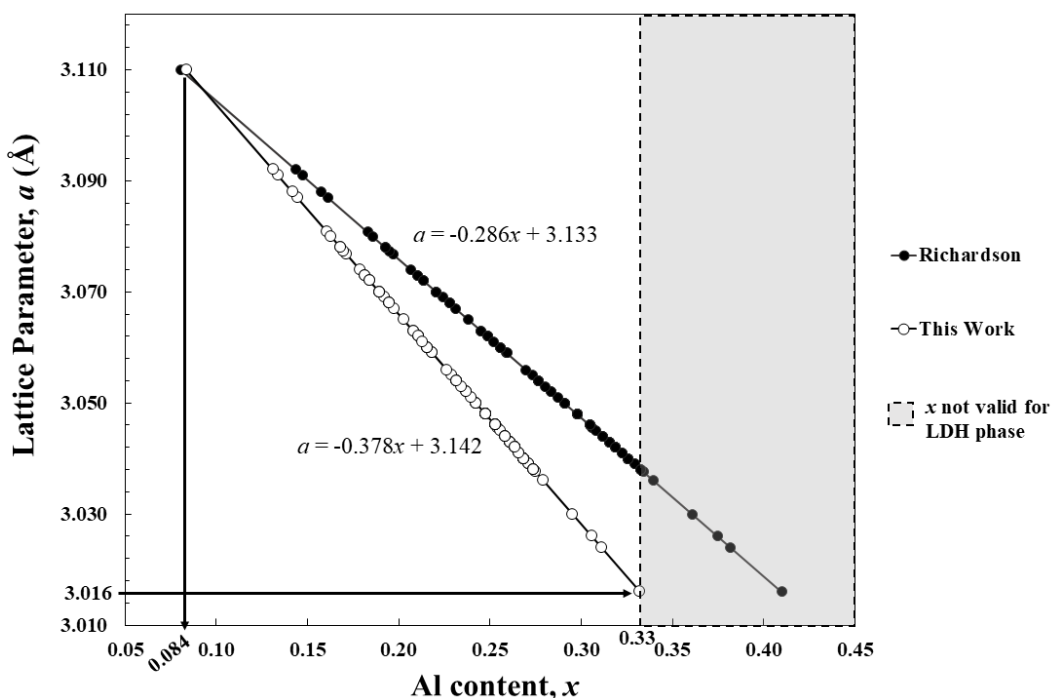
Figure 5.5 - Calculated x from the data points presented in Figure 5.4 and from the crystal chemical models compared in present work; Richardson model (Filled point) and present work model (Empty points)

Nevertheless, the a value that corresponds to the maximum Al^{3+} substitution ($x = 0.33$) is still not found yet. According to the prediction made by our model in Table 5.3, the a value corresponds to this composition would be 3.017 Å. Interestingly, we did discover a study which reported a synthetic LDH phase having a value almost identical to this value, i.e., 3.016 Å [318]. However, the work is not widely cited, including in Richardson's work. The author provided XRD analysis of the sample (Sample O, Mao *et al.*, 1993), confirmed it being a single phase LDHs. Using our model, the x for this LDH phase is 0.33 whereas Richardson's model gives 0.41.

As briefly described earlier, the lowest limit for the x composition remains unclear. Previous attempts to identify this lowest x value for LDH phases were mainly based on experimental observations, but wide different values were reported. For example, Gastuche

et al. (1967) found the lowest x s to form pure phase LDHs is 0.17, Miyata (1971) concluded it being 0.1 whereas Brindley & Kikkawa (1979) suggested that the lowest substitution is around $0.15 - 0.20$, with evidence of $Mg(OH)_2$ impurities phase in the LDHs synthesized below this x. Such observations were also observed in more recent experimental works [259], [319], [320]. All these studies demonstrated the challenge to experimentally determine the lowest value of x for LDH phases, especially in those conditions ($x < 0.15$) where the Mg^{2+} concentration became sufficiently high enough to form Mg-based impurities phase, e.g., $Mg(OH)_2$ and hydromagnesite.

Richardson (2013) suggested the lowest value of x to be at 0.151, based on his crystal chemical model and the largest a value (3.091 Å) considered in his analysis [279]. However, if the previously reported largest a value (i.e., 3.110 Å; Gastuche *et al.,* 1967) is considered instead, then the lowest x obtained from Richardson model would be 0.080. For the same a value of 3.110 Å, an x value of 0.084 is obtained from our model. Interestingly, this is the point where the two crystal chemical models overlap each other, despite the huge deviation at high x values (Figure 5.5). As a matter of fact, this value of x (0.084) corresponds to one of the possible ordered distributions of trivalent cations for LDH phases, i.e., to a M^{2+}/M^{3+} ratio of 11 [220]. For x below 0.083, theory estimates that the bonding between the LDH layer and interlayer will become too weak to keep the LDH structure stable [321]. It will be thermodynamically more stable to exist as $Mg(OH)_2$ phase rather than LDHs phase. Kim *et al.* (2014) attempted to synthesize LDHs with high Mg/Al ratios by varying the Mg/Al molar ratio (3 - 30) in the precursors. From the given PXRD patterns (Figure 1, Kim *et al.,* 2014), the LDHs having Mg/Al ratio between 3 to 9 clearly show a single phase LDHs whereas impure $Mg(OH)_2$ phases started to form when the Mg/Al ratio increased to 12 and beyond [319].

Based on the above arguments, we postulate that the minimum possible x for LDH phase is 0.083 and it corresponds probably to an uncommon case among synthetic LDHs, where such ordered distributions at extreme low x are observed. Most lab synthesized LDH samples are finely dispersed powder, so such a long-range cation order is unlikely to be present. We argue that the occurrence of such a rare sample, synthesized by Gastuche *et al.* (1967), was likely due to the meticulous treatment employed during the preparation stage,

i.e., a synthesis protocol was followed that allowed for enough time for crystallization and an ordered crystal distribution with low Al content to be precipitated [316]. Nevertheless, we noticed that the synthesis method (co-precipitation method) and the metal salt precursors (metal chlorides) may have played a role in producing such low x composition for LDHs. The LDH having the second largest a-values (3.092 Å) reported by Miyata (1980) also employed a similar method and salt precursors [261]. This matches well with the conclusion of our previous study, where the metal chlorides were found a more effective precursor to synthesize LDHs with the desired composition.

So far, the present work model has been proven to fit well all the LDH a-parameters previously published in literature, and it also provides values of x that agree with the new possible x range defined for LDH phases (0.083 – 0.33).

5.3.4 Thermodynamic preference to form LDHs with x = 0.25 and x = 0.33

It is well-known that amid the cation avoidance rule, the cation ordering in the LDH structure having x of 0.25 or 0.33 is energetically favored due to the trivalent cations are arranged in such a way that they are completely shielded from each other and impart least lattice strain [219]. This explains the ubiquity of these two compositions found in natural LDHs, i.e., Hydrotalcite ($x = 0.25$) and Quintinite ($x = 0.33$). Thermodynamically speaking, the lower the formation energy, the more stable the LDH phase. Thus, a minimum value in the heat of formation should be observed at either $x = 0.25$ or $x = 0.33$. Trave *et al.* (2002) performed first principles molecular dynamics on Mg-Al LDH phase, and they found that the formation energy as a function of composition x shows a minimum at 0.25 [322]. Allada *et al.* (2005) attempted to measure the heat of formation of synthetic LDHs of varied composition but did not observe any minimum value at either $x = 0.25$ or 0.33, which led the authors to conclude that the formation heat of LDHs varies very little with composition [323]. However, LDHs examined in that study were from different sources and were characterized based on bulk Mg/Al ratio. We then argue that, for such observation, the LDHs employed in that work had very similar composition or were compared with the wrong chemical composition. This shows the necessity to confirm the true composition of synthesized LDHs, in order to obtain meaningful conclusions from those studies.

Table 5. 4 - Structural refinement data of synthetic Mg-Al-LDHs in literature

Synthesis method/sources	x^*	Angle, α (°)	d(M-O) (Å)	a (Å)	x obtained from crystal chemical models		Reference
					Richardson	This work	
Synthetic, co-precipitation method	0.33	98.34	2.013	3.046	0.30	0.25	[312]
Synthetic, co-precipitation method	0.20	98.11	2.040	3.082	0.18	0.16	
Synthetic, urea hydrolysis method	0.33	98.45	2.011	3.045	0.31	0.25	[250]
Synthetic, urea hydrolysis method	0.33	99.64	1.991	3.042	0.32	0.26	[255]

*The chemical composition x of LDHs reported by literature.

As an attempt to provide an explanation for the thermodynamic preference to synthesize LDHs of certain composition, we apply the Richardson's crystal chemical model and the present work model on synthetic LDHs for which that detailed structural investigation has been provided. Table 5.4 shows all the structural refinement data that have been reported so far on synthetic Mg-Al-LDHs as well as the synthesis method employed.

As shown in Table 5.4, there is very limited information about the crystal structure of synthetic LDHs in literature. The obtained structural refinements were mainly from LDHs prepared from co-precipitation and hydrothermal urea hydrolysis methods. Interestingly, none of the studies have investigated the LDHs having the composition $x = 0.25$, despite being regarded as one of two energetically most favorable stoichiometries for Mg-Al-LDHs. Nevertheless, all three studies attempted to investigate LDHs with a composition x equal to 0.33 and they all arrived at similar structural information, i.e., close value of a, bond angles and d(M-O) lengths. It is important to point out that in these studies, the chemical composition x for these samples (denoted x^*, with an asterisk) is based on the nominal composition, which is likely not the actual x for these LDHs. This is supported by the findings of our previous work, which demonstrated the non-stoichiometric nature of urea hydrolysis and co-precipitation reactions to synthesize LDHs close to this composition ($x = 0.33$). As an example, the PXRD pattern that was reported by Radha *et al.* (2007) showed

additional reflection peaks other than LDH phase. In fact, this limitation to identify the actual composition of synthesized LDHs have been acknowledged by Belloto *et al.* (1996) and Radha *et al.* (2007) as they fixed the site occupancies of the refinement result according to the nominal composition. This suggests there might be a discrepancy between the refinement parameters and composition *x*.

Table 5.4 also presents the *x* calculated by the crystal chemical models developed by Richardson and the present work. The *x* obtained from Richardson's model is very close to the nominal composition, which is somewhat anticipated as the model was obtained based on data reported by nominal composition. A remarkable observation is that the *x* obtained from our model shows an unexpected value of 0.25 for all the LDHs reported as Al-rich (0.33). Even more, these LDHs have the same composition (*x* = 0.25) as the naturally occurring mineral Hydrotalcite, $Mg_6Al_2(OH)_{16}[CO_3] \cdot 4H_2O$ [221]. Although LDH with *a* value close to 3.04 Å is commonly associated to composition of maximum Al^{3+} substitution [147], [324], but according to our data analysis, there are indeed a number of pure phase LDHs with lower values of *a* (e.g., < 3.02 Å). Considering that the 3.04 Å value is very close to the median value of *a* range revealed for Mg-Al-LDH phase (3.02 – 3.11 Å), the inference drawn from our model is highly plausible. This finding might explain why LDHs synthesized by the urea hydrolysis method tend to show close values of *a* (3.03 - 3.04 Å), given the fact that the synthetic condition in hydrothermal method is actually very similar to the condition where the natural LDHs forms, e.g., high temperature (~ 100 ˚C - 1000 ˚C) and elevated pressure.

Based on our results, the minimum formation energy value for synthetic LDH phase likely occurs at *x* = 0.25, due to the abundant of the specific compositions found in LDHs synthesis studies. In contrast, the composition *x* = 0.33 seems rarely formed under synthetic conditions. Despite having claimed by many authors, most of the synthetic Al-rich LDH phase reported so far do not show an *a* value small enough for a maximum Al^{3+} substitution (*x* = 0.33). In fact, Zhitova *et al.* (2018) have clarified that Quintinite, the mineral form of Mg-Al-LDHs with *x* = 0.33, is a last-stage hydrothermal mineral, which usually goes through a series of (high and low) temperature events during the crystallization process [325]. This is probably the reason why that composition is less likely observed in synthetic

LDHs, which are usually synthesized in a stable environment. On the other hand, a number of extreme a values discovered for LDH phase were from non-carbonate intercalating LDHs, e.g., ferrocyanide ($[Fe(CN)_6]^{4-}$), terephthalate dianions $[C_6H_4(COO)_2]^{2-}$ and nitrilotriacetate (NTA). This suggests the type of interlayer anions might affect the chemical composition of LDH phase under lab synthesis conditions.

As a result of the abovementioned observations, it seems clear that our crystal chemical model successfully establishes a reliable relationship between the lattice parameter a and chemical composition x, which holds true throughout the entire x range for LDHs. However, validation of our proposed crystal-chemical model is likely a challenging task. Synthetic LDHs, especially the ones synthesized from co-precipitation method, are usually obtained as microcrystalline powder and are heterogeneous in nature, therefore resulting on a broadened *(110)* reflection in PXRD analyses [326]. Previous solid-state nuclear magnetic resonance (NMR) experiments have confirmed the presence of several Mg and Al environments in a single Mg-Al-LDH sample and quantifiable amount of detects in the cation distribution [224], [225], [231], [327]. It is foreseeable that computational stimulations of these complex atomic structure, i.e., Rietveld refinement and DFT calculations, are very demanding to arrive at satisfactory conclusions. The calculations are further complicated by the other structural aspects of LDHs, such as structural disorders[326], stacking faults[231], [328], interlayer species arrangement[288], [329], effect of hydration[330]–[332], extent of polytypism[333], [334], extent of cation ordering[335]–[337], etc, which all of these are still under debate in the literature. Nevertheless, the findings of the present work which are based on a wide range of Mg-Al-LDHs data, provide further insights on the structural-composition relationship of LDH phases, and hopefully lead to a new trend of LDH nature discussion, by highlight the importance and need of proper crystal chemical investigation coupled with analytical chemistry.

5.4 Conclusions

A new crystal chemical model was developed for Mg-Al based LDHs, to determine the true chemical composition (i.e., Mg^{2+}/Al^{3+} ratio or x) from the unit cell parameter a of the crystalline phase. The model is a further improvement to the existing ones by employing a top-down theoretical approach, and it is built on crystal chemically sound arguments, e.g., Vegard's law and geometrical-structural investigations into the LDH phase. The advantage of such approach is the use of more reliable input parameters from the two pure constituents (e.g., Brucite, $Mg(OH)_2$ and Gibbsite, $Al(OH)_3$) and it can account for the different local geometry due to two cation sites in LDHs, e.g., bond length d(M-O) and flattened angle, α. This contrasts with previous crystal chemical models, which were developed based on empirical observations and regression analysis on literature data; however, the accuracy of these models relies heavily upon the quality of data and are critically impacted by various variables, e.g., synthesis method and characterization technique for composition x.

The implementation of the new crystal chemical model reported here gives new insights into the chemical composition for LDHs phase. For the first time, the solid solution limits for the Al^{3+} substitution in the Mg-Al-LDH phase are clearly justified (x = 0.083 - 0.33). In addition, the new model also revealed the actual composition x of some Al-rich LDHs, which is in fact much lower than the previously reported one (x = 0.33). This work shows the importance of the crystal chemical approach as a reliable method to identify the true chemical composition of LDH phases, which is a step forward towards the understanding of structural-composition-property of LDHs materials. It also offers an alternative standpoint to address the current challenges and limitations to develop LDH-related materials with better physical properties.

Chapter 6: Intermediate temperature CO_2 capture process using LDH-based MMOs sorbents

Overview

This work is a collaborative work between the Laboratory of Separation and Reaction Engineering (LSRE), Associate Laboratory LSRE-LCM from the University of Porto, Portugal, and Research Centre for Carbon Solutions (RCCS) from Heriot-Watt University, UK. Experiments and data acquisition was completed in the laboratories of LSRE, within a three-month internship period. The work is co-supervised by Associate Professors, Alexandre F.P. Ferreira and Ana M. Ribeiro and Emeritus Professor, Alirio E. Rodrigues from the LSRE group. Author Contributions statement: LC, GM, SG and AFPF: conceptualization and design of the study. LC: experiments, acquisition and interpretation of data, visualization, and writing of the first draft of the manuscript. LC, AFPF, AMR and SG: analysis of data. SG: writing—review and editing for important intellectual content. SG, MM-V and AER: supervision, project administration, and funding acquisition.

6.1 Introduction

Since the first publication of LDH-derived MMOs as CO_2 sorbent in 1996, detailed investigations of the sorbent material has been done by various research groups [69], [109], [172], [268], [338]. LDH-derived MMOs sorbent is well-suited for the capture of CO_2 under elevated temperature (200 – 500 ˚C) and high-pressure conditions (up to 45 bar), which are suitable for processes such as SEWGS and SE-SMR. Pilot-scale tests using this class of material has proven their good CO_2 capture characteristics, including stable cycling and mechanical stability (up to 1000 hours at 400 ˚C and 30 bar), high selectivity for CO_2, can withstand moisture and are tolerant to sulphur content (H_2S) [76], [77], [176], [339]. However, despite the numerous efforts to improve this material, the working capacity of LDH-derived MMOs seems to be restricted to around 0.3 – 0.8 mol/kg, which is relatively low for CO_2 capture applications (compared to benchmark material, Zeolite 13X at 1.2 mol/kg). Although the current CO_2 sorption performance of LDH-derived MMOs is considered satisfactory for SEWGS process [112], [340], a few studies have indicated that the working capacity of MMOs sorbent needs to reach above 1.35 mol/kg to make the SEWGS substantially cheaper than the more conventional carbon capture technology [69], [74], [190], [191].

However, in order to design MMOs with better sorption capacities, there are still several mysteries that need to be solved, particularly regarding the role of Mg-O in the CO_2 uptake of MMOs. Despite extensive *in-situ* studies of CO_2 sorption mechanism and chemistry aspects, many hypotheses still revolve around the CO_2 adsorbing species of MMOs. Previously, the MgO species was widely agreed to be the CO_2 adsorbing species of LDH-derived MMOs sorbent. If this is the case, assuming each Mg^{2+} is a basic site for CO_2 adsorption, MMOs derived from a Mg/Al ratio of 3 should have a theoretical CO_2 uptake of 16.27 mmol/g. However, using in-situ PXRD measurement, Walspurger *et al.* (2008) demonstrated that the dawsonite phase, $KAlCO_3(OH)_2$, a product formed after the reaction between the K^+ ions from K_2CO_3, aluminium oxides and the water in the feed stream, was actually dominating the adsorption of CO_2 in the K-promoted MMOs sorbents [173]–[175]. If this is the case, then the need for the Mg-O species of MMOs in CO_2 adsorption is questionable. Nevertheless, the same research group also found that Mg content in K-promoted LDH-derived MMOs is necessary for achieving a high conversion rate of CO to CO_2 in the SEWGS rection (> 98 %) [148]. A more recent publication by Zhu *et al.* (2019) found that there was a synergistic effect between K_2CO_3 and the Mg/Al ratio of LDH-derived MMOs [109]. In K-promoted LDHs with high Mg/Al ratios, the predominant CO_2 capture was from the bulk K_2CO_3, and the crystal structures of MgO were well preserved. In LDHs with lower Mg/Al ratios, the partial substitution of Mg^{2+} with Al^{3+} created more unsaturated oxygen on the surface, which reacted with K^+ from K_2CO_3 to form K-O-Mg adsorption sites with higher basicity. Interestingly, the study also observed a positive correlation between Mg content and CO_2 adsorption capacity in K_2CO_3 promoted LDH-derived MMOs sorbent, compared to the unpromoted ones.

With all the hypotheses revolving around the Mg content in the CO_2 adsorption of LDHs-derived sorbents, there is a need to revisit this aspect. However, as demonstrated in previous chapters, most of the LDH phases reported in the literature were poorly characterized, and the Mg/Al ratio reported may not reflect the true composition of the sorbent material. Additionally, the sorbent used in CO_2 adsorption studies is usually purchased from a commercial vendor, which may have used binder material during the pelletization process, and thus the measured CO_2 adsorption capacities does not necessary reflect the adsorption from the LDH phase. Moreover, the LDH-derived MMOs sorbent

171

that has been studied are those promoted with potassium carbonates. Based on this context and from a material development point of view, there is a clear need to re-evaluate the CO_2 adsorption properties of MMOs derived from unpromoted and well-characterized LDH to design better CO_2 sorbents.

To address this gap, this work aims to re-investigate the CO_2 adsorption behaviour of Mg-Al LDH-derived MMOs at an intermediate temperature range (200 – 400 ˚C). First, a full characterization of precursor LDH is carried out with various techniques such as Powder X-ray Diffraction (PXRD), Fourier Transform Infrared Ray (FTIR), and Elemental Analysis. The LDH precursor material is a commercial product that is available in kilogram scale and pelletized using a tablet press, thus is free from any binder material. The crystal-chemistry model developed in Chapter 5 is used to obtain the true chemical composition "x" of LDH crystals. The resultant MMOs sorbent's adsorption characteristics are then measured, including pure component equilibrium isotherms (CO_2 and N_2) using a gravimetric method (Magnetic Suspension Balance) and intraparticle diffusion using the Zero Length Column (ZLC) method. With the information obtained, it is possible to gain better insight into the true sorption behaviour of LDH-derived MMOs, enabling the design of sorbents with better characteristics for CO_2 capture applications.

6.2 Experimental Details

6.2.1 Sorbent Preparation

The sorbent used, Hydrotalcite with the chemical formula $Mg_{0.75}Al_{0.25}(OH)_2(CO_3)\cdot H_2O$, was obtained from Sigma Aldrich in the powder form (pack size: 1 kg; bulk density: 2000 kg/m^3) and pelletized into cylindrical-shape pellets (2 mm diameter, 2-2.35 mm length) using a tablet press, without any binder material (Figure 6.1). MMOs were prepared by calcinating the LDH pellets at 400 ˚C for 4 hours, in a stainless steel fixed-bed reactor under a simulated air flow (21 % O_2, purity 99.95 % and 79 % N_2, purity 99.995 %; Gas flow rate = 50 Ncm^3/min; Air Liquide). After calcined, the MMOs sorbents were colded down to room temperature (25 ˚C) and left overnight under a continuous flow of simulated air flow (50 mL/min) before storage in a vacuum environment.

Figure 6.1 - Image of obtained 2mm diameter LDH-based MMOs pellets

6.2.2 Characterization

Pristine LDH samples were characterized using Powder X-ray Diffraction (PXRD), Fourier Transform Infrared (FT-IR) and Elemental analysis (ICP-OES), to determine their true chemical composition. PXRD patterns were obtained using a Bruker D8 Advance powder diffractometer, using Cu-K$_\alpha$ radiation ($\lambda = 1.5406$ Å), and data were collected over an angular range of 5–85 °2θ (one-hour span; step size = 0.009 °2θ per second). FTIR spectra were measured using a Perkin Elmer frontier IR single-range spectrometer under Attenuated Total Reflectance (ATR) mode, in the range of 4000 to 600 cm^{-1} with 4 cm^{-1} resolution. ICP-OES was used to analyse the elemental composition of the LDH samples, carried out using an atomic emission spectrum (Perkin Elmer Optima 5300DV) and after dissolving 30 mg of them in concentrated sulphuric acid and diluting with 25 ml of deionized water. The true chemical composition, x (equivalent to Al/(Mg+Al)), was calculated using a crystal-chemical model developed for Mg-Al LDHs [Eq. 6.1], which uses the unit cell parameter a. The lattice parameter a ($a = 2 \times d_{001}$) was determined from the position of the *(110)* reflection by PXRD pattern.

$$\text{Lattice parameter, } a_{LDH} = 3.142 - 0.378x$$

[Eq. 6.1]

Mercury porosimetry and nitrogen adsorption at 77 K were performed to study the textural properties of calcined MMOs sorbents. The Mercury Intrusion Porosimetry method was used to analyze the pore structures of the sorbents using a Pore Size Analyzer (Micrometritics AutoPore IV 9500, USA), over a range of pressure (0.0007 – 227.5 MPa), after activation at 300 ˚C for 4 hours under an inert environment (continuous flow of N_2). The surface area of the MMOs pellets was determined by N_2 adsorption isotherms at 77 K, performed with an Accelerated Surface Area and Porosimetry System (Micrometrics ASAP 2420, USA), after activation at 300 ˚C for 4 hours under an inert environment (continuous flow of N_2). The density and apparent volume of adsorbent pellets were obtained with Helium Pycnometer.

6.2.3 Pure Gas Adsorption Isotherms by Gravimetric method

The pure component adsorption isotherms were measured with a gravimetric Magnetic Suspension Balance (MSB) in a static (i.e., batch) mode. The MSB system was chosen for its ability to obtain highly precise adsorption isotherm measurements under the conditions relevant to industrial CO_2 capture and CCUS-enabled hydrogen production, such as intermediate temperature (200 – 400 ˚C) and elevated pressure (atmospheric to 30 bar).

One of the advantages of the MSB system is that the microbalance, the most sensitive part of the system and measuring cells are physically separated, which allows for measurement of weights under extreme conditions. This eliminates the disadvantage of conventional gravimetric systems. The MSB system enables measurement in the pressure range up to 700 bar, and a maximum temperature of 400 ˚C is possible [341]. Thanks to its contactless feature, the MSB system can measure adsorption isotherms of a variety of fluids, including those aggressive, toxic, supercritical, and flammable gases [341]. The MSB system is also used to measure adsorption kinetics as it avoids the inevitable shock caused by the introduction of adsorbate that is commonly observed in TGA systems. Thus, MSB resolves many of the sample mass measuring issues encountered with a common gravimetric system.

Figure 6.2 shows the schematic diagram of the experimental set-up with the MSB system used in this work. The MSB system used is a commercially available instrument developed by Rubotherm (Germany), with high weighing precision of 0.01 mg. It is connected to a three-port valve to control gas flow, pressure transducers to measure the pressure within the

adsorption cell, a calibrated thermocouple for temperature monitoring, and a vacuum pump to depressurize the system before activating the sample.
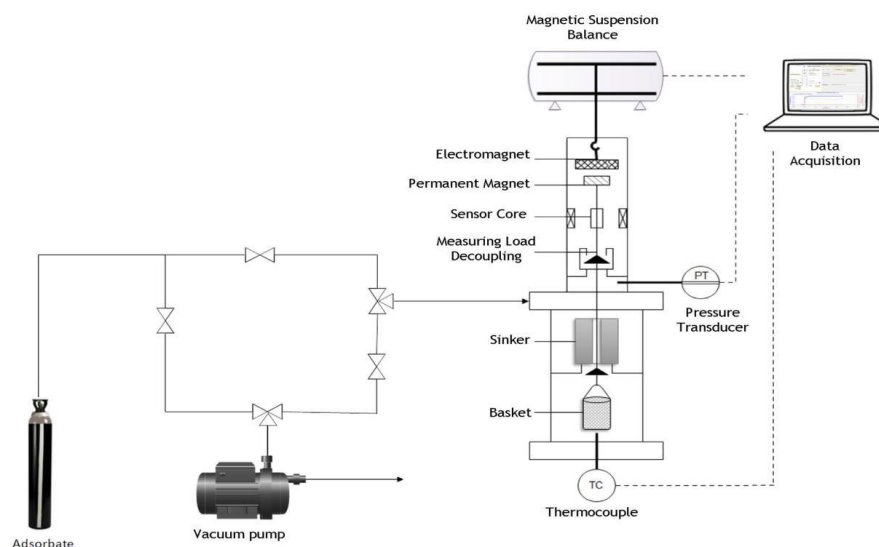
Figure 6.2 - The schematic diagram of the apparatus used for the measurement adsorption isotherm with magnetic suspension balance [304]

The adsorption equilibrium isotherms of CO_2 were measured at three different temperatures (200, 300 and 400 ˚C) and up to 30 bar partial pressure. New batches of pre-calcined MMOs pellets were used for each adsorption isotherms measurement. Before the measurement, the MMOs pellets were activated at 400 ˚C for 1 hour, in a vacuum environment and left overnight to desorb any air or moisture pre-adsorbed due to exposure to atmospheric air during the loading of samples into the MSB system.

Due to the slow kinetics of CO_2 in the LDH-derived MMOs sorbents, the equilibration time after each pressure change can take up to three to four days to complete. Thus, only five points (0.4, 1, 4, 8 and 30 bar) have been recorded for each adsorption isotherms. In our experiments, equilibrium is considered reached when there is no longer any change in the sample mass, i.e., when the weight of the sample remains constant for 5 - 6 hours.

For the measurement of N_2 adsorption isotherms, only up to 8 bar partial pressure was recorded at three different temperatures (200, 300 and 400 ˚C) and the same batch of sorbent were used for all three adsorption isotherms measurement.

To calculate the absolute adsorption from the measured data obtained from the gravimetric method, a buoyancy correction is required. Here, we present a summary of the steps followed to obtain absolute adsorption of measured data by buoyancy corrections. The full derivation that allows the offset of buoyancy effects on CO_2 adsorption equilibrium isotherm can be found in Appendix A6.2.

The absolute adsorbed amount is the variable of interest in the modelling of adsorption units. The general equation to calculate the absolute adsorbed concentration from the experimental data is:

$$q = \frac{\Delta m + \rho_G (V_s + V_i)}{m_s M_w} \frac{\rho_{ads}}{\rho_{ads} - \rho_G}$$

[Eq. 6.2]

Where Δm is the weight difference between measurements, ρ_s is the density of the gas phase under the measuring conditions (T, P), V_s is the volume of the solid adsorbent, V_i is the volume of the measuring cell, sample basket, and glass wool used to hold the sample, m_s is the adsorbent mass measured before the experiments, M_w is the molecular weight of the adsorbate and ρ_{ads} is the density of the adsorbed phase. Both volumes, V_s and $V_{i,}$ are determined by a helium pycnometer.

For a pressure range below 6 bar, the density of the adsorbed phase, ρ_{ads} can be assumed to be the liquid density of CO_2, i.e., $\rho_{ads} \approx \rho_l$. Details of this assumption are included in Appendix A6.3.

For the pressure range above 6 bar, compression caused the density of CO_2 in the adsorbed phase to deviate from the liquid density. Thus, the actual value of ρ_{ads} needs to be determined independently to obtain the absolute adsorbed amount.

In this work, the adsorbed phase density, ρ_{ads}, was determined using the reduced mass Ω method for high-pressure adsorption isotherm measurement described by Dreisbach *et al.* (2002) [342], [343]. The reduced mass, Ω, refers to the experimental reading directly obtained from the MSB. The surface excess mass, m^σ can be obtained by correcting the

reduced mass by the bulk density of the gas phase, ρ_{bulk} and specific adsorbent volume V_{As}^{He}, calculated from the helium measurement, using the equation expressed below:

$$m^\sigma = \Omega + \rho_{bulk}V_{As}^{He}$$

[Eq. 6.3]

The absolute adsorbed amount, m_{ads}, is the quantity of interest. Once the surface excess mass quantity is obtained, the values are used to determine the absolute amount adsorbed, m_{ads} and the relationship between them can be described by the expression:

$$m_{ads} = m^\delta + \rho_{bulk}V_{ads}$$

[Eq. 6.4]

Where m^σ represents the surface excess mass, ρ_{bulk} is the density of the gas phase and V_{ads} is the volume of the adsorbed phase. Although the volume of adsorbed phase is unknown, it can be obtained from the expression, $V_{ads} = m_{ads}/\rho_{ads}$. Thus, Eq. 6.4 can be written as follows:

$$m^\delta = m_{ads}(1 - \frac{\rho_{ads}}{\rho_{bulk}})$$

[Eq. 6.5]

where the m_{ads} refer to the amount of adsorbed buoyancy corrected with the Helium-volume method and ρ_{ads} assume to be the liquid density of CO_2. Then, by substituting the adsorbed mass with $m_{ads} = V_{ads}\rho_{ads}$, the equation can be rearranged in the following way:

$$m^\sigma = (\rho_{ads} - \rho_{bulk}V_{ads}).$$

[Eq. 6.6]

If a straight line can be obtained in the linear zone of surface excess isotherms, then the y-intercept of the line would represent the actual ρ_{ads} at high pressures.

6.2.4 Zero Length Column Apparatus

The Zero Length Column (ZLC) technique was originally introduced by Eic and Ruthven in 1988 as a macroscopic means of measuring the intercrystallite diffusivities in microporous sorbents [344]. Fundamentally, the ZLC is an adsorption column but has

almost zero length. This main feature allows it to eliminate the axial dispersion effect of conventional fixed-bed columns, enabling the direct derivation of diffusion coefficient parameters for gas molecules in the sorbent phase. The small size of the ZLC also allows for experiments to be run with a very small amounts of sorbent material, typically less than 50 mg. Currently, the ZLC column technique has been applied to measure diffusivity parameters in bi-porous sorbents, liquid phase adsorption systems, nonlinear systems, systems with heat effects and water adsorption isotherms [345]–[349].

In the present work, ZLC experiments have been performed to obtain the diffusion coefficients of CO_2 in LDH-derived sorbents. The ZLC experiments were carried out with a 1 vol% CO_2-He mixture for different flow rates (20, 30 and 40 cm^3/min) and three different temperatures (200, 300 and 400 ˚C). The adsorbate concentration was selected to allow the adsorption equilibrium to be described by using Henry's law.
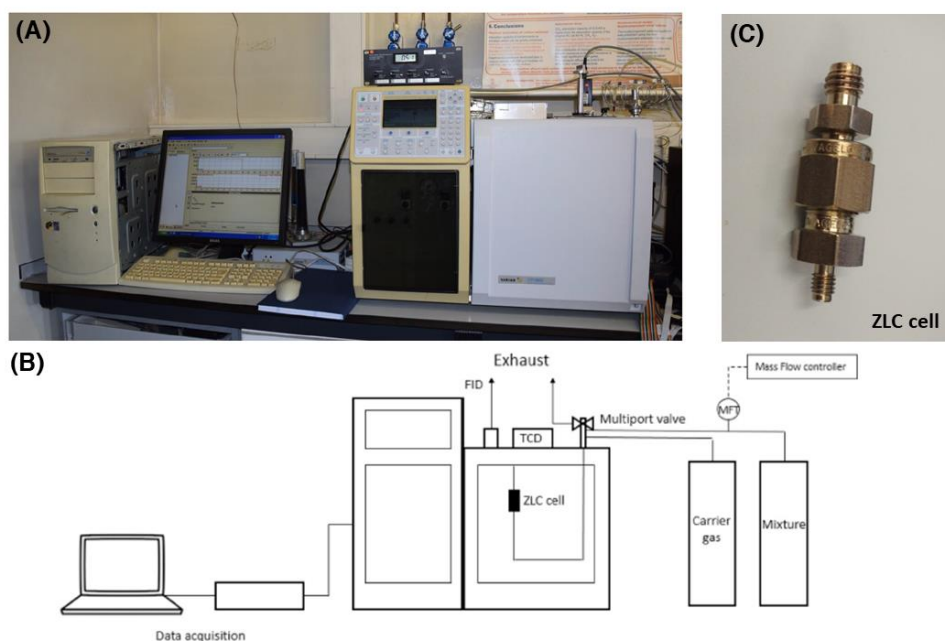
Figure 6.3 - The experimental set-up, (B) schematic diagram and (C) ZLC cell for the measurement of adsorption diffusion coefficient by Zero Length Column [350], [351]

Figure 6.3 illustrates the experimental setup for ZLC experiments used in this work. The ZLC column (Figure 6.3C) is located within a modified gas Chromatograph (Varian, Holland). The inlet stream of the ZLC cell was connected to a multiport valve to switch the

178

inlet stream from the adsorbate mixture (helium + CO_2) for saturation to the purge gas (pure helium) for desorption. The outlet stream was connected to a thermal conductivity detector (TCD), which measured the gas concentration.

For our experiments, approximately 10 pellets of LDH adsorbents (approximately 50 - 60 mg) were loaded into the ZLC cell. Prior to the ZLC experiments, LDH adsorbents were calcined at 400 °C for 4 hours under a continuous flow of simulated air for activation (21 % O_2, purity 99.95 % and 79 % N_2, purity 99.995 %; Gas flow rate = 50 Ncm^3/min; Air Liquide). Once the activation step was completed, the system temperature was cool down to the testing temperature. The LDH-based MMOs were pre-saturated with a gas mixture at a very low concentration and under the kinetic-controlled regime. Then, at time zero, an inert carrier gas was purged through the ZLC cell, and the desorption curve was measured as a function of time. The measurement of the desorption curve was stopped as soon as a plateau was reached.

All the ZLC experiments were performed using the same batch of sorbents, except for the small pellets experiments used to determine the diffusional controlling mechanism in the LDH-derived MMOs sorbent. Table 6.1 summarizes the characteristics of the ZLC cell and adsorbent pellets studied in this work.

Table 6. 1 - Characteristics of ZLC cell with LDH-derived MMOs full pellets (original size) and small pellets

		Full pellets	**Small pellets**
CO_2 partial pressure	bar	0.01	0.01
Mass of adsorbent	kg	0.064×10^{-3}	0.068×10^{-3}
Cell Diameter	M	4.29×10^{-3}	4.29×10^{-3}
Cell Height	M	9.73×10^{-3}	14.25×10^{-3}
Cell Volume	m^3	1.41×10^{-7}	2.06×10^{-7}
Cell porosity	%	47.5	49.0
Pellet Diameter	M	2.00×10^{-3}	1.12×10^{-3}
Average Pellets Length	M	2.35×10^{-3}	2.44×10^{-3}
Apparent Pellets Volume	m^3	7.39×10^{-8}	10.51×10^{-8}

The mathematical model used for the analysis of ZLC systems is obtained from the overall mass balance for a column and based on the following assumptions:

1. The adsorbent pellet has a bidiperse porous structure containing macropores and crystals (micropores)
2. Fick's law for diffusion is valid for macropore and crystals diffusion
3. Macropore and micropore diffusion mechanisms are in series
4. Adsorption in macropores in negligible
5. Adsorption equilibrium in crystals is described by a linear isotherm (operates in Henry's region)
6. The ZLC cell is equivalent to a continuous stirred tank adsorber

Taking all the assumptions into account, the analytical solution for the outlet concentration of ZLC can be described through Equation 6.7, which is commonly referred to as the complete ZLC model. The full derivation of ZLC model is available in various articles [347], [352], [353].

ZLC complete model:

$$\frac{c}{c_0} = 2L \sum_{n=1}^{\infty} \frac{e^{-\beta_n^2 \frac{D_{ap}}{l^2} t}}{\beta_n^2 + L(L+1-n)}$$

[Eq. 6.7]

Where n is equal to 0, 1 or 2 for slab, infinite cylinder, and spherical dimensions, c is the outlet concentration of the ZLC, c_0 is the concentration at the time, $t = 0$, D_{ap} is the apparent diffusivity, l is the representative spatial dimension of the pellet, and L is the ZLC model parameter. β_1 are the roots of transcendental equation. Since the LDH-derived MMOs pellets can be approximated as a sphere (*2mm x 2mm*), the equation has the following form, and β_1 can be calculated as follow:

$$\frac{c}{c_0} = 2L \sum_{n=1}^{\infty} \frac{e^{-\beta_n^2 \frac{D_{ap}}{l^2} t}}{\beta_n^2 + L(L-1)}$$

[Eq. 6.8]

Sphere:
$$\beta_j \cot(\beta_j) + L - 1 = 0$$

[Eq. 6.9]

J_0 and J_1 are Bessel functions of the first kind of order zero and one respectively.

The ZLC model parameter L has a general formula of:

$$L = \frac{1}{(n+1)} \frac{F}{K^* V_s} \frac{l^2}{D_{ap}}$$

[Eq. 6.10]

Where F is the purge flow rate, V_s is the volume of adsorbent in the cell and K^* is the dimensionless adsorption equilibrium constants related to Henry's law constant. K^* can be obtained using the following equations: $K^* = \varepsilon_p + (1 - \varepsilon_p)K_{eq}$, where ε_p is the porosity of the pellet and $K_{eq} = \rho_s HR_g T$, where ρ_s is the solid density and H is the Henry constant.

However, the problem with using Equation 6.7 or 6.8 to determine the diffusivity coefficient values of the sorbent is that the initial part of the desorption curve may be affected by the washing of the cell and dead volume effects, which can obsecure the actual diffusivity values. Therefore, the determination of diffusivity coefficients is usually obtained from the long-time asymptote of the ZLC desorption curves, which contains information about the adsorption kinetics. This method is known as the Long-Time response (LTR) method. The LTR mathematical model is derived from the first term of the series represented by the complete ZLC model, by approximating the tail of the desorption curves as a straight line. The LTR model is described as follow:

Long-time Response (LTR) model for spherical particle:

$$\ln\left(\frac{c}{c_0}\right) = \ln\left(\frac{2L}{\beta_1^2 + L(L-1)}\right) - \beta_1^2 \frac{D_{ap}}{l^2} t$$

[Eq. 6.11]

To obtain accurate results from the LTR analysis, the ideal range of L should be between 10 and 50 [347], [352]. Nevertheless, using all the information from the experiment provides a more reliable analysis, such as incorporating more terms (β roots) to model Eq.

181

6.8. Therefore, both the ZLC complete model and the LTR model were applied in this study to obtain the diffusivity coefficient of LDH-derived MMOs sorbent.

Determination the diffusion limiting step in LDH-based MMO can be achieved by using smaller pellets. LDH-based MMOs sorbent was broken in half to reduce the effective time constant ratio and the dimensions are shown in Figure 6.5. Both LTR and ZLC complete model analysis was employed to obtain the diffusivity coefficient values of the small pellets, but with the equation for slab geometry:

ZLC complete model for slab geometry:

$$\frac{c}{c_0} = 2L \sum_{n=1}^{\infty} \frac{e^{-\beta_n^2 \frac{D_{ap}}{l^2} t}}{\beta_n^2 + L(L+1)}$$

[Eq. 6.12]

Long-time Response (LTR) model for slab geometry:

$$\ln\left(\frac{c}{c_0}\right) = \ln\left(\frac{2L}{\beta_1^2 + L(L+1)}\right) - \beta_1^2 \frac{D_{ap}}{l^2} t$$

[Eq. 6.13]

The equation of β_1 for slab geometry:

$$\beta_1 \tan(\beta_1) - L = 0$$

[Eq. 6.14]

The ZLC model parameter L for slab geometry:

$$L = \frac{F}{K^* V_s} \frac{l^2}{D_{ap}}$$

[Eq. 6.15]

Figure 6.4 - Image of obtained 2mm diameter LDH-based MMOs pellets broken into half for the determination of diffusional controlling mechanism

6.3 Results and Discussions

6.3.1 Adsorbent Characterization

Figure 6.5 shows the PXRD diffractogram and FTIR spectra of pristine LDH precursor and the calcined MMOs sorbent used in the present study. Figure 6.6A confirms that the commercial LDH product obtained from Sigma Aldrich is indeed an $Mg-Al-CO_3$ LDHs phase, with no obvious secondary crystalline phase being observed. All the detected diffraction signals are matching with the characteristic peaks of $Mg-Al-CO_3$ LDH. For example, the strong reflections at a low angle ($2\theta = 11.7$ °) that yield a *d* spacing value of 7.56 Å, correspond to the basal spacings (d_{003}) of a carbonate intercalating Mg-AL LDHs that are normal to the *(00l)* plane, and its sub-peak is seen at higher reflection around 23.4 °2θ (d_{006} = 3.80 Å). The reflections of the *(01l)* plane at intermediate angles, e.g., *(012)*, *(015)* and *(018),* correspond to the stacking arrangement of LDH layers. The "saw tooth" peaks at a high angle (near 60 °2θ) give the position of *(110)*, allowing the lattice parameter *a* to be determined using the equation *a = 2d(110).* The evidence of the as-purchased LDH sample being a carbonate-intercalating LDH phase is further confirmed by the FTIR spectra (Figure 6.6B), with the broad vibration at 3400 cm^{-1} is attributed due to hydrogen-bonded hydroxyl ion, the sharp signal at 1360 cm^{-1} due to the carbonate vibrations, and a strong vibration at 767 cm^{-1} due to metal-oxygen bonds.
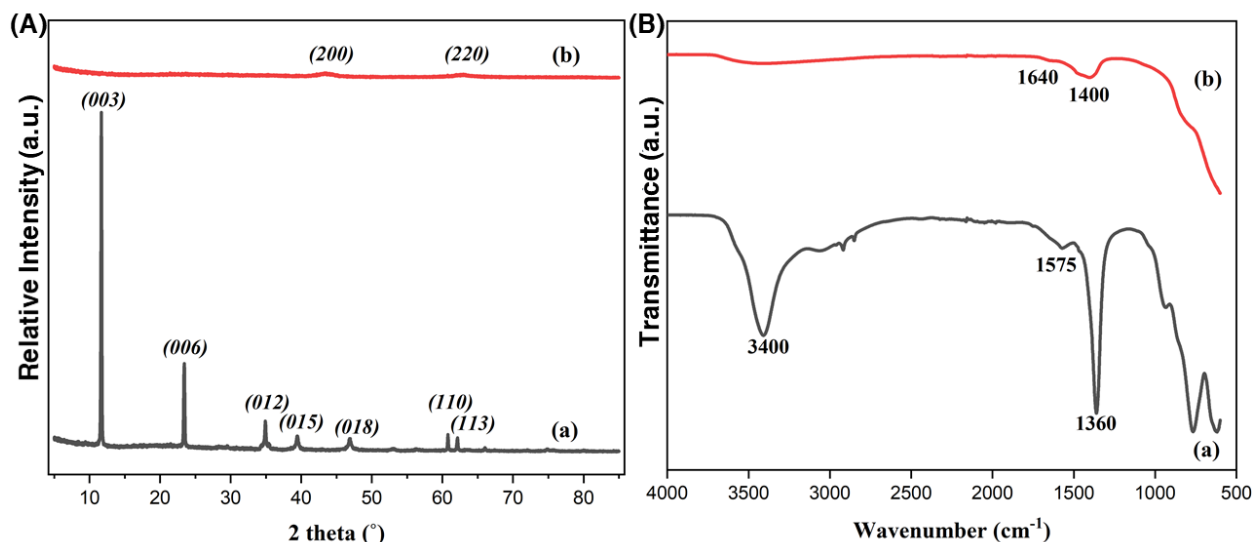
Figure 6.5 - (A) PXRD patterns and (B) FTIR spectra of LDH and the derived MMOs

Upon calcination at 400 °C for 4 hours under a simulated air condition, the characteristics peaks of LDHs became visibly disappeared in the PXRD diffractogram, and new diffractions at positions of *(200)* and *(220)* are observed (Figure 6.6A). These reflections correspond to the characteristic peaks of Mg-O species, which indicate the collapse of LDH-layered structures and formed mixed metal oxide phases. A similar observation is seen in the FTIR spectra of MMOs as well, where the characteristic vibration due to LDH has disappeared, and new vibrations at 1400 cm^{-1} and 1640 cm^{-1} correspond to the absorption of atmospheric CO_2 and water molecules during the handling step. Thus far, the PXRD patterns and FTIR spectra of commercial LDHs obtained from Sigma Aldrich and the derived MMOs sorbent agree well with the lab-synthesized samples presented in previous chapters.

The importance of combining *a*-parameter and analytical chemistry in the determination of true chemical composition for LDH phases has been thoroughly discussed in previous chapters. Using the *a*-parameter obtained (3.046 Å) and the crystal chemistry model previously developed [Eq. 6.1], the *x* of LDH precursors employed, which essentially is the Mg/Al ratio in the crystalline phase, is estimated to be 0.25. Elemental analysis (ICP-OES) was carried out to measure the bulk chemical composition of the LDH precursor. The result reveals that the apparent *x* of LDHs in the bulk phase is 0.30. This discrepancy between the

184

crystal and bulk *x* (i.e., Mg/Al ratios) suggests the presence of a secondary phase in the LDH precursor, most likely being an amorphous Al-based impurities phase as it was not detected by PXRD. The ICP-OES also reveals the presence of a small amount of sodium in the LDH samples (0.4 wt %).

Table 6. 2 - Chemical and Physical properties of commercial LDH-derived MMO sorbent after activated at 400 ˚C for 4 hours.

Properties	Unit	
Dimension		
Sorbent Material		$Mg_{0.75}Al_{0.25}(OH)_2(CO_3)\cdot H_2O$
Pellet Shape		Cylinder
Pellet Diameter	10^3 m	2
Pellet Length	10^3 m	2 - 2.35
Chemical Composition		
Al content, *x* (crystalline phase)		0.25
Al content, *x* (bulk phase)		0.30
Sodium content, Na	wt %	0.4
Physical Properties		
Total Intrusion Volume	m^3/kg	1.26×10^{-4}
Surface Area (Mercury intrusion)	m^2/kg	1.71×10^4
Surface Area (N_2 Physisorption 77 K)	m^2/kg	1.39×10^5
Average Pore Diameter	Nm	29.5
Apparent Solid Density (ρ_{ap} = M/V)	kg/m^3	868.99
Solid Density (Mercury Intrusion)	kg/m^3	2116.6
Skeleton Density (Helium Pycnometer)	kg/m^3	2768.3
Pellet Porosity, ε_p		0.31

Physical properties of MMOs sorbents, such as pore distribution, density and surface area, were characterized by mercury intrusion, helium pycnometer and nitrogen adsorption isotherms at 77 K. A summary of the main measured properties is presented in Table 6.2. The apparent density of the pellets was obtained from the equation ρ_{ap} = mass/pellet volume, where the pellet volume was directly measured from the pellet dimensions. The solid density was calculated using the equation $\rho_{s,Hg}$ = *mass/(pellet volume − (macro +*

meso + micro) pore volume), with the pore volume determined from Mercury Intrusion. The skeleton solid density was determined using a helium pycnometer. The pellet porosity, ε_p was obtained by dividing the apparent solid density, ρ_{ap}, by the skeleton solid density.

Figure 6.6A displayes the N_2 adsorption isotherm at 77K of the calcined MMOs sorbent. The isotherm depicted here is a typical IUPAC Type (II) isotherm, characterized by an identifiable knee at low relative partial pressure (*P/P₀* < 0.05 kPa) and without a final saturation plateau at a high *P/P₀* value. This observation is consistent with the results obtained from the powder MMOs sorbents prepared using the co-precipitation method, as presented in Chapter 4 (Figure 4.8). No significant modification of the pore structure resulting from the pelletizing process is observed, except for a smaller hysteresis, indicating less capillary condensation due to network effects. The pore structure of the LDH-derived MMOs sorbent in the macropore range is examined using the Mercury Intrusion method. Figure 6.6B confirms the high macroporosity of the LDH-derived MMOs, and Figure 6.6C shows that the predominance pore width of the macropore is 29.5 nm. By IUPAC classification, LDH-derived MMOs sorbents is a mesoporous sorbent, with pore width in the range between 2 – 50 nm.
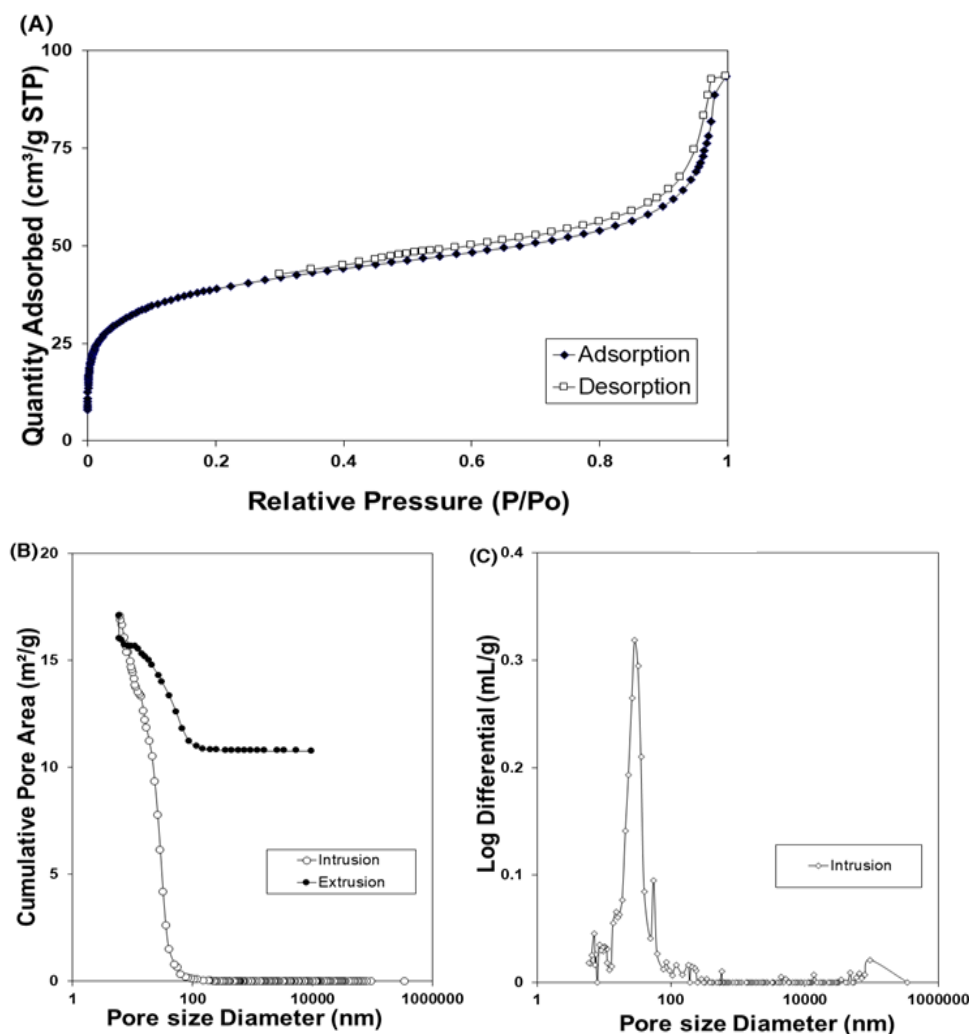
**Figure 6.6 - (A) N₂ adsorption isotherm at 77 K, (B) Cumulative Pore area and (C)
Log differential by Mercury Intrusion method**

6.3.2 CO₂ adsorption Isotherms at High Temperatures (200, 300 and 400 ˚C)

The high-pressure CO_2 sorption isotherms of the prepared LDH-derived MMOs sorbents were measured using a gravimetric method at three different temperatures (200, 300 and 400 ˚C) and under dry condition. As a standard procedure, all the equilibrium points were corrected for buoyancy using the Helium-volume method (Eq. 6.3) to obtain the absolute adsorption capacity of LDH-derived MMOs sorbent. As previously mentioned, the absolute adsorption capacity is necessary for modelling an adsorption unit. Figure 6.7A compares the CO_2 adsorption isotherms obtained before and after the Helium correction. It should be noted that the adsorption of CO_2 on LDH-derived MMOs sorbent at 400 ˚C and 30 bar was

incomplete due to the set point temperature (400 ˚C) not being achieved throughout the experiment. This is likely due to strong convection that occurred between wall of the measuring vessel and room temperature under the testing conditions (Figure 6.7B).
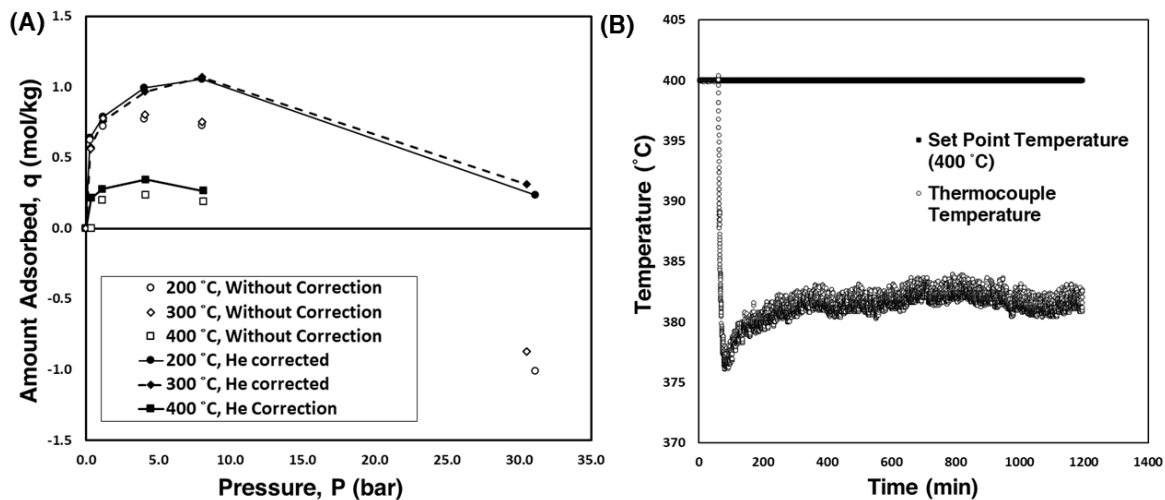
Figure 6.7 - CO₂ adsorption isotherms of LDH-derived MMOs sorbents (A) exp. data with only He correction and (B) absolute adsorption after correction

In Figure 6.7A, despite after corrected for buoyancy with the Helium-volume method, all the CO_2 equilibrium isotherms still show a clear downward trend at high pressure range, and none of them reaches a saturation capacity, suggesting that the buoyancy effect has not been fully compensated. The likely culprit is the value of adsorbed phase density used in the calculations. To perform buoyancy correction using the helium-volume method (Eq. 6.3), the adsorbed phase density is assumed to be the same as the liquid density of CO_2. Normally, the liquid density is calculated using Dubinin's assumptions (see Appendix A6.3), where the increase in liquid density over the range of temperatures from the boiling point to the critical temperature is assumed to be linear. However, in this work, such assumptions were used to correct equilibrium isotherms, but it was found that the liquid density calculated using this method is not accurate enough. This is likely because the adsorbed phase is more compressed than the liquid phase at high pressure, which causes the increase in molar volume due to pressure to be non-linear.

Using the reduced mass method described in section 6.5.1, the surface excess adsorption isotherm for CO_2 adsorption at 200 and 300 ˚C was obtained (Figure 6.8). As the linear

188

region of the last point of adsorption isotherms measured at 400 °C and 30 bar was not completed, the density of adsorbed phase could not be determined. However, by plotting a straight line at the linear region of the surface excess isotherms, the adsorbed phase density can be obtained from the value of the y-intercepts.
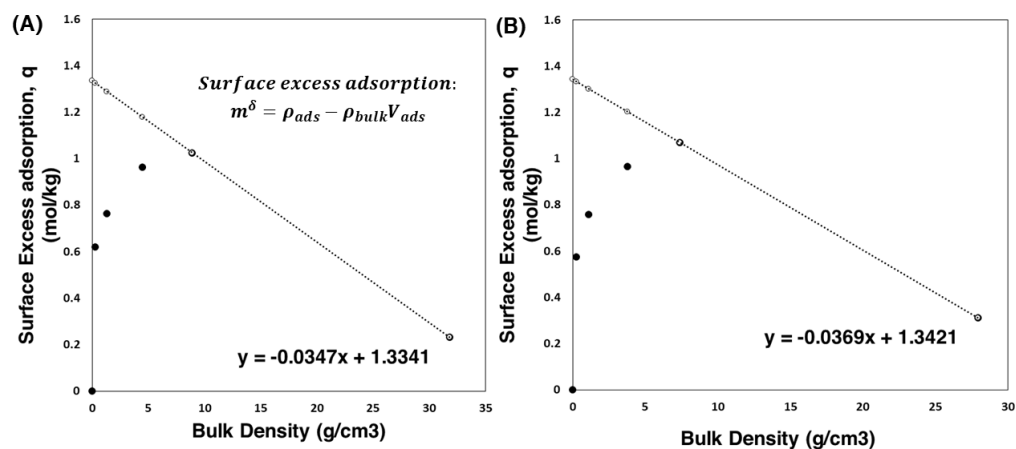
Figure 6.8 - Surface excess isotherms of CO₂ on LDH-based MMOs at (A) 200 °C and (B) 300 °C
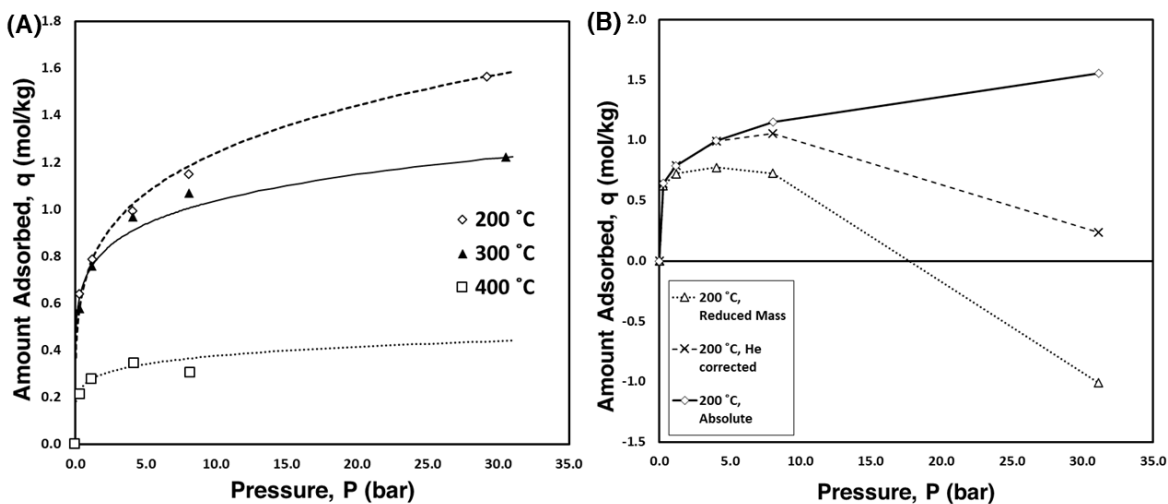
Figure 6.9 - (A) Absolute adsorption equilibrium isotherms of CO₂ of LDH-based MMOs at 200, 300 and 400 °C; experimental data (points) and Freundlich fittings (lines) and (B) comparison between the reduced mass, He-corrected sorption capacities and absolute sorption capacity

The adsorbed phase density, ρ_{ads} at 30 bar, identified from the surface excess isotherms measured at 200 and 300 °C, were found to be very close to each other (between 1.33 and 1.34 g/cm^3). Although this value is slightly higher than the liquid density of CO_2 at its triple point (1.18 g/cm^3, T_P = 216.6 K), it is still lies well within the liquid density regime in its phase diagram, suggesting the good agreement between the ρ_{ads} measured from MSB and thermodynamics properties of CO_2 at high-pressure region [354]. By substituting these ρ_{ads} values into Eq 6.3, we derived the CO_2 absolute adsorption isotherms of LDH-derived MMOs (Figure 6.9).

The absolute equilibrium isotherms of CO_2 in the LDH-derived MMOs at three different temperatures (200, 300 and 400 °C) and the complete pressure range measured (0 – 30 bar) are shown in Figure 6.10A. Figure 6.10B compares the adsorption isotherms of CO_2 on LDH-derived MMOs at 200 °C, before and after the correction. The Freundlich isotherm equation (solid line) was found to fit the isotherms the best. This observation is consistent with previous findings on AMS-promoted MMOs sorbents (e.g., K_2CO_3, cesium-, sodium-, etc) [193], [153]. The Freundlich equation is expressed as:

$$Amount\ adsorbed, q = KP^{\frac{1}{n}}$$

Where q is the amount of the adsorbed species, P is the partial pressure of sorbate species in the unit of bar, K and n are the Freundlich equilibrium constants and are generally temperature dependent.

The parameters K and n were obtained by plotting $\log_{10}$ q versus $\log_{10}$ P and determining the slope and y-intercept of the straight line. These values are tabulated in Table 6.3.

Although the DSL equation would be a better choice to use for modelling adsorption units, as it is thermodynamically sound and can be used to predict mixed gas adsorption equilibria with the Ideal Adsorbed Solution Theory (IAST); while Freundlich equation is just an empirical model. However, in the present work, the DSL equation is not suitable to use for the fitting of CO_2 adsorption isotherms measured due to the significant lower sorption capacities measured at 400 °C.

Table 6. 3 - Freundlich fitting parameters and the confidence limits (R^2) obtained after fitting the experimental CO_2 adsorption equilibrium data of LDH-based MMOs at 200, 300 and 400 ˚C.

Temperature (˚C)	200	300	400
K	0.75	0.74	0.27
n	4.61	6.80	7.07
R^2	0.9880	0.9772	0.9958

As a matter of fact, the low CO_2 sorption capacities observed at 400 ˚C deserve some comments. In the present study, a clear descending temperature-dependence trend of CO_2 adsorption isotherm in LDH-derived MMOs sorbent, up to a very high-pressure range (30 bar), was observed. This piece of information is valuable, as the adsorption isotherm of this class of material is known to be dispersed and often contradicting. For instance, in a study conducted by Oliveira et al. (2008), a maximum was seen in the CO_2 adsorption isotherms measured at 403 ˚C, showing a remarkably higher equilibrium capacities than the other two temperatures measured (306 and 510 ˚C) [154]. A later study conducted by the research same group also found very similar observations [159]. A separate study from Moreno et al. (2014) seems to echo this finding, but they found that the adsorption isotherms measured at 300 ˚C give the highest equilibrium capacities than any other temperature measured [197]. In other studies conducted by Allam et al. (2005) and Zhu et al. (2017), a descending temperature-dependence trend was observed [111], [186]. These inconsistent observations make it difficult to understand the true adsorption properties of the sorbent, which are required to design better MMOs sorbents. However, note that most of these studies obtained the CO_2 adsorption isotherms through breakthrough experiments and operate under wet feed conditions, which may lead to uncertainties (± 10 % error) due to the difficulties in maintaining the desired operating condition and the contribution of dead volume. On the other hand, in a fixed bed operation, the adsorption of CO_2 in LDH-derived MMOs usually does not allow enough time to reach the equilibrium state, as it needed for this class of material (i.e., up to 3 days). Note also that the sorbents employed in these

studies were all K_2CO_3-promoted MMOs, hence the preparation method may have contributed to these inconsistencies.

As our aim is to investigate the true adsorption capacities of LDH-derived MMOs, an environment that can unambiguously measure the equilibrium capacities is required. The magnetic suspension balance system is a good fit for this purpose, as it allows a stable CO_2 uptake environment (i.e., batch) and high weighting precision up to 0.01 mg. The main obstacle is to obtain accurate absolute capacities at the high-pressure range with suitable means of buoyancy correction, but this has been addressed in this work by using the reduced mass method proposed by Dreisbach et al. (2002). In our opinion, the values of absolute capacities obtained in the high-pressure region are fair. Interestingly, the absolute adsorption isotherm recorded in the present work also observed that up to 4 bar, the points of the CO_2 adsorption isotherms measured at 200 ˚C and 300 ˚C overlapped each other and show very similar equilibrium capacities. The distinction in sorption isotherm only became significant at the high-pressure range, above 8 bar. This might explain the observation of Oliverira's et al. (2008). As the temperature increases, the adsorption isotherm became increasingly equilibrium limited, i.e., no increase in sorption capacities despite the increase in pressure. This is most notable at 400 ˚C, where the plateau begins at a very low partial pressure point (~ 0.4 bar). All the sorption equilibrium points are consistent at around 0.20 – 0.27 mol/kg, making the adsorption isotherm at 400 ˚C almost a rectangular isotherm. The problem with this type of isotherm is that the desorption of CO_2 is more difficult using PSA method (i.e., requires more stringent vacuum condition) and the actual working capacity may be low, if incomplete desorption occurs.

Nevertheless, much of the literature on LDH-derived MMOs sorbent reports high sorption capacities at 400 ˚C, particularly those promoted with alkali metal salts (AMS), such as K_2CO_3, KNO_3, etc. On the contrary, the MMOs sorbent prepared from pristine LDHs employed in this work shows the highest sorption capacities at a much lower temperature (200 ˚C). This suggests perhaps there may be a synergy effect between AMS and LDH-derived MMOs sorbents, which allows the sorption capacities of LDH-derived MMOs to improve remarkably at higher temperature range (~ 400 ˚C). This corroborates several thermodynamic assessments conducted to investigate the impact of AMS promoter on the

high-pressure CO_2 adsorption properties of MgO sorbent, which found the MgO promoted with AMS shows a notable increase in the equilibrium temperature at a given pressure compared to pure MgO species [188], [355]. This provides an exciting opportunity for LDH-derived MMOs, as it means the possibility to tune the adsorption operating temperature window with the promotion by AMS.

At 200 ˚C and 30 bar, a high sorption capacity reaching 1.56 mol/kg was recorded in this work, which is perhaps the highest sorption capacities recorded for pristine MMOs sorbent. There is no plateau observed yet, suggesting that the sorption capacities can improve further at higher pressure (> 30 bar). However, despite already being exposed to a very high partial pressure of CO_2 (30 bar), these values are still far from the theoretical sorption capacities postulated for MMOs derived from LDH with an Mg/Al ratio of 3 (16.3 mol/kg). Even though there is a small possibility that LDH-derived MMOs might achieve this theoretical sorption capacity, it would be likely impossible to realize under practical industrial conditions. The adsorption equilibrium capacities measured at a lower pressure range (< 8 bar) are more relevant to most of the flue gas conditions under industrial processes. At 1 bar partial pressure of CO_2, where most of the adsorption capacities in literature were measured, the equilibrium capacity measured from this work gives 0.79 mol/kg, which is almost the same as the adsorption capacities measured in Chapter 4 using a TGA and within 30 mins and 2 hours, i.e., CPNI3 0.81 mol/kg. This means that almost all the adsorption occurs within the first 30 mins of adsorption. The rest of the uptake is due to the slow carbonization reaction of MgO species. This observation matches with the one published by Zhu et al. (2017), who found that most of the adsorption and desorption (under vacuum) occur within the first 30 mins[188].

Currently, the highest sorption equilibrium capacity for this class of sorbent material under conditions relevant to the present study was found close to 3.3 mol/kg (300 ˚C & 30 bar, dry CO_2), as measured from a K-promoted MMOs [197]. In the same study, a further increase in CO_2 sorption capacities due to pressure was also recorded, e.g., 4.73 mol/kg at 42 bar. In a breakthrough study, Allam et al. (2005) found the sorption capacities of K_2CO_3 promoted LDH-based sorbents were 2.8 mol/kg at $P_{co2} = 28$ bar and T = 400 ˚C [110]. Another high sorption capacity close to 2.0 mol/kg was found from an LDH-based MMOs

sorbent promoted with gallium and potassium, but under a significantly lower partial pressure of CO_2 (P_{co2} = 1.1 bar) and 300 ˚C [153]. Thus, it seems the addition of AMS into LDH-based MMOs not only increases the adsorption temperature but also improves the sorption capacities of the sorbent. Table 6.4 presents a comparison of the CO_2 equilibrium capacities from various LDH-based sorbents measured at the conditions of interest identified for the present work (industrial CO_2 capture and CCUS-enabled hydrogen production).

Based on Table 6.4, under the process condition relevant to industrial CO_2 capture, i.e., blast furnace gas, P_{co2} ~ 0.4 bar, the sorption capacities of MMOs sorbent prepared in the present work are comparable to those measured from potassium-promoted sorbents. However, under the process stream relevant to hydrogen production, i.e., water gas shift reactor outlet and integrated coal gasification combined cycle (IGCC) feed, P_{co2} ~ 8 bar and T > 400 ˚C, the potassium-promoted LDH-based MMOs are superior in terms of sorption capacities. Nevertheless, the assessment of CO_2 adsorption performance does not only rely on the equilibrium capacities, and sorption kinetics also play a key role. The ZLC method was employed to obtain the diffusion coefficient of CO_2 in LDH-derived MMOs sorbents.

Table 6. 4 - Adsorption equilibrium capacities of LDH-derived MMOs sorbents relevant to industrial CO_2 capture and CCUS-enabled hydrogen production

Author	Sorbent material	Testing Method	Condition (°C)	Adsorption equilibrium capacity (mol/kg)		
				0.4 bar	8 bar	28 bar
Present work	Pristine LDH-derived MMOs sorbent	Gravimetric	200 (dry)	0.62	1.18	1.56
			300 (dry)	0.65	1.00	1.21
			400 (dry)	0.24	0.36	-
Ding & Alpay (2000, 2001) [150], [151]	K-promoted hydrotalcite	Breakthrough	208 (wet)	~0.82	-	-
			302 (wet)	~0.70	-	-
			400 (wet)	~0.58	-	-
			480 (wet)	~0.51	-	-
			400 (dry)	~0.55	-	-
			480 (dry)	~0.45	-	-
Allam *et al.* (1996) [110]	K_2CO_3-promoted hydrotalcite	Breakthrough	400 (wet)	~0.2 – 0.3	~1.8	~2.9
Lee *et al.* (2007) [192]	K_2CO_3-promoted hydrotalcite (Air products Ltd.)	Breakthrough	400 (dry)	~0.35	-	-
			520 (dry)	~0.26	-	-
Oliveira *et al.* (2008) [154]	20 wt% K_2CO_3 - promoted PURAL MG30, MG50, MG70 (Sasol)	Breakthrough	306 (wet)	~0.4	-	-
			403 (wet)	~0.4	-	-
			510 (wet)	~0.36	-	-
Halabi *et al.* (2012) [193]	22 wt% K_2CO_3-promoted PURAL MG61 (Sasol)	Breakthrough	400 (dry)	~0.49	-	-
			400 (wet)	~0.66	-	-
Chanburanasiri *et al.* (2013) [158]	K_2CO_3 – promoted PURAL MG31w (Sasol)	Breakthrough	360 (wet)	~0.2 – 0.3	~0.8	-
			416 (wet)	~0.2 – 0.3	~0.7	-
			467 (wet)	~0.4	~0.64	-
Wu *et al.* (2013) [159]	KNO_3 – promoted PURAL MG30 (Sasol)	Breakthrough	335 (dry)	~0.77	-	-
			383 (dry)	~0.99	-	-
			438 (dry)	~1.03	-	-

Ramírez-Moreno & Pfeiffer [197]	K₂CO₃ promoted LDH-derived MMOs	Volumetric method	300 (dry)	~0.11	~0.8	~3.3
Boon *et al.* (2014) [44], [185]	20 wt% K₂CO₃ – promoted Hydrotalcite (Sasol)	Breakthrough	400 (dry)	~0.2 – 0.3	~1.1	~1.4
Zhu *et al.* (2019) [188]	K-MG30 (Sasol)	Breakthrough (Desorption capacities)	300 (dry)	N/A	~0.18	N/A
			350 (dry)	N/A	~0.35	N/A
			400 (dry)	N/A	~0.45	N/A
			450 (dry)	N/A	~0.6	N/A

6.3.3 Diffusion coefficients of CO_2 in LDH-based MMOs by ZLC method

The measurement of diffusion coefficient values for CO_2 in the unpromoted LDH-derived MMOs was carried out using the ZLC method over a range of temperatures (200, 300 and 400 ˚C) and flow rates, while maintaining the same CO_2 partial pressure of 0.01 bar. To identify whether the LDH-derived MMOs sorbent is macropore or micropore (crystal) diffusion limited, the ZLC experiment was replicated with smaller LDH-derived MMOs pellets.

To establish an equilibrium state within the ZLC column, all experiments were equilibrated for 1 hour before desorption occured. The desorption curve was recorded to obtain the diffusion coefficient values of CO_2 in LDH-derived MMOs. This was accomplished in two steps: 1) obtaining an initial estimate of the parameters from the complete ZLC model described in Eq. 6.8 and 2) improve the accuracy of parameters by fitting them to the long-time asymptote (Long time analysis, LTR method) using Eq. 6.11. Figure 6.10 shows examples of the desorption curves analysed using the LTR method and the complete ZLC model method.
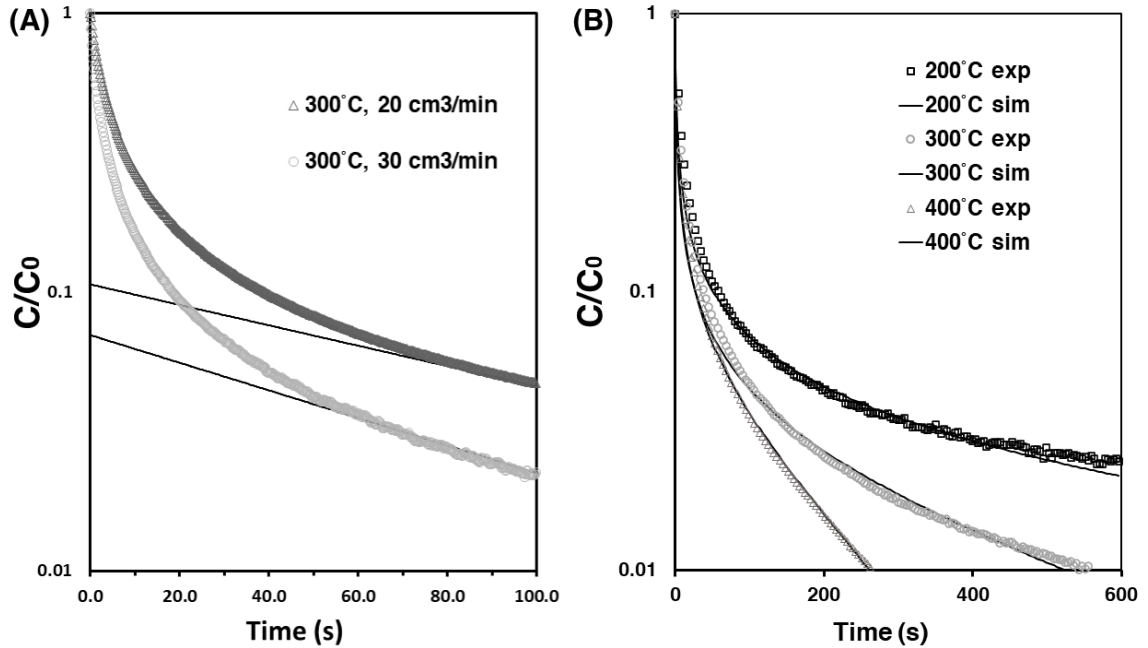
Figure 6.10 - Example of ZLC desorption curves fitted with (A) Long time analysis (LTR) and (B) simulations of complete model analysis

Technically, obtaining one desorption curve from the ZLC experiment is sufficient to obtain the diffusion coefficient parameter of the sorbent at the operation condition. However, it is safer to conduct a few more experiments with different flowrates to check whether the ZLC system is indeed operating in the kinetically controlled regime (or Henry's regime) and to check for consistency in ZLC response curves. This can be done with a simple graphical check, by plotting the *Ft* curve, i.e., the plot of desorption curves *versus* the product of flowrates and time [356]. If the ZLC system operates in the equilibrium-controlled regime, the desorption curves at different flow rates will coincide. As flow rates increases, desorption curves should respond with a steeper initial signal and then a less steep signal towards the end. Thus, the desorption curves may cross once as the flow rate increases but should never coincide either at the initial signal or near the end of the signal. The *Ft* plot of desorption curves at different temperatures and flow rates is included in Appendix A6.4. The desorption curves measured at 200 ˚C demonstrate that all experiments were conducted within the kinetic controlled regime. However, the desorption curves were measured at 300 and 400 ˚C, with the flow rate of 40 cm^3/min, showing overlap of signals, indicating that the system is within the equilibrium-controlled region.

For this reason, these desorption curves were not analysed further using the LTR and complete model analysis.

Table 6.5 presents all the diffusion coefficients of CO_2 in LDH-derived MMOs sorbents obtained from the LTR analysis of the ZLC experiments. The parameters have been compared with the ones calculated from the complete ZLC model and show good agreement in the obtained values. The results and simulations of the ZLC complete model are included in Appendix A6.4. Table 6.6 summarizes the CO_2 diffusion coefficient value reported for the LDH-based MMOs sorbent.

Table 6. 5 - Diffusion coefficients of CO_2 in LDH-based MMOs sorbents (full pellet) obtained from the LTR analysis.

Temperature (˚C)	Slope x 10^3	Intercept	D_{ap}/l^2 x 10^4 (s^{-1})	K^*
200	-6.23	-2.52	6.3 ± 0.6	200.0
300	-8.62	-2.20	8.7 ± 0.3	170.9
400	-13.09	-1.99	13.3 ± 1.7	164.0

Table 6. 6 - Summary of CO_2 diffusion coefficients for LDH-based MMOs reported in the literature.

Author	Sorbent material	Method	Conditions	Diffusion coefficients or LDF parameter (s^{-1})
Ding & Alpay [150], [151]	K-promoted hydrotalcite	Breakthrough	ads, dry, 400 ˚C, P_{CO2} = 0.12 bar,	7.5 x 10^{-3}
			ads, wet, 400 ˚C , P_{CO2} = 0.12 bar	1 x 10^{-2}
			des, dry, 400 ˚C , P_{N2} = 1.14 bar	5.0 x 10^{-4}
Moreira *et al.* [155]	PURAL MG50 (Sasol)	ZLC	dry, 150 ˚C	8.2 x 10^{-3}
			dry, 250 ˚C	8.2 x 10^{-3}
			dry, 350 ˚C	10.4 x 10^{-3}

Oliveira *et al.* [154]	20 wt% K_2CO_3 - promoted PURAL MG30, MG50, MG70 (Sasol)	Breakthrough	wet, 403 ˚C, P_{CO2} = 0.05 – 0.40 bar,	2.9×10^{-3}
			wet, 510 ˚C, P_{CO2} = 0.05 – 0.40 bar,	1.2×10^{-2}
Chanburanasiri *et al.* [158]	K_2CO_3 – promoted PURAL MG31w (Sasol)	Breakthrough	ads, wet, 360 ˚C	1.66×10^{-2}
Miguel *et al.* [357]	K-promoted Mg-Ga-LDH	Gravimetric (MSB)	ads, dry, 200 ˚C, P_{CO2} = 0.05 bar	Cycle 1: (fast)15.55×10^{-4}; (slow) 7.41×10^{-4} Cycle 5: (fast)9.08×10^{-4}; (slow) 6.01×10^{-4}
			ads, dry, 300 ˚C, P_{CO2} = 0.05 bar	Cycle 1: (fast)7.57×10^{-4}; (slow) 12.26×10^{-4} Cycle 5: (fast)9.08×10^{-4}; (slow) 6.01×10^{-4}
			des, dry, 200 ˚C, P_{CO2} < 0.001 bar	(fast)1.17×10^{-4} (slow) 0.55×10^{-4}
			des, dry, 300 ˚C, P_{CO2} <0.001 bar	(fast) 1.0×10^{-4} (slow) 2.54×10^{-4}

The diffusion time constant (D_{ap}/l^2) value was shown to increase with temperature, with an order of magnitude increase in the diffusion time constant measured at 400 ˚C (1.33×10^{-3} s^{-1}), compared to the values at 200 ˚C (6.3×10^{-4} s^{-1}) and 300 ˚C (8.7×10^{-4} s^{-1}). The Henry's constant coefficient, K^* obtained from the LTR analysis was found to be within the region of the heat of adsorption due to chemisorption, ~ 200 kJ/mol. As temperature increased, K^* decreased. The diffusion coefficient values obtained in Table 6.5 are consistent with the literature-reported values, suggesting that the diffusional coefficient of CO_2 in unpromoted LDH-derived MMOs is comparable to that of promoted sorbent. Most of the literature-reported diffusion coefficients measured under wet conditions were about an order of

magnitude (10^{-2}) higher than those measured under dry conditions at a given temperature, indicating the effect of moisture on the CO_2 sorption kinetics of LDH-derived MMOs.

The determination of the diffusion controlling mechanism is achieved by running ZLC experiments using a smaller size pellets to reduce the effective time constant ratio. For cylindrical-shaped pellets, the effective time constant is determined by the pellet radius. If micropore (crystal) diffusion was the controlling mechanism, then the diffusion time constant of smaller-size pellets should be the same as that calculated for the original pellets. If the macropore diffusion is the controlling mechanism, then the diffusion time constant (D_{ap}/l^2) should vary with pellet size and correspond to that in the large pellet multiplied by the ratio of the square of the radius of each pellet ($R_{p,normal}^2/R_{p,small}^2$). Table 6.7 gives the new CO_2 diffusion time constant measured in the small pellets of LDH-derived MMOs sorbent at 200 ˚C and 300 ˚C.

Table 6. 7 - Diffusion coefficients of CO_2 in LDH-based MMOs sorbents (small pellet) obtained from the LTR analysis.

Temperature (˚C)	Slope x 10^3	Intercept	D_{ap}/l^2 x 10^4 (s^{-1})	K^*	$(D_{ap}/l^2) \times (R_{p,normal}^2/R_{p,small}^2)$
200	-5.69	-1.96	24.8 ± 0.7	202.1	25.2
300	-8.18	-2.04	35.3 ± 0.5	148.7	38.8

The obtained CO_2 diffusion coefficient of small pellets is approximately four times that of original pellets, which matches with the value corresponds to the diffusion time constant in large pellets multiplied by the ratio of the square of the radius of each pellet. This suggests that the dominant controlling mechanism is in the macropores. If macropore diffusion is the limiting resistance, the pellet size and porosity of adsorbent need to be optimised to achieve a compromise between mass-transfer limitations in the macropore space and reduction of energy cost associated with the pressure drop across the bed. In contrast, if the diffusion resistance is in the micropore, there is more freedom in choosing pellet size and porosity since these parameters do not affect the sorption kinetics of adsorbent. The Henry's constant coefficients, K^* obtained from the small pellets also agree well with the heat of adsorption due to chemisorption and are close to the values of the original pellets presented in Table 6.5.

Overall, this section demonstrates that the sorption kinetics of unpromoted LDH-derived MMOs sorbent is comparable to the K_2CO_3-promoted MMOs sorbent. However, due to the significant lower equilibrium capacities of the unpromoted MMOs sorbent, the working capacity deemed to be lower than those promoted ones.

6.4 Conclusions

In the present work, the CO_2 adsorption performance of unpromoted LDH-derived MMOs pellets was re-evaluated. The novelty of the work lies in the fact that for the first time, the MMOs sorbent was unambiguously characterized; and its true chemical composition was obtained using a combination of crystal chemistry and analytical methods. The crystal chemistry model developed in Chapter 4 was also demonstrated to be application not only to lab synthesized LDHs, but also to commercial LDHs that are synthesized on a kilogram scale.

The CO_2 adsorption isotherms were measured using a gravimetric method with a magnetic suspension balance (MSB) system. The MSB system allows for the accurate measurement for high-pressure CO_2 adsorption isotherms up to 30 bar and at high temperatures (200 - 400 ˚C). To the best of our knowledge, this is the first-time high-pressure CO_2 adsorption isotherms of LDHs derived MMOs were measured using a gravimetric method. The CO_2 adsorption isotherms show clear temperature-dependent behavior, with the highest sorption capacity measured at 200 ˚C, followed by the ones measured at 300 ˚C and 400 ˚C. The highest sorption capacity (1.5 mol/kg) was obtained at 200 ˚C and 30 bar. In the low-pressure region (< 8 bar), the equilibrium capacities of unpromoted MMOs are comparable to those promoted with AMS. However, in the high-pressure region (8 - 30 bar) and high temperature (300 – 400 ˚C), the AMS-promoted LDH-derived MMOs are superior as they show almost a two-fold increase in sorption capacities.

The CO_2 sorption kinetics of LDH-derived MMOs sorbent was measured by the Zero Length Column (ZLC) method. The diffusional coefficient parameters obtained for unpromoted LDH-derived MMOs were found to be in the same order of magnitude of those obtained for K_2CO_3-promoted MMOs sorbents. The macropore diffusion limitations were found in the LDH-derived MMOs sorbent. The presence of water can improve the sorption

kinetics in LDH-derived MMOs sorbent. Overall, the present work sets a reference case for the CO_2 adsorption performance of LDH-derived MMOs.

Appendices

Appendix A6.1 Helium Pycnometer
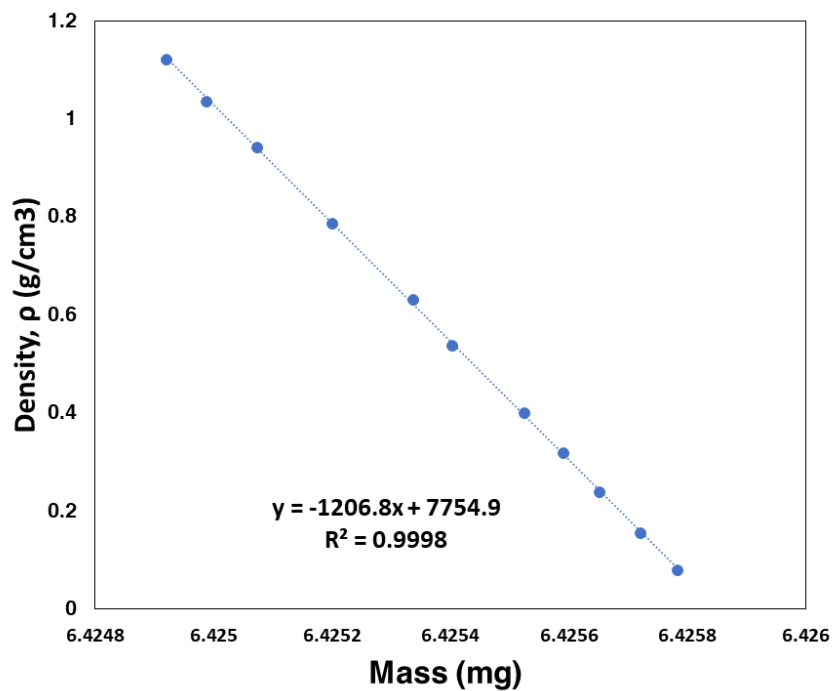
Figure A6.1 - Helium pycnometer for the MSB system with the basket, permanent magnet, and suspension shaft

Appendix A6.2 Derivation of buoyancy correction equation

The specific amount of gas adsorbed can be then calculated from:

$$q = \frac{\text{adsorbed moles}}{\text{mass of adsorbent}} = \frac{m_{\text{ads}}}{m_s M} \text{,} \tag{S.1}$$

where m_{ads} is the mass of adsorbed gas, M is the molecular weight of the adsorbate, and m_s is the mass of the activated sample.

Buoyancy is the upward force exerted over an object's immersed fluid. It is equal to the weight of the fluid displaced by the object. Although buoyancy does not affect the mass of an object, it can affect its measure, so correction might be necessary.

The weight of the fluid displaced by the sample, the adsorbed gas and the sample container are:

$$\text{Mass of displaced gas} = (V_s + V_{ads} + V_i)\rho_g \tag{S.2}$$

Where V_s is the volume of the solid adsorbent, V_{ads} is the volume of adsorbed gas, V_i is the volume of the measuring cell (axis, basket and glass wool) and ρ_g is the density of the gas at measuring conditions $\rho_g = z\dfrac{PM}{\Re T}$, where z is the acentric factor obtained from the virial equation of state [1].

Then, the real mass of the sample, m_{real}, the adsorbed gas and the sample container is:

$$m_{\text{real}} = m + (V_s + V_{ads} + V_i)\rho_g \tag{S.3}$$

where m is the mass given by the magnetic balance.

The adsorbed mass is calculated from the mass difference between the real mass and the initial mass of the activated sample and the measuring cell ($m_s + m_i$)

$$m_{\text{ads}} = m + (V_s + V_{ads} + V_i)\rho_g - (m_s + m_i) \tag{S.4}$$

Assuming that the adsorbed phase presents a density similar to that of the liquid phase:

$$V_{\text{ads}} = \frac{m_{\text{ads}}}{\rho_{\text{ads}}} = \frac{m_{\text{ads}}}{\rho_1} \tag{S.5}$$

and

$$\rho_1 = \frac{M}{v} \tag{S.6}$$

Where v is the molar volume calculated by the Gunn-Yamada method [1].

Then:

$$m_{ads} = m - (m_s + m_c) + \left(V_s + \frac{m_{ads}}{\rho_1} + V_i\right)\rho_g \qquad (S.7)$$

Solving equation S.6 as a function of m_{ads} we get

$$m_{ads} = \left[\Delta m + (V_s + V_i)\rho_g\right]\frac{\rho_1}{\rho_1 - \rho_g} , \qquad (S.8)$$

where Δm represents the mass difference between the mass given by the microbalance and the initial mass of the basket loaded with the activated sample and the glass wool.

Finally, the adsorption capacity can be calculated from:

$$q = \frac{\Delta m + (V_s + V_i) \times \rho_g}{m_s M}\frac{\rho_l}{\rho_l - \rho_g} , \qquad (S.9)$$

The volume of the basket with $(V_i + V_s)$ and without (V_i) the sample, and the respective mass, $m_i + m_s$ and m_i, were calculated by a helium pycnometer.

Appendix A6.3 Liquid Densities

This information present in this section was obtained from a previous publication from the same group[351]. For relatively low temperatures, the molar volume of the substance in the adsorbed state, $v*$, may be taken as the molar volume of the substance in the bulk liquid phase, according to Dubinin's assumption[358].

Over the range of temperatures from the boiling point to the critical temperature, there is a considerable decrease in the liquid phase density as the critical temperature is approached (Figure A6.2). However, there's also a sharp increase in the compressibility of the liquid and since an adsorbed substance in micropores is in a strongly compressed state, its density is considerably greater than the liquid density and can be expressed as linear (line BD).
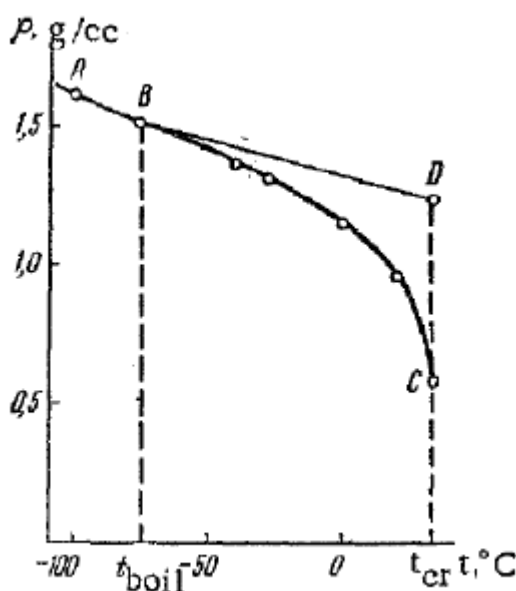
Figure A6.2 - Temperature dependence of the density of liquid tetrafluoroethylene
[359]

Therefore, above boiling point temperature and under the critical temperature, the molar volume is calculated through Equation A6.3.1.

$$v^* = v_b + \left[\frac{T - T_b}{T_c - T_b}\right](b - v_b)$$

207

where v_b is the molar volume at the boiling temperature, T_b, and T_c the critical temperature. For temperatures above the critical temperature, the molar volume is equal to Van der Waal's volume:

$$v^* = b$$

where b is the Van der Waal's volume.

References

[1] Dubinin, M.M., 1960. Theory of the physical adsorption of gases and vapors and adsorption properties of adsorbents of various natures and porous structures. *Bulletin of the Academy of Sciences of the USSR, Division of Chemical Science*, *9*(7), pp.1072-1078.

[2] Al-Baghli, N.A. and Loughlin, K.F., 2005. Adsorption of methane, ethane, and ethylene on titanosilicate ETS-10 zeolite. *Journal of Chemical & Engineering Data*, *50*(3), pp.843-848.

Appendix A6.4 Zero Length Column *Ft* plots
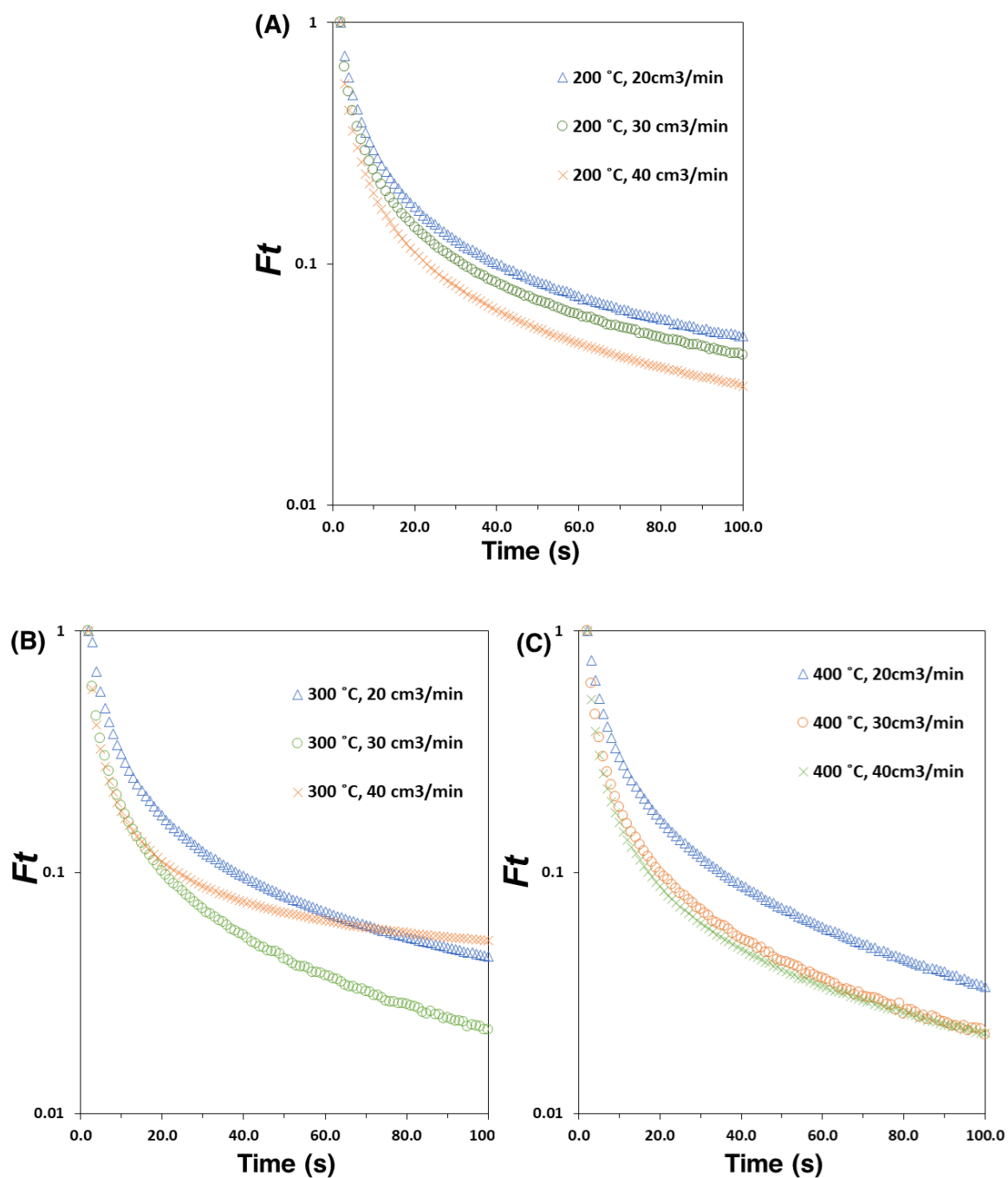
Figure A6.3 - Experimental Ft plot of LDH-derived MMOs at 0.01 vol% of CO_2 in He at three different temperatures (200 ˚C, 300 ˚C & 400 ˚C) and various flowrates (20, 30 & 40 cm³/min)

Appendix A6.5 Zero Length Column Results
Experimental results in each ZLC column

Table A6.1- Long-time response and the complete ZLC model parameters for CO_2 in LDH-derived MMOs full pellets at 200 , 573, and 400 ˚C .

Temperature (K)	D_{ap}/l^2 x 10^{-4} (s^{-1})		$K*$	
	LTR	TS	LTR	TS
200	6.3 ± 0.6	5.9 ± 0.8	200	183.1
573	8.7 ± 0.3	8.5 ± 1.6	170.9	156.8
673	13.3 ± 1.7	13.1 ± 0.9	164.8	142.9

Table A6.2 - Long time response and the complete ZLC model parameters for CO_2 in LDH-derived MMOs small pellets at 200 , 573, and 400 ˚C .

Temperature (K)	D_{ap}/l^2 x 10^{-4} (s^{-1})		$K*$		β
	LTR	TS	LTR	TS	LTR
200	24.8 ± 0.7	2.9	202.1	540.2	1.524
573	35.3 ± 0.5	5.8	148.7	418.9	1.523

*LTR = Long Time Analysis; TS = Complete ZLC model

Appendix A6.6 GC Calibration for ZLC experiments

Calibration was made to convert the arbitrary units of the gas chromatographer flow rate indicator to cubic centimetres per second. The volumetric flow rate at 1 bar and 273 K is presented in Figure A6.4
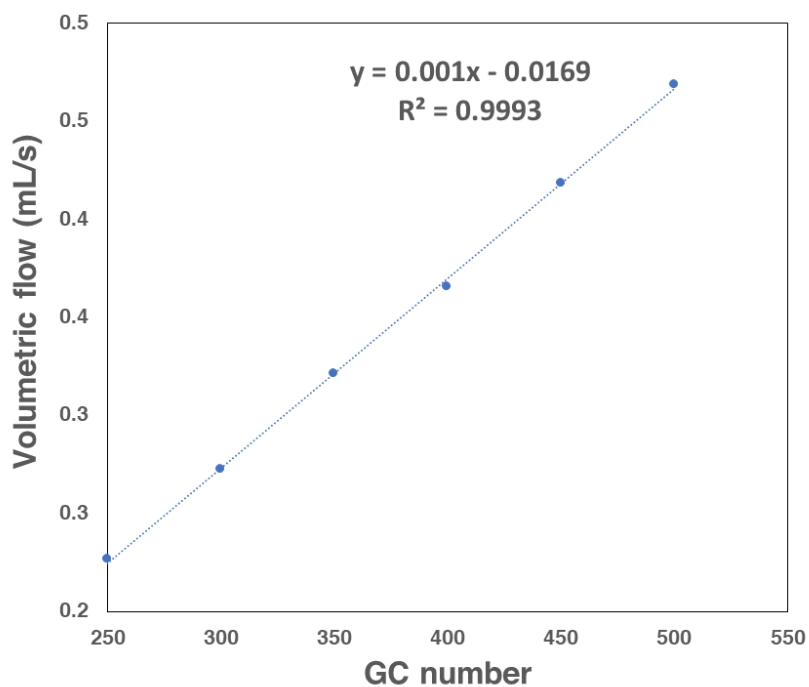
Figure A6.4 - Calibration of Helium gas flow in the gas chromatographer at PTN conditions

.

Chapter 7: Conclusions and Future Work

7.1 Conclusions

In this work, CO_2 capture by adsorption in an intermediate temperature range (200 – 400 ˚C) was studied, using mixed metal oxides (MMOs) derived from layered double hydroxides (LDHs) as the solid sorbent. The use of LDH-derived MMOs as CO_2 capture sorbents has been demonstrated at a high TRL level (6) for the sorption enhanced water gas shift (SEWGS) reaction, which is close to the demonstration stage. From pilot tests, LDH-derived MMOs sorbents have demonstrated promising CO_2 capture characteristics, such as good cyclic stability (> 1000 testing hours; 2000 adsorption and desorption cycles), high CO_2 recoveries well above 90 %, tolerant to sulphur content, ability to withstand moisture, and regenerable by steam. In addition, the manufacturing cost of LDH is generally low, and the material is environmentally benign. These properties are highly desired for solid CO_2 adsorbents. Since the 1990s, many efforts have been devoted to improving the capture properties of these types of materials.

Despite this fact, there has been little progress in the material development of LDH-derived MMOs. Although the working capacities of the material have improved from 0.3 mol/kg in 1996 to 1.1 mol/kg at present. However, techno-economic analysis indicates that to obtain significant cost savings with this class of sorbent material, the capture capacity needs to be at least above 1.35 mol/kg.

There are two common routes to improving the CO_2 adsorption capacities of LDH-derived MMOs: 1) doping with alkali metal salt (AMS) promoter and 2) precursor engineering. Based on literature reviews, the majority of the relevant studies rely on the addition of alkali metal salt (AMS) promoter to improve the CO_2 capture capacity of MMOs sorbents; while the potential to improve the capacity from the material itself is largely unexplored. For example, with an Mg/Al ratio of 3 and without any promoter, the theoretical capture capacity of LDH-derived MMOs is estimated to be 16.3 mol/kg. If this theoretical capacity can be unlocked, even just 10 %, the capture capacities of LDH-derived MMOs sorbent should live up to expectation. One way of achieving this is through the precursor engineering approach, by modifying the LDHs precursors to achieve highly dispersed phase of MMOs. Nevertheless, there is very little research have been done on this aspect.

The main reason is likely linked to a lack of agreement on the material properties and its CO_2 adsorption performance. On the materials side, both LDHs and MMOs phases remain poorly understood as of yet. From a very basic level, there is still no reliable method to accurately derive the chemical composition of LDHs in the crystal phase. This matter is further complicated with the MMOs, which forms after the collapse of LDH structure and comprises of mixed MgO and amorphous Al_2O_3 phase that is even harder to characterize. This is arguably why a chemically meaningful relationship between composition and adsorption performance of LDH-derived MMOs has not been established yet, which added substantial obstacles to the efforts to improve this material. In terms of CO_2 adsorption properties, the discussion mainly centres around the adsorption mechanism, enhancement mechanism of AMS promoter and adsorption kinetics of LDH-derived MMOs sorbents. However, the exact implications of how these aspects can aid in the development of LDH-derived MMOs with capacity-optimized performance remains an open question. To overcome this, a systematic approach has been employed to investigate the various aspects of LDH and MMO sorbents, starting from the very fundamental aspect, i.e., crystal. The objective of this work is to obtain better insights into the LDHs and MMOs phases, and ultimately design better MMOs for CO_2 capture.

The first step of this study was to establish a chemically meaningful relationship between Mg/Al ratios of precursors LDHs and the CO_2 capture capacities of derived MMOs. Four LDH samples with varied Mg/Al ratios (2, 3, 4, & 5) were synthesized by the co-precipitation method and their CO_2 capture capacities were measured at 200 ˚C. A crystal-chemical approach was taken to determine the actual chemical composition of LDHs synthesized, by using lattice parameter a, and coupled with various characterization techniques such as elemental Analysis and solid-state ^{27}Al NMR. From the lattice parameter observation, it was found that the synthesized LDHs do not necessarily arrive at the desired compositions and a tendency to form LDHs with a composition close to that of its mineral form, Hydrotalcite ($x = 0.25$), is found. In addition to that, at least two amorphous impure phases were found in all LDH samples, i.e., sodium and Al-based impurities. This confirms the non-stoichiometric nature of the co-precipitated method. Interestingly, instead of the Mg/Al ratios, the sodium content was found strongly correlated to the CO_2 capture capacities of MMO sorbents. This is perhaps the reason behind the

213

inconsistent CO_2 capture capacities observed for LDH-derived MMOs and causing the disputable relationship between Mg/Al ratios and CO_2 capture capacities. This new finding prompted us to face the existence of impurities more seriously and their impact on the CO_2 adsorption capacities of MMOs derived from LDHs.

Since it is almost impossible to completely remove the sodium content from LDHs synthesized from the co-precipitated method, another synthesis method was considered. The urea hydrolysis method was viewed as a viable alternative to the co-precipitation method, as it does not require a sodium precipitating agent during synthesis and can be easily scaled up to produce LDHs in large quantities. In Chapter 4, the impacts of different synthesis methods and metal salt precursors on the properties of LDHs and the CO_2 adsorption performance of MMOs were investigated. Two different synthesis methods (i.e., urea hydrolysis and co-precipitation methods) were employed to synthesize 12 different LDHs with varying Mg/Al ratios (2, 3, & 4) and different metal salt precursors (i.e., metal nitrates and metal chlorides). The evaluation of synthesis method and metal salt precursors was based on the synthetic efficiency, using metrics such as yields, purity and percentage of unreacted reactants in filtrates, which concerns the sustainability aspects of LDHs production. This was then correlated with the CO_2 adsorption performance of MMOs derived. Compared to Chapter 3, the investigation into the CO_2 adsorption performance of LDH-derived MMOs sorbent was expanded to adsorption kinetics and cyclic stability. The study concludes that LDHs synthesized by the co-precipitation method are in general more suitable for CO_2 capture, due to their high LDH purity, close to maximum product yields (~100 %), a lesser amount of wasted unreacted reactants, high adsorption capacities (0.54 to 0.95 mol/kg) and better sorption kinetics. On the other hand, the urea hydrolysis method gives lower LDH purity, low product yields (54 – 81 %), a larger number of unreacted reactants, and lower adsorption capacities (0.30 to 0.70 mol/kg). For both methods, LDHs with higher Mg content tend to exhibit slower CO_2 adsorption kinetics, i.e., a higher rate of slow carbonation step. The cyclic stability of LDH-derived MMOs tends to be better than the pure MgO sorbents.

Chapter 5 presents the development of a new crystal-chemical model to determine the true chemical composition of the Mg-Al phase, using the lattice parameter "*a*". This approach

was previously employed in Chapter 3 but was found that there is still room for improvement in crystal-chemical arguments presented so far, i.e., from Brindley & Kikkawa (1979) and Richardson (2013). In this work, a theoretical top-down approach has been employed to develop the crystal-chemical model, which is based on Vegard's law. Vegard's law states that a linear relationship should be observed between the lattice parameter and chemical composition in a substitutional solid solution like LDHs. Through the validation of a large amount of experimental data and comparison with previous models, the new crystal-chemical model demonstrated its capacity to assign more reasonable values of x for the a parameters obtained. For example, the a-parameter (3.04 Å) that is commonly associated with a maximum substitution of Al^{3+} in LDH phases (i.e., $x = 0.33$) was revealed to have a significantly lower x value than previously imagined (i.e., 0.25). Nevertheless, this aligns with our findings in Chapter 4, where LDHs synthesized from the urea hydrolysis method with this nominal composition (0.33) were found to be non-stoichiometric but give the same a-parameter (~ 3.04 Å). Another important result from the model was that the precise boundaries of x that are valid for Mg-Al-LDHs are unambiguously defined for the first time, i.e., 0.083 – 0.33. The findings in this study is anticipated can lead to a new trend of LDH development and further, aid in the design of LDH and MMOs material for optimized performance in CO_2 capture applications.

To understand the true adsorption behaviour of LDH-derived MMOs and establish a reference case for this type of material, the CO_2 adsorption equilibrium isotherms and sorption kinetics of the sorbent material were re-evaluated. The sorbent material used was a commercial LDHs powder obtained from Sigma Aldrich and pelletized with a tablet press, so no binder material was used. The adsorption equilibrium isotherms of CO_2 in the MMOs sorbents were measured at three different temperatures (200, 300 & 400 ˚C) and a pressure range up to 30 bar, using a Magnetic Suspension Balance system with high weighing precision up to 0.01 mg. The obtained CO_2 isotherms were then compared with various other CO_2 isotherms available in the literature, including those obtained from alkali metal-promoted MMOs (mainly the K_2CO_3-promoted ones).

In general, the CO_2 adsorption isotherms obtained from this work show a very similar shape (Freundlich isotherms) to those obtained for AMS-promoted MMOs, which is likely

a feature of chemisorption. The main distinction lies in the high-temperature and high-pressure region, where the alkali metal MMOs show a remarkable increase in the CO_2 equilibrium capacities at 400 ˚C and 30 bar, about 6-7 times higher than the unpromoted MMOs sorbent. As this condition is desirable for CCUS-enabled hydrogen production, it seems that the AMS promoted LDH-derived MMOs are more suitable for this type of application, compared to the unpromoted MMOs used in the present work. Nevertheless, for the milder conditions, the equilibrium capacities of unpromoted MMOs are comparable to those promoted with K_2CO_3.

The sorption kinetics of unpromoted LDH-derived MMOs were measured by the Zero Length Column (ZLC) Technique, and the diffusion coefficient parameters at three different temperatures were obtained (200, 300 & 400 ˚C). The diffusional coefficient values of LDH-derived MMOs obtained were in the range of $6.3 – 13.3 \times 10^{-4}$, and good agreement was found between the heat of adsorption due to chemisorption and Henry's coefficients (K^*) obtained from ZLC experiments, e.g., ~ 150 - 200 kJ/mol. There is an order of magnitude difference in diffusion coefficient between 200 and 400 ˚C. Interestingly, the diffusion coefficient values of unpromoted MMOs at 400 ˚C are found in the same order of magnitude (10^{-3}) as the K_2CO_3-promoted MMOs sorbent. The presence of moisture in gas feed seems to improve the sorption kinetics of MMO sorbents, as there is an order of magnitude increase in the diffusional coefficient values when a wet testing condition were used.

7.2 Critical Review and Suggestions for Future Work

The sorption capacities of LDH-derived MMOs sorbents prepared in this work range from 0.5 – 1.0 mol/kg, which is still not reached the expected values of 1.35 mol/kg. To enable the use of LDH-derived MMOs under elevated temperature, such as those encountered in process streams related to CCUS-enabled hydrogen production, the promotion with alkali metal salt (AMS) is likely one of the best options. AMS can extend the operational temperature window of LDH-derived MMOs to a higher range (300 - 400 ˚C), resulting in the desired higher sorption capacities for the process.

Although the CO_2 desorption kinetics of LDH-derived MMOs were not investigated in this work, it is concerning that the reported desorption kinetics from fixed bed tests are usually an order of magnitude lower than the adsorption kinetics. Slow desorption kinetics may necessitate sacrificing the working capacity of the sorbent for shorter desorption cycles. Therefore, study the CO_2 desorption kinetics of LDH-derived MMOs and exploring methods to improve would be interesting.

The crystal-chemical model developed in this study allows for the estimation of the the chemical composition of LDHs in the crystal phase. This has significant implications, especially for the development of LDH-derived MMOs sorbents. First, it provides a reliable means to verify the Mg/Al ratio of as-synthesized LDHs, ensuring that meaningful conclusions can be drawn from studies using these materials. Secondly, knowledge the chemical composition enables the possibility to engineer and optimize the material, as the chemical composition of LDHs is closely related to their crystal structure and physical properties. For instance, the Mg/Al ratio affects the layer charge density, number of intercalated anions, anion exchange properties of LDHs and basicity of adsorption sites in MMOs. Thus, knowing the true chemical composition of LDHs in the crystal phase allows for the tuning of these properties in a more effective manner. Finally, the presence of amorphous impurity phase can be easily detected using this method, which may otherwise remain unnoticed and could affect the performance of related materials.

Although the experiments in this work indicate that the Mg/Al ratios of precursors LDHs have very little influence on the sorption capacities of the derived MMOs, Mg/Al ratios are still an important aspect to study for many reasons. One reason is the issue encounter in the

Air Product's SEWGS pilot test study, where after long cycles of adsorption, the sorbent material lost its mechanical strength and turned into powder, accumulating at the bottom of the reactor. This was attributed to the formation of $MgCO_3$, and the slow swinging between MgO and $MgCO_3$. The ratio of molar volume of $MgCO_3$ to molar volume of MgO is 2.53, which likely causes the sorbent material to expand and contract until it falls apart. To overcome this, a research consortium between Air Products and ECN proposed a new sorbent, ALKASORB, for the process, which showed no issues with $MgCO_3$ formation. As the material specifications were kept confidential, there is very little information on how this was achieved. Nevertheless, the presence of Mg in the LDH-derived MMOs was found crucial to catalysing the CO into H_2 via WGS reaction, which means the Mg-Al-MMOs are sufficient to act as the WGS catalyst and CO_2 adsorption in the SEWGS reaction. Thus, it would be interesting to find out the optimum Mg content for SEWGS reaction while ensuring good mechanical stability for MMO sorbent. Additionally, efforts are being made to combine the conventional WGS catalyst with Mg-Al-LDHs, i.e., K-promoted Co-Mg-Al oxides. An interesting area for research would be to find the optimal ratio between Co, Mg and Al for intermediate CO_2 capture.

It might be likely that the Mg content would not be a problem if the mechanical strength of MMOs sorbents could be improved. The main issue with $MgCO_3$ formation is the expansion in volume, thus it may be solved by providing more space for expansion, i.e., increased porosity. However, this has to be done discreetly as large void space in sorbent material usually leads to a reduction in overall mechanical strength and exacerbates the diffusion limitations in macropores of LDH-derived MMOs. Furthermore, lower process efficiency may also result due to the lower uptake per unit volume and the requirement for a larger reactor vessel to maintain the same capture capacity.

Otherwise, support materials may be used. The easiest route is through the physical mixing of MMOs and the support material; however, the sorption capacities and kinetics are usually sacrificed. Another route is through the development of novel/hybrid MMOs that incorporate support material in the LDH matrix. Although this field is still in its early stage of development, it is foreseeable the potential for this type of material for catalytic and adsorption applications. The cyclic stability of MMOs can be improved with this method.

In this work, the re-evaluation of CO_2 adsorption performance in LDH-derived MMOs sorbent was done on cylindrical pellets with the following dimensions: 2mm diameter x 2mm length. Although this dimension is common for normal ambient temperature adsorption, a larger particle size is generally preferred for high-temperature adsorption, as the gas velocities under high temperature are higher than the normal ambient temperature adsorption process, which means the pressure drops would be higher if not compensated with larger particle size. Nevertheless, the ZLC experiments present in this work show that the mass transfer of CO_2 in unpromoted LDH-derived MMOs is predominantly controlled by diffusion in macropores. A similar result is obtained for K_2CO_3-promoted MMOs. This means the increase in particle size will likely impact the diffusional coefficient values of sorbent material. Thus, future work may focus on finding the optimal particle size or shape for LDH-derived MMOs sorbent.

Overall, this work demonstrates that understanding sorbent materials from the fundamental aspects, such as crystal structure, can help the design MMOs with better properties.

Appendices

Appendix A.1 Published Paper

acs.chemmater.1c031
01.pdf

Characterization of Chemisorbed Species and Active Adsorption Sites in Mg-Al Mixed Metal Oxides for High Temperature CO_2 Capture

Alicia Lund[a], Manohara Gudiyor[b], Ah-Young Song[a], Kevin Maik Jablonka[c], Christopher Ireland[c], Li Anne Cheah[b], Berend Smit[c], Susana Garcia[b], Jeffrey Reimer[a,*]

[a]Materials Science Division, Lawrence Berkeley National Laboratory, Berkeley, California 94720,
United States; Department of Chemical and Biomolecular Engineering, University of California, Berkeley, California 94720, United States

[b]Research Center for Carbon Solutions, (RCCS), School of Engineering and Physical Sciences, Heriot-
Watt University, Edinburgh EH14 4AS, U.K.

[c]Laboratory of Molecular Simulation (LSMO), Institut des Sciences et Ingénierie Chimiques, École
Polytechnique Fédérale de Lausanne (EPFL), Sion CH-1951 Switzerland
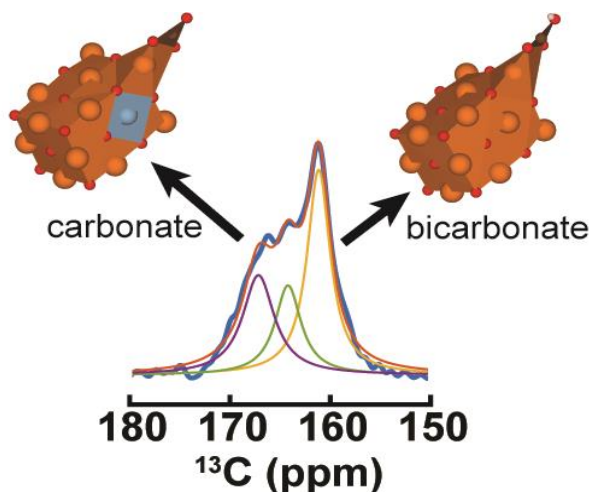
Figure A.1 - Table of Content Entry

Abstract

Mg-Al mixed metal oxides (MMOs), derived from the decomposition of layered double hydroxides (LDHs), have been purposed as a material for CO_2 capture of industrial plant emissions. To aid in the design and optimization of these materials for CO_2 capture at 200 °C, we have used the combination of solid state nuclear magnetic resonance (ssNMR) and density function theory (DFT) to characterize the CO_2 gas sorption products and determine the various sorption sites in the Mg-Al MMOs. Comparison of DFT cluster calculations with ^{13}C chemical shift of the chemisorbed products indicates that mono and bi-dentate carbonate are formed at the Mg-O site with an adjacent Al substitution of an Mg atom, while bicarbonate is form at Mg-OH sites without adjacent Al substitution. Quantitative ^{13}C NMR shows an increase in the relative amount of strongly basic sites, where the monodentate carbonate product is formed, with increasing Al mole % in the MMOs. This detailed understanding of the various basic Mg-O sites presents in the MMOs material, and the formation of the carbonate, bidentate carbonate and bicarbonate chemisorbed species yields new insight into the mechanism of CO_2 adsorption at 200 °C which can further aid in the design and capture capacity optimization of the materials.

Characterization of Chemisorbed Species and Active Adsorption Sites in Mg–Al Mixed Metal Oxides for High-Temperature CO_2 Capture

Alicia Lund, G. V. Manohara, Ah-Young Song, Kevin Maik Jablonka, Christopher P. Ireland, Li Anne Cheah, Berend Smit, Susana Garcia, and Jeffrey A. Reimer*

ABSTRACT: Mg–Al mixed metal oxides (MMOs), derived from the decomposition of layered double hydroxides (LDHs), have been purposed as adsorbents for CO_2 capture of industrial plant emissions. To aid in the design and optimization of these materials for CO_2 capture at 200 °C, we have used a combination of solid-state nuclear magnetic resonance (ssNMR) and density functional theory (DFT) to characterize the CO_2 gas sorption products and determine the various sorption sites in Mg–Al MMOs. A comparison of the DFT cluster calculations with the observed ^{13}C chemical shifts of the chemisorbed products indicates that mono- and bidentate carbonates are formed at the Mg–O sites with adjacent Al substitution of an Mg atom, while the bicarbonates are formed at Mg–OH sites without adjacent Al substitution. Quantitative ^{13}C NMR shows an increase in the relative amount of strongly basic sites, where the monodentate carbonate product is formed, with increasing Al/Mg molar ratios in the MMOs. This detailed understanding of the various basic Mg–O sites presented in MMOs and the formation of the carbonate, bidentate carbonate, and bicarbonate chemisorbed species yields new insights into the mechanism of CO_2 adsorption at 200 °C, which can further aid in the design and capture capacity optimization of the materials.
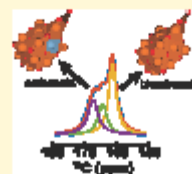
INTRODUCTION

Carbon dioxide capture, utilization, and storage (CCUS) are expected to play a key role in reducing atmospheric CO_2 and mitigating global warming.[1,2] Capturing CO_2 from industrial emissions is one of the several approaches toward this end.[3] Solid sorbents such as zeolites,[4] metal–organic frameworks (MOFs),[5,6] covalent organic frameworks (COFs),[7] mesoporous carbon,[8] and metal oxides[9] have all shown to be promising materials for CO_2 capture. Among the solid CO_2 sorbents, layered double hydroxide (LDH)-derived mixed metal oxides (MMOs) have shown promising CO_2 capture performance at the 200–500 °C temperature range that is associated with industrial emissions such as iron and steel plants.[10–13] LDHs derive their structure from the mineral brucite $Mg(OH)_2$, while partial isomorphous substitution of Mg^{2+} ions with higher valent cations (Al^{3+}, Fe^{3+} Ga^{3+}, etc.) leads to positively charged hydroxide layers. Charge-compensating anions and water molecules are incorporated into the interlayer galleries leading to the formation of the LDHs. LDHs are represented by the general formula $[M^{2+}_{1-x}M^{3+}_x(OH)_2]^{x+}(A^{-x/n})\cdot yH_2O$, where M^{2+} = Mg, Co, Ni, Ca, and Zn, M^{3+} = Al, Fe, and Ga, and A = anion (organic or inorganic ions), $0.15 \leq x \leq 0.33$ and $0.5 \leq y \leq 1.0$.[14] Due to their physicochemical properties, LDHs and LDH-derived MMOs have proved to be useful materials in various industrial applications including catalysis and sorption.[15–17] The substitution of Mg^{2+} with Al^{3+} also helps prevent the sintering of MgO. In the recent past, LDH-derived MMOs have gained prominence as CO_2 capture sorbents due to their high theoretical capture capacity, tolerance to moisture and hydrogen sulfide (H_2S), ease of preparation/handling, economical cost, and their environmentally friendly nature.[18–22] Interestingly, LDH-derived MMOs have shown unique CO_2 capture performance under both pre- and postcombustion conditions.[23] While the CO_2 capture properties are very promising, the performance of LDH-derived MMOs has yet to live up to the theoretical promise, with the typical measured CO_2 capture capacities being in the range of 0.05–1.39 mmol/g.[21] Moreover, MMOs have shown poor carbonation/regeneration cycling stability with the capture capacities decreasing by 30–50% over 10–20 cycles; overcoming these challenges has been the focus of much ongoing research.[21,24,25]

It is clear from this literature that a detailed atomistic understanding of the CO_2 capture process, including identification of the chemisorbed products, is needed to further drive the development of MMOs for increased capture capacity. Solid-state nuclear magnetic resonance (ssNMR)

222
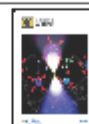
References

[1]   Climate Watch, 'CAIT data: Greenhouse Gas (GHG) Emissions', *World Resources Institute*, 2020. Accessed: May 02, 2022. [Online] Available: https://www.climatewatchdata.org/ghg-emissions?end_year=2018&start_year=1990

[2]   C. D. Keeling *et al.*, 'Atmospheric carbon dioxide variations at Mauna Loa observatory, Hawaii', *Tellus*, vol. 28, no. 6, pp. 538–551, 1976.

[3]   IPCC, 'Global Warming of 1.5°C. An IPCC Special Report on the impacts of global warming of 1.5°C above pre-industrial levels and related global greenhouse gas emission pathways, in the context of strengthening the global response to the threat of climate change, sustainable development, and efforts to eradicate poverty', Cambridge, Jun. 2018. doi: 10.1017/9781009157940.001.

[4]   UNFCCC, 'The Paris Agreement', 2016. Accessed: Jul. 13, 2022. [Online] Available: https://unfccc.int/process-and-meetings/the-paris-agreement/the-paris-agreement (accessed Jul. 13, 2022).

[5]   IPCC, 'Climate Change 2020: Mitigation of Climate Change', Geneva, Switzerland, 2022. Accessed: May 06, 2022. [Online]. Available: https://report.ipcc.ch/ar6wg3/pdf/IPCC_AR6_WGIII_FinalDraft_FullReport.pdf

[6]   UK Government, 'UK becomes first major economy to pass net zero emissions law'. Accessed: Jun. 27, 2019. [Online] Available: https://www.gov.uk/government/news/uk-becomes-first-major-economy-to-pass-net-zero-emissions-law (accessed May 02, 2022).

[7]   BEIS, '2020 UK greenhouse gas emissions, provisional figures', 2021.

[8]   BEIS, '2019 UK Greenhouse Gas Emissions', Feb. 2021. Accessed: May 02, 2022. [Online]. Available: https://www.ipcc-nggip.iges.or.jp/public/wetlands/index.html;

[9]   IEA, 'World Energy Outlook 2021', 2021. Accessed: May 02, 2022. [Online]. Available: www.iea.org/weo

[10]   W. R. Brock and L. A. Bryan, 'Summary Results of CO_2 EOR Field Tests, 1972-1987', Mar. 1989, doi: 10.2118/18977-MS.

[11]   IPCC, 'Special Report on Carbon Capture and Storage', Cambridge, UK, 2005.

[12]   IEA, 'Putting CO_2 to Use Creating value from emissions', 2019.

[13]   BEIS, 'UK Hydrogen Strategy', 2021, Accessed: Jun. 16, 2022. [Online]. Available: www.gov.uk/official-documents

[14]   IEAGHG, 'The Carbon Capture Project at Air Products' Port Arthur Hydrogen Production Facility', Dec. 2018. Accessed: Jul. 14, 2022. [Online]. Available: http://documents.ieaghg.org/index.php/s/4hyafrmhu2bobOs

[15]   A. Halladay, V. Oropeza Bacci, S. O'Brien, J. Duer, L. Rock, and S. Kassam, 'Quest CCS at two million tonnes', *4th Sustainable Earth Sciences Conference and Exhibition 2017, Held at Near Surface Geoscience Conference and Exhibition 2017*, vol. 2017, no. 1, pp. 81–85, 2017, doi: 10.3997/2214-4609.201702141/CITE/REFWORKS.

[16]   A. Busse, P. Gloria, and J. MacMurray, 'Demonstration of Carbon Capture and Sequestration of Steam Methane Reforming Process Gas Used for Large-Scale Hydrogen Production', United States, 2018. Accessed: Jul. 14, 2022. [Online]. Available: https://www.osti.gov/servlets/purl/1437618

[17]   Shell Global, 'Carbon capture: the quest for cleaner energy'. Accessed: Jul. 14, 2022. [Online] Available: https://www.shell.com/inside-energy/carbon-capture-the-quest-for-cleaner-energy.html

[18]   Y. J. Wu, P. Li, J. G. Yu, A. F. Cunha, and A. E. Rodrigues, 'Progress on sorption-enhanced reaction process for hydrogen production', *Rev Chem Eng*, vol. 32, no. 3, pp. 271–303, 2016, doi: 10.1515/REVCE-2015-0043/XML.

[19]   B. T. Carvill, J. R. Hufton, M. Anand, and S. Sircar, 'Sorption-enhanced reaction process', *AIChE Journal*, vol. 42, no. 10, pp. 2765–2772, 1996, doi: 10.1002/AIC.690421008.

[20]   IEA, 'Direct Air Capture', Nov. 2021. Accessed: May 02, 2022. [Online]. Available: https://www.iea.org/reports/direct-air-capture

[21]   P. Noothout, F. Wiersma, O. Hurtado, D. Macdonald, J. Kemper, and K. van Alphen, 'CO_2 pipeline infrastructure - lessons learnt', *Energy Procedia*, vol. 63, pp. 2481–2492, 2014, doi: 10.1016/J.EGYPRO.2014.11.271.

[22]   J. M. Race, B. Wetenhall, P. N. Seevam, and M. J. Downie, 'Towards a CO_2 Pipeline Specification: Defining Tolerance Limits for Impurities', *J Pipeline Eng*, vol. 11, no. 3, pp. 173–190, 2012.

[23]   P. N. Seevam, J. M. Race, and M. J. Downie, 'Infrastructure and pipeline technology for carbon dioxide (CO_2) transport', *Developments and Innovation in Carbon Dioxide (CO_2) Capture and Storage Technology*, pp. 408–434, 2010, doi: 10.1533/9781845699574.4.408.

[24]   K. Michael *et al.*, 'CO_2 storage in saline aquifers I - Current state of scientific knowledge', *Energy Procedia*, vol. 1, no. 1, pp. 3197–3204, 2009, doi: 10.1016/J.EGYPRO.2009.02.103.

[25]   Global CCS Institute, 'Global Status of CCS 2020', 2021.

[26]   D. Winslow, 'Industry Experience with CO_2 for Enhanced Oil Recovery Workshop on California Opportunities for CCUS/EOR', 2012.

[27]   'Can CO_2-EOR really provide carbon-negative oil? – Analysis - IEA'. Accessed: Jul. 14, 2022. [Online]. Available: https://www.iea.org/commentaries/can-co2-eor-really-provide-carbon-negative-oil

[28]   IEA, 'Net Zero by 2050', Paris, 2021. Accessed: May 02, 2022. [Online]. Available: www.iea.org/t&c/

[29]   K. Zenz, C. F. Harvey, M. J. Aziz, D. P. Schrag, and K. Zenz House, 'The energy penalty of post-combustion CO_2 capture & storage and its implications for retrofitting the U.S. installed base', *Energy Environ Sci*, vol. 2 pp.193 – 205, 2009, doi: 10.1039/b811608c.

[30]   IEA, 'Is carbon capture too expensive?', 2021. Accessed Aug. 03, 2022. [Online]. Available: https://www.iea.org/commentaries/is-carbon-capture-too-expensive.

[31]   Global CCS Institute, 'Global costs of carbon capture and storage 2017 Update', 2017.

[32]   AER, 'Quest Carbon Capture and Storage Project: ANNUAL SUMMARY REPORT', 2020. Accessed: Jul. 14, 2022. [Online]. Available: https://open.alberta.ca/dataset/d5694c02-019d-4650-8b09-3b5a9afff181/resource/5343e39b-64c7-4c27-a580-c5b13dce71d9/download/quest-annual-summary-report-alberta-department-of-energy-2020.pdf

[33]   BEIS, 'The Ten Point Plan for a Green Industrial Revolution: Building back better, supporting green jobs, and accelerating our path to net zero.', London, UK, Nov. 2020. Accessed: May 06, 2022. [Online]. Available: https://assets.publishing.service.gov.uk/government/uploads/system/uploads/attachment_data/file/936567/10_POINT_PLAN_BOOKLET.pdf

[34]   BEIS, 'Net Zero Strategy: Build Back Greener', Cambridge, UK, Oct. 2021.

[35]   BEIS, 'Energy White Paper: Powering our Net Zero Future', London, 2020. Accessed: May 06, 2022. [Online]. Available: https://assets.publishing.service.gov.uk/government/uploads/system/uploads/attachment_data/file/945899/201216_BEIS_EWP_Command_Paper_Accessible.pdf

[36]   BEIS, 'British Energy Security Strategy: Secure, clean and affordable British energy for the long term', London, UK, 2022. Accessed: May 06, 2022. [Online]. Available: https://assets.publishing.service.gov.uk/government/uploads/system/uploads/attachment_data/file/1069969/british-energy-security-strategy-web-accessible.pdf

[37]   Elemental energy, 'Shipping CO_2 – UK Cost Estimation Study', Cambridge UK, Nov. 2018. Accessed: May 06, 2022. [Online]. Available: https://assets.publishing.service.gov.uk/government/uploads/system/uploads/attachment_data/file/761762/BEIS_Shipping_CO2.pdf

[38]   Reiner, D., 'Carbon Capture and Storage', Dec. 2019, doi: 10.1039/9781788012744.

[39]   K. Jiang, P. Feron, A. Cousins, R. Zhai, and K. Li, 'Achieving Zero/Negative-Emissions Coal-Fired Power Plants Using Amine-Based Postcombustion CO_2

Capture Technology and Biomass Cocombustion', *Environ Sci Technol*, vol. 54, no. 4, pp. 2429–2438, 2020, doi: 10.1021/ACS.EST.9B07388/SUPPL_FILE/ES9B07388_SI_001.PDF.

[40] H. Panahi, A. Eslami, M. A. Golozar, A. Ashrafi Laleh, M. Aryanpur, and M. Mazarei, 'Failure analysis of type 304 stainless steel amine exchanger sheets in a gas sweetening plant', *Case Stud Eng Fail Anal*, vol. 9, pp. 87–98, 2017, doi: 10.1016/J.CSEFA.2017.08.002.

[41] B. Dutcher, M. Fan, and A. G. Russell, 'Amine-based CO_2 capture technology development from the beginning of 2013 - A Review', *ACS Appl Mater Interfaces*, vol. 7, no. 4, pp. 2137–2148, 2015.

[42] S. Mokhatab, J. Y. Mak, J. v Valappil, and D. A. Wood, *Liquefied Natural Gas Safety and Security Aspects*. 2014. Accessed: Jul. 27, 2022. [Online]. Available: http://www.sciencedirect.com/science/article/pii/B978012404585900009X

[43] A. K. Coker, 'Petroleum, Complex-Mixture Fractionation, Gas Processing, Dehydration, Hydrocarbon Absorption and Stripping', *Ludwig's Applied Process Design for Chemical and Petrochemical Plants*, pp. 269–344, 2010, doi: 10.1016/B978-0-7506-8366-1.10011-8.

[44] J. W. Dijkstra, S. Walspurger, G. D. Elzinga, J. A. Z. Pieterse, J. Boon, and W. G. Haije, 'Evaluation of Postcombustion CO_2 Capture by a Solid Sorbent with Process Modeling Using Experimental CO_2 and H_2O Adsorption Characteristics', *Ind Eng Chem Res*, vol. 57, no. 4, pp. 1245–1261, 2018, doi: 10.1021/acs.iecr.7b03552.

[45] Mr Adam Siemenski, 'Technology Readiness and Costs of CCS Technology Readiness and costs of CCS 2: The Circular Carbon Economy: Keystone to Global Sustainability Series, 2021.

[46] C. Font-Palma, D. Cann, C. Udemu, and O. García, 'Review of Cryogenic Carbon Capture Innovations and Their Potential Applications', *J Carbon Res*, vol. 7, no. 3, p. 58, 2021, doi: 10.3390/C7030058.

[47]   A. Brunetti, F. Scura, G. Barbieri, and E. Drioli, 'Membrane technologies for CO2 separation', *J Memb Sci*, vol. 359, no. 1–2, pp. 115–125, 2010, doi: 10.1016/J.MEMSCI.2009.11.040.

[48]   BEIS, 'Hydrogen Production Costs 2021', 2021.

[49]   A. D. Ebner and J. A. Ritter, 'State-of-the-art adsorption and membrane separation processes for carbon dioxide production from carbon dioxide emitting industries', *Separation Sci Technol*, vol. 44, no. 6. pp. 1273–1421, 2009. doi: 10.1080/01496390902733314.

[50]   P. Nikolaidis and A. Poullikkas, 'A comparative overview of hydrogen production processes', *Renew Sustain Energy Rev*, vol. 67, pp. 597–611, 2017. doi: 10.1016/j.rser.2016.09.044.

[51]   S. Sircar and T. C. Golden, 'Pressure swing adsorption technology for hydrogen production', *Hydrogen and syngas production and purification technologies*, vol. 10, pp. 414–450, 2009.

[52]   S. Ahn, Y. W. You, D. G. Lee, K. H. Kim, M. Oh, and C. H. Lee, 'Layered two- and four-bed PSA processes for H_2 recovery from coal gas', *Chem Eng Sci*, vol. 68, no. 1, pp. 413–423, 2012, doi: 10.1016/J.CES.2011.09.053.

[53]   J. A. Ritter and A. D. Ebner, 'State-of-the-Art Adsorption and Membrane Separation Processes for Hydrogen Production in the Chemical and Petrochemical Industries', *Separation Sci Technol*, vol. 42, no. 6, pp. 1123–1193, 2007, doi: 10.1080/01496390701242194.

[54]   L. O. Nord, R. Anantharaman, and O. Bolland, 'Design and off-design analyses of a pre-combustion CO_2 capture process in a natural gas combined cycle power plant', *Int J Greenhouse Gas Control*, vol. 3, no. 4, pp. 385–392, 2009, doi: 10.1016/J.IJGGC.2009.02.001.

[55]   G. Bang, D. K. Moon, J. H. Kang, Y. J. Han, K. M. Kim, and C. H. Lee, 'High-purity hydrogen production via a water-gas-shift reaction in a palladium-copper

catalytic membrane reactor integrated with pressure swing adsorption', *Chem Eng J*, vol. 411, 2021, doi: 10.1016/J.CEJ.2021.128473.

[56]   K. Kian *et al.*, 'Prospects of CO_2 capture via 13X for low-carbon hydrogen production using a Pd-based metallic membrane reactor', *Chem Eng J*, vol. 407, p. 127224, 2021, doi: 10.1016/j.cej.2020.127224.

[57]   F. Gallucci, E. Fernandez, P. Corengia, and M. van Sint Annaland, 'Recent advances on membranes and membrane reactors for hydrogen production', *Chem Eng Sci*, vol. 92, pp. 40–66, 2013, doi: 10.1016/J.CES.2013.01.008.

[58]   A. Basile, A. Iulianelli, and J. Tong, 'Single-stage hydrogen production and separation from fossil fuels using micro- and macromembrane reactors', *Compendium of Hydrogen Energy*, pp. 445–468, 2015, doi: 10.1016/B978-1-78242-361-4.00015-7.

[59]   C. A. Scholes, K. H. Smith, S. E. Kentish, and G. W. Stevens, 'CO_2 capture from pre-combustion processes—Strategies for membrane gas separation', *Int J Greenhouse Gas Control*, vol. 4, no. 5, pp. 739–755, 2010, doi: 10.1016/J.IJGGC.2010.04.001.

[60]   H. Lin *et al.*, 'CO_2-selective membranes for hydrogen production and CO_2 capture – Part I: Membrane development', *J Memb Sci*, vol. 457, pp. 149–161, 2014, doi: 10.1016/J.MEMSCI.2014.01.020.

[61]   H. Lin *et al.*, 'CO_2-selective membranes for hydrogen production and CO_2 capture - Part II: Techno-economic analysis', *J Memb Sci*, vol. 493, pp. 794–806, 2015, doi: 10.1016/J.MEMSCI.2015.02.042.

[62]   M. de Falco, A. Salladini, E. Palo, and G. Iaquaniello, 'Pd-Alloy Membrane Reactor for Natural Gas Steam Reforming: an Innovative Process Design for the Capture of CO_2', *Ind Eng Chem Res*, vol. 54, no. 27, pp. 6950–6958, 2015, doi: 10.1021/acs.iecr.5b01141.

[63]   S. Yun and S. Ted Oyama, 'Correlations in palladium membranes for hydrogen separation: A review', *J Memb Sci*, vol. 375, no. 1–2, pp. 28–45, 2011, doi: 10.1016/J.MEMSCI.2011.03.057.

[64]   M. A. Habib *et al.*, 'Palladium-Alloy Membrane Reactors for Fuel Reforming and Hydrogen Production: A Review', 2021, doi: 10.1021/acs.energyfuels.0c04352.

[65]   D. Alique, D. Martinez-Diaz, R. Sanz, and J. A. Calles, 'Review of Supported Pd-Based Membranes Preparation by Electroless Plating for Ultra-Pure Hydrogen Production', *Membranes,* vol. 8, no. 1, p. 5, 2018, doi: 10.3390/MEMBRANES8010005.

[66]   N. A. Al-Mufachi, N. v. Rees, and R. Steinberger-Wilkens, 'Hydrogen selective membranes: A review of palladium-based dense metal membranes', *Renew Sustain Energy Rev*, vol. 47, pp. 540–551, 2015, doi: 10.1016/J.RSER.2015.03.026.

[67]   N. Pomerantz and M. Yi Hua, 'Effect of H_2S on the Performance and Long-Term Stability of Pd/Cu Membranes', *Ind Eng Chem Res*, vol. 48, no. 8, pp. 4030–4039, 2009, doi: 10.1021/IE801947A.

[68]   E. Palo, A. Salladini, B. Morico, V. Palma, A. Ricca, and G. Iaquaniello, 'Application of Pd-Based Membrane Reactors: An Industrial Perspective', *Membranes,* vol. 8, no. 4, p. 101, 2018, doi: 10.3390/MEMBRANES8040101.

[69]   J. Hufton, S. Mayorga, T. Gaffney, S. Nataraj, M. Rao, and S. Sircar, 'Sorption Enhanced Reaction Process (SERP) For the Production of Hydrogen', *U.S. DOE Hydrogen Program Review*, vol. 2, pp. 693–705, 1996.

[70]   R. Belén, B. Menendez, C. Graschinsky, and N. E. Amadeo, 'Sorption-Enhanced Ethanol Steam Reforming Process in a Fixed-Bed Reactor', 2018, doi: 10.1021/acs.iecr.8b01657.

[71]   R. B. Menendez, C. Graschinsky, and N. E. Amadeo, 'Sorption-enhanced ethanol steam reforming process in a fixed-bed reactor', *Ind Eng Chem Res*, vol. 57, no. 34, pp. 11547–11553, 2018, doi:

10.1021/ACS.IECR.8B01657/ASSET/IMAGES/MEDIUM/IE-2018-01657K_0009.GIF.

[72]   H. A. J van Dijk *et al.*, 'STEPWISE Project: Sorption-Enhanced Water-Gas Shift Technology to Reduce Carbon Footprint in the Iron and Steel Industry An introduction to the project, its aims and its technology Leon van de Water Calin-Cristian Cormos', *Technol. Rev*, vol. 62, no. 4, pp. 395–402, 2018, doi: 10.1595/205651318X15268923666410.

[73]   S. Masoudi Soltani, A. Lahiri, H. Bahzad, P. Clough, M. Gorbounov, and Y. Yan, 'Sorption-enhanced Steam Methane Reforming for Combined CO_2 Capture and Hydrogen Production: A State-of-the-Art Review', *Carbon Capture Sci & Technol*, vol. 1, p. 100003, 2021, doi: 10.1016/J.CCST.2021.100003.

[74]   D. Jansen *et al.*, 'SEWGS Technology is Now Ready for Scale-up!', *Energy Procedia*, vol. 37, pp. 2265–2273, 2013, doi: 10.1016/j.egypro.2013.06.107.

[75]   G. Manzolini, A. Giuffrida, P. D. Cobden, H. A. J. van Dijk, F. Ruggeri, and F. Consonni, 'Techno-economic assessment of SEWGS technology when applied to integrated steel-plant for CO_2 emission mitigation', *Int J Greenhouse Gas Control*, vol. 94, p. 102935, 2020, doi: 10.1016/J.IJGGC.2019.102935.

[76]   M. Gazzani, M. C. Romano, and G. Manzolini, 'CO_2 capture in integrated steelworks by commercial-ready technologies and SEWGS process', *Int J Greenhouse Gas Control*, vol. 41, pp. 249–267, 2015.

[77]   D. Jansen *et al.*, 'SEWGS technology is now ready for scale-up!', *Energy Procedia*, vol. 37, pp. 2265–2273, 2013.

[78]   L. Petrescu, D. A. Chisalita, C. C. Cormos, G. Manzolini, P. Cobden, and H. A. J. van Dijk, 'Life cycle assessment of SEWGS technology applied to integrated steel plants', *Sustainability (Switzerland)*, vol. 11, no. 7, 2019, doi: 10.3390/su11071825.

[79]   R. Quinn, R. J. Kitzhoffer, J. R. Hufton, and T. C. Golden, 'A High Temperature Lithium Orthosilicate-Based Solid Absorbent for Post Combustion CO_2 Capture', *Ind Eng Chem Res*, vol. 51, no. 27, pp. 9320–9327, 2012, doi: 10.1021/IE300157M.

[80] Y. Wang *et al.*, 'A review of CO_2 sorbents for promoting hydrogen production in the sorption-enhanced steam reforming process', *Int J Hydrogen Energy*, vol. 46, no. 45, pp. 23358–23379, 2021, doi: 10.1016/J.IJHYDENE.2021.01.206.

[81] BEIS, 'Industrial Decarbonisation Strategy', 2021.

[82] 'CO_2 Capture In The Cement Industry - Technical Study', 2008. Accessed: Aug. 26, 2022. [Online]. Available: www.ieagreen.org.uk

[83] S. M. N. Hassan, P. L. Douglas, and E. Croiset, 'Techno-Economic Study of CO_2 Capture from an Existing Cement Plant Using MEA Scrubbing', *Int J Green Energy*, vol. 4, no. 2, pp. 197–220, 2007, doi: 10.1080/01971520600873418.

[84] L.-M. Bjerge and P. Brevik, 'CO_2 Capture in the Cement Industry, Norcem CO_2 Capture Project (Norway)', *Energy Procedia*, vol. 63, pp. 6455–6463, 2014, doi: 10.1016/j.egypro.2014.11.680.

[85] A. Arasto, E. Tsupari, J. Kärki, E. Pisilä, and L. Sorsamäki, 'Post-combustion capture of CO_2 at an integrated steel mill – Part I: Technical concept analysis', *Int J Greenhouse Gas Control*, vol. 16, pp. 271–277, 2013, doi: 10.1016/J.IJGGC.2012.08.018.

[86] W. Uribe-Soto, J. F. Portha, J. M. Commenge, and L. Falk, 'A review of thermochemical processes and technologies to use steelworks off-gases', *Renew Sustain Energy Rev*, vol. 74, pp. 809–823, 2017, doi: 10.1016/J.RSER.2017.03.008.

[87] IEAGHG, 'CO_2 Abatement In Oil Refineries: Fired Heaters CO_2 abatement in oil refineries: fired heaters Background', Cheltenham, 2000. Accessed: Aug. 26, 2022. [Online]. Available: https://ieaghg.org/docs/General_Docs/Reports/Ph3_31%20Oil%20refinery%20fired %20heaters.PDF

[88] J. van Straelen, F. Geuzebroek, N. Goodchild, G. Protopapas, and L. Mahony, 'CO_2 capture for refineries, a practical approach', *Energy Procedia*, vol. 1, no. 1, pp. 179–185, 2009, doi: 10.1016/j.egypro.2009.01.026.

[89]   M. P. S. Santos, V. Manovic, and D. P. Hanak, 'Unlocking the potential of pulp and paper industry to achieve carbon-negative emissions via calcium looping retrofit', *J Clean Prod*, vol. 280, p. 124431, 2021, doi: 10.1016/J.JCLEPRO.2020.124431.

[90]   D. M. Ruthven, 'Past Progress and Future Challenges in Adsorption Research', *Ind Eng Chem Res*, vol. 39, no. 7, pp. 2127–2131, 2000, doi: 10.1021/ie000060d.

[91]   P. A. Jacobs, E. M. Flanigen, J. C. Jansen, and H. van Bekkum, *Introduction to zeolite science and practice*. Elsevier, 2001.

[92]   P. W. Atkins, 'The kinetic theory of gases', *Physical chemistry, 4th edition. Oxford University Press, Oxford*, p. 730, 1990.

[93]   R. T. Yang, *Adsorbents: fundamentals and applications*. John Wiley & Sons, 2003.

[94]   J.-R. Li, R. J. Kuppler, and H.-C. Zhou, 'Selective gas adsorption and separation in metal–organic frameworks', *Chem Soc Rev*, vol. 38, no. 5, p. 1477, 2009, doi: 10.1039/b802426j.

[95]   D. M. Ruthven, *Principles of adsorption and adsorption processes*. John Wiley & Sons, 1984.

[96]   G. Fiandaca, E. S. Fraga, and S. Brandani, 'Multicriteria Design framework for CO_2 capture by multi-step PSA cycles', 2009, pp. 603–608. doi: 10.1016/S1570-7946(09)70101-4.

[97]   C. Dhoke, A. Zaabout, S. Cloete, and S. Amini, 'Review on Reactor Configurations for Adsorption-Based CO_2 Capture', *Ind Eng Chem Res*, vol. 60, no. 10, pp. 3779–3798, 2021, doi: 10.1021/acs.iecr.0c04547.

[98]   A. Streb, M. Hefti, M. Gazzani, and M. Mazzotti, 'Novel Adsorption Process for Co-Production of Hydrogen and CO_2 from a Multicomponent Stream', *Ind Eng Chem Res*, vol. 58, no. 37, pp. 17489–17506, 2019, doi: 10.1021/acs.iecr.9b02817.

[99]   Y. Ju, H.-T. Oh, J.-C. Lee, and C.-H. Lee, 'Performance and dynamic behavior of sorption-enhanced water-gas shift reaction in a fluidized bed reactor for H_2

production and CO_2 capture', *Chem Eng J*, vol. 410, p. 127414, 2021, doi: 10.1016/j.cej.2020.127414.

[100] G. Schöny, F. Dietrich, J. Fuchs, T. Pröll, and H. Hofbauer, 'A multi-stage fluidized bed system for continuous CO_2 capture by means of temperature swing adsorption – First results from bench scale experiments', *Powder Technol*, vol. 316, pp. 519–527, 2017, doi: 10.1016/j.powtec.2016.11.066.

[101] G. E. Keller, 'Pressure swing adsorption. By Douglas M. Ruthven, Shamsuzzaman Farooq, and Kent S. Knaebel, VCH Publishers, New York, 1994', *AIChE J*, vol. 41, no. 1, pp. 201–201, 1995, doi: 10.1002/AIC.690410122.

[102] C. W. Skarstrom, 'Method and apparatus for fractionating gaseous mixtures by adsorption.', US2944627A, Jul. 12, 1960

[103] D. Diagne, M. Goto, and T. Hirose, 'Numerical analysis of a dual refluxed PSA process during simultaneous removal and concentration of carbon dioxide dilute gas from air', *J Chem Technol Biotechnol*, vol. 65, no. 1, pp. 29–38, 1996, doi: 10.1002/(SICI)1097-4660(199601)65:1<29::AID-JCTB388>3.0.CO;2-P.

[104] A. D. Ebner and J. A. Ritter, 'Equilibrium theory analysis of rectifying PSA for heavy component production', *AIChE J*, vol. 48, no. 8, pp. 1679–1691, 2002, doi: 10.1002/aic.690480810.

[105] J. Zhang and P. A. Webley, 'Cycle Development and Design for CO2 Capture from Flue Gas by Vacuum Swing Adsorption', *Environ Sci Technol*, vol. 42, no. 2, pp. 563–569, 2008, doi: 10.1021/es0706854.

[106] R. T. Yang, *Adsorbents: Fundamentals and Applications*. Hoboken, NJ, USA: John Wiley & Sons, Inc., 2003. doi: 10.1002/047144409X.

[107] S. Sircar, 'Pressure swing adsorption', *Ind Eng Chem Res*, vol. 41, no. 6. American Chemical Society, pp. 1389–1392, 20, 2002. doi: 10.1021/ie0109758.

[108] X. Zhu, S. Li, Y. Shi, and N. Cai, 'Recent advances in elevated-temperature pressure swing adsorption for carbon capture and hydrogen production', *Prog Energy Combust Sci*, vol. 75, p. 100784, 2019, doi: 10.1016/j.pecs.2019.100784.

[109] X. Zhu, S. Li, Y. Shi, and N. Cai, 'Recent advances in elevated-temperature pressure swing adsorption for carbon capture and hydrogen production', *Prog Energy Combust Sci*, vol. 75, 2019. doi: 10.1016/j.pecs.2019.100784.

[110] J. Hufton *et al.*, 'Sorption Enhanced Water Gas Shift Process', *US DOE Hydrogen Program Review*, vol. 2, pp. 693 - 706, 1996.

[111] R. J. Allam, R. Chiang, J. R. Hufton, P. Middleton, E. L. Weist, and V. White, 'Development of the sorption enhanced water gas shift process', *Carbon dioxide capture for storage in deep geologic formations*, vol. 1, pp. 227–256, 2005.

[112] M. G. Beaver, H. S. Caram, and S. Sircar, 'Selection of CO_2 chemisorbent for fuel-cell grade H_2 production by sorption-enhanced water gas shift reaction', *Int J Hydrogen Energy*, vol. 34, no. 7, pp. 2972–2978, 2009, doi: 10.1016/j.ijhydene.2009.01.065.

[113] B. Verougstraete, A. Martín-Calvo, S. van der Perre, G. Baron, V. Finsy, and J. F. M. Denayer, 'A new honeycomb carbon monolith for CO_2 capture by rapid temperature swing adsorption using steam regeneration', *Chem Eng J*, vol. 383, p. 123075, 2020, doi: 10.1016/J.CEJ.2019.123075.

[114] S. E. Zanco, M. Ambrosetti, G. Groppi, E. Tronconi, and M. Mazzotti, 'Heat transfer intensification with packed open-cell foams in TSA processes for CO_2 capture', *Chem Eng J*, vol. 430, p. 131000, 2022, doi: 10.1016/J.CEJ.2021.131000.

[115] E. Meloni, M. Martino, P. Pullumbi, F. Brandani, and V. Palma, 'Intensification of TSA processes using a microwave-assisted regeneration step', *Chem Eng Process*, vol. 160, p. 108291, Mar. 2021, doi: 10.1016/J.CEP.2020.108291.

[116] G. Mondino, C. A. Grande, R. Blom, and L. O. Nord, 'Evaluation of MBTSA technology for CO_2 capture from waste-to-energy plants', *Int J Greenhouse Gas Control*, vol. 118, p. 103685, 2022, doi: 10.1016/J.IJGGC.2022.103685.

[117] C. A. Grande, H. Kvamsdal, G. Mondino, and R. Blom, 'Development of Moving Bed Temperature Swing Adsorption (MBTSA) Process for Post-combustion CO2

Capture: Initial Benchmarking in a NGCC Context', *Energy Procedia*, vol. 114, pp. 2203–2210, 2017, doi: 10.1016/J.EGYPRO.2017.03.1357.

[118] L. Chen, S. Deng, R. Zhao, Y. Zhu, L. Zhao, and S. Li, 'Temperature swing adsorption for CO2 capture: Thermal design and management on adsorption bed with single-tube/three-tube internal heat exchanger', *Appl Therm Eng*, vol. 199, p. 117538, 2021, doi: 10.1016/J.APPLTHERMALENG.2021.117538.

[119] J. R. McDonough, R. Law, D. A. Reay, and V. Zivkovic, 'Intensified carbon capture using adsorption: Heat transfer challenges and potential solutions', *Therm Sci Eng Prog*, vol. 8, pp. 17–30, 2018, doi: 10.1016/J.TSEP.2018.07.012.

[120] C. A. Grande, 'Advances in Pressure Swing Adsorption for Gas Separation', *ISRN Chem Eng J*, vol. 2012, pp. 1–13, 2012, doi: 10.5402/2012/982934.

[121] P. Pullumbi, F. Brandani, and S. Brandani, 'Gas separation by adsorption: technological drivers and opportunities for improvement', *Curr Opin Chem Eng*, vol. 24, pp. 131–142, 2019, doi: 10.1016/j.coche.2019.04.008.

[122] J. Wang *et al.*, 'Recent advances in solid sorbents for CO_2 capture and new development trends', *Energy Environ Sci*, vol. 7, no. 11, pp. 3478–3518, 2014.

[123] Y. Hu, Y. Guo, J. Sun, H. Li, and W. Liu, 'Progress in MgO sorbents for cyclic CO_2 capture: a comprehensive review', *J Mater Chem A*, vol. 7, no. 35, pp. 20103–20120, Sep. 2019, doi: 10.1039/C9TA06930E.

[124] A. H. Ruhaimi, M. A. A. Aziz, and A. A. Jalil, 'Magnesium oxide-based adsorbents for carbon dioxide capture: Current progress and future opportunities', *J CO2 Util*, vol. 43, p. 101357, 2021, doi: 10.1016/J.JCOU.2020.101357.

[125] Y. Hu, W. Liu, Y. Yang, M. Qu, and H. Li, 'CO_2 capture by Li_4SiO_4 sorbents and their applications: Current developments and new trends', *Chem Eng J*, vol. 359, pp. 604–625, 2019, doi: 10.1016/J.CEJ.2018.11.128.

[126] Y. Zhang *et al.*, 'Recent advances in lithium containing ceramic based sorbents for high-temperature CO_2 capture', *J Mater Chem A*, vol. 7, no. 14, pp. 7962–8005, 2019, doi: 10.1039/C8TA08932A.

[127] J. Chen, L. Duan, and Z. Sun, 'Review on the Development of Sorbents for Calcium Looping', *Energy & Fuels*, vol. 34, no. 7, pp. 7806–7836, 2020, doi: 10.1021/ACS.ENERGYFUELS.0C00682/ASSET/IMAGES/MEDIUM/EF0C00682 _0010.GIF.

[128] A. M. Kierzkowska, R. Pacciani, and C. R. Müller, 'CaO-Based CO_2 Sorbents: From Fundamentals to the Development of New, Highly Effective Materials', *ChemSusChem*, vol. 6, no. 7, pp. 1130–1148, 2013, doi: 10.1002/CSSC.201300178.

[129] M. T. Dunstan, F. Donat, A. H. Bork, C. P. Grey, and C. R. Müller, 'CO_2 Capture at Medium to High Temperature Using Solid Oxide-Based Sorbents: Fundamental Aspects, Mechanistic Insights, and Recent Advances', *Chem Rev*, vol. 121, no. 20, pp. 12681–12745, 2021, doi: 10.1021/ACS.CHEMREV.1C00100/ASSET/IMAGES/MEDIUM/CR1C00100_002 2.GIF.

[130] F. Donat and C. R. Müller, 'Prospects of MgO-based sorbents for CO_2 capture applications at high temperatures', *Curr Opin Green Sustain Chem*, vol. 36, p. 100645, 2022, doi: 10.1016/j.cogsc.2022.100645.

[131] A. Dal Pozzo, A. Armutlulu, M. Rekhtina, P. M. Abdala, and C. R. Müller, 'CO_2 Uptake and Cyclic Stability of MgO-Based CO_2 Sorbents Promoted with Alkali Metal Nitrates and Their Eutectic Mixtures', *ACS Appl Energy Mater*, vol. 2, no. 2, pp. 1295–1307, 2019, doi: 10.1021/ACSAEM.8B01852.

[132] Y. Qiao *et al.*, 'Alkali Nitrates Molten Salt Modified Commercial MgO for Intermediate-Temperature CO_2 Capture: Optimization of the Li/Na/K Ratio', *Ind Eng Chem Res*, vol. 56, no. 6, pp. 1509–1517, 2017, doi: 10.1021/ACS.IECR.6B04793.

[133] H. Pang, H. Xu, A. Sun, and G. Xiao, 'Characteristics of MgO-based sorbents for CO_2 capture at elevated temperature and pressure', *Appl Surf Sci*, vol. 598, p. 153852, 2022, doi: 10.1016/J.APSUSC.2022.153852.

[134] W. Gao, T. Zhou, Y. Gao, B. Louis, D. O'Hare, and Q. Wang, 'Molten salts-modified MgO-based adsorbents for intermediate-temperature CO_2 capture: A review', *J Energy Chem*, vol. 26, no. 5, pp. 830–838, 2017, doi: 10.1016/J.JECHEM.2017.06.005.

[135] S. J. Mills, A. G. Christy, J.-M. R. Génin, T. Kameda, and F. Colombo, 'Nomenclature of the hydrotalcite supergroup: natural layered double hydroxides', *Mineral Mag*, vol. 76, no. 5, pp. 1289–1336, 2012, doi: 10.1180/minmag.2012.076.5.10.

[136] D. M. C. Huminicki and F. C. Hawthorne, 'THE CRYSTAL STRUCTURE OF NIKISCHERITE, Na Fe^{2+}_6 $Al_3(SO_4)^2$ $(OH)_{18}$ $(H_2O)_{12}$, A MINERAL OF THE SHIGAITE GROUP', *Can Mineral*, vol. 41, no. 1, pp. 79–82, 2003, doi: 10.2113/gscanmin.41.1.79.

[137] M. A. Cooper and F. C. Hawthorne, 'The crystal structure of shigaite, [AlMn2+2(OH)6]3(SO4)Na(H2O)6{H2O}6 , hydrotalcite-group mineral', *Can Mineral*, vol. 34, no. 1, pp. 91–97, 1996.

[138] J. Rius and R. Allmann, 'The superstructure of the double layer mineral wermlandite [Mg_7($Al_{0.57}$, $Fe^{3+}_{0.43}$) $(OH)_{18}$]$^{2+}$ · [($Ca_{0.6}Mg_{0.4}$)$(SO_4)_2(H_2O)_{12}$]$^{2-}$', *Z Kristallogr Cryst Mater*, vol. 168, no. 1–4, pp. 1–12, 1984, doi: 10.1524/zkri.1984.168.14.133.

[139] A. S. Bookin, V. I. Cherkashin, and V. A. Drits, 'Polytype diversity of the hydrotalcite-like minerals II. determination of the polytypes of experimentally studied varieties', *Clays Clay Miner*, vol. 41, no. 5, pp. 558–564, 1993, doi: 10.1346/CCMN.1993.0410505.

[140] A. S. Bookin and V. A. Drits, 'Polytype diversity of the hydrotalcite-like minerals I. possible polytypes and their diffraction features', *Clays Clay Miner*, vol. 41, no. 5, pp. 551–557, 1993, doi: 10.1346/CCMN.1993.0410504.

[141] F. Li and X. Duan, 'Applications of Layered Double Hydroxides', in *Layered Double Hydroxides*, X. Duan and D. G. Evans, Eds. Berlin, Heidelberg: Springer Berlin Heidelberg, 2006, pp. 193–223. doi: 10.1007/430_007.

[142] G. v. Manohara, M. M. Maroto-Valer, and S. Garcia, 'The effect of the layer-interlayer chemistry of LDHs on developing high temperature carbon capture materials', *Dalton Trans*, vol. 49, no. 3, pp. 923–931, 2020, doi: 10.1039/C9DT03913A.

[143] F. J. Broecker *et al.*, 'Catalyst for the manufacture of gases containing methane ', US3941721A, Mar. 02, 1976 Accessed: Oct. 03, 2022. [Online]. Available: https://patents.google.com/patent/US3941721A/en?q=Catalyst+for+the+manufacture +of+gases+containing+methane&assignee=BASF+Aktiengesellschaft

[144] T. Baskaran, J. Christopher, and A. Sakthivel, 'Progress on layered hydrotalcite (HT) materials as potential support and catalytic materials', *RSC Adv*, vol. 5, no. 120, pp. 98853–98875, 2015, doi: 10.1039/c5ra19909c.

[145] Q. Wang and D. O'Hare, 'Recent Advances in the Synthesis and Application of Layered Double Hydroxide (LDH) Nanosheets', *Chem Rev*, vol. 112, no. 7, pp. 4124–4155, 2012, doi: 10.1021/cr200434v.

[146] F. Cavani, F. Trifiro, and A. Vaccari, 'Hydrotalcite-type anionic clays: Preparation, properties and applications.', *Catal Today*, vol. 11, no. 2, pp. 173–301, 1991.

[147] C. Forano, U. Costantino, V. Prévot, and C. T. Gueho, 'Layered Double Hydroxides (LDH)', *Dev Clay Sci*, vol. 5, pp. 745–782, 2013, doi: 10.1016/B978-0-08-098258-8.00025-0.

[148] B. Arstad *et al.*, 'Synthesis and Evaluation of K-Promoted Co3-xMgxAl-Oxides as Solid CO_2Sorbents in the Sorption-Enhanced Water-Gas Shift (SEWGS) Reaction', *Ind Eng Chem Res*, vol. 59, no. 40, pp. 17837–17844, 2020, doi: 10.1021/acs.iecr.0c02322.

[149] H. Tagaya, K. Tsunaki, M. Hasegawa, M. Karasu, and K. Chiba, 'Adsorption of CO_2 into hydrotalcite like compound', *Bul Yam Univ (Eng)*, vol. 22, pp. 21–26, 1992.

[150] Y. Ding and E. Alpay, 'Equilibria and kinetics of CO_2 adsorption on hydrotalcite adsorbent', *Chem Eng Sci*, vol. 55, 2000.

[151] Y. Ding and E. Alpay, 'High temperature recovery of CO_2 from flue gases using hydrotalcite adsorbent', *Process Saf*, vol. 79, no. 1, pp. 45–51, 2001, doi: 10.1205/095758201531130.

[152] Z. Yong, V. Mata, and A. E. Rodrigues, 'Adsorption of carbon dioxide onto hydrotalcite-like compounds (HTlcs) at high temperatures', *Ind Eng Chem Res*, vol. 40, no. 1, pp. 204–209, 2001, doi: 10.1021/ie000238w.

[153] C. v. Miguel *et al.*, 'High temperature CO_2 sorption with gallium-substituted and promoted hydrotalcites', *Sep Purif Technol*, vol. 127, pp. 202–211, 2014, doi: 10.1016/j.seppur.2014.03.007.

[154] E. L. G. Oliveira, C. A. Grande, and A. E. Rodrigues, 'CO_2 sorption on hydrotalcite and alkali-modified (K and Cs) hydrotalcites at high temperatures', *Sep Purif Technol*, vol. 62, no. 1, pp. 137–147, 2008, doi: 10.1016/j.seppur.2008.01.011.

[155] R. F. P. M. Moreira, J. L. Soares, G. L. Casarin, and A. E. Rodrigues, 'Adsorption of CO_2 on hydrotalcite-like compounds in a fixed bed', *Sep Sci Technol*, vol. 41, no. 2, pp. 341–357, 2006, doi: 10.1080/01496390500496827.

[156] J. Jos´ *et al.*, 'Experimental and Theoretical Analysis for the CO_2 Adsorption on Hydrotalcite', *Adsorption*, vol. 11, pp. 237-241, 2005, doi: 10.1007/s10450-005-5930-7.

[157] J. L. Soares, R. F. P. M. Moreira, H. J. José, C. A. Grande, and A. E. Rodrigues, 'Hydrotalcite materials for carbon dioxide adsorption at high temperatures: Characterization and diffusivity measurements', *Sep Sci Technol*, vol. 39, no. 9, pp. 1989–2010, 2004, doi: 10.1081/SS-120039307.

[158] N. Chanburanasiri, A. M. Ribeiro, A. E. Rodrigues, N. Laosiripojana, and S. Assabumrungrat, 'Simulation of methane steam reforming enhanced by in situ CO_2 Sorption Using K_2CO_3-promoted hydrotalcites for H_2 production', *Energy & Fuels*, Aug. 2013, vol. 27, no. 8, pp. 4457–4470. doi: 10.1021/ef302043e.

[159] Y. J. Wu, P. Li, J. G. Yu, A. F. Cunha, and A. E. Rodrigues, 'K-Promoted Hydrotalcites for CO_2 Capture in Sorption Enhanced Reactions', *Chem Eng Technol*, vol. 36, no. 4, pp. 567–574, 2013, doi: 10.1002/ceat.201200694.

[160] N. Chanburanasiri *et al.*, 'Hydrogen production via sorption enhanced steam methane reforming process using Ni/CaO multifunctional catalyst', *Ind Eng Chem Res*, vol. 50, no. 24, pp. 13662–13671, 2011, doi: 10.1021/ie201226j.

[161] A. F. Cunha, Y. J. Wu, F. A. Diaz Alvarado, J. C. Santos, P. D. Vaidya, and A. E. Rodrigues, 'Steam reforming of ethanol on a Ni/Al_2O_3 catalyst coupled with a hydrotalcite-like sorbent in a multilayer pattern for CO_2 uptake', *Can J Chem Eng*, vol. 90, no. 6, pp. 1514–1526, 2012.

[162] S. Li, A. M. Ribeiro, Y. Shi, M. N. Moreira, N. Cai, and A. E. Rodrigues, 'Synthesis, Pelleting, and Performance Evaluation of a Novel K-Promoted γ-Alumina/MgAl-Layered Double Oxide Composite Adsorbent for Warm Gas H_2/CO_2 Separation', *Ind Eng Chem Res*, vol. 54, no. 28, pp. 7154–7163, 2015, doi: 10.1021/acs.iecr.5b01342.

[163] S. P. Reynolds, A. D. Ebner, and J. A. Ritter, 'Stripping PSA Cycles for CO_2 Recovery from Flue Gas at High Temperature Using a Hydrotalcite-Like Adsorbent', *Ind Eng Chem Res*, vol. 45, no. 12, pp. 4278–4294, 2006, doi: 10.1021/IE051232F.

[164] H. Du, A. D. Ebner, and J. A. Ritter, 'Pressure dependence of the nonequilibrium kinetic model that describes the adsorption and desorption behavior of CO_2 in K-promoted hydrotalcite like compound', *Ind Eng Chem Res*, vol. 50, no. 1, pp. 412–418, 2011, doi: 10.1021/ie100965b.

[165] S. P. Reynolds, A. D. Ebner, and J. A. Ritter, 'Carbon dioxide capture from flue gas by pressure swing adsorption at high temperature using a K-promoted HTlc: Effects of mass transfer on the process performance', *Environ*, vol. 25, no. 4, pp. 334–342, 2006, doi: 10.1002/ep.10167.

[166] A. D. Ebner, S. P. Reynolds, and J. A. Ritter, 'Understanding the adsorption and desorption behavior of CO_2 on a K-promoted hydrotalcite-like compound (HTlc)

through nonequilibrium dynamic isotherms', *Ind Eng Chem Res*, vol. 45, no. 18, pp. 6387–6392, 2006, doi: 10.1021/ie060389k.

[167] A. D. Ebner, S. P. Reynolds, and J. A. Ritter, 'Nonequilibrium kinetic model that describes the reversible adsorption and desorption behavior of CO_2 in a K-promoted hydrotalcite-like compound', *Ind Eng Chem Res*, vol. 46, no. 6, pp. 1737–1744, 2007, doi: 10.1021/ie061042k.

[168] H. Du, C. T. Williams, A. D. Ebner, and J. A. Ritter, 'In situ FTIR spectroscopic analysis of carbonate transformations during adsorption and desorption of CO_2 in K-promoted HTlc', *Chem Mater*, vol. 22, no. 11, pp. 3519–3526, 2010, doi: 10.1021/cm100703e.

[169] H. T. J. Reijers, S. E. A. Valster-Schiermeier, P. D. Cobden, and R. W. van den Brink, 'Hydrotalcite as CO_2 Sorbent for Sorption-Enhanced Steam Reforming of Methane', *Ind Eng Chem Res*, vol. 45, no. 8, pp. 2522–2530, 2005, doi: 10.1021/IE050563P.

[170] E. R. van Selow, P. D. Cobden, A. D. Wright, R. W. van den Brink, and D. Jansen, 'Improved sorbent for the sorption-enhanced water-gas shift process', *Energy Procedia*, vol. 4, pp. 1090–1095, 2011, doi: 10.1016/j.egypro.2011.01.159.

[171] E. R. van Selow, P. D. Cobden, P. A. Verbraeken, J. R. Hufton, and R. W. van den Brink, 'Carbon capture by sorption-enhanced water-gas shift reaction process using hydrotalcite-based material', *Ind Eng Chem Res*, vol. 48, no. 9, pp. 4184–4193, 2009, doi: 10.1021/ie801713a.

[172] D. P. Harrison, 'Sorption-enhanced hydrogen production: A review', *Ind Eng Chem Res*, Sep. 2008, vol. 47, no. 17, pp. 6486–6501. doi: 10.1021/ie800298z.

[173] S. Walspurger, P. D. Cobden, O. v. Safonova, Y. Wu, and E. J. Anthony, 'High CO_2 storage capacity in alkali-promoted hydrotalcite-based material: In situ detection of reversible formation of magnesium carbonate', *Chem Eur J*, vol. 16, no. 42, pp. 12694–12700, 2010, doi: 10.1002/chem.201000687.

[174] S. Walspurger, P. D. Cobden, W. G. Haije, R. Westerwaal, G. D. Elzinga, and O. v. Safonova, 'In situ XRD detection of reversible dawsonite formation on alkali promoted alumina: A cheap sorbent for CO_2 capture', *Eur J Inorg Chem*, no. 17, pp. 2461–2464, 2010, doi: 10.1002/ejic.201000263.

[175] S. Walspurger, L. Boels, P. D. Cobden, G. D. Elzinga, W. G. Haije, and R. W. van den Brink, 'The crucial role of the K^+-aluminium oxide interaction in K^+-promoted alumina-and hydrotalcite-based materials for CO_2 sorption at high temperatures', *ChemSusChem*, vol. 1, no. 7, pp. 643–650, 2008, doi: 10.1002/cssc.200800085.

[176] H. A. J. van Dijk, S. Walspurger, P. D. Cobden, R. W. van den Brink, and F. G. de Vos, 'Testing of hydrotalcite-based sorbents for CO_2 and H_2S capture for use in sorption enhanced water gas shift', *Int J Greenhouse Gas Control*, vol. 5, no. 3, pp. 505–511, 2011, doi: 10.1016/j.ijggc.2010.04.011.

[177] K. Coenen, F. Gallucci, E. Hensen, and M. van Sint Annaland, 'Adsorption behavior and kinetics of H_2S on a potassium-promoted hydrotalcite', *Int J Hydrogen Energy*, vol. 43, no. 45, pp. 20758–20771, 2018, doi: 10.1016/j.ijhydene.2018.09.146.

[178] H. T. J. Reijers, J. Boon, G. D. Elzinga, P. D. Cobden, W. G. Haije, and R. W. van den Brink, 'Modeling study of the sorption-enhanced reaction process for CO_2 capture. I. Model development and validation', *Ind Eng Chem Res*, vol. 48, no. 15, pp. 6966–6974, 2009, doi: 10.1021/ie801319q.

[179] K. Coenen *et al.*, 'On the influence of steam on the CO_2 chemisorption capacity of a hydrotalcite-based adsorbent for SEWGS applications', *Chem Eng J*, vol. 314, pp. 554–569, 2017, doi: 10.1016/j.cej.2016.12.013.

[180] K. Coenen, F. Gallucci, E. Hensen, and M. van Sint Annaland, 'CO_2 and H_2O chemisorption mechanism on different potassium-promoted sorbents for SEWGS processes', *J CO2 Util*, vol. 25, pp. 180–193, 2018, doi: 10.1016/j.jcou.2018.04.002.

[181] K. Coenen, F. Gallucci, E. Hensen, and M. van Sint Annaland, 'Kinetic model for adsorption and desorption of H_2O and CO_2 on hydrotalcite-based adsorbents', *Chem Eng J*, vol. 355, pp. 520–531, 2019, doi: 10.1016/j.cej.2018.08.175.

[182] K. Coenen, F. Gallucci, B. Mezari, E. Hensen, and M. van Sint Annaland, 'An in-situ IR study on the adsorption of CO_2 and H_2O on hydrotalcites', *J CO2 Util*, vol. 24, pp. 228–239, 2018, doi: 10.1016/j.jcou.2018.01.008.

[183] K. Coenen, F. Gallucci, P. Cobden, E. van Dijk, E. J. M. Hensen, and M. V. S. Annaland, 'Chemisorption of H_2O and CO_2 on Hydrotalcites for Sorption-enhanced Water-gas-Shift Processes', in *Energy Procedia*, 2017, vol. 114, pp. 2228–2242. doi: 10.1016/j.egypro.2017.03.1360.

[184] K. Coenen, F. Gallucci, P. Cobden, E. van Dijk, E. Hensen, and M. van Sint Annaland, 'Influence of material composition on the CO_2 and H_2O adsorption capacities and kinetics of potassium-promoted sorbents', *Chem Eng J*, vol. 334, pp. 2115–2123, 2018, doi: 10.1016/j.cej.2017.11.161.

[185] J. Boon, P. D. Cobden, H. A. J. van Dijk, C. Hoogland, E. R. van Selow, and M. van Sint Annaland, 'Isotherm model for high-temperature, high-pressure adsorption of CO_2 and H_2O on K-promoted hydrotalcite', *Chem Eng J*, vol. 248, pp. 406–414, 2014, doi: 10.1016/j.cej.2014.03.056.

[186] X. Zhu, Y. Shi, and N. Cai, 'High-pressure carbon dioxide adsorption kinetics of potassium-modified hydrotalcite at elevated temperature', *Fuel*, vol. 207, pp. 579–590, 2017, doi: 10.1016/j.fuel.2017.06.137.

[187] X. Zhu, Y. Shi, and N. Cai, 'Characterization on trace carbon monoxide leakage in high purity hydrogen in sorption enhanced water gas shifting process', *Int J Hydrogen Energy*, vol. 41, no. 40, pp. 18050–18061, 2016, doi: 10.1016/j.ijhydene.2016.07.057.

[188] X. Zhu, C. Chen, Q. Wang, Y. Shi, D. O'Hare, and N. Cai, 'Roles for K_2CO_3 doping on elevated temperature CO_2 adsorption of potassium promoted layered double oxides', *Chem Eng J*, vol. 366, pp. 181–191, 2019, doi: 10.1016/J.CEJ.2019.01.192.

[189] X. Zhu *et al.*, 'Synthesis of elevated temperature CO_2 adsorbents from aqueous miscible organic-layered double hydroxides', *Energy*, vol. 167, pp. 960–969, 2019, doi: 10.1016/j.energy.2018.11.009.

[190] E. R. van Selow, P. D. Cobden, H. A. J. van Dijk, S. Walspurger, P. A. Verbraeken, and D. Jansen, 'Qualification of the ALKASORB sorbent for the sorption-enhanced water-gas shift process', *Energy Procedia*, vol. 37, pp. 180–189, 2013, doi: 10.1016/j.egypro.2013.05.100.

[191] G. Manzolini, E. MacChi, and M. Gazzani, 'CO_2 capture in Integrated Gasification Combined Cycle with SEWGS – Part B: Economic assessment', *Fuel*, vol. 105, pp. 220–227, 2013, doi: 10.1016/J.FUEL.2012.07.043.

[192] K. B. Lee, A. Verdooren, H. S. Caram, and S. Sircar, 'Chemisorption of carbon dioxide on potassium-carbonate-promoted hydrotalcite', *J Colloid Interface Sci*, vol. 308, no. 1, pp. 30–39, 2007, doi: 10.1016/j.jcis.2006.11.011.

[193] M. H. Halabi, M. H. J. M. de Croon, J. van der Schaaf, P. D. Cobden, and J. C. Schouten, 'High capacity potassium-promoted hydrotalcite for CO_2 capture in H_2 production', *Int J Hydrogen Energy*, vol. 37, no. 5, pp. 4516–4525, 2012, doi: 10.1016/j.ijhydene.2011.12.003.

[194] X. Zhu, C. Chen, Q. Wang, Y. Shi, D. O'Hare, and N. Cai, 'Roles for K_2CO_3 doping on elevated temperature CO2 adsorption of potassium promoted layered double oxides', *Chem Eng J*, vol. 366, pp. 181–191, 2019, doi: 10.1016/J.CEJ.2019.01.192.

[195] H. J. Th Reijers, S. E. A Valster-Schiermeier, P. D. Cobden, and R. W. van den Brink, 'Hydrotalcite as CO_2 Sorbent for Sorption-Enhanced Steam Reforming of Methane', 2006, doi: 10.1021/ie050563p.

[196] S. Li, Y. Shi, Y. Yang, Y. Zheng, and N. Cai, 'High-performance CO_2 adsorbent from interlayer potassium-promoted stearate-pillared hydrotalcite precursors', *Energy & Fuels*, vol. 27, no. 9, pp. 5352–5358, 2013, doi: 10.1021/ef400914r.

[197] M. J. Ramírez-Moreno, I. C. Romero-Ibarra, M. A. Hernández-Pérez, and H. Pfeiffer, 'CO_2 adsorption at elevated pressure and temperature on Mg-Al layered double hydroxide', *Ind Eng Chem Res*, vol. 53, no. 19, pp. 8087–8094, 2014, doi: 10.1021/ie5010515.

[198] S. Albertazzi, F. Basile, and A. Vaccari, 'Catalytic Properties of Hydrotalcite-Type Anionic Clays', 2004, pp. 496–546. doi: 10.1016/S1573-4285(04)80052-8.

[199] Y. Gao *et al.*, 'Comprehensive investigation of CO_2 adsorption on Mg-Al-CO_3 LDH-derived mixed metal oxides', *J Mater Chem A*, vol. 1, no. 41, pp. 12782–12790, 2013, doi: 10.1039/c3ta13039h.

[200] U. Sharma, B. Tyagi, and R. v. Jasra, 'Synthesis and characterization of Mg-Al-CO_3 layered double hydroxide for CO_2 adsorption', *Ind Eng Chem Res*, vol. 47, no. 23, pp. 9588–9595, Dec. 2008, doi: 10.1021/ie800365t.

[201] M. K. Ram Reddy, Z. P. Xu, G. Q. Lu, and J. C. Diniz da Costa, 'Layered double hydroxides for CO_2 capture: structure evolution and regeneration', *Ind Eng Chem Res*, vol. 45, no. 22, pp. 7504–7509, 2006.

[202] N. N. A. H. Meis, J. H. Bitter, and K. P. D. Jong, 'Support and size effects of activated hydrotalcites for precombustion CO_2 capture', *Ind Eng Chem Res*, 2010, vol. 49, no. 3, pp. 1229–1235. doi: 10.1021/ie901114d.

[203] D. Dobos and S. Wawzonek, 'Electrochemical Data', *J Electrochem Soc*, vol. 123, no. 10, p. 348C, 1976, doi: 10.1149/1.2132648.

[204] C. A. Johnson and F. P. Glasser, 'Hydrotalcite-like minerals ($M_2Al(OH)_6(CO_3)_{0.5}.XH_2O$, where M = Mg, Zn, Co, Ni) in the environment: synthesis, characterization and thermodynamic stability', *Clays Clay Mineral 2003 51:1*, vol. 51, no. 1, pp. 1–8, 2003, doi: 10.1346/CCMN.2003.510101.

[205] M. K. Ram Reddy, Z. P. Xu, G. Q. Lu, and J. C. D. da Costa, 'Layered double hydroxides for CO_2 capture: Structure evolution and regeneration', *Ind Eng Chem Res*, vol. 45, no. 22, pp. 7504–7509, 2006, doi: 10.1021/ie060757k.

[206] J. W. Boclair and P. S. Braterman, 'Layered double hydroxide stability. 1. Relative stabilities of layered double hydroxides and their simple counterparts', *Chem Mater*, vol. 11, no. 2, pp. 298–302, 1999, doi: 10.1021/cm980523u.

[207] A. v Radha and P. V. Kamath, 'Aging of trivalent metal hydroxide/oxide gels in divalent metal salt solutions: Mechanism of formation of layered double hydroxides (LDHs)', *Bull Mater Sci*, vol. 26, no. 7, pp. 661–666, 2003.

[208] M. Jobbágy and A. E. Regazzoni, 'Dissolution of nano-size Mg-Al-Cl hydrotalcite in aqueous media', *Appl Clay Sci*, vol. 51, no. 3, pp. 366–369, 2011, doi: 10.1016/j.clay.2010.11.027.

[209] Z. P. Xu and H. C. Zeng, 'Abrupt structural transformation in hydrotalcite-like compounds $Mg_{1-x}Al_x(OH)_2(NO_3)_x \cdot H_2O$ as a continuous function of nitrate anions', *J Phys Chem B*, vol. 105, no. 9, pp. 1743–1749, 2001, doi: 10.1021/jp0029257.

[210] S. Miyata and T. Kumura, 'Synthesis of new hydrotalcite-like compounds and their physico-chemical properties', *Chem Lett*, vol. 2, no. 8, pp. 843–848, 1973.

[211] K. J. Pike, R. P. Malde, S. E. Ashbrook, J. McManus, and S. Wimperis, 'Multiple-quantum MAS NMR of quadrupolar nuclei. Do five-, seven-and nine-quantum experiments yield higher resolution than the three-quantum experiment?', *Solid State Nucl Magn Reson*, vol. 16, no. 3, pp. 203–215, 2000.

[212] F. Zigan and R. Rothbauer, 'Neutronenbeugungsmessungen am brucit', *Neues Jahrb für Mineral Monatshefte*, vol. 1967, p. 137-143, 1967.

[213] R. D. t Shannon and C. T. Prewitt, 'Revised values of effective ionic radii', *Acta Crystallogr B*, vol. 26, no. 7, pp. 1046–1048, 1970.

[214] A. R. Denton and N. W. Ashcroft, 'Vegard's law', *Phys Rev A (Coll Park)*, vol. 43, no. 6, p. 3161, 1991.

[215] M. J. Hernandez-Moreno, M. A. Ulibarri, J. L. Rendon, and C. J. Serna, 'IR characteristics of hydrotalcite-like compounds', *Phys Chem Miner*, vol. 12, no. 1, pp. 34–38, 1985.

[216] G. W. Brindley, and C. Kao, 'Structural and IR Relations Among Brucite-Like Divalent Metal Hydroxides', *Phys Chem Miner*, vol. 10, no.4, pp. 187-191, 1984.

[217] R. M. Hazen, 'Effects of temperature and pressure on the cell dimension and X-ray temperature factors of periclase', *Am Mineral*, vol. 61, no. 3–4, pp. 266–271, 1976.

[218] N. S. Puttaswamy and P. V. Kamath, 'Reversible thermal behaviour of layered double hydroxides: a thermogravimetric study', *J Mater Chem*, vol. 7, no. 9, pp. 1941–1945, 1997.

[219] G. W. Brindley and S. Kikkawa, 'A crystal-chemical study of Mg, Al and Ni, N hydroxy-perchlorates and hydroxycarbonates', *Am Mineral*, vol. 64, no. 7–8, pp. 836–843, 1979.

[220] I. G. Richardson, 'The importance of proper crystal-chemical and geometrical reasoning demonstrated using layered single and double hydroxides', *Acta Crystallogr B*, vol. 69, no. 2, pp. 150–162, 2013, doi: 10.1107/S205251921300376X.

[221] R. Allmann and H. P. Jepsen, 'Die struktur des hydrotalkits', *Neues Jahrb für Mineral Monatshefte*, vol. 1969, p. 544-551, 1969.

[222] S. Miyata, 'Physico-chemical properties of synthetic hydrotalcites in relation to composition', *Clays Clay Miner*, vol. 28, no. 1, pp. 50–56, 1980.

[223] M. C. Gastuche, G. Brown, and M. M. Mortland, 'Mixed Magnesium-Aluminium Hydroxides I. Preparation and Characterization of Compounds Formed In Dialysed Systems', *Clay Mineral*, vol. 7, no. 2, pp. 177-192, 1967.

[224] S. Cadars *et al.*, 'Identification and quantification of defects in the cation ordering in Mg/Al layered double hydroxides', *Chem Mater*, vol. 23, no. 11, pp. 2821–2831, 2011, doi: 10.1021/cm200029q.

[225] P. J. Sideris, F. Blanc, Z. Gan, and C. P. Grey, 'Identification of cation clustering in Mg-Al layered double hydroxides using multinuclear solid state nuclear magnetic resonance spectroscopy', *Chem Mater*, vol. 24, no. 13, pp. 2449–2461, 2012, doi: 10.1021/cm300386d.

[226] K. J. D. MacKenzie and M. E. Smith, *Multinuclear solid-state nuclear magnetic resonance of inorganic materials*. Elsevier, 2002.

[227] V. J. Ingram-Jones, R. C. T. Slade, T. W. Davies, J. C. Southern, and S. Salvador, 'Dehydroxylation sequences of gibbsite and boehmite: study of differences between soak and flash calcination and of particle-size effects', *J Mater Chem*, vol. 6, no. 1, pp. 73–79, 1996.

[228] R. H. Meinhold, R. C. T. Slade, and R. H. Newman, 'High field MAS NMR, with simulations of the effects of disorder on lineshape, applied to thermal transformations of alumina hydrates', *Appl Magn Reson*, vol. 4, no. 1–2, pp. 121–140, 1993, doi: 10.1007/BF03162559.

[229] R. C. T. Slade and T. W. Davies, 'Evolution of structural changes during flash calcination of kaolinite. A ^{29}Si and ^{27}Al nuclear magnetic resonance spectroscopy study', *J Mater Chem*, vol. 1, no. 3, pp. 361–364, 1991.

[230] A. Vyalikh, D. Massiot, and U. Scheler, 'Structural characterisation of aluminium layered double hydroxides by ^{27}Al solid-state NMR', *Solid State Nucl Magn Reson*, vol. 36, no. 1, pp. 19–23, 2009, doi: 10.1016/j.ssnmr.2009.04.002.

[231] J. Rocha, M. del Arco, V. Rives, and M. A. Ulibarri, 'Reconstruction of layered double hydroxides from calcined precursors: a powder XRD and ^{27}Al MAS NMR study', *J Mater Chem*, vol. 9, no. 10, pp. 2499–2503, 1999, doi: 10.1039/A903231B.

[232] A. Vyalikh, F. R. Costa, U. Wagenknecht, G. Heinrich, D. Massiot, and U. Scheler, 'From layered double hydroxides to layered double hydroxide-based nanocomposites - A solid-state NMR study', *J Phys Chem C*, vol. 113, no. 51, pp. 21308–21313, 2009, doi: 10.1021/jp9069338.

[233] M. León, E. Díaz, S. Bennici, A. Vega, S. Ordóñez, and A. Auroux, 'Adsorption of CO_2 on hydrotalcite-derived mixed oxides: Sorption mechanisms and consequences for adsorption irreversibility', *Ind Eng Chem Res*, vol. 49, no. 8, pp. 3663–3671, 2010, doi: 10.1021/ie902072a.

[234] B. Wiyantoko, P. Kurniawati, T. E. Purbaningtias, and I. Fatimah, 'Synthesis and characterization of hydrotalcite at different Mg/Al molar ratios', *Procedia Chem*, vol. 17, pp. 21–26, 2015.

[235] H. E. Cross and D. R. Brown, 'Entrained sodium in mixed metal oxide catalysts derived from layered double hydroxides', *Catal Commun*, vol. 12, no. 3, pp. 243–245, 2010.

[236] D. Iruretagoyena, M. S. P. Shaffer, and D. Chadwick, 'Layered Double Oxides Supported on Graphene Oxide for CO_2 Adsorption: Effect of Support and Residual Sodium', *Ind Eng Chem Res*, vol. 54, no. 26, pp. 6781–6792, 2015, doi: 10.1021/acs.iecr.5b01215.

[237] M. Adachi-Pagano, C. Forano, and J. P. Besse, 'Synthesis of Al-rich hydrotalcite-like compounds by using the urea hydrolysis reaction - Control of size and morphology', *J Mater Chem*, vol. 13, no. 8, pp. 1988–1993, 2003, doi: 10.1039/b302747n.

[238] J. He, M. Wei, B. Li, Y. Kang, D. G. Evans, and X. Duan, 'Preparation of layered double hydroxides', *Struct Bond*, vol. 119, pp. 89–119, 2005, doi: 10.1007/430_006.

[239] F. Prinetto, G. Ghiotti, P. Graffin, and D. Tichit, 'Synthesis and characterization of sol–gel Mg/Al and Ni/Al layered double hydroxides and comparison with co-precipitated samples', *Microporous and Mesoporous Materials*, vol. 39, no. 1–2, pp. 229–247, 2000, doi: 10.1016/S1387-1811(00)00197-9.

[240] D. Tichit, G. Layrac, and C. Gérardin, 'Synthesis of layered double hydroxides through continuous flow processes: A review', *Chem Eng J*, vol. 369. Elsevier B.V., pp. 302–332, 2019. doi: 10.1016/j.cej.2019.03.057.

[241] F. L. Theiss, G. A. Ayoko, and R. L. Frost, 'Synthesis of layered double hydroxides containing Mg^{2+}, Zn^{2+}, Ca^{2+} and Al^{3+} layer cations by co-precipitation methods - A review', *Appl Surf Sci*, vol. 383, pp. 200–213, 2016, doi: 10.1016/j.apsusc.2016.04.150.

[242] T. Hibino and H. Ohya, 'Synthesis of crystalline layered double hydroxides: Precipitation by using urea hydrolysis and subsequent hydrothermal reactions in aqueous solutions', *Appl Clay Sci*, vol. 45, no. 3, pp. 123–132, 2009, doi: 10.1016/j.clay.2009.04.013.

[243] L. A. Cheah, G. v. Manohara, M. M. Maroto-Valer, and S. Garcia, 'Layered Double Hydroxide (LDH)-Derived Mixed Metal Oxides (MMOs): A Systematic Crystal-Chemical Approach to Investigating the Chemical Composition and its Effect on High Temperature CO_2 capture.', *ChemistrySelect*, vol. 5, no. 19, pp. 5587–5594, 2020, doi: 10.1002/slct.201904447.

[244] T. C. Drage *et al.*, 'Materials challenges for the development of solid sorbents for post-combustion carbon capture', *J. Mater. Chem.*, vol. 22, no. 7, pp. 2815–2823, 2012, doi: 10.1039/C2JM12592G.

[245] R. A. Sheldon, 'Metrics of Green Chemistry and Sustainability: Past, Present, and Future', *ACS Sustain Chem Eng*, vol. 6, no. 1. American Chemical Society, pp. 32–48, 2018. doi: 10.1021/acssuschemeng.7b03505.

[246] X. Kou *et al.*, 'Adsorption of CO_2 on MgAl-CO_3 LDHs-Derived Sorbents with 3D Nanoflower-like Structure', *Energy & Fuels*, vol. 32, no. 4, pp. 5313–5320, 2018, doi: 10.1021/acs.energyfuels.8b00024.

[247] T. Hibino and H. Ohya, 'Synthesis of crystalline layered double hydroxides: Precipitation by using urea hydrolysis and subsequent hydrothermal reactions in aqueous solutions', *Appl Clay Sci*, vol. 45, no. 3, pp. 123–132, 2009, doi: 10.1016/j.clay.2009.04.013.

[248] Oza *et al*, 'Process For Preparing Hydrotalcite And Brucite Type Posite Charged Layers', 2006

[249] S. Miyata and T. Kumura, 'Synthesis of new hydrotalcite-like compounds and their physico-chemical properties', *Chem Lett*, vol. 2, no. 8, pp. 843–848, 1973.

[250] U. Costantino, F. Marmottini, M. Nocchetti, and R. Vivani, 'New Synthetic Routes to Hydrotalcite-Like Compounds− Characterisation and Properties of the Obtained Materials', *Eur J Inorg Chem*, vol. 1998, no. 10, pp. 1439–1446, 1998.

[251] M. J. Hernandez-Moreno, M. A. Ulibarri, J. L. Rendon, and C. J. Serna, 'IR characteristics of hydrotalcite-like compounds', *Phys Chem Miner*, vol. 12, no. 1, pp. 34–38, 1985.

[252] I. G. Richardson, 'The importance of proper crystal-chemical and geometrical reasoning demonstrated using layered single and double hydroxides', *Acta Crystallogr B*, vol. 69, no. 2, pp. 150–162, 2013, doi: 10.1107/S205251921300376X.

[253] S. Marappa and P. V. Kamath, 'Structure of the Carbonate-Intercalated Layered Double Hydroxides: A Reappraisal', *Ind Eng Chem Res*, vol. 54, no. 44, pp. 11075–11079, 2015, doi: 10.1021/acs.iecr.5b03207.

[254] A. Radha, P. V. Kamath, and C. Shivakumara, 'Order and disorder among the layered double hydroxides: combined Rietveld and DIFFaX approach', *Acta Crystallogr B Struct Sci*, vol. 63, no. 2, pp. 243–250, 2007.

[255] P. Benito, F. M. Labajos, and V. Rives, 'Uniform fast growth of hydrotalcite-like compounds', *Cryst Growth Des*, vol. 6, no. 8, pp. 1961–1966, 2006, doi: 10.1021/cg0506222.

[256] V. R. L. Constantino and T. J. Pinnavaia, 'Basic properties of $Mg^{2+}_{1-x}Al^{3+}_{x}$ layered double hydroxides intercalated by carbonate, hydroxide, chloride, and sulfate anions', *Inorg Chem*, vol. 34, no. 4, pp. 883–892, 1995.

[257] R. K. Kukkadapu, M. S. Witkowski, and J. E. Amonette, 'Synthesis of a low-carbonate high-charge hydrotalcite-like compound at ambient pressure and atmosphere', *Chem Mater*, vol. 9, no. 2, pp. 417–419, 1997.

[258] M. Kaneyoshi and W. Jones, 'Formation of Mg-Al layered double hydroxides intercalated with nitrilotriacetate anions', *J Mater Chem*, vol. 9, no. 3, pp. 805–811, 1999, doi: 10.1039/a808415g.

[259] A. Seron and F. Delorme, 'Synthesis of layered double hydroxides (LDHs) with varying pH: A valuable contribution to the study of Mg/Al LDH formation mechanism', *J Phys Chem*, vol. 69, no. 5–6, pp. 1088–1090, 2008, doi: 10.1016/J.JPCS.2007.10.054.

[260] S. Miyata, 'Physoco-chemical Properties of synthetic Hydrotalcites in relation to composition', *Clays Clay Mineral*, vol. 28, no. 1. pp. 50–56, 1980.

[261] L. Pausch, H.-H. Lohse, K. Schurmann, and R. Allmann, 'Syntheses of Disordered and Al-rich Hydrotalcite-like compounds.", *Clays Clay Minerals*, vol. 34, no. 5. pp. 507–510, 1986.

[262] G. Mascolo and O. Marino, 'A new synthesis and characterization of magnesium-aluminium hydroxides 1', *Mineral Mag*, vol. 43, no. 329, pp. 619–621, Mar. 1980, doi: 10.1180/MINMAG.1980.043.329.09.

[263] D. Iruretagoyena, M. S. P. Shaffer, and D. Chadwick, 'Layered Double Oxides Supported on Graphene Oxide for CO_2 Adsorption: Effect of Support and Residual Sodium', *Ind Eng Chem Res*, vol. 54, no. 26, pp. 6781–6792, 2015, doi: 10.1021/acs.iecr.5b01215.

[264] S. Walspurger, P. D. Cobden, O. V. Safonova, Y. Wu, and E. J. Anthony, 'High CO_2 storage capacity in alkali-promoted hydrotalcite-based material: In situ detection of reversible formation of magnesium carbonate', *Chem Eur J*, vol. 16, no. 42, pp. 12694–12700, 2010, doi: 10.1002/chem.201000687.

[265] A. D. Ebner, S. P. Reynolds, and J. A. Ritter, 'Nonequilibrium kinetic model that describes the reversible adsorption and desorption behavior of CO_2 in a K-promoted hydrotalcite-like compound', *Ind Eng Chem Res*, vol. 46, no. 6, pp. 1737–1744, 2007, doi: 10.1021/ie061042k.

[266] H. Du, A. D. Ebner, and J. A. Ritter, 'Pressure dependence of the nonequilibrium kinetic model that describes the adsorption and desorption behavior of CO_2 in K-promoted hydrotalcite like compound', *Ind Eng Chem Res*, vol. 50, no. 1, pp. 412–418, 2011, doi: 10.1021/ie100965b.

[267] A. D. Ebner, S. P. Reynolds, and J. A. Ritter, 'Understanding the adsorption and desorption behavior of CO 2 on a K-promoted hydrotalcite-like compound (HTlc) through nonequilibrium dynamic isotherms', *Ind Eng Chem Res*, vol. 45, no. 18, pp. 6387–6392, 2006, doi: 10.1021/ie060389k.

[268] D. Jansen *et al.*, 'SEWGS technology is now ready for scale-up!', *Energy Procedia*, vol. 37, pp. 2265–2273, 2013.

[269] H. J. Jang, C. H. Lee, S. Kim, S. H. Kim, and K. B. Lee, 'Hydrothermal synthesis of K_2CO_3-promoted hydrotalcite from hydroxide-form precursors for novel high-temperature CO_2 sorbent', *ACS Appl Mater Interfaces*, vol. 6, no. 9, pp. 6914–6919, 2014, doi: 10.1021/am500720f.

[270] J. M. Lee, Y. J. Min, K. B. Lee, S. G. Jeon, J. G. Na, and H. J. Ryu, 'Enhancement of CO_2 sorption uptake on hydrotalcite by impregnation with K_2CO_3', *Langmuir*, vol. 26, no. 24, pp. 18788–18797, 2010, doi: 10.1021/la102974s.

[271] Q. Liu, Y. Zhao, Z. Jiang, Y. Cui, J. Wang, and N. Ai, 'Computational and experimental studies on the CO_2 adsorption of layered double hydroxide intercalated by anionic surfactant', *Appl Clay Sci*, vol. 190, no. March, p. 105556, 2020, doi: 10.1016/j.clay.2020.105556.

[272] C. Megías-Sayago, R. Bingre, L. Huang, G. Lutzweiler, Q. Wang, and B. Louis, 'CO_2 Adsorption Capacities in Zeolites and Layered Double Hydroxide Materials', *Front Chem*, vol. 7, no. August, pp. 1–10, 2019, doi: 10.3389/fchem.2019.00551.

[273] M. K. Ram Reddy, Z. P. Xu, G. Q. Lu, and J. C. D. Da Costa, 'Layered double hydroxides for CO_2 capture: Structure evolution and regeneration', *Ind Eng Chem Res*, vol. 45, no. 22, pp. 7504–7509, 2006, doi: 10.1021/ie060757k.

[274] Q. Wang, H. H. Tay, Z. Zhong, J. Luo, and A. Borgna, 'Synthesis of high-temperature CO_2 adsorbents from organo-layered double hydroxides with markedly improved CO_2 capture capacity', *Energy Environ Sci*, vol. 5, no. 6, pp. 7526–7530, 2012, doi: 10.1039/c2ee21409a.

[275] X. Kou *et al.*, 'Adsorption of CO_2 on MgAl-CO_3 LDHs-Derived Sorbents with 3D Nanoflower-like Structure', *Energy & Fuels*, vol. 32, no. 4, pp. 5313–5320, 2018, doi: 10.1021/acs.energyfuels.8b00024.

[276] S. Kim, S. G. Jeon, and K. B. Lee, 'High-Temperature CO_2 Sorption on Hydrotalcite Having a High Mg/Al Molar Ratio', *ACS Appl Mater Interfaces*, vol. 8, no. 9, pp. 5763–5767, 2016, doi: 10.1021/acsami.5b12598.

[277] M. M. Rao, B. R. Reddy, M. Jayalakshmi, V. S. Jaya, and B. Sridhar, 'Hydrothermal synthesis of Mg-Al hydrotalcites by urea hydrolysis', *Mater Res Bull*, vol. 40, no. 2, pp. 347–359, 2005, doi: 10.1016/j.materresbull.2004.10.007.

[278] I. G. Richardson, 'Clarification of possible ordered distributions of trivalent cations in layered double hydroxides and an explanation for the observed variation in the lower solid-solution limit', *Acta Crystallogr B Struct Sci*, vol. 69, no. 6, pp. 629–633, 2013, doi: 10.1107/S2052519213027905.

[279] Q. Wang, H. H. Tay, Z. Zhong, J. Luo, and A. Borgna, 'Synthesis of high-temperature CO_2 adsorbents from organo-layered double hydroxides with markedly improved CO2 capture capacity', *Energy Environ Sci*, vol. 5, no. 6, pp. 7526–7530, 2012, doi: 10.1039/c2ee21409a.

[280] A. V Radha and P. V. Kamath, 'Aging of trivalent metal hydroxide/oxide gels in divalent metal salt solutions: Mechanism of formation of layered double hydroxides (LDHs)', *Bull. Mater. Sci*, vol. 26, no. 7. pp. 661–666, 2003.

[281] J. Rocha, M. Del Arco, V. Rives, and M. A. Ulibarri, 'Reconstruction of layered double hydroxides from calcined precursors: A powder XRD and 27A1 MAS NMR study', *J Mater Chem*, vol. 9, no. 10, pp. 2499–2503, 1999, doi: 10.1039/a903231b.

[282] E. S. Zhitova, S. V. Krivovichev, I. Pekov, and H. C. Greenwell, 'Crystal chemistry of natural layered double hydroxides. 5. Single-crystal structure refinement of hydrotalcite, $[Mg_6Al_2(OH)_{16}](CO_3) \cdot (H_2O)_4$', *Mineral Mag*, vol. 83, no. 02, pp. 269–280, 2019, doi: 10.1180/mgm.2018.145.

[283] S. J. Mills, A. G. Christy, and R. T. Schmitt, 'The creation of neotypes for hydrotalcite', *Mineral Mag*, vol. 80, no. 6, pp. 1023–1029, 2016, doi: 10.1180/minmag.2016.080.040.

[284] E. S. Zhitova, V. N. Yakovenchuk, S. v. Krivovichev, A. A. Zolotarev, Y. A. Pakhomovsky, and G. Yu. Ivanyuk, 'Crystal chemistry of natural layered double hydroxides. 3. The crystal structure of Mg,Al-disordered quintinite-2H', *Mineral Mag*, vol. 74, no. 5, pp. 841–848, 2010, doi: 10.1180/MINMAG.2010.074.5.841.

[285] S. v. Krivovichev, V. N. Yakovenchuk, E. S. Zhitova, A. A. Zolotarev, Y. A. Pakhomovsky, and G. Yu. Ivanyuk, 'Crystal chemistry of natural layered double hydroxides. 2. Quintinite-1M: first evidence of a monoclinic polytype in M^{2+}-M^{3+} layered double hydroxides', *Mineral Mag*, vol. 74, no. 5, pp. 833–840, 2010, doi: 10.1180/MINMAG.2010.074.5.833.

[286] L. Vegard, 'Die Konstitution der Mischkristalle und die Raumfüllung der Atome', *Zeitschrift für Physik*, vol. 5, no. 1, pp. 17–26, Jan. 1921, doi: 10.1007/BF01349680.

[287] S. Marappa and P. V. Kamath, 'Structure of the Carbonate-Intercalated Layered Double Hydroxides: A Reappraisal', *Ind Eng Chem Res*, vol. 54, no. 44, pp. 11075–11079, 2015, doi: 10.1021/acs.iecr.5b03207.

[288] E. S. Zhitova, S. v. Krivovichev, I. v. Pekov, V. N. Yakovenchuk, and Y. A. Pakhomovsky, 'Correlation between the d-value and the M^{2+}:M^{3+} cation ratio in Mg–Al–CO_3 layered double hydroxides', *Appl Clay Sci*, vol. 130, pp. 2–11, 2016, doi: 10.1016/j.clay.2016.01.031.

[289] H. D. Megaw, 'The Crystal Structure of Hydrargillite, $Al(OH)_3$.', *Z Kristallogr Cryst Mater*, vol. 87, no. 1–6, 1934, doi: 10.1524/zkri.1934.87.1.185.

[290] R. Rothbauer, F. Zigan, and H. O′Daniel, 'Verfeinerung der Struktur des Bayerits, $Al(OH)_3$', *Z Kristallogr Cryst Mater*, vol. 125, no. 1–6, 1967, doi: 10.1524/zkri.1967.125.16.317.

[291] H. J. Bosmans, 'Unit cell and crystal structure of nordstrandite, $Al(OH)_3$', *Acta Crystallogr B Struct Sci*, vol. 26, no. 5, pp. 649–652, 1970, doi: 10.1107/S0567740870002911.

[292] G. R. Clark, K. A. Rodgers, and G. S. Henderson, 'The crystal chemistry of doyleite, $Al(OH)_3$', *Z Kristallogr Cryst Mater*, vol. 213, no. 2, 1998, doi: 10.1524/zkri.1998.213.2.96.

[293] R. D. Shannon and C. T. Prewitt, 'Revised values of effective ionic radii', *Acta Crystallogr B Struct Sci*, vol. 26, no. 7, pp. 1046–1048, 1970.

[294] R. Schoen and C. E. Roberson, 'Structures of aluminum hydroxide and geochemical implications1', *Am Mineral*, vol. 55, no. 1–2, pp. 43–77, 1970.

[295] W. Hofmeister and H. v. Platen, 'Crystal chemistry and atomic order in brucite-related double-layer structures', *Crystallogr Rev*, vol. 3, no. 1, pp. 3–26, 1992, doi: 10.1080/08893119208032964.

[296] H. F. W. Taylor, 'Crystal structures of some double hydroxide minerals', *Mineral Mag*, vol. 39, no. 304, pp. 377–389, 1973, doi: 10.1180/minmag.1973.039.304.01.

[297] R. K. Kukkadapu, M. S. Witkowski, and J. E. Amonette, 'Synthesis of a low-carbonate high-charge hydrotalcite-like compound at ambient pressure and atmosphere', *Chem material*, vol. 9, no. 2, pp. 417–419, 1997.

[298] M. Kaneyoshi and W. Jones, 'Formation of Mg-Al layered double hydroxides intercalated with nitrilotriacetate anions', *J Mater Chem*, vol. 9, no. 3, pp. 805–811, 1999, doi: 10.1039/a808415g.

[299] A. Livingstone and D. L. Bish, 'On the new mineral theophrastite, a nickel hydroxide, from Unst, Shetland, Scotland', *Mineral Mag*, vol. 46, no. 338, pp. 1–5, 1982, doi: 10.1180/minmag.1982.046.338.01.

[300] H. Bode, K. Dehmelt, and J. Witte, 'Zur kenntnis der nickelhydroxidelektrode-I. Über das nickel (II)-hydroxidhydrat', *Electrochim Acta*, vol. 11, no. 8, pp. 1079–1087, 1966, doi: 10.1016/0013-4686(66)80045-2.

[301] L. A. Cheah, G. v. Manohara, M. M. Maroto-Valer, and S. Garcia, 'Impact of Synthesis Method and Metal Salt Precursors on the CO_2 Adsorption Performance of Layered Double Hydroxides Derived Mixed Metal Oxides', *Front Energy Res*, vol. 0, p. 522, 2022, doi: 10.3389/FENRG.2022.882182.

[302] Z. P. Xu and H. C. Zeng, 'Decomposition pathways of hydrotalcite-like compounds $Mg_{1-x}Al_x(OH)_2(NO_3)_x \cdot nH_2O$ as a continuous function of nitrate anions', *Chem Material*, vol. 13, no. 12, pp. 4564–4572, 2001, doi: 10.1021/cm010347g.

[303] J. S. Valente, H. Pfeiffer, E. Lima, J. Prince, and J. Flores, 'Cyanoethylation of alcohols by activated Mg-Al layered double hydroxides: Influence of rehydration

conditions and Mg/Al molar ratio on Brönsted basicity', *J Catal*, vol. 279, no. 1, pp. 196–204, 2011, doi: 10.1016/j.jcat.2011.01.018.

[304] K. K. Rao, M. Gravelle, J. S. Valente, and F. Figueras, 'Activation of Mg-Al Hydrotalcite Catalysts for Aldol Condensation Reactions', *J Catal*, vol. 173. pp. 115–121, 1998.

[305] J. Shen, J. M. Kobe, Y. Chen, and J. A. Dumesic, 'Synthesis and Surface Acid/Base Properties of Magnesium-Aluminum Mixed Oxides Obtained from Hydrotalcites', *Langmuir*, vol. 10, no. 10, pp. 3902–3908, 1994, doi: 10.1021/la00022a082.

[306] I. Pausch, H.-H. Lohse, K. Schi~rmann, and R. Allmann, 'Syntheses of disordered and Al-rich Hydrotalcite-like compounds', *Clays Clay Minerals*, vol. 34, no. 5. pp. 507–510, 1986.

[307] T. Sato, H. Fujita, T. Endo, M. Shimada, and A. Tsunashima, 'Synthesis of hydrotalcite-like compounds and their physico-chemical properties', *Reactivity of Solids*, vol. 5, no. 2–3, pp. 219–228, 1988, doi: 10.1016/0168-7336(88)80089-5.

[308] G. Mascolo and O. Marino, 'A new synthesis and characterization of magnesium-aluminium hydroxides 1', *Mineral Mag*, vol. 43, no. 329, pp. 619–621, 1980.

[309] E. López-Salinas, M. García-Sánchez, J. A. Montoya, D. R. Acosta, J. A. Abasolo, and I. Schifter, 'Structural Characterization of Synthetic Hydrotalcite-like [Mg$_{1-x}$Ga$_x$(OH)$_2$](CO$_3$)$_{x/2}$·mH$_2$O', *Langmuir*, vol. 13, no. 17, pp. 4748–4753, 1997, doi: 10.1021/la970192k.

[310] C. M. Jinesh, C. A. Antonyraj, and S. Kannan, 'Allylbenzene isomerisation over as-synthesized MgAl and NiAl containing LDHs: Basicity-activity relationships', *Appl Clay Sci*, vol. 48, no. 1–2, pp. 243–249, 2010, doi: 10.1016/j.clay.2009.11.026.

[311] S. Han, W. Hou, C. Zhang, D. Sun, X. Huang, and A. Gouting Wang, 'Structure and the point of zero charge of magnesium aluminium hydroxide', *J Chem Soc,* vol. 94, no. 7, pp. 915–918, 1998, doi: 10.1039/a706607d.

[312] W. N. Budhysutanto, D. van Agterveld, E. Schomaker, B. D. Rossenaar, G. M. van Rosmalen, and H. J. M. Kramer, 'Chemical composition and interlayer arrangement

of polytype 3R2 Mg-Al layered double hydroxides', *Appl Clay Sci*, vol. 52, no. 4, pp. 374–380, 2011, doi: 10.1016/j.clay.2011.03.020.

[313] R. Bîrjega, O. D. Pavel, G. Costentin, M. Che, and E. Angelescu, 'Rare-earth elements modified hydrotalcites and corresponding mesoporous mixed oxides as basic solid catalysts', *Appl Catal A Gen*, vol. 288, no. 1–2, pp. 185–193, 2005, doi: 10.1016/j.apcata.2005.04.030.

[314] M. Bellotto, B. Rebours, O. Clause, J. Lynch, D. Bazin, and E. Elkaïm, 'A Reexamination of Hydrotalcite Crystal Chemistry', *J Phys Chem*, vol. 100, no. 20, pp. 8527–8534, Jan. 1996, doi: 10.1021/jp960039j.

[315] S. K. Yun and T. J. Pinnavaia, 'Water Content and Particle Texture of Synthetic Hydrotalcite-like Layered Double Hydroxides', *Chem. Mater*, vol. 7. pp. 348–354, 1995.

[316] C. Barriga, M. Gaitán, I. Pavlovic, M. A. Ulibarri, M. C. Hermosĭn, and J. Cornejo, 'Hydrotalcites as sorbent for 2,4,6-trinitrophenol: Influence of the layer composition and interlayer anion', *J Mater Chem*, vol. 12, no. 4, pp. 1027–1034, 2002, doi: 10.1039/b107979b.

[317] M. Tsuji, G. Mao, T. Yoshida, and Y. Tamaura, 'Hydrotalcites with an extended Al3+-substitution: Synthesis, simultaneous TG-DTA-MS study, and their CO2 adsorption behaviors', *J Mater Res*, vol. 8, no. 5, pp. 1137–1142, 1993, doi: 10.1557/JMR.1993.1137.

[318] G. Mao, M. Tsuji, and Y. Tamaura, 'Synthesis and CO_2 Adsorption Features of a Hydrotalcite-Like compound of the Mg^{2+}-Al^{3+}-$Fe(CN)_6^{4-}$ system with high layer-charge density', *Clays Clay Miner*, vol. 41, no. 6, pp. 731–737, 1993.

[319] S. Kim, S. G. Jeon, and K. B. Lee, 'High-Temperature CO_2 Sorption on Hydrotalcite Having a High Mg/Al Molar Ratio', *ACS Appl Mater Interfaces*, vol. 8, no. 9, pp. 5763–5767, Mar. 2016, doi: 10.1021/acsami.5b12598.

[320] M. M. Rao, B. R. Reddy, M. Jayalakshmi, V. S. Jaya, and B. Sridhar, 'Hydrothermal synthesis of Mg-Al hydrotalcites by urea hydrolysis', *Mater Res Bull*, vol. 40, no. 2, pp. 347–359, 2005, doi: 10.1016/j.materresbull.2004.10.007.

[321] E. S. Zhitova, S. V. Krivovichev, I. V. Pekov, V. N. Yakovenchuk, and Ya. A. Pakhomovsky, 'Correlation between the d-value and the $M^{2+}:M^{3+}$ cation ratio in Mg–Al–CO_3 layered double hydroxides', *Appl Clay Sci*, vol. 130, pp. 2–11, 2016, doi: 10.1016/J.CLAY.2016.01.031.

[322] A. Trave, A. Selloni, A. Goursot, D. Tichit, and J. Weber, 'First Principles Study of the Structure and Chemistry of Mg-Based Hydrotalcite-Like Anionic Clays', *J Phys Chem B*, vol. 106, no. 47, pp. 12291–12296, 2002, doi: 10.1021/JP026339K.

[323] R. K. Allada, A. Navrotsky, and J. Boerio-Goates, 'Thermochemistry of hydrotalcite-like phases in the MgO-Al_2O_3-CO_2-H_2O system: A determination of enthalpy, entropy, and free energy', *Am Mineral*, vol. 90, no. 2–3, pp. 329–335, 2005, doi: 10.2138/am.2005.1737.

[324] D. G. Evans and R. C. T. Slade, 'Structural Aspects of Layered Double Hydroxides', *Struct Bond*, vol. 119, pp. 1–87, 2006, doi: 10.1007/430_005.

[325] E. S. Zhitova, S. V. Krivovichev, V. N. Yakovenchuk, G. Yu. Ivanyuk, Y. A. Pakhomovsky, and J. A. Mikhailova, 'Crystal chemistry of natural layered double hydroxides: 4. Crystal structures and evolution of structural complexity of quintinite polytypes from the Kovdor alkaline-ultrabasic massif, Kola peninsula, Russia', *Mineral Mag*, vol. 82, no. 2, pp. 329–346, 2018, doi: 10.1180/minmag.2017.081.046.

[326] G. S. Thomas and P. Vishnu Kamath, 'Line broadening in the PXRD patterns of layered hydroxides: The relative effects of crystallite size and structural disorder', *J. Chem. Sci*, vol. 118, no. 1, pp. 127–133, 2006.

[327] A. Vyalikh, D. Massiot, and U. Scheler, 'Structural characterisation of aluminium layered double hydroxides by 27Al solid-state NMR', *Solid State Nucl Magn Reson*, vol. 36, no. 1, pp. 19–23, 2009, doi: 10.1016/j.ssnmr.2009.04.002.

[328] A. v. Radha, C. Shivakumara, and P. V. Kamath, 'DIFFaX simulations of stacking faults in layered double hydroxides (LDHs)', *Clays Clay Miner*, vol. 53, no. 5, pp. 520–527, 2005, doi: 10.1346/CCMN.2005.0530508.

[329] J. M. R. Génin and C. Ruby, 'Anion and cation distributions in Fe(II–III) hydroxysalt green rusts from XRD and Mössbauer analysis (carbonate, chloride, sulphate, …); the "fougerite" mineral', *Solid State Sci*, vol. 6, no. 7, pp. 705–718, 2004, doi: 10.1016/J.SOLIDSTATESCIENCES.2004.03.021.

[330] L. Pesic, S. Salipurovic, V. Markovic, D. Vucelic, W. Kagunya, and W. Jones, 'Thermal characteristics of a synthetic hydrotalcite-like material', *J Mater Chem*, vol. 2, no. 10, pp. 1069–1073, 1992, doi: 10.1039/JM9920201069.

[331] X. Hou, D. L. Bish, S. L. Wang, C. T. Johnston, and R. J. Kirkpatrick, 'Hydration, expansion, structure, and dynamics of layered double hydroxides', *Am Mineral*, vol. 88, no. 1, pp. 167–179, 2003, doi: 10.2138/AM-2003-0120.

[332] J. T. Kloprogge, L. Hickey, and R. L. Frost, 'Heating stage Raman and infrared emission spectroscopic study of the dehydroxylation of synthetic Mg-hydrotalcite', *Appl Clay Sci*, vol. 18, no. 1–2, pp. 37–49, 2001, doi: 10.1016/S0169-1317(00)00028-4.

[333] S. Britto and P. V. Kamath, 'Polytypism in the lithium-aluminum layered double hydroxides: The $[LiAl_2(OH)_6]^+$ layer as a structural synthon', *Inorg Chem*, vol. 50, no. 12, pp. 5619–5627, 2011, doi: 10.1021/ic200312g.

[334] G. S. Thomas, M. Rajamathi, and P. V. Kamath, 'DiffaX simulations of polytypism and disorder in hydrotalcite', *Clays Clay Miner*, vol. 52, no. 6, pp. 693–699, 2004, doi: 10.1346/CCMN.2004.0520603.

[335] S. Radha and P. V. Kamath, 'Polytypism in sulfate-intercalated layered double hydroxides of Zn and M(III) (M = Al, Cr): Observation of cation ordering in the metal hydroxide layers', *Inorg Chem*, vol. 52, no. 9, pp. 4834–4841, 2013, doi: 10.1021/ic3023198.

[336] R. Ma, J. Liang, X. Liu, and T. Sasaki, 'General insights into structural evolution of layered double hydroxide: Underlying aspects in topochemical transformation from brucite to layered double hydroxide', *J Am Chem Soc*, vol. 134, no. 48, pp. 19915–19921, 2012, doi: 10.1021/JA310246R/ASSET/IMAGES/MEDIUM/JA-2012-10246R_0010.GIF.

[337] M. Vucelic, G. D. Moggridge, and W. Jones, 'Thermal properties of terephthalate- and benzoate-intercalated LDH', J *Phys Chem*, vol. 99, no. 20, pp. 8328–8337, 1995, doi: 10.1021/J100020A068/ASSET/J100020A068.FP.PNG_V03.

[338] K. Coenen, F. Gallucci, P. Cobden, E. van Dijk, E. Hensen, and M. van Sint Annaland, 'Influence of material composition on the CO_2 and H_2O adsorption capacities and kinetics of potassium-promoted sorbents', *Chem Eng J*, vol. 334, pp. 2115–2123, 2018, doi: 10.1016/j.cej.2017.11.161.

[339] M. Maroño, Y. Torreiro, and L. Gutierrez, 'Influence of steam partial pressures in the CO_2 capture capacity of K-doped hydrotalcite-based sorbents for their application to SEWGS processes', *Int J Greenhouse Gas Control*, vol. 14, pp. 183–192, 2013, doi: 10.1016/j.ijggc.2013.01.024.

[340] K. B. Lee, M. G. Beaver, H. S. Caram, and S. Sircar, 'Reversible Chemisorbents for Carbon Dioxide and Their Potential Applications', *Ind Eng Chem Res*, vol. 47, no. 21, pp. 8048–8062, 2008, doi: 10.1021/ie800795y.

[341] 'Rubolab'. Acccessed Jun. 25, 2022. [Online] Available: https://www.rubolab.de/magnetic-suspension-balance.

[342] F. Dreisbach, H. W. L. ¨ Osch, and P. Harting, 'Highest Pressure Adsorption Equilibria Data: Measurement with Magnetic Suspension Balance and Analysis with a New Adsorbent/Adsorbate-Volume', 2002.

[343] F. Dreisbach, R. Staudt, and J. U. Keller, 'High Pressure Adsorption Data of Methane, Nitrogen, Carbon Dioxide and their Binary and Ternary Mixtures on Activated Carbon', 1999.

[344] M. Eic and D. M. Ruthven, 'A new experimental technique for measurement of intracrystalline diffusivity', *Zeolites*, vol. 8, no. 1, pp. 40–45, Jan. 1988, doi: 10.1016/S0144-2449(88)80028-9.

[345] S. Brandani and D. M. Ruthven, 'Analysis of ZLC desorption curves for liquid systems', *Chem Eng Sci*, vol. 50, no. 13, pp. 2055–2059, Jul. 1995, doi: 10.1016/0009-2509(95)00048-A.

[346] S. Brandani, 'Effects of nonlinear equilibrium on zero length column experiments', *Chem Eng Sci*, vol. 53, no. 15, pp. 2791–2798, Aug. 1998, doi: 10.1016/S0009-2509(98)00075-X.

[347] J. A. Silva and A. E. Rodrigues, 'Analysis of ZLC technique for diffusivity measurements in bidisperse porous adsorbent pellets', *Gas Separation and Purification*, vol. 10, no. 4, pp. 207 – 224, 1996, doi: 10.1016/S0950-4214(96)00021-7

[348] J. C. A. Silva, F. A. da Silva, and A. E. Rodrigues, 'An analytical solution for the analysis of zero-length-column experiments with heat effects', *Ind Eng Chem Res*, vol. 40, no. 16, pp. 3697–3702, 2001, doi: 10.1021/ie001045b.

[349] A. Centineo and S. Brandani, 'Measurement of water vapor adsorption isotherms in mesoporous materials using the zero length column technique', *Chem Eng Sci*, vol. 214, p. 115417, 2020, doi: 10.1016/J.CES.2019.115417.

[350] R. Seabra, 'Carbon Dioxide Separation from Industrial Streams', Integrated Master in Chemical Engineering, University of Porto, Porto, Portugal, 2017.

[351] R. Seabra, A. M. Ribeiro, K. Gleichmann, A. F. P. Ferreira, and A. E. Rodrigues, 'Adsorption equilibrium and kinetics of carbon dioxide, methane and nitrogen on binderless zeolite 4A adsorbents', *Microporous and Mesoporous Materials*, vol. 277, pp. 105–114, Mar. 2019, doi: 10.1016/j.micromeso.2018.10.024.

[352] S. Brandani and E. Mangano, 'The zero length column technique to measure adsorption equilibrium and kinetics: lessons learnt from 30 years of experience', *Adsorption*, vol. 27, pp. 319–351, 2021, doi: 10.1007/s10450-020-00273-w.

[353] E. Mangano, S. Brandani, and D. M. Ruthven, 'Analysis and Interpretation of Zero Length Column Response Curves', *Chemie Ingenieur Technik*, vol. 85, no. 11, pp. 1714–1718, 2013, doi: 10.1002/cite.201300083.

[354] R. Span and W. Wagner, 'A New Equation of State for Carbon Dioxide Covering the Fluid Region from the Triple-Point Temperature to 1100 K at Pressures up to 800 MPa', *J Phys Chem Ref Data*, vol. 25, no. 6, pp. 1509–1596, 1996, doi: 10.1063/1.555991.

[355] Y. Duan *et al.*, 'ab initio Thermodynamic Study of the CO_2 Capture Properties of M_2CO_3 (M = Na, K)- and $CaCO_3$-Promoted MgO Sorbents Towards Forming Double Salts', *Aerosol Air Qual Res*, vol. 14, no. 2, pp. 470–479, 2014, doi: 10.4209/AAQR.2013.05.0178.

[356] S. Brandani, 'A Simple Graphical Check of Consistency for Zero Length Column Desorption Curves', *Chem Eng Technol*, vol. 39, no. 6, pp. 1194–1198, 2016, doi: 10.1002/CEAT.201500634.

[357] C. v. Miguel *et al.*, 'High temperature CO2 sorption with gallium-substituted and promoted hydrotalcites', *Sep Purif Technol*, vol. 127, pp. 202–211, 2014, doi: 10.1016/j.seppur.2014.03.007.

[358] M. M. Dubinin, 'Theory of the physical adsorption of gases and vapors and adsorption properties of adsorbents of various natures and porous structures', *Bulletin of the Academy of Sciences of the USSR, Division of chemical science 1961 9:7*, vol. 9, no. 7, pp. 1072–1078, Jul. 1960, doi: 10.1007/BF01161525.

[359] N. A. Al-Baghli and K. F. Loughlin, 'Adsorption of Methane, Ethane, and Ethylene on Titanosilicate ETS-10 Zeolite', *J Chem Eng Data*, vol. 50, no. 3, pp. 843–848, 2005, doi: 10.1021/je0496793.

Submission of Thesis Declaration by Supervisor
Strictly Confidential

<u>Candidate</u>

Name *(in capitals):*	LI ANNE CHEAH	HW Person ID:	H00206888
School:	EPS	Degree Sought:	PHD (research)

<u>Declaration</u>

I believe the thesis to contain the sole work of the candidate, with other work adequately referenced.	Yes	Y	No

The thesis has been checked using an approved plagiarism detection application e.g. Turnitin.	Yes	Y	No

I believe the thesis to be in a suitable presentational form and is ready for examination.*	Yes	Y	No
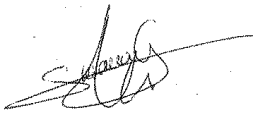
* For guidance on the format for presentation please refer to:
  <u>https://www.hw.ac.uk/students/studies/examinations/thesis.htm</u>

If you do not believe the thesis to be in a suitable form and should not be examined, or if you have any concerns about the thesis being submitted, please give details below:

Primary Supervisor

Print Name:	SUSANA GARCIA LOPEZ	Date:	01.03.2022
Signature:		School:	EPS

Notes

This form should be completed after the thesis has been bound. The thesis must conform in layout, binding and presentation to the requirements prescribed by the Senate. The completed form must be lodged with the Student Service Centre at the time when the thesis is submitted.

Internal Examiners Declaration Form

(This form must be typed and all sections completed)

Candidate's Name:	Li Anne Cheah	Heriot-Watt Person ID:	H000206888
School:	Engineering and Physical Sciences	Degree Sought:	Doctor of Philosophy
Campus: *(If off-campus please state location)*	Edinburgh		

Declaration

1. I confirm that the corrections to the thesis of the above named have been carried out to the satisfaction of the examiners

   Yes [x]   No [ ]   N/A [ ]

2. I confirm that the Joint Examiners Report Form states recommendation (c) - 'Award degree following satisfactory completion of significant corrections to the satisfaction of the Internal Examiner'

   Yes [ ]   No [x]

   If yes,

   - Please provide details below to demonstrate that the particular corrections are satisfactory.
   - Confirm that the corrections have been completed within the period of time given, if not please give an explanation.

3. I confirm that the Joint Examiners Recommendation was originally: Re-submit

   (decision (d or e) on the previous Joint Examiners Form)

   Yes [ ]   No [x]

4. I confirm that thesis title has changed since the temporary thesis was submitted. **If yes,** please provide details of amended title here:

   Yes [ ]   No [x]

5. I confirm that I have seen the final version of this thesis and it has been presented in

    accordance with University regulations.

    Yes [x]

Internal Examiner

Print Name:	Ruaraidh McIntosh	Date:	23/2/22
Signature:		School:	EPS

Notes

1. The Internal Examiner's Declaration Form should be submitted along with the final electronic copy of the thesis through the Postgraduate Research Thesis Submission site